HIGH ENERGY COLLIDERS AND HIDDEN SECTORS

A Dissertation

Presented to the Faculty of the Graduate School

of Cornell University

in Partial Fulfillment of the Requirements for the Degree of

Doctor of Philosophy

by

Asaf Jeff Dror

December 2017

HIGH ENERGY COLLIDERS AND HIDDEN SECTORS

Asaf Jeff Dror, Ph.D.

Cornell University 2017

This thesis explores two dominant frontiers of theoretical physics, high energy colliders and hidden sectors. The Large Hadron Collider (LHC) is just starting to reach its maximum operational capabilities. However, already with the current data, large classes of models are being put under significant pressure. It is crucial to understand whether the (thus far) null results are a consequence of a lack of solution to the hierarchy problem around the weak scale or requires expanding the search strategy employed at the LHC. It is the duty of the current generation of physicists to design new searches to ensure that no stone is left unturned. To this end, we study the sensitivity of the LHC to the couplings in the Standard Model top sector. We find it can significantly improve the measurements on Zt_Rt_R coupling by a novel search strategy, making use of an implied unitarity violation in such models. Analogously, we show that other couplings in the top sector can also be measured with the same technique. Furthermore, we critically analyze a set of anomalies in the LHC data and how they may appear from consistent UV completions. We also propose a technique to measure lifetimes of new colored particles with non-trivial spin.

While the high energy frontier will continue to take data, it is likely the only collider of its kind for the next couple decades. On the other hand, low-energy experiments have a promising future with many new proposed experiments to probe the existence of particles well below the weak scale but with small couplings to the Standard Model. In this work we survey the different possibilities, focusing

on the constraints as well as possible new hidden sector dynamics. In particular, we show that vector portals which couple to an anomalous current, e.g., baryon number, are significantly constrained from flavor changing meson decays and rare Z decays. Furthermore, we present a new mechanism for dark matter freezeout which depletes the dark sector through an out-of-equilibrium decay into the Standard Model.

BIOGRAPHICAL SKETCH

Jeff Dror was born in Israel on May 25th, 1990. He moved to Toronto, Canada at age 5 and stayed there until he was 21 (other than a one year stint back in Israel). Over this time he attended several public schools: West Preparatory Junior Public School, Brenner Public School,Pleasant Public School, Fisherville Senior Public School, and Westmount Collegiate Institute, which managed to prepare him with a decent understanding of Mathematics and minimal social skills. Out of a desire to have a career with actual prospects, he enrolled at York University in a Biology program with the intention of applying to Medical School. A few months into his first year at the university, the graduate student and contract workers union went on strike, shutting down the institution for almost 3 months. Out of severe boredom, he began to routinely visit the local library to pick up books to read. He quickly found he was primarily taking out physics books and what started as an aimless exercise, resulted in a passion for physics. Shortly after the resumption of classes, he switched his major to physics and never looked back.

After four years of pursuing his undergraduate degree, Jeff was accepted into a Ph.D. program at Cornell University. There he began learning to become a full time researcher under the guidance of Yuval Grossman. To Jeff's great pleasure, Yuval provided Jeff with a mentor-ship style filled with a tremendous amount of intellectual freedom to pursue his own ideas, find his niche in the field, and develop as a physicist. After a successful Ph.D. he will be continuing his work in theoretical high energy physics as a postdoctoral researcher at University of California, Berkeley.

This work is dedicated to the amazing collection of people that helped me get to where I am today

ACKNOWLEDGEMENTS

After so many years leading up to this dissertation, it's humbling to realize how many people have made significant contributions to my studies. I start with an apology to those that I will inevitably overlook. Nevertheless, I will try to do as best I can.

First and foremost I want to thank my advisor, Yuval Grossman, for teaching me how to be real life physicist. I cannot emphasize enough how much I appreciate the time and effort spent on ensuring my success in the field. I could not have asked for a better mentor. Furthermore, I want my committee members Csaba Csaki and Julia Thom as well as Maxim Perelstein for many insightful discussions on physics, and general guidance.

Next I want to thank Lisa Senensky for supporting me throughout all my studies. Her constant encouragement has given me the confidence and focus that I have today. It may say my name on the dissertation, but if I could, I would make her a co-author. Secondly, I thank my family for their help along with the love and support. My father, Yigal Dror, has always been my academic role model that I strive to live up to. My mother, Irit Dror, has provided me with endless care and help in keeping me on my feet. My brother, Boaz Dror, has been an example for me to follow. Lastly, my sister, Amber Dror, never wavered her faith in my abilities.

I also want to thank the many friends who've propelled forward my career during my time at Cornell. I consider my success today to have been strongly influenced by the endless discussions which resulted in the cementing of my understanding of physics. In particular, I thank Moshe Kellerstein for the thousands of Skype conversations (yes I think that number is correct...) and for always being available to discuss physics and reserving judgment during my barrage of dumb

questions. Next I want to thank Salvator Lombardo (for constantly willing to give me advice as well as keeping me physically and mentally strong), Eric Kuflik (for providing me with new ideas and prospective), Wee Hao Ng (for having the patience to explain both high school and graduate level physics to me), Jack Collins (for evaluating every new paper on the arXiv with me), Ofri Telem (for keeping me sane in crazier times), and Gowri Kurup (for putting up with my occasional ridiculousness).

I also want the thank the many professors who have acted as my mentors throughout my time at York University. Roman Koniuk, Randy Lewis, Veronica Sanz, Eric Hessels, Cody Storry, and A Kumarakrishnan, you have had a profound influence on me, both in my understanding of physics and on my prospects in the field.

Lastly, there have been many people who passed through Cornell and had a significant positive impact on my time here. I want to thank John Stout, Liam McAllister, Tom Hartman, Marco Farina, Simon Lowe, and Yu-Dai Tsai.

TABLE OF CONTENTS

LIST OF TABLES

LIST OF FIGURES

CHAPTER 1

INTRODUCTION

1.1 Inspirational preface

The field of fundamental physics has reached a cross-roads. The focus of the community has long been on the high energy frontier and the hope that large-scale colliders will lead the searches for physics beyond the Standard Model (SM). However, with the lack of clear direction from the experimental side, it's not clear how to invest our future intellectual and financial efforts.

It is possible the Large Hadron Collider (LHC) will be the only collider to probe the TeV-scale in the coming decades. The current LHC search program was originally designed to test particular classes of models that have dominated the field for the past decades, namely ones which solve the hierarchy problem (the observation that in the absence of fine-tuning, quantum corrections drive scalar masses to the scale of the cutoff of the theory, in contrast to the observed Higg's mass in the SM which is much below the Planck scale). However, as experiments put more pressure on the standard candidates to surpass the SM, it becomes increasingly likely that the LHC will not play the role of a discovery machine, but instead of a precision machine. With this in mind, it is time to re-evaluate the type of measurements we want to carry out to maximize the potential to probe, not only the interesting prospects of today's generation of physicists, but also to measure quantities which will be relevant in the long-term future.

At the same time, particle physics in the coming decades will be largely focused on the, lower-energy, intensity frontier. Smaller-scale experiments generically aim

to probe hidden-sectors (new particles lighter than the electroweak scale with small couplings to the SM). Such particles are primarily theoretically motivated by the existence of dark matter, the potential of axions to solve the strong-CP problem, and attempts to address observed experimental anomalies. However, more generally, hidden sectors are an experimentally viable, simple, extension of the Standard Model that could easily have evaded current experiments. Improving our understanding of low energy physics has a prosperous future and a lot of room for new ideas.

The focus of the work in this thesis is to explore new physics from both these perspectives. We begin with studies utilizing the high energy frontier proposing new searches as well as analyze several anomalies which have surfaced over the past few years. Then we move on to explorations into possible hidden sectors coupling to the Standard Model, with an emphasis on new constraints and dark matter model building.

1.2 Novel high energy measurements

In the high energy frontier there are essentially two types of experimental searches

1. Direct searches for a new physics model
2. Measurements of the consistency of the Standard Model

The first type of measurement, direct searches for new physics, are far and away the most popular approach at the LHC. They have the advantage that they are usually more sensitive to the model of interest. This makes this strategy an ideal tool to constrain well-motivated extensions to the SM, however they are usually

optimized for a particular production/decay chain limiting their utility to discover alternative models. Nevertheless, the incredibly broad program underway at the LHC does result in some sensitivity to variations of the standard paradigms.

In this work, we study a variation of one such paradigm, the Minimal Supersymmetric Standard Model (MSSM), where a partner for each particle in the SM is added with different spin. Putting the particles into multiplets with their "opposite spin"-partners enforces a cancellation between the corrections to the scalar masses rendering the theories stable under renormalization group corrections. However, the robustness to quantum corrections is only efficient if there exists an approximate degeneracy between the fermionic and bosonic partners. Therefore, models make a striking prediction: to ensure the Higg's remains light, new particles should exist around the weak scale. However, the lack of any hint of these new states has urged the community to reconsider the assumptions that went in to building this framework. Popular modifications include allowing for baryon/lepton number violation (as in R-parity violating supersymmetry [4]), rearranging the mass spectrum (as in split supersymmetry [5]), and expanding the scalar sector (as in the NMSSM [6] and stealth SUSY [7]). In part of this work, we reanalyze the constraints on a different modification of the MSSM framework where the Higg's boson is identified with the bosonic partner of one of the leptons.

If new physics is to appear at the collider frontier it will inevitably start off as a small excess in experimental data. Scrutinizing these anomalies experimentally and theoretically has a two-fold benefit. Firstly, searches often use intricate tools which may overlook subtle features of the backgrounds. Additional theoretical input can ensure that the experimental procedure correctly estimates the uncertainties and the Standard Model contribution to the measurements. Furthermore, experimental

anomalies help drive the theoretical community into new avenues of model building. The most prominent examples of these features was in light dark matter research which was largely spurred by DAMA [1,2] and CoGenT [3] anomalies (see e.g., [8]). As expected from any such experiment the LHC experiments have produced several anomalies, most of which have now been all but ruled out with more data. Most prominently have been the $eejj/e\nu jj$ [9,10], on-Z+jets [11], 750 GeV diphoton [12, 13], and the diboson excess [14]. In this work we explore the first three in some detail.

In addition to direct searches for new physics, we can also perform tests on the consistency of the Standard Model. This typically involves measuring cross-sections or decay rates which puts constraints on deviations from the SM-predictions for the couplings or the scale of any higher dimensional operators. On a whole, a hadron collider is not the optimal tool to measure such quantities as it has an irreducible systematic uncertainty at roughly the 10% level primarily arising from the Jet Energy Scale [15, 16]. Nevertheless, for rare processes (that usually require a substantial center of mass energy), the LHC is still our current best estimate of such parameters.

The Standard Model with massless neutrinos has 19 free parameters (4 mixing angles and phase in the quark sector, 9 masses for the quarks and leptons, 3 gauge couplings, the Higg's mass and self-coupling, and the θ angle). For the most part, the parameters for which the LHC has sensitivity are the top, bottom,charm, and tau masses, the gauge couplings, and the Higg's mass and self-coupling (it may have some sensitivity to the quark mixing angles and the muon mass though this is yet to be seen). Other than the Higg's parameters these have all been measured at previous machines, giving the LHC a unique opportunity to check the consistency

of previous measurements with new experiments. The most poorly tested parts of the Standard Model are the Higgs and top coupling making them an important target for the LHC.

Checking the consistency of the Standard Model between different experiments is far from trivial check. As one example, consider the top mass parameter, known to be about 175 GeV. This parameter is indirectly probed through many processes at the LHC. In particular, measurements such as the inclusive $t\bar{t}$ [17,18] probe the mass of the tops through the overall cross-section and $t\bar{t}h$ production [19,20] probes the couplings of the top to the Higgs. Extensions of the Standard Model often lead to discrepancies between these predictions (one popular example would be two higgs doublet models) making such measurements useful in constraining any deviations from the SM. Furthermore, such measurements offer a robust, generic, test of new physics without reliance on any beyond SM framework. In this work we review the current constraints on the top couplings. We show that the most poorly measured parameters are the $Z\bar{t}_R t_R$ and $h\bar{t}t$ couplings and offer novel ways to probe any deviations in the couplings directly.

1.3 Hidden sectors

Hidden sectors can interact with the SM in many different ways. We can characterize these by the type of mediator connecting the two sectors. At dimension four there are three types of interactions or portals (there is one portal at dimension 3, $S|H|^2$). Which of these are present, if any, depends on the particle content. The three possible portals are the scalar, fermionic, and vector portals, depicted schematically in Fig. 1.1.

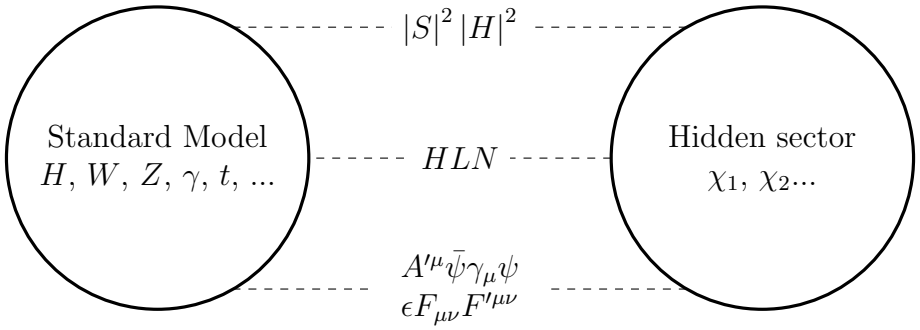

Figure 1.1: The different possible portals connected the dark and Standard Model sectors. The top portal corresponds to the scalar portal with adding a new scalar, S. The middle portal corresponds to the fermionic portal where we introduce a new SM singlet, N, also known as the right-handed neutrino portal. The bottom portal corresponds to the vector portal with a new light vector coupled to the SM either through charging the SM under a new gauge symmetry or kinetic mixing.

There is a large-scale effort to better constrain each portal and its possible relation to existence of dark matter. The scalar portal is the most minimal as it only requires adding one additional degree of freedom [23]. The scalar can act as dark matter on its own or through coupling to additional SM-singlet fields. It also makes a robust prediction of additional Higgs decays. It is generically still allowed though with many constraints from both low and high energy physics, particularly if it is the mechanism that drives dark matter freezeout [23, 24]. The fermionic portal is naturally motivated by the observation of neutrino masses as the fermionic mediator can be identified with a light sterile neutrino. The right handed neutrinos themselves can act as dark matter though then they can never thermalize (see e.g., [25] for a review). Alternatively, they can act as a mediator to the dark sector [26, 27].

Lastly, the vector portal has probably received the most attention. Adding elementary vectors in a way that preserves unitarity requires imposing gauge invariance. Perhaps the simplest possibility is to keep the SM particle content in-

variant under the new gauge symmetry. If this is the case, the new vector can still couple to the SM through kinetic mixing [28]. Even if kinetic mixing is set to zero at tree-level it will be induced through loop corrections if there are some (heavy) particles charged under both the dark and SM sectors. Alternatively, one could consider gauging (approximate) symmetries of the SM. The only anomaly-free combination available in the SM is that of $B-L$ (after adding 3 right-handed neutrinos) [1]. Keeping right-handed neutrinos from over-closing the universe and evading experimental constraints is very restrictive and leads to the requirement of vector masses above the TeV scale [29]. The requirement of the gauge symmetry being anomaly-free can be relaxed if new heavy fermions unitarize the theory at the higher scale. In this case, one can gauge other combinations of SM fermions. This has the advantage that the constraints can be significantly relaxed, allowing for much light vectors. A popular example is gauge baryon number, where the new vector doesn't couple to leptons at tree level alleviating the constraints.

Allowing for non-traditional portals between the SM and the dark sector has profound implications for the thermal history of the universe. In particular, dynamics in the dark sector can be drastically different then the standard Weakly Interacting Massive Particle (WIMP) paradigm. This permits dark matter candidates with masses widely different from the weak scale, spanning a wide range of masses from about 10^{-22}eV (keV) for a scalar (fermion) to 10^{55}eV [30]. However, the situation isn't as bleak as it seems as most thermal dark matter candidates must freeze-out before big bang nucleosynthesis and within the unitarity bound, restricting their masses to roughly between the electron mass and hundreds of TeV.

[1] One can also gauge linear combinations of $B-L$ and EM, though it requires adding in new electroweak-charged states.

1.4 Thesis Map

This thesis is structured as follows. In chapters 2,3,4 we focus on physics at high energy colliders, studying new search strategies as well as implications on alternative model-building efforts. In chapters 5,6 we move on to hidden sectors, considering both alternative thermal histories for dark matter and new constraints on a prominent portal between the SM and dark sector. Lastly in chapters 7,8,9 we consider a few experimental anomalies at the LHC, analyzing their validity and how they can be included in a more complete framework.

This work was done in collaboration with an extensive list of collaborators. Chapter 5 is based on [31] and was done with in collaboration with Robert Lasenby and Maxim Pospelov. Chapter 6 is based on [32] and completed with Wee Hao Ng and Eric Kuflik. Chapter 2 is based on [33] and was done in collaboration with Marco Farina, Ennio Salvioni, and Javi Serra. Chapter 4 is based on work done with Yuval Grossman in [34]. Chapter 3 is based on work done in collaboration with Carla Biggio, Yuval Grossman, and Wee Hao Ng in [35]. Chapter 7 is based on [36] and completed with Josh Berger and Wee Hao Ng. Chapter 8 is based on work done with Jack Collins, Csaba Csaki, and Salvator Lombardo presented in [37]. Lastly, the work in Chapter 9 was done in collaboration with Jack Collins and Marco Farina and is based on [38].

BIBLIOGRAPHY

[1] R. Bernabei *et al.* [DAMA Collaboration], Eur. Phys. J. C **56**, 333 (2008) doi:10.1140/epjc/s10052-008-0662-y [arXiv:0804.2741 [astro-ph]].

[2] R. Bernabei *et al.* [DAMA and LIBRA Collaborations], Eur. Phys. J. C **67**, 39 (2010) doi:10.1140/epjc/s10052-010-1303-9 [arXiv:1002.1028 [astro-ph.GA]].

[3] C. E. Aalseth *et al.* [CoGeNT Collaboration], Phys. Rev. Lett. **106**, 131301 (2011) doi:10.1103/PhysRevLett.106.131301 [arXiv:1002.4703 [astro-ph.CO]].

[4] R. Barbier *et al.*, Phys. Rept. **420**, 1 (2005) doi:10.1016/j.physrep.2005.08.006 [hep-ph/0406039].

[5] N. Arkani-Hamed and S. Dimopoulos, JHEP **0506**, 073 (2005) doi:10.1088/1126-6708/2005/06/073 [hep-th/0405159].

[6] U. Ellwanger, C. Hugonie and A. M. Teixeira, Phys. Rept. **496**, 1 (2010) doi:10.1016/j.physrep.2010.07.001 [arXiv:0910.1785 [hep-ph]].

[7] J. Fan, M. Reece and J. T. Ruderman, JHEP **1111**, 012 (2011) doi:10.1007/JHEP11(2011)012 [arXiv:1105.5135 [hep-ph]].

[8] M. I. Gresham and K. M. Zurek, Phys. Rev. D **89**, no. 1, 016017 (2014) doi:10.1103/PhysRevD.89.016017 [arXiv:1311.2082 [hep-ph]].

[9] CMS Collaboration [CMS Collaboration], CMS-PAS-EXO-12-041.

[10] V. Khachatryan *et al.* [CMS Collaboration], Eur. Phys. J. C **74**, no. 11, 3149 (2014) doi:10.1140/epjc/s10052-014-3149-z [arXiv:1407.3683 [hep-ex]].

[11] G. Aad *et al.* [ATLAS Collaboration], Eur. Phys. J. C **75**, no. 7, 318 (2015) Erratum: [Eur. Phys. J. C **75**, no. 10, 463 (2015)] doi:10.1140/epjc/s10052-015-3661-9, 10.1140/epjc/s10052-015-3518-2 [arXiv:1503.03290 [hep-ex]].

[12] The ATLAS collaboration, ATLAS-CONF-2015-081.

[13] CMS Collaboration [CMS Collaboration], collisions at 13TeV," CMS-PAS-EXO-15-004.

[14] G. Aad *et al.* [ATLAS Collaboration], JHEP **1512**, 055 (2015) doi:10.1007/JHEP12(2015)055 [arXiv:1506.00962 [hep-ex]].

[15] M. Aaboud *et al.* [ATLAS Collaboration], arXiv:1703.09665 [hep-ex].

[16] V. Khachatryan *et al.* [CMS Collaboration], JINST **12** (2017) no.02, P02014 doi:10.1088/1748-0221/12/02/P02014 [arXiv:1607.03663 [hep-ex]].

[17] G. Aad *et al.* [ATLAS Collaboration], Eur. Phys. J. C **74**, no. 10, 3109 (2014) Addendum: [Eur. Phys. J. C **76**, no. 11, 642 (2016)] doi:10.1140/epjc/s10052-016-4501-2, 10.1140/epjc/s10052-014-3109-7 [arXiv:1406.5375 [hep-ex]].

[18] V. Khachatryan *et al.* [CMS Collaboration], JHEP **1608**, 029 (2016) doi:10.1007/JHEP08(2016)029 [arXiv:1603.02303 [hep-ex]].

[19] The ATLAS collaboration [ATLAS Collaboration], ATLAS-CONF-2016-068.

[20] CMS Collaboration [CMS Collaboration], CMS-PAS-HIG-17-004.

[21] G. Aad *et al.* [ATLAS Collaboration], Phys. Lett. B **756**, 228 (2016) doi:10.1016/j.physletb.2016.03.017 [arXiv:1511.05980 [hep-ex]].

[22] N. Faltermann [CMS Collaboration], arXiv:1611.08443 [hep-ex].

[23] C. P. Burgess, M. Pospelov and T. ter Veldhuis, Nucl. Phys. B **619**, 709 (2001) doi:10.1016/S0550-3213(01)00513-2 [hep-ph/0011335].

[24] G. Krnjaic, Phys. Rev. D **94**, no. 7, 073009 (2016) doi:10.1103/PhysRevD.94.073009 [arXiv:1512.04119 [hep-ph]].

[25] B. Shakya, Mod. Phys. Lett. A **31**, no. 06, 1630005 (2016) doi:10.1142/S0217732316300056 [arXiv:1512.02751 [hep-ph]].

[26] M. Escudero, N. Rius and V. Sanz, JHEP **1702**, 045 (2017) doi:10.1007/JHEP02(2017)045 [arXiv:1606.01258 [hep-ph]].

[27] M. Escudero, N. Rius and V. Sanz, arXiv:1607.02373 [hep-ph].

[28] B. Holdom, Phys. Lett. **166B**, 196 (1986). doi:10.1016/0370-2693(86)91377-8

[29] N. Okada and S. Okada, Phys. Rev. D **93**, no. 7, 075003 (2016) doi:10.1103/PhysRevD.93.075003 [arXiv:1601.07526 [hep-ph]].

[30] M. Lisanti, doi:10.1142/97898131494410007 arXiv:1603.03797 [hep-ph].

[31] J. A. Dror, R. Lasenby and M. Pospelov, arXiv:1705.06726 [hep-ph].

[32] J. A. Dror, E. Kuflik and W. H. Ng, Phys. Rev. Lett. **117**, no. 21, 211801 (2016) doi:10.1103/PhysRevLett.117.211801 [arXiv:1607.03110 [hep-ph]].

[33] J. A. Dror, M. Farina, E. Salvioni and J. Serra, JHEP **1601**, 071 (2016) doi:10.1007/JHEP01(2016)071 [arXiv:1511.03674 [hep-ph]].

[34] J. A. Dror and Y. Grossman, JHEP **1406**, 171 (2014) doi:10.1007/JHEP06(2014)171 [arXiv:1311.4542 [hep-ph]].

[35] C. Biggio, J. A. Dror, Y. Grossman and W. H. Ng, JHEP **1604**, 150 (2016) doi:10.1007/JHEP04(2016)150 [arXiv:1602.02162 [hep-ph]].

[36] J. Berger, J. A. Dror and W. H. Ng, JHEP **1509**, 156 (2015) doi:10.1007/JHEP09(2015)156 [arXiv:1506.08213 [hep-ph]].

[37] J. H. Collins, C. Csaki, J. A. Dror and S. Lombardo, Phys. Rev. D **93**, no. 11, 115001 (2016) doi:10.1103/PhysRevD.93.115001 [arXiv:1603.09350 [hep-ph]].

[38] J. H. Collins, J. A. Dror and M. Farina, Phys. Rev. D **92**, no. 9, 095022 (2015) doi:10.1103/PhysRevD.92.095022 [arXiv:1508.02419 [hep-ph]].

CHAPTER 2

STRONG tW SCATTERING AT THE LHC

2.1 Introduction

The large center of mass energies accessible at the LHC make it the optimal machine to explore the electroweak scale. This has already been confirmed by the discovery of the Higgs boson [1,2], which represents the main achievement of Run-1 and a major step forward for particle physics. Another important example of the power of the LHC is the large rate for production of the top quark, the particle in the Standard Model (SM) with the largest coupling to the Higgs field. However, our knowledge of the properties of both the Higgs and the top is still relatively poor. Since these two particles play a central role in theories beyond the SM (BSM) that provide a deeper understanding of electroweak symmetry breaking (EWSB), the program of Higgs and top coupling measurements is one of the priorities of LHC Run-2. The importance of this task is reinforced by the thus far lack of evidence for direct production of BSM particles, which may suggest that probes of the Higgs and top sectors are our best opportunity to gain new insights into the mechanism of EWSB.

The complicated hadronic environment at the LHC, however, does not facilitate the desired experimental precision. For example, experimental tests of the Ztt and htt couplings are very challenging: the conventional strategy consists in measuring the cross section for $t\bar{t}Z$ and $t\bar{t}h$ production, respectively. These processes have a relatively high mass threshold and thus suppressed production rates at the LHC. This leads to very loose constraints on the top couplings, currently well above the SM expectations. On the other hand, projections indicate that the htt coupling

could be measured with 15% accuracy by the end of Run-2 [3], whereas the expected precision on Ztt is worse, and deviations as large as 50-100% will not be excluded [4–6].

One is then prompted to ask if there exists another avenue to probe the properties of the Higgs and the top. An answer has been given already for the couplings of the Higgs boson: if the Higgs couplings to the electroweak gauge bosons depart from the SM predictions, the amplitudes for the scattering of the longitudinally polarized $V = W, Z$ and Higgs h undergo a rapid growth with momentum above the weak scale $v \simeq 246\,\text{GeV}$. The prime example is $VV \to VV$ scattering, which grows with momenta as p^2/v^2 whenever the hVV coupling deviates from the SM [7], while the process $VV \to hh$ provides complementary information [8]. Such growth with energy is a distinctive feature of models where the Higgs emerges as a pseudo-Goldstone boson from a strongly-coupled sector [9–11]. In this class of theories, the high-energy enhancement can be accessed without directly producing the BSM resonances, which are strongly coupled to the Higgs but heavy. In complete analogy, the electroweak couplings of the top could be probed in the high-energy scattering of third generation fermions and longitudinal gauge bosons or Higgses. A growth with energy of the associated amplitudes would constitute a genuine signal of the strong coupling of the top to the BSM sector [12–14]. It was observed a long time ago [15] that a deviation from the SM in the $h\psi\psi$ coupling (with ψ a SM fermion) leads to a growth proportional to $m_\psi p/v^2$ of scattering amplitudes such as $\psi\bar{\psi} \to VV$, and this observation was recently exploited in Refs. [16, 17] to constrain the htt coupling at the LHC, via the scattering $bW \to th$ in the $pp \to thj$ process [18].

In this paper we perform a general analysis of the scattering of tops (and bot-

toms) with the longitudinal W, Z or the Higgs. We point out that in the presence of deviations in the Ztt couplings, certain amplitudes grow like p^2/v^2 (rather than $m_t p/v^2$), leading to an enhanced sensitivity at the LHC. The $tW \to tW$ amplitude is singled out as the most promising one, because deviations in either the $Zt_L t_L$ or $Zt_R t_R$ couplings lead to the strong high-energy behavior. Furthermore, the corresponding LHC process is $pp \to t\bar{t}Wj$, which gives a clean same-sign leptons signature. We perform a detailed analysis of this signal, exploiting the information contained in the CMS 8 TeV search for $t\bar{t}W$ of Ref. [19], and show that it gives stronger constraints than the conventional strategy relying on $pp \to t\bar{t}Z$. Motivated by the effectiveness of our approach at 8 TeV, we then design a specific search for Run-2 at 13 TeV, which we hope will help in refining the physics analyses of the experimental collaborations.

We also interpret our analysis in terms of non-standard top couplings arising from dimension-6 (dim-6) operators added to the SM Lagrangian, and show that competitive bounds are obtained in this case too. In this framework, correlations arise between the couplings of the top to the Z and to the W. Moreover, deviations in these couplings imply a p^2/v^2 growth not only of the tV scattering amplitudes, but also of those involving the Higgs, such as $bW \to th$ [20]. Thus, the interest of our approach does not end here: we discuss several other amplitudes that we believe to be promising in probing the top electroweak couplings, and that warrant further work to assess the expected sensitivity at the LHC.

Our paper is organized as follows. In Sec. 2.2 we introduce our parameterization of couplings in the top-Higgs sector, discuss the current experimental constraints and outline the generic aspects of the scattering of third generation fermions with electroweak vector bosons and Higgses. Section 2.3 contains the discussion of the

$tW \to tW$ scattering and the associated LHC process $pp \to t\bar{t}Wj$, as well as the main results of our paper. Section 2.4 contains the technical details of our collider analysis of $t\bar{t}Wj$, as well as the description of the method we use to obtain constraints on the top-Z interactions. This section can be omitted by the reader interested only in the results, who can move on to Sec. 2.5, where we discuss other scattering processes that may provide additional information on the top-Higgs sector. Finally, Sec. 2.6 contains our conclusions. Three Appendices complete the paper: App. 2.A presents the electroweak chiral Lagrangian for the top sector, App. 2.B summarizes the current and projected constraints on top-Z couplings obtained from $pp \to t\bar{t}Z$, and App. 2.C details the procedure we adopt to simulate 'fake' leptons, which constitute one of the main backgrounds to our $t\bar{t}Wj$ signal.

2.2 Parameterization of top and Higgs couplings

In this section we introduce the general parameterization of the couplings relevant for the scattering of top quarks with the electroweak vector bosons W and Z and with Higgs boson h. The interactions of the top (and bottom) are encoded in the phenomenological Lagrangian

$$\begin{aligned}\mathcal{L}_t = {} & Z_\mu\, \bar{t}\gamma^\mu \big[c_L(h)\, g_{Zt_Lt_L} P_L + c_R(h)\, g_{Zt_Rt_R} P_R\big] t + Z_\mu\, \bar{b}\gamma^\mu \big[c_{L^b}(h)\, g_{Zb_Lb_L} P_L + c_{R^b}(h)\, g_{Zb_Rb_R} P_R\big] b \\ & + g_{Wt_Lb_L} W^+_\mu \bar{t}\gamma^\mu \big[c_{LL}(h) P_L + c_{RR}(h) P_R\big] b + \text{h.c.} - c_t(h) \frac{m_t}{v} h\, \bar{t}t \ , \end{aligned} \tag{2.1}$$

where $P_{L,R}$ are the left (L) and right (R) chiral projectors, $g_{Wt_Lb_L} = g/\sqrt{2}$, $g_{Zf_Rf_R} = -(gs_w^2/c_w)Q_f$, $g_{Zf_Lf_L} = (g/c_w)(T^3_{L,f} - Q_f s_w^2)$ are the SM gauge couplings, and $v \simeq 246\,\text{GeV}$. We have defined the coefficients above as linear functions of h,

$$c_i(h) \equiv c_i + 2c_i^h \frac{h}{v} \ , \tag{2.2}$$

($i = \{L, R, L^b, R^b, LL, RR, t\}$), such that they also encode BSM couplings of the Higgs. We will also describe the hVV and Higgs cubic couplings with the Lagrangian

$$\mathcal{L}_h = c_V \frac{m_W^2}{v} h \left(2W_\mu^+ W^{-\mu} + \frac{1}{c_w^2} Z_\mu Z^\mu \right) - c_3 \frac{m_h^2}{2v} h^3 \ . \tag{2.3}$$

The coefficients c_i, c_i^h, c_V and c_3 parameterize the relevant couplings of the third generation fermions, W, Z, and h. The SM Lagrangian is reproduced for

$$c_L = c_R = c_{L^b} = c_{R^b} = c_{LL} = c_t = c_V = c_3 = 1 \ , \quad c_{RR} = 0 \ , \quad c_i^h = 0 \, . \tag{2.4}$$

We now wish to comment on the rationale behind our parameterization. As explained in App. 2.A, the phenomenological Lagrangian in Eqs. (2.1) and (2.3) can be regarded as the unitary gauge version of the leading set of operators, in an expansion in derivatives, of the electroweak chiral Lagrangian [21, 22] (for recent thorough discussions of the electroweak chiral Lagrangian, see Refs. [8,23]). We are neglecting, for instance, BSM chirality-flipping interactions of the fermions with W and Z, which arise at the next order in the derivative expansion. Denoting by Λ the mass scale of the new physics resonances, such interactions are generically suppressed by p/Λ with respect to the ones we consider here, with p characterizing the momenta of the process. Due to the chirality flip, they are further suppressed by y_t/g_*, with g_* a generic BSM coupling satisfying $g_* \leqslant 4\pi$. A notable class of chirality-flipping interactions are dipole-type operators, whose schematic structure is, for example, $\sim \bar{t}_L \sigma^{\mu\nu} t_R Z_\mu p_\nu$. In addition to the previous considerations, dipole operators are not generated at tree level if the transverse SM gauge fields are external to the BSM sector and coupled to it through weak gauging of the corresponding symmetries, as we assume.[1] We also set the triple gauge interactions to their SM values. We choose to do so because in theories where the SM gauge bosons are

[1]Besides, constraints on top dipole moments, either direct from top decay and single top production measurements [24], or indirect from the experimental limits on $b \to s$ transitions [25], are already significant.

weakly coupled to the BSM sector, generic deformations of the triple gauge interactions yield small effects in the processes we are interested in [20].[2] Finally, we will also be neglecting the small effects due to the bottom Yukawa coupling.

Theories where the typical scale of the BSM sector can be decoupled from the electroweak scale, $\Lambda/g_* \gg v$, admit a further expansion in the Higgs doublet field H. In such a case BSM effects from heavy resonances can be parameterized by operators of dimension larger than four built out of the SM fields. We are particularly interested in the dim-6 operators [9, 13]

$$\begin{aligned}\Delta\mathcal{L}_t = &\frac{i\bar{c}_L^{(1)}}{v^2} H^\dagger \overleftrightarrow{D_\mu} H \bar{q}_L \gamma^\mu q_L + \frac{i\bar{c}_L^{(3)}}{v^2} H^\dagger \sigma^a \overleftrightarrow{D_\mu} H \bar{q}_L \gamma^\mu \sigma^a q_L \\ &+ \frac{i\bar{c}_R}{v^2} H^\dagger \overleftrightarrow{D_\mu} H \bar{t}_R \gamma^\mu t_R + \frac{i\bar{c}_R^b}{v^2} H^\dagger \overleftrightarrow{D_\mu} H \bar{b}_R \gamma^\mu b_R + \left(\frac{i\bar{c}_R^{tb}}{v^2} \tilde{H}^\dagger \overleftrightarrow{D_\mu} H \bar{t}_R \gamma^\mu b_R + \text{h.c.} \right) \\ &+ \frac{\bar{c}_u y_t}{v^2} H^\dagger H \bar{q}_L \tilde{H} t_R + \text{h.c.} \,, \end{aligned} \tag{2.5}$$

where $\tilde{H} = i\sigma_2 H^*$ and we defined $H^\dagger \overleftrightarrow{D_\mu} H \equiv H^\dagger (D_\mu H) - (D_\mu H)^\dagger H$, etc.. These operators modify the couplings of the top (and bottom) to the W, Z, and h with respect to the SM, such that

$$c_L - 1 = c_L^h = \frac{\bar{c}_L^{(3)} - \bar{c}_L^{(1)}}{1 - \frac{4}{3}s_w^2} \,, \quad c_{L^b} - 1 = c_{L^b}^h = \frac{\bar{c}_L^{(1)} + \bar{c}_L^{(3)}}{1 - \frac{2}{3}s_w^2} \,, \quad c_{LL} - 1 = c_{LL}^h = \bar{c}_L^{(3)} \,, \tag{2.6}$$

$$c_R - 1 = c_R^h = \frac{\bar{c}_R}{\frac{4}{3}s_w^2} \,, \quad c_{R^b} - 1 = c_{R^b}^h = -\frac{\bar{c}_R^b}{\frac{2}{3}s_w^2} \,, \quad c_{RR} = c_{RR}^h = \bar{c}_R^{tb} \,, \tag{2.7}$$

$$c_t - 1 = \tfrac{4}{3} c_t^h = -\bar{c}_u \,. \tag{2.8}$$

Notice that at the dim-6 level none of the c_i^h coefficients is independent from the c_i's. Furthermore, while each of the R-handed couplings in Eq. (2.7) is affected by an independent dim-6 operator, the deviations in the L-handed ones, Eq. (2.6), are partially correlated. This is due to a remnant custodial symmetry of the dim-6 Lagrangian, which is broken by dim-8 operators [27], or absent altogether in the

[2] Additionally, current bounds on these couplings are already below 10%, and improved sensitivities from diboson production measurements are expected at the 13 TeV LHC run [26].

electroweak chiral Lagrangian, see App. 2.A. The dim-6 operators giving rise to non-standard contributions to the terms in Eq. (2.3) can be written as

$$\Delta\mathcal{L}_h = \frac{\bar{c}_H}{2v^2}(\partial_\mu|H|^2)^2 - \frac{\bar{c}_6\lambda}{v^2}|H|^6 \ , \tag{2.9}$$

with $c_V - 1 = -\bar{c}_H/2$ and $c_3 - 1 = \bar{c}_6 - 3\bar{c}_H/2$. The operator $\bar{c}_H$ also contributes to c_t by an amount $-\bar{c}_H/2$. The set of dim-6 operators in Eqs. (2.5) and (2.9) encode the leading non-standard effects in theories where both the Higgs and either the L- or R-handed top are strongly coupled to a BSM sector whose generic coupling strength is $g_* > g_{\rm SM}$, with $g_{\rm SM}$ the weak gauge or top Yukawa couplings. In such scenarios the corresponding $\bar{c}$ coefficients can be as large as

$$\bar{c} \lesssim \frac{g_*^2 v^2}{\Lambda^2} \equiv \xi \tag{2.10}$$

with $g_* \leqslant 4\pi$, barring $O(1)$ factors. Particularly relevant examples of such a situation are composite Higgs models with top partial compositeness [10, 11].[3] In such models the need to reproduce the large top Yukawa coupling forces one or both of the top chiral states to couple strongly to the composite sector. We would also like to stress that when $g_* \gg g_{\rm SM}$, the relative importance of probing non-standard top couplings versus direct searches for BSM resonances increases, given that larger values of the resonance mass Λ can be considered.[4]

Out of the BSM effects introduced above, in this work we will mostly focus on the couplings of the top to the Z, c_L and c_R, not only because of their impact on top scattering processes, but also because they are very weakly constrained by direct measurements. Up to date, the only bound comes from the analysis of $t\bar{t}Z$ production at the 7 TeV LHC [6], from which $O(1)$ deviations in c_L or c_R cannot

[3] In those models the Higgs field arises as a Nambu-Goldstone boson, and the parameter ξ defined in Eq. (2.10) is identified with v^2/f^2, where f is the Higgs decay constant.

[4] This is of special relevance, for instance, in composite Twin Higgs models, where the composite resonances, despite being heavy, remain strongly coupled to the Higgs and the top [28–30].

be excluded. In contrast, other BSM effects are already subject to significant constraints. The most stringent one is on the Zbb coupling: LEP1 measurements directly constrain c_{L^b} at the per-mille level, while the bound on c_{R^b} is at a few per-cent [31]. Due to the former constraint, BSM sectors are typically assumed to couple to q_L such that a custodial P_{LR} symmetry is preserved [32], yielding $c_{L^b} = 1$ to leading approximation. In terms of dim-6 operators, this implies $\bar{c}_L^{(1)} = -\bar{c}_L^{(3)}$. On the other hand, direct bounds on the Wtb coupling coefficients c_{LL} and c_{RR} from single top production [33] and W helicity fraction measurements are around 10% [24, 34]. Notice that in terms of dim-6 operators, the combined constraints on the Zb_Lb_L and Wt_Lb_L couplings, which bound both $\bar{c}_L^{(1)}$ and $\bar{c}_L^{(3)}$, imply BSM effects of at most $\sim 10\%$ on the Zt_Lt_L coupling. However, it should be kept in mind that the experimental status is not yet such as to fully motivate the hypothesis of a large new physics scale Λ compared to the electroweak scale, at least for what regards direct probes of the top sector.

We now turn to the discussion of the indirect bounds. The L- and R-handed top couplings to the W and Z are indirectly probed by electroweak precision data, via top loop contributions to the $\widehat{S}$ and $\widehat{T}$ parameters as well as to the Zb_Lb_L coupling, all of which have been measured with per-mille accuracy. The contribution of $\bar{c}_L^{(1)}$, $\bar{c}_L^{(3)}$, $\bar{c}_R$ to the renormalization group running of the dim-6 operators associated to the aforementioned observables can be consistently computed within the effective theory [13,20]. For instance, assuming $\bar{c}_L^{(3)} = -\bar{c}_L^{(1)}$ at the scale Λ, the $\widehat{T}$-parameter is renormalized by $\Delta\widehat{T} = N_c y_t^2 (\bar{c}_L^{(1)} - \bar{c}_R) \log(\Lambda/\mu)/(4\pi^2)$, and similar log-divergent terms are generated for $\widehat{S}$ and Zb_Lb_L. Taken at face value, this set of contributions imply the bounds $\bar{c}_L^{(1)}, \bar{c}_R \lesssim 5\%$ [35]. This is analogous to the indirect bound set on $\bar{c}_H$ from log-divergent Higgs loop contributions to $\widehat{S}$ and $\widehat{T}$ [36], which nevertheless does not undermine the relevance of a direct measurement of the hVV ($V = W, Z$)

coupling at the LHC. The same logic should apply to direct measurements of the top-Z couplings, even more so after taking into account that, in the cases of interest in this work, $\widehat{S}$, $\widehat{T}$ and Zb_Lb_L are dominated by incalculable ultraviolet (UV) contributions: Since it is not protected by any symmetry, $\widehat{S}$ generically receives UV contributions at tree level. On the other hand, even though $\widehat{T}$ and Zb_Lb_L can be UV protected if the BSM sector is custodial and P_{LR} symmetric, contributions to $\widehat{T}$ from top loops with two insertions of $\bar{c}_L^{(1)}$ or $\bar{c}_R$ are actually quadratically divergent and dominant whenever these coefficients are large. The situation is similar for loop contributions to Zb_Lb_L from one insertion of $\bar{c}_L^{(1)} = -\bar{c}_L^{(3)}$ and another of four-fermion operators [13].[5] Finally, we briefly mention bounds from flavor observables. The $\bar{c}_R^{tb}$ coefficient contributes at one loop to the $b \to s\gamma$ decay rate, with an amplitude enhanced by m_t/m_b, and is thus constrained at the per-mille level. In addition, Z-mediated penguin contributions to rare B and K meson decays lead to constraints on $\bar{c}_L^{(1)}$, $\bar{c}_L^{(3)}$ and $\bar{c}_R$ [37], which are at the same level of those from electroweak precision data. All these bounds, however, strongly depend on the assumed underlying flavor structure. In conclusion, currently little can be said with confidence about the couplings of the top to the Z, which motivates the new approach for probing them presented in this work.

As far as the couplings of the Higgs boson are concerned, constraints are still relatively mild. Global fits to inclusive signal strengths give $c_V \lesssim 20\%$ [38], whereas searches for the $t\bar{t}h$ signal still allow $O(1)$ deviations in c_t [39–42]. On the other hand, no experimental constraint currently exists on the Higgs cubic coupling c_3, nor on the c_i^h defined in Eqs. (2.1, 2.2).

The strength of the constraints discussed above relies on the relative precision

[5] The four-fermion operators are irrelevant for the scattering processes we study in this work, but nevertheless large in the same type of BSM scenarios.

of the experimental measurements compared to the BSM effects, which are of size ξ or smaller, see Eq. (2.10). In particular, the large uncertainty that affects the LHC measurement of the $t\bar{t}Z$ production cross section is behind the weakness of the direct bounds on modified top-Z couplings. However, there is another avenue for constraining non-standard top interactions, which relies on the large center of mass energies that can be reached at the LHC: departures from the SM prediction of certain top couplings imply that some scattering amplitudes will diverge with the momenta of the process. An analogy can be drawn with $VV \to VV$ scattering, where non-SM values of c_V lead to a growth of the amplitude with energy. In our case, the scatterings of interest are $tV \to tV$ and its crossings. Both in VV and tV scattering, the amplitudes that grow the most with energy involve the longitudinal polarizations of the $W^\pm$ and the Z. For tV scattering this can be clearly seen by inspecting the interactions of the top in a gauge where the Nambu-Goldstone bosons eaten by the W and Z, which we label χ_a ($a = 1, 2, 3$), appear explicitly in the Lagrangian, see Eqs. (2.37) and (2.40) in App. 2.A. For non-SM values of c_L, c_R, etc., four-point contact interactions of the form $\epsilon_{abc}\chi_b\partial_\mu\chi_c(\bar{\psi}\gamma^\mu\psi)_a/v^2$, with $\psi = \{t, b\}$, are generated, implying a p^2/v^2 growth of the amplitudes $\psi\chi \to \psi\chi$. Notice that the symmetry structure of the interaction is such as to include, for example, $tW^\pm \to tW^\pm$, but not $tZ \to tZ$. Likewise, certain scattering amplitudes involving the Higgs, such as $bW^+ \to th$, also display the same divergent behavior at high energies. This follows from the interactions $h\partial_\mu\chi_a(\bar{\psi}\gamma^\mu\psi)_a/v^2$, also shown in App. 2.A. The relation between the tV and th scattering amplitudes is also obvious when interpreted in terms of dim-6 operators, given the relations in Eqs. (2.6–2.8). The p^2/v^2 growth should be contrasted with the $m_t p/v^2$ growth that arises if the Higgs couplings c_t or c_V deviate from the SM [15] (see also [43]), whereas no enhancement with energy is generated by deviations in the Higgs cubic coupling c_3.

Thus, Higgs coupling modifications only give subleading effects in the high-energy scattering processes we are interested in.

To summarize, in certain two to two scattering processes the sensitivity to non-standard top-Z couplings is enhanced at high energies, possibly overcoming the limited experimental precision. The enhancement scales as $\bar{c}\,p^2/v^2 \sim g_*^2 p^2/\Lambda^2$, which can be much larger than one in models where $g_* \gg 1$, without being in conflict with the effective field theory expansion, that is $p^2 < \Lambda^2$. This approach then takes advantage of the high scattering energies accessible at the LHC. We explicitly demonstrate its effectiveness in the next section, focusing on $tW \to tW$.

2.3 $tW \to tW$ scattering as case study

Our goal is to study the scattering amplitudes involving tops (and/or bottoms) and W, Z or h that increase at high energies, and to exploit this growth to probe top-Z interactions. After examining all the possible combinations, we focus on the process $tW \to tW$. Our motivation for this choice is threefold:

1. The amplitude for $tW \to tW$ scattering grows with the square of the energy if either the Zt_Lt_L or the Zt_Rt_R couplings deviate from their SM values.
2. The corresponding collider process, $pp \to t\bar{t}Wj$, gives rise to same-sign leptons (SSL), an extremely rare final state in the SM. This process arises at $O(g_s g_w^3)$ in the gauge couplings, where g_s denotes the strong coupling and g_w any electroweak coupling, as shown in Fig. 2.1.
3. The main irreducible background, $pp \to t\bar{t}W + \text{jets}$ at $O(g_s^{2+n} g_w)$ with $n \geq 0$ the number of jets, is insensitive to the details of the top sector, because the

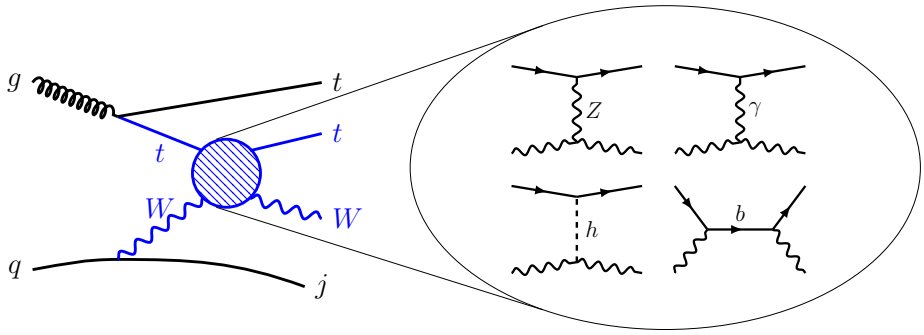

Figure 2.1: $tW \to tW$ scattering at the LHC. For definiteness, in the inset we show the diagrams corresponding to $tW^- \to tW^-$.

W is radiated off a light quark.

The amplitude for two to two scattering processes of the type $\psi_1+\phi_1 \to \psi_2+\phi_2$, where $\psi_{1,2} = \{t, b\}$ and $\phi_{1,2} = \{\chi^\pm \equiv (\chi_1 \mp i\chi_2)/\sqrt{2},\ \chi_3, h\}$ are the longitudinal $W^\pm, Z$ or h, is most conveniently expressed in the basis of chirality eigenstate spinors. Retaining only terms that grow with energy, we find

$$\begin{pmatrix} \mathcal{M}_{LL} & \mathcal{M}_{RL} \\ \mathcal{M}_{LR} & \mathcal{M}_{RR} \end{pmatrix} = \frac{\kappa\, g^2}{2m_W^2} \begin{pmatrix} e^{i\varphi}\sqrt{\hat{s}(\hat{s}+\hat{t})}A_{LL} & m_t\sqrt{-\hat{t}}\,A_{RL} \\ -e^{i\varphi}m_t\sqrt{-\hat{t}}\,A_{LR} & \sqrt{\hat{s}(\hat{s}+\hat{t})}A_{RR} \end{pmatrix}\ , \tag{2.11}$$

where κ and A_{ij} $(i, j = L, R$, with i indicating the chirality of ψ_1 and j the chirality of $\psi_2)$ are process-dependent coefficients.[6] In particular, the A_{ij} encode the dependence on the anomalous couplings: A_{LL} and A_{RR} control the leading amplitudes, which grow as $\hat{s}$, whereas A_{LR} and A_{RL} control the subleading pieces, growing as $\sqrt{\hat{s}}$. All the A_{ij} vanish in the SM, where the amplitude must tend to a

[6]We take initial state momenta as ingoing, and final state momenta as outgoing. The Mandelstam variables are defined as $\hat{s} = (p_{\psi_1} + p_{\phi_1})^2$ and $\hat{t} = (p_{\phi_1} - p_{\phi_2})^2$, and φ is the azimuthal angle around the z axis, defined by the direction of motion of ϕ_1.

constant limit at large $\sqrt{\hat{s}}$. For $tW^- \to tW^-$ scattering we have $\kappa = 1$ and

$$\begin{aligned} A_{LL} &= -c_{LL}^2 + c_L - \tfrac{4}{3}s_w^2(c_L - 1)\,, \\ A_{RR} &= -c_{RR}^2 - \tfrac{4}{3}s_w^2(c_R - 1)\,, \\ A_{LR} &= A_{RL} = \tfrac{1}{2}\left[(c_L - c_t c_V) - \tfrac{4}{3}s_w^2(c_L + c_R - 2)\right]. \end{aligned} \tag{2.12}$$

For $tW^+ \to tW^+$, we find again that $\kappa = 1$, A_{LL} and A_{RR} are identical to those in Eq. (2.12), whereas the subleading pieces read

$$A_{LR} = A_{RL} = c_{LL}^2 + c_{RR}^2 - \tfrac{1}{2}\left[(c_L + c_t c_V) - \tfrac{4}{3}s_w^2(c_L + c_R - 2)\right]. \tag{2.13}$$

We see that whenever $c_L(c_R) \neq 0$ (and barring accidental cancellations), the $LL(RR)$ amplitude grows like $\hat{s}$. This has to be contrasted with the weaker growth like $\sqrt{\hat{s}}$ caused by deviations in the Higgs couplings c_V or c_t. Because their effect is subleading, in our analysis of tW scattering we will set $c_V = c_t = 1$, and focus exclusively on modifications of top-Z interactions. For the latter we will consider two different theoretical interpretations. The first one targets the Zt_Lt_L and Zt_Rt_R couplings, by taking $\Delta_{L,R} \equiv c_{L,R} - 1 \neq 0$ in Eq. (2.8), whereas all other coefficients are set to their SM values. Under this assumption, the leading terms in the amplitude read

$$A_{LL} = \left(1 - \tfrac{4}{3}s_w^2\right)\Delta_L\,, \qquad\qquad A_{RR} = -\tfrac{4}{3}s_w^2\Delta_R\,. \tag{2.14}$$

We note that the sensitivity to Δ_R is lower than to Δ_L due to the s_w^2 suppression of A_{RR}. In addition, we present results in the framework of higher-dimensional operators (HDO), where the deviations in the top-Z couplings are correlated with those in other interactions of the third generation fermions. As discussed in Sec. 2.2, the per-mille constraint on the Zb_Lb_L vertex forces us to assume $\bar{c}_L^{(3)} = -\bar{c}_L^{(1)}$. We thus take $\bar{c}_L \equiv \bar{c}_L^{(1)} = -\bar{c}_L^{(3)}$ and $\bar{c}_R$ as BSM parameters, whereas all the other $\bar{c}_i$ coefficients in Eqs. (2.5) and (2.9) are set to zero. Notice that under these assumptions,

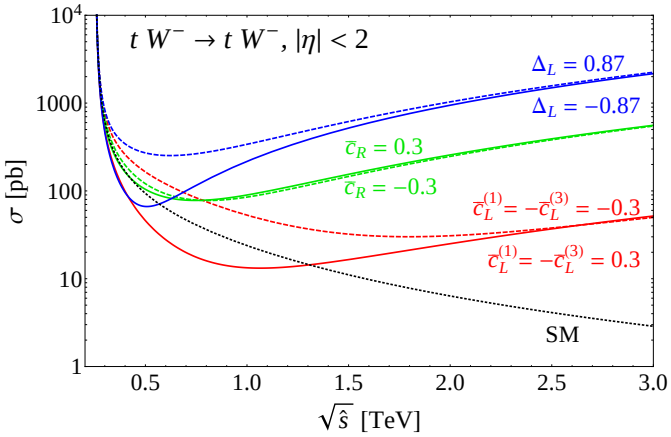

Figure 2.2: Partonic cross section for the process $tW^- \to tW^-$ as a function of the center of mass energy $\sqrt{\hat{s}}$. The values of Δ_L and $\bar{c}_L^{(1)} = -\bar{c}_L^{(3)}$ are chosen to obtain the same Zt_Lt_L coupling for the blue and red solid curves ($\Delta_L < 0$) and for the blue and red dashed curves ($\Delta_L > 0$). For the Zt_Rt_R coupling there is a one-to-one correspondence between $\bar{c}_R$ and Δ_R, so we show only one set of curves. A pseudorapidity cut $|\eta| < 2$ has been applied to remove the forward singularity, whereas the soft singularity $\hat{s} \to (m_W + m_t)^2$ is evident from the plot. Both singularities arise due to the diagram where a photon is exchanged in the t-channel. At large energy, the red, blue and green curves diverge like $\hat{s}$, whereas the SM cross section (dotted black) falls off as $1/\hat{s}$.

$\bar{c}_L$ also modifies the Wt_Lb_L vertex, which contributes to $tW \to tW$ scattering via the b-exchange diagram in Fig. 2.1. The leading amplitudes read

$$A_{LL} = -\bar{c}_L^2\,, \qquad A_{RR} = -\bar{c}_R\,. \tag{2.15}$$

We note that in A_{LL} the term linear in $\bar{c}_L$ vanishes. This can be traced back to the absence of the contact interaction $i\chi_+\partial_\mu\chi_-\bar{t}_L\gamma^\mu t_L/v^2 + \text{h.c.}$ when $\bar{c}_L^{(1)} + \bar{c}_L^{(3)} = 0$, see App. 2.A.

The cross section for $tW \to tW$ scattering is shown in Fig. 2.2, assuming representative values of the parameters (Δ_L, Δ_R) and $(\bar{c}_L, \bar{c}_R)$. As we already discussed, while there is a one-to-one correspondence between Δ_R and $\bar{c}_R$, the coupling and HDO hypotheses genuinely differ in the left-handed interactions, because in the HDO case the Wt_Lb_L vertex is also modified. To facilitate the

comparison, in Fig. 2.2 we choose values of Δ_L and $\bar{c}_L$ that yield the same Zt_Lt_L coupling. The resulting difference is striking: for $\bar{c}_L \neq 0$, the cross section is strongly suppressed compared to the case where $\Delta_L \neq 0$. This is mainly due to the cancellation of the $O(\bar{c}_L)$ piece in the leading amplitude, see Eq. (2.15), which implies that the leading term of the cross section is $O(\bar{c}_L^4)$. This in turn translates into a weaker sensitivity to $\bar{c}_L$ with respect to Δ_L, because the latter appears in the leading term of the cross section at $O(\Delta_L^2)$. Additionally, from Fig. 2.2 we learn that the cross section is enhanced for all energies, compared to the SM, if $\Delta_L > 0\,(\bar{c}_L < 0)$, while for the opposite sign it is actually suppressed at low values of $\sqrt{\hat{s}}$. Once the LHC parton luminosities are taken into account, we thus expect a weaker sensitivity to the region with $\Delta_L < 0\,(\bar{c}_L > 0)$. The effect is particularly striking for $\bar{c}_L > 0$, in which case the cross section becomes larger than the SM one only well above 1 TeV. These preliminary considerations, which were derived by simple inspection of the cross section of the hard scattering process $tW \to tW$, will find confirmation in the results presented below.

We now turn to the discussion of the $pp \to t\bar{t}Wj$ process at the LHC. In the following we denote our signal, which arises at $O(g_s g_w^3)$, as $(t\bar{t}Wj)_{\rm EW}$, to distinguish it from the leading mechanism for $t\bar{t}W$ production at the LHC, $pp \to t\bar{t}W$+jets at $O(g_s^{2+n} g_w)$ (with $n \geq 0$ the number of jets), which we denote as $(t\bar{t}W{+}{\rm jets})_{\rm QCD}$. Due to its high mass threshold, the latter process was not observed at the Tevatron, therefore the ATLAS and CMS experiments have designed searches aimed at extracting it from 8 TeV LHC data, focusing on the SSL final state and vetoing events that contain a leptonic Z, to remove the contribution from $t\bar{t}Z$ production. The main background is constituted by processes (mostly $t\bar{t}$+jets) giving *misidentified leptons* (misIDℓ), which primarily arise from the decay of heavy flavor hadrons. The latest searches [44, 45] make use of multivariate techniques and thus cannot

be straightforwardly reinterpreted, but the CMS cut-and-count analysis [19] contains all the information required to set a first bound on top-Z interactions by exploiting the growth with energy of the $(t\bar{t}Wj)_{\rm EW}$ process. While this search was not optimized for our signal, we will use it to demonstrate the effectiveness of our approach. It is important to notice that since $(t\bar{t}Wj)_{\rm EW}$ is formally of higher order in the weak coupling compared to $(t\bar{t}W{+}{\rm jets})_{\rm QCD}$, it was neglected by CMS in the SSL analysis of Ref. [19]. Thus we perform a Monte Carlo (MC) simulation of the signal and apply the cuts chosen by CMS, obtaining the number of events expected in 8 TeV data as function of the parameters (Δ_L, Δ_R) or $(\bar{c}_L, \bar{c}_R)$. We find

$$N_{(t\bar{t}Wj)_{\rm EW}}(\Delta_L, \Delta_R) = 1.6 + 1.0\,\Delta_L + 4.1\,\Delta_L^2 + 0.3\,\Delta_R + 1.1\,\Delta_L\Delta_R + 1.0\,\Delta_R^2\,, \tag{2.16}$$

$$N_{(t\bar{t}Wj)_{\rm EW}}(\bar{c}_L, \bar{c}_R) = 1.6 - 6.2\,\bar{c}_L + 8.7\,\bar{c}_L^2 - 7.0\,\bar{c}_L^3 + 11.2\,\bar{c}_L^4 + 0.8\,\bar{c}_R - 2.1\,\bar{c}_L\bar{c}_R - 4.1\,\bar{c}_L^2\bar{c}_R + 10.3\,\bar{c}_R^2\,. \tag{2.17}$$

Notice that the cross section is a polynomial of second order in the coupling deviations $\Delta_{L,R}$, whereas in the HDO case it is of quartic order, because two $\bar{c}_L$ insertions are possible in the diagram with b-exchange, see Fig. 2.1. Inspecting Eq. (2.16) (Eq. (2.17)), we confirm that the pure new physics contributions, which according to the expressions of the leading amplitudes in Eq. (2.14) (Eq. (2.15)) are proportional to Δ_L^2, Δ_R^2 $(\bar{c}_L^4, \bar{c}_R^2)$, dominate over the interference and the SM terms. In addition, based on the form of the leading amplitudes we expect the following relations to hold approximately: the ratio of the coefficients of Δ_L^2 $(\bar{c}_L^4)$ to Δ_R^2 $(\bar{c}_R^2)$ should be equal to $\left[1 - 3/(4s_w^2)\right]^2 (1)$. These equalities are indeed satisfied within 15%.

For comparison, CMS quotes an expected yield of 14.5 events for $(t\bar{t}W + {\rm jets})_{\rm QCD}$. Thus from Eqs. (2.16, 2.17) we see that while in the SM $(t\bar{t}Wj)_{\rm EW}$

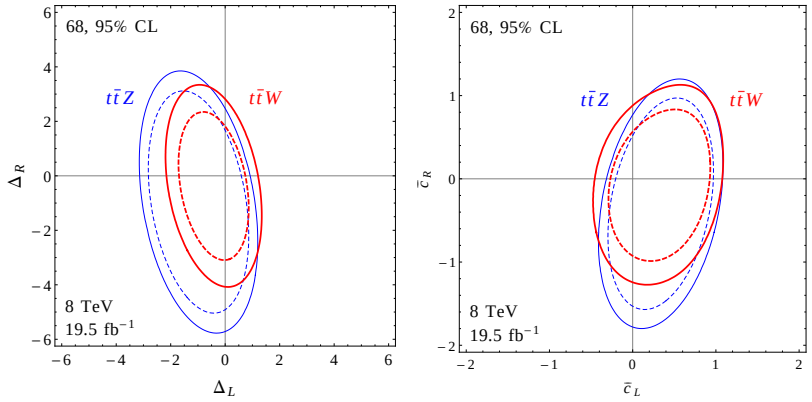

Figure 2.3: In red, the constraints on top-Z coupling deviations (left panel) and HDO coefficients (right panel) derived from the $t\bar{t}W$ analysis at 8 TeV. For comparison, in blue we show the constraint obtained from the 8 TeV $t\bar{t}Z$ analysis.

only provides a $\sim 10\%$ correction to the $(t\bar{t}W + \text{jets})_{\text{QCD}}$ yield, it grows rapidly moving away from the SM point. This, together with the fact that CMS did not observe any excess over the SM expectation, allows us to set a bound on $\Delta_{L,R}$ or $\bar{c}_{L,R}$. The results are shown in Fig. 2.3, where for comparison we also display the bounds obtained from the $t\bar{t}Z$ CMS analysis in the trilepton final state [19], which according to common wisdom provides the best constraint on top-Z couplings at the LHC. Strikingly, we find that the best current constraints are instead provided by the $t\bar{t}W$ channel, so far thought to be insensitive to top-Z interactions. This result becomes even more remarkable when we consider that the CMS analysis was optimized to increase the sensitivity not to our signal, but to the main irreducible background $(t\bar{t}W+\text{jets})_{\text{QCD}}$. Inspecting the HDO bound in the right panel of Fig. 2.3, we note that the coefficients of the dim-6 operators are allowed to be of $O(1)$. Thus the interpretation of the result in terms of HDO is not truly justified, and should be intended as purely illustrative of the current sensitivity. Assuming

only a modification of the Zt_Rt_R coupling, we find for 8 TeV, 19.5 fb^{-1} at 95% CL[7]

$$-3.6 < \Delta_R < 2.4 \qquad \text{or} \qquad -1.13 < \bar{c}_R < 0.74\,. \tag{2.18}$$

Having proven the effectiveness of our method, we move on to designing a search at 13 TeV that specifically targets the process $(t\bar{t}Wj)_{\rm EW}$. The latter has two distinctive features that can be exploited to separate it from the background: a tW pair with large invariant mass (where t can be either top or antitop, and W either of $W^\pm$), due to the growth with energy of the hard scattering process, and a highly energetic forward jet arising from the radiation of a W off an initial-state quark. We devise cuts that single out events with these properties and thus increase the significance of the signal over the background, which is mainly composed by $(t\bar{t}W{+}\text{jets})_{\rm QCD}$ and misIDℓ. We validate our background simulations against the CMS 8 TeV results, and perform the cut optimization using the point $(\Delta_L, \Delta_R) = (0, 1)$ as signal benchmark. This choice is motivated by the fact that the Zt_Rt_R coupling is currently very weakly constrained even under the assumption of heavy new physics, in contrast with the Zt_Lt_L coupling, which within the HDO framework is already bounded by the measurements of Zb_Lb_L and of Wt_Lb_L. Our basic selection requires two SSL and ≥ 4 jets, among which ≥ 1 must be b-tagged. We identify a set of useful kinematic variables to enhance the significance of the signal, which are discussed in detail in Sec. 2.4.3. For illustration, in Fig. 2.4 we show the normalized distributions of signal and backgrounds for a subset of these variables: the transverse momentum of the leading lepton, $p_T^{\ell_1}$, the invariant mass of the two leading leptons, $m_{\ell_1\ell_2}$, and the pseudorapidity of the forward jet, $|\eta_{j_{\rm fw}}|$.

[7]Given the very large Ztt coupling deviations allowed by 8 TeV data, one may wonder about effects in the $t\bar{t}$ forward-backward asymmetry measured at the Tevatron. The tree-level contribution due to $q\bar{q} \to Z, \gamma \to t\bar{t}$ is $\sim 0.2\%$ in the SM [46], and we estimate that, within the allowed region shown in the left panel of Fig. 2.3, it is enhanced by a factor $\lesssim 5$, thus remaining strongly subdominant to the QCD contribution, which amounts to approximately 8% [46]. Interestingly, at the LHC the $t\bar{t}$ charge asymmetry in the $t\bar{t}W$ process is significantly larger than in inclusive $t\bar{t}$ production [47].

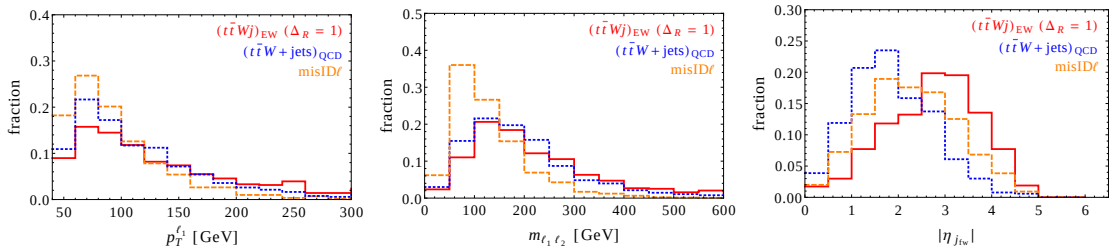

Figure 2.4: Normalized distributions for the signal $(t\bar{t}Wj)_{\rm EW}$ and the two main backgrounds $(t\bar{t}W+{\rm jets})_{\rm QCD}$ and misIDℓ at 13 TeV, after the $4j$ pre-selection.

It is apparent that the leptonic variables are effective in suppressing the misIDℓ background, whereas a lower cut on the pseudorapidity of the forward jet helps to suppress $(t\bar{t}W{+}{\rm jets})_{\rm QCD}$. The event yields after all cuts, assuming an integrated luminosity of 300 fb^{-1}, are given by

$$N_{(t\bar{t}Wj)_{\rm EW}}(\Delta_L,\Delta_R) = 16.9 + 12.7\,\Delta_L + 172.4\,\Delta_L^2 + 0.5\,\Delta_R + 37.2\,\Delta_L\Delta_R + 40.8\,\Delta_R^2\,, \tag{2.19}$$

$$N_{(t\bar{t}Wj)_{\rm EW}}(\bar{c}_L,\bar{c}_R) = 16.7 - 73.2\,\bar{c}_L + 145.0\,\bar{c}_L^2 - 164.2\,\bar{c}_L^3 + 408.3\,\bar{c}_L^4 + 6.3\,\bar{c}_R - 4.1\,\bar{c}_L\bar{c}_R - 121.8\,\bar{c}_L^2\bar{c}_R + 412.3\,\bar{c}_R^2\,. \tag{2.20}$$

The expected background yield is of 51 events for $(t\bar{t}W+{\rm jets})_{\rm QCD}$, and of 34 events for misIDℓ. By performing a simple likelihood analysis, we obtain the constraints on $\Delta_{L,R}$ and $\bar{c}_{L,R}$ shown as red contours in Fig. 2.5. The solid contours assume no systematic uncertainty on the background, whereas the dotted contours include the dominant 50% systematic uncertainty on the misIDℓ component. For comparison, in the same figure we show the projected 13 TeV bounds from the $t\bar{t}Z$ process, as derived in Ref. [6]. This comparison is meant to be illustrative, because the projection of Ref. [6] is based on a NLO-QCD analysis of the signal, without the inclusion of detector effects nor backgrounds. The two main effects

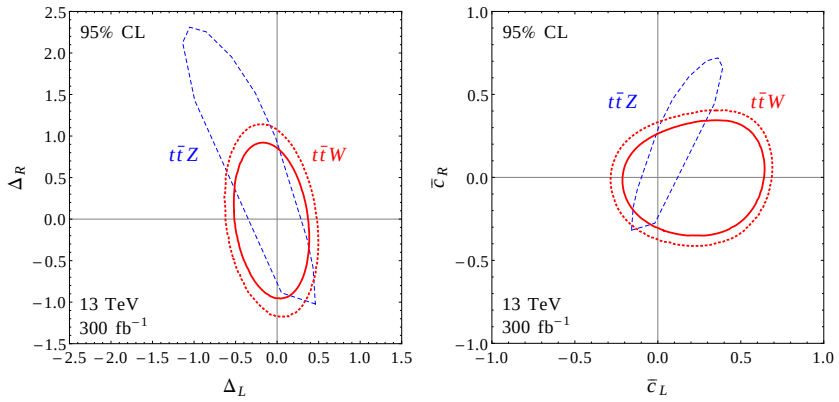

Figure 2.5: In red, the constraints on top-Z coupling deviations (left panel) and HDO coefficients (right panel) derived from our $4j$ $t\bar{t}W$ analysis at 13 TeV. The solid contour assumes no systematic uncertainty on the background, whereas the dotted one includes a 50% systematic on the misIDℓ component. For comparison, in dashed blue we show the constraint obtained from $t\bar{t}Z$, as derived in Ref. [6] by means of a NLO-QCD signal-only analysis.

that were gleaned by inspecting the partonic cross section in Fig. 2.2 are now manifest in Fig. 2.5. First, the sensitivity to $\bar{c}_L$ is weaker than to Δ_L, because the former appears in the leading term of the cross section at $O(\bar{c}_L^4)$ while the latter at $O(\Delta_L^2)$, see Eqs. (2.14) and (2.15). Second, the $\bar{c}_L > 0$ direction is less strongly constrained than $\bar{c}_L < 0$, because in the former case the partonic cross section for $tW \to tW$ scattering is smaller than the SM one for $\sqrt{\hat{s}} \lesssim$ TeV, where the bulk of the LHC parton luminosity is concentrated. Comparing with the $t\bar{t}Z$ process, we find that our $t\bar{t}W$ analysis gives a significantly stronger bound on the coupling deviations $\Delta_{L,R}$, and comparable sensitivity to the HDO coefficients $\bar{c}_{L,R}$. We also note that in the HDO case the shape of the $t\bar{t}W$ contours is rather different from that of the $t\bar{t}Z$ ones, leading to an interesting complementarity of the two measurements. Assuming only a modification of the Zt_Rt_R coupling, our analysis gives for 13 TeV, 300 fb^{-1} at 95% CL

$$-0.83 < \Delta_R < 0.74 \qquad \text{or} \qquad -0.26 < \bar{c}_R < 0.23 \,, \tag{2.21}$$

with no systematics on the background, while if a 50% systematic uncertainty on the misIDℓ component is included, we find $-1.04 < \Delta_R < 0.95$ or $-0.32 < \bar{c}_R < 0.30$. Based on these results, we urge the ATLAS and CMS collaborations to search for the $(t\bar{t}Wj)_{\rm EW}$ signal in the upcoming 13 TeV data. The necessary technical details of our analysis are presented in the next section, which the reader interested only in the discussion of our results can omit, to move directly to Sec. 2.5.

2.4 $t\bar{t}W$ analysis

In this section we present the technicals details of our analysis. Frequent reference will be made to the 8 TeV CMS cut-and-count search for $t\bar{t}W$ [19], based on the requirements of two SSL and a leptonic Z veto. After reinterpreting this search to obtain the 8 TeV bounds on top-Z interactions, we employ its results to validate our background simulations. We then propose a dedicated 13 TeV analysis that targets the signal process $(t\bar{t}Wj)_{\rm EW}$.

2.4.1 8 TeV bounds

The SSL analysis of Ref. [19] was aimed at measuring the $(t\bar{t}W{+}{\rm jets})_{\rm QCD}$ process, while our signal process $(t\bar{t}Wj)_{\rm EW}$ was neglected. On the other hand, the $(t\bar{t}Wj)_{\rm EW}$ amplitude interferes with the one-jet component of $(t\bar{t}W{+}{\rm jets})_{\rm QCD}$, which we will label $(t\bar{t}Wj)_{\rm QCD}$, thus *a priori* our signal cannot be generated separately from the $(t\bar{t}W{+}{\rm jets})_{\rm QCD}$ process. A further subtlety arises because the $t\bar{t}W$ final state can also be produced purely from weak interactions, at $O(g_w^3)$. To quantify these effects, we compute inclusive parton-level cross sections for the SM

and one representative signal point, which is chosen to be $\Delta_R = 3.2$ at 8 TeV and $\Delta_R = 1$ at 13 TeV, roughly corresponding to the sensitivity of our analysis (see Figs. 2.3 and 2.5, respectively). The cross sections are computed with MadGraph5 [49], employing a FeynRules [67] model that allows us to add to the SM either the corrections $\Delta_{L,R}$ to the top-Z couplings, or the dim-6 operators proportional to $\bar{c}_L^{(1)}, \bar{c}_L^{(3)}, \bar{c}_R$. The model was validated against analytical computations of several $2 \to 2$ amplitudes, and employed for all the MC simulations used in this paper. For the SM parameters we take the values

$$m_Z = 91.19 \text{ GeV}\,, \qquad \alpha(m_Z) = 1/127.9\,, \qquad G_F = 1.166 \times 10^{-5} \text{ GeV}^{-2}\,,$$
$$\alpha_s(m_Z) = 0.1184\,, \qquad m_t = 173 \text{ GeV}\,. \tag{2.22}$$

Inspection of the inclusive cross sections in Table 2.1 shows that the pure electroweak contribution to $t\bar{t}W$ is very small, thus we will neglect it in our study. On the other hand, the effect of the interference between the $(t\bar{t}Wj)_{\text{QCD}}$ and $(t\bar{t}Wj)_{\text{EW}}$ amplitudes on the deviation from the SM cross section in presence of anomalous top-Z couplings is at most 20%. Given the exploratory nature of our study, for simplicity we choose to perform our analysis neglecting the interference, and take into account its effect by including a conservative 20% systematic uncertainty on the $(t\bar{t}Wj)_{\text{EW}}$ signal.

Because we neglect the interference, to compute the constraints on top-Z interactions we need to apply the CMS cuts to the $(t\bar{t}Wj)_{\text{EW}}$ process, and extract the dependence of the signal event yield on the parameters $\Delta_{L,R}$ and $\bar{c}_{L,R}$. The signal yield will then be summed to those of the processes already simulated in Ref. [19], including $(t\bar{t}W + \text{jets})_{\text{QCD}}$. Signal events are generated with MadGraph5, employing our FeynRules model. Showering and hadronization effects are accounted for with Pythia 6.4 [51], and the detector simulation is performed using PGS4 [41].

		$(t\bar{t}W)_{\rm QCD}$	$(t\bar{t}W)_{\rm EW}$	$(t\bar{t}Wj)_{\rm QCD}$	$(t\bar{t}Wj)_{\rm EW}$	$(t\bar{t}Wj)_{\rm full}$	$1-\frac{\delta_{\rm full}}{\delta_{\cancel{\rm int}}}$
8 TeV	SM	130.6	0.99	94.0	12.6	104.1	0.19(4)
	$\Delta_R = 3.2$	130.6	1.73	94.0	64.9	146.5	
13 TeV	SM	347.9	2.85	341.3	56.0	386.1	0.02(15)
	$\Delta_R = 1$	347.9	2.71	341.3	94.6	423.9	

Table 2.1: Parton-level cross sections in femtobarns. By $(t\bar{t}Wj)_{\rm full}$ we denote the full amplitude including the interference. For the $t\bar{t}Wj$ process we imposed the cuts $p_T^j > 20$ GeV and $|\eta| < 5$. The quantity $\delta_{\rm full,\cancel{int}} \equiv \sigma^{\Delta_R\neq 0}_{(t\bar{t}Wj)_{\rm full,\,EW}} - \sigma^{\rm SM}_{(t\bar{t}Wj)_{\rm full,\,EW}}$ is the deviation from the SM, computed either including ('full') or neglecting ('~~int~~') the interference. In the last column, the uncertainty in parentheses refers to the last digit.

To match Ref. [19], the following changes are made to the default CMS settings in PGS: the b-tagging is modified to reproduce the performance of the medium working point of the CSV algorithm, and the jet reconstruction algorithm is set to anti-k_T with distance parameter of 0.5. In addition, the calorimeter coverage for jets is extended up to $|\eta| = 5$. We make use of NN23LO1 parton distribution functions [53], and factorization and renormalization scales are set to the default MadGraph5 event-by-event value. Unless otherwise noted, the above settings are used for all the event samples used in this paper. The event selection requirements follow closely those listed in Sec. 4 of Ref. [19], and are as follows:

1. Two SSL, each with $|\eta| < 2.4$ and $p_T > 40$ GeV;
2. At least three jets with $|\eta| < 2.4$ and $p_T > 30$ GeV, among which at least one must be b-tagged;
3. An event is rejected if it contains, in addition to the SSL pair, 2 or more leptons with $|\eta| < 2.4$ and $p_T > 10$ GeV, or if it contains one such lepton forming, with one of the two SSL, a same-flavour opposite-sign pair whose invariant mass is within 15 GeV of m_Z;

$(t\bar{t}W+\text{jets})_{\text{QCD}}$	misIDℓ	irreducible	$t\bar{t}Z$	misIDQ	WZ	total	observed
14.5	12.1	5.8	3.9	2.2	1.3	39.8	36

Table 2.2: Expected and observed background yields for the 8 TeV SSL analysis, after summing over all SSL categories. The numbers are taken from Ref. [19].

4. $H_T > 155$ GeV, where H_T is the scalar sum of the transverse momenta of all jets as defined in point 2;

5. The CMS lepton isolation is approximated by requiring that $\Delta R(\ell, j) > 0.3$ for each of the SSL and for all jets as defined in point 2.

The events are divided in 6 categories depending on the flavor/charge combination of the SSL. The expected event yields for all the processes considered in Ref. [19], after summing over all SSL categories, are shown in Table 2.2. The largest SM contribution is given by $(t\bar{t}W+\text{jets})_{\text{QCD}}$, which was considered as signal in Ref. [19], but will be a background in our analysis. The second contribution is given by the misIDℓ background, composed of processes with one prompt and one non-prompt lepton. The latter arises from the decay of a heavy flavor hadron, and is misidentified as prompt. The misIDℓ background is dominated by $t\bar{t}$ events. Subleading contributions are given by the 'irreducible' processes, which include $t\bar{t}h$ and same-sign WW production in association with jets, and by $t\bar{t}Z$. A minor background is given by processes where the misidentification of the charge of one electron leads to the SSL final state. This contribution, dominated by $t\bar{t}$ and Drell-Yan (DY)+jets events, is labeled *misidentified charge* (misIDQ) background. Finally, WZ+jets production is also a minor background.

To efficiently compute the signal yield after cuts as function of the parameters $\Delta_{L,R}$ and $\bar{c}_{L,R}$, we exploit the fact that formally the $(t\bar{t}Wj)_{\text{EW}}$ cross section is a polynomial of second order in $\Delta_{L,R}$, and of quartic order in $\bar{c}_{L,R}$. Thus it is sufficient

to generate a small number of signal samples and perform a fit, which yields semi-numerical formulas parameterizing the signal predictions. For brevity, only the sum over all flavor/charge combinations of the SSL was reported in Eqs. (2.16, 2.17). The statistical uncertainty on the signal yields computed using those equations is approximately 10%. The fact that CMS observed a number of events compatible with the SM prediction (see Table 2.2) allows us to set a bound on top-Z interactions. Denoting by $\vec{p}$ either $\{\Delta_L, \Delta_R\}$ or $\{\bar{c}_L, \bar{c}_R\}$, we thus consider the following likelihood

$$\begin{aligned}
L(\vec{p}\,; r, t) &= \prod_{i=1}^{6} \frac{(N^i_{S+B})^{N^i_{\rm obs}} e^{-N^i_{S+B}}}{N^i_{\rm obs}!}\, P_{\sigma_r}(r,1) P_{\sigma_t}(t,1)\,, \\
P_\sigma(x, x_0) &= \frac{1}{\frac{1}{2}\left[1 + {\rm erf}\left(\frac{1}{\sqrt{2}\,\sigma}\right)\right]} \frac{1}{\sqrt{2\pi}\sigma} e^{-\frac{(x-x_0)^2}{2\sigma^2}}\,, \\
N^i_{S+B} &= r N^i_{B,\,{\rm misID}\ell} + N^i_{B,\,{\rm other}} + N^i_{(t\bar{t}Wj)_{\rm EW}}(\vec{0}) \\
&\quad + t(N^i_{(t\bar{t}Wj)_{\rm EW}}(\vec{p}) - N^i_{(t\bar{t}Wj)_{\rm EW}}(\vec{0}))\,, \qquad (2.23)
\end{aligned}$$

where the dominant systematic uncertainty of 50% on the misIDℓ background was included[8] by setting $\sigma_r = 0.5$, and we also took into account the already mentioned 20% systematic uncertainty on the signal by setting $\sigma_t = 0.2$. The index i runs over the 6 SSL categories. Maximizing the marginalized log-likelihood, defined as $\ell_m(\vec{p}) = \log\left(\int_0^{+\infty} L(\vec{p}\,; r, t) dr\, dt\right)$, and taking standard confidence intervals we obtain the exclusion contours shown in Fig. 2.3. To put our constraints in perspective, we compare them with those derived from the CMS 8 TeV $t\bar{t}Z$ analysis in the trilepton final state, also performed in Ref. [19] (see App. 2.B for details). Setting $\Delta_L = 0$ (or equivalently, $\bar{c}_L = 0$) in the likelihood, we obtain the one-dimensional bounds reported in Eq. (2.18). Notice that, as shown in Table 2.2, despite the leptonic Z veto the $t\bar{t}Z$ process gives a small contribution to the SSL signal region.

[8] We have verified that by assuming 50% on the misIDℓ background as the only systematic uncertainty, we reproduce to good accuracy the measurement of the $t\bar{t}W$ cross section quoted in Ref. [19]: we find 178^{+106}_{-101} fb, to be compared with 170^{+114}_{-106} fb.

For the sake of consistency, to generate the $t\bar{t}W$ contours in Fig. 2.3 we have taken into account the dependence of the $t\bar{t}Z$ event yield on the parameters $\vec{p}$, rescaling the value quoted by CMS for the SM (3.9 events) by the ratio $\sigma_{t\bar{t}Z}(\vec{p})/\sigma^{\rm SM}_{t\bar{t}Z}$, with $\sigma_{t\bar{t}Z}$ the inclusive cross section for $pp \to t\bar{t}Z$ at 8 TeV. This is based on the assumption that the selection efficiency is independent of $\vec{p}$, which is expected to be a reasonable approximation, since the leading $pp \to t\bar{t}Z$ amplitude does not grow with energy for non-SM top-Z couplings. On the other hand, the subleading contribution $pp \to t\bar{t}Zj$, which is the analogue of our signal with $W \to Z$, does grow with energy, and one may wonder if it is justified to discard it. However, as discussed in Sec. 2.5.4, the $tZ \to tZ$ amplitude only grows with energy as $\sqrt{\hat{s}}$, as opposed to $\hat{s}$ for $tW \to tW$. We can thus safely neglect this piece. The effect of the $t\bar{t}Z$ contamination on the $t\bar{t}W$ bounds in Fig. 2.3 is small.

2.4.2 Background simulation

To set bounds from the 8 TeV CMS data, it was sufficient to simulate the $(t\bar{t}Wj)_{\rm EW}$ signal and make use of the expected background yields quoted by CMS. Thus it was not necessary to simulate all the backgrounds listed in Table 2.2. However, because our aim is also to devise an analysis at 13 TeV, which we will specifically tailor to improve the sensitivity to top-Z interactions, we first need to make sure that our simulation can reproduce the 8 TeV results contained in Ref. [19] for all the processes listed in Table 2.2. The salient features of the simulation are summarized below for each background. Unless otherwise specified, jet matching is performed using the shower $k_\perp$ scheme [54] with matching scale set to 30 GeV, and the definition of jet includes b-jets.

- $(t\bar{t}W+\text{jets})_{\text{QCD}}$: we generate a matched sample of $t\bar{t}W + 0, 1$ jets, and normalize it to the NLO cross section of 206 fb [19]. Notice that in Ref. [55] the $(t\bar{t}Wj)_{\text{QCD}}$ component was shown to have dramatic effects in some regions of phase space. However, the NLO corrections to $(t\bar{t}Wj)_{\text{QCD}}$ were also computed, finding that they have a small effect.[9] This supports the use of a LO matched sample with $0, 1$ jets, at least for our exploratory analysis.

- MisIDℓ: CMS estimated this background by means of a data-driven method. We follow the approach of Ref. [48], where it was proposed to exploit the relationship between the misidentified (or 'fake') lepton and the heavy flavor jet from which it originated. The method consists of applying certain probability and transfer functions to MC events containing heavy flavor jets. In our case, we consider a matched sample of $t\bar{t} + 0, 1, 2$ jets, normalized to the NNLO cross section of 245.8 pb [56]. More details about the method are given in App. 2.C. Here we only stress that the overall efficiency of the fake lepton generation is a free parameter of the method, and we simply fix it to reproduce the CMS yield reported in Table 2.2.

- Irreducible: this background is composed mainly by $\bar{t}t$ production in association with a Higgs, with a $\sim 10\%$ component of same-sign WW. For the former process, we generate a matched sample of $t\bar{t}h + 0, 1$ jets, and normalize it to the NLO cross section of 129.3 fb [57]. For the latter, we generate $W^{\pm}W^{\pm} + 3j$ with matching, with LO normalization.

- $t\bar{t}Z$: we generate a matched sample of $t\bar{t}Z + 0, 1$ jets, and normalize it to the NLO cross section of 197 fb [19].

- misIDQ: this background was estimated by CMS using a combination of data and MC. We mimic their method by selecting MC events that contain

[9] We thank F. Maltoni for pointing this out to us.

	$(t\bar{t}W+\text{jets})_{\text{QCD}}$	misIDℓ	irreducible	$t\bar{t}Z$	misIDQ	WZ
$\frac{\text{CMS}}{\text{our MC}}$	0.62	–	1.09	1.20	0.28	0.83

Table 2.3: Multiplicative factors we need to apply to the normalization of our MC samples to match the CMS results in Table 2.2. The normalization of the misIDℓ background is not predicted by the fake lepton simulation.

opposite-sign $e\mu$ or ee and pass all the cuts except for the same-sign requirement, and weighting them with the probability for the charge of each electron to be mismeasured (the probability of the charge of a μ being mismeasured is negligible). We take the probabilities to be 2.3×10^{-3} for the endcaps ($|\eta| > 1.479$) and 2×10^{-4} for the barrel ($|\eta| < 1.479$) [58]. These probabilities correspond to the 'selective' charge identification method [58], and agree with the order-of-magnitude values quoted in Ref. [19]. Two processes contribute: $t\bar{t}$, and DY+jets. For the former, which amounts to $\sim 70\%$ of the total, we generate a matched sample of $t\bar{t}+0,1,2$ jets, normalized to the NNLO cross section of 245.8 pb [56]. For the latter, we generate a sample of $\ell^+\ell^-+3j$ with matching, with LO normalization.

- WZ: we generate $WZ+3j$ with matching and LO normalization.

For each of the above processes, we compare the distributions of the leading lepton p_T and H_T with those reported in Fig. 2 of Ref. [19]. The shapes of the distributions are reproduced in all cases, including misIDℓ and misIDQ, which were predicted by CMS using data. This gives us, in particular, confidence in our treatment of the fake leptons, which together with $(t\bar{t}W+\text{jets})_{\text{QCD}}$ will dominate the background in the 13 TeV analysis. On the other hand, as shown in Table 2.3, the normalization agrees reasonably well with the CMS result for all the processes except misIDQ, for which our simulation overestimates the event yield by a factor ~ 3.5. Nevertheless, once we normalize to the CMS rate, the misIDQ distributions are reproduced to

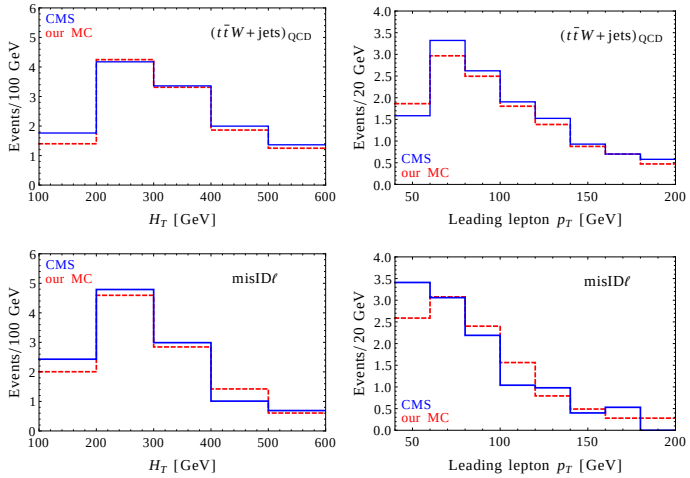

Figure 2.6: 8 TeV distributions for $(t\bar{t}W+\text{jets})_{\text{QCD}}$ (upper row) and misIDℓ (lower row). The blue histograms show the CMS result, whereas the red histograms show our prediction, after normalizing to the CMS total yields.

good accuracy. In addition, we checked that for all processes we reproduce, within errors, the relative contributions to the 6 SSL categories shown in Table 1 of Ref. [19]. The 8 TeV distributions for $(t\bar{t}W+\text{jets})_{\text{QCD}}$ and misIDℓ are shown in Fig. 2.6, after normalization to the respective CMS yields. Having validated our background simulations against data, we will confidently make use of them in the 13 TeV analysis, by generating each process with the same settings employed at 8 TeV, including jet multiplicity. The normalization will be fixed to the best available calculation (see Table 2.4), multiplied by the rescaling factor given in Table 2.3, which brings our 8 TeV rate in agreement with the one predicted by CMS.[10] The misIDℓ process will be simulated with the same parameters that match the CMS results at 8 TeV, because we do not expect a significant variation going to the higher collider energy.

[10]The irreducible and misIDQ backgrounds are composed by two distinct processes. In these cases, the rescaling factor of Table 2.3 is applied to each of the component processes.

	$(t\bar{t}W+\text{jets})_{\text{QCD}}$	$t\bar{t}$ (misIDℓ, misIDQ)	$t\bar{t}h$	$t\bar{t}Z$
$\sigma_{13\text{ TeV}}$	566.3 fb [59]	788.2 pb [60]	508.5 fb [61]	771 fb [59]

Table 2.4: Inclusive cross sections used to normalize the 13 TeV samples. The $t\bar{t}$ cross section is at approximate NNLO, whereas the others are at NLO. For the processes not listed here, LO normalization was used.

2.4.3 13 TeV analysis

The $(t\bar{t}Wj)_{\text{EW}}$ process is characterized by the presence of a highly energetic forward jet, which provides a natural handle to separate the signal from the background. In our analysis, we thus select a candidate forward jet, and make use of kinematic variables constructed out of it. However, forward jet tagging is known to face issues in high-pileup conditions, like those of LHC Run-2, and what level of performance will be achieved is still an open question. Interestingly, it was suggested [62], in the context of a study of heavy top partners in the very $t\bar{t}Wj$ final state, that clustering forward jets with a radius parameter smaller than the standard one can greatly improve the forward jet tagging. Yet in our analysis we go beyond tagging, making use of the reconstructed four-momentum of the forward jet. Because this aspect of the analysis may be affected by pileup, we choose to also perform a separate analysis where we do not make any reference to forward jets, and only employ central jets with $|\eta| < 2.4$. The results of this second analysis (which will be labeled $3j$ analysis) are very robust and likely conservative, whereas the first ($4j$ analysis) illustrates the potential of forward jet variables in suppressing the background.

$4j$ analysis

In the $4j$ analysis, we make use of the forward jet that characterizes the signal. The event pre-selection requires the following:

1. The cuts on leptons are identical to the 8 TeV analysis;
2. We require at least four jets with $p_T > 30$ GeV and $|\eta| < 5$, among which at least three must be central, *i.e.* must satisfy $|\eta| < 2.4$ (at least one of the central jets must be b-tagged), and at least one must not be b-tagged;
3. No cut is applied on H_T, defined as the scalar sum of the p_T of all the central jets as defined in point 2;
4. The CMS lepton isolation is approximated by requiring that $\Delta R(\ell, j) > 0.3$ for each of the SSL and for all central jets.

After the pre-selection, to find the best set of cuts we perform an optimization based on the signal point $(\Delta_L, \Delta_R) = (0, 1)$, which corresponds roughly to the target sensitivity at 13 TeV with 300 fb^{-1}. For the optimization, we include only the two main backgrounds $(t\bar{t}W + \text{jets})_{\text{QCD}}$ and misIDℓ. The optimization is performed by maximizing the statistical significance of the exclusion[11]

$$\mathcal{S} \equiv \frac{S}{\sqrt{S+B}} = \frac{N_{(t\bar{t}Wj)_{\text{EW}}}(\Delta_R = 1) - N_{(t\bar{t}Wj)_{\text{EW}}}(\text{SM})}{\sqrt{N_{(t\bar{t}Wj)_{\text{EW}}}(\Delta_R = 1) + N_{(t\bar{t}W+\text{jets})_{\text{QCD}}} + N_{\text{misID}\ell}}} \,, \tag{2.24}$$

where S and B indicate the signal and background, respectively. The luminosity is assumed to be 300 fb^{-1}. We consider a number of candidate variables in order to enhance $\mathcal{S}$. The best are found to be the transverse momentum of the leading lepton, $p_T^{\ell_1}$, the invariant mass of the two leading leptons, $m_{\ell_1\ell_2}$, the missing

[11] The 95% CL exclusion corresponds to $\mathcal{S} \simeq 1.64$.

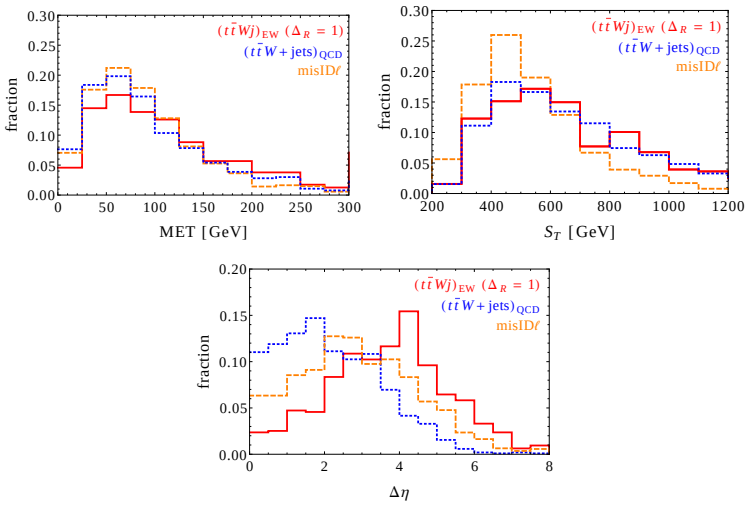

Figure 2.7: Normalized distributions for $(t\bar{t}Wj)_{\rm EW}$ and the two main backgrounds $(t\bar{t}W{+}{\rm jets})_{\rm QCD}$ and misIDℓ at 13 TeV, after the $4j$ pre-selection. The other relevant distributions were shown in Fig. 2.4.

transverse energy, MET, the scalar sum of H_T and the p_T of the two leading leptons, S_T, and two angular variables that involve the forward jet, namely $|\eta_{j_{\rm fw}}|$ and $\Delta\eta \equiv |\eta_{j_{\rm fw2}} - \eta_{j_{\rm fw}}|$, where the forward jet $j_{\rm fw}$ and the 'second forward jet' $j_{\rm fw2}$ are defined as

- $j_{\rm fw}$ is the non-b-tagged jet with largest $|\eta|$,
- $j_{\rm fw2}$ is the jet with the largest invariant mass with $j_{\rm fw}$.

The normalized signal and background distributions of these variables after the pre-selection cuts are shown in Figs. 2.4 and 2.7. The cut-flow for our optimal cuts is in Table 2.5. We see that the cuts on the leptons effectively suppress the fake lepton background, while the cuts on the forward jet are successful against the $(t\bar{t}W{+}{\rm jets})_{\rm QCD}$ background. After all cuts, we achieve a significance of 3.5 and a signal to background ratio of approximately 0.4. In Table 2.6 we report the event yields for the subleading backgrounds. We note that because our selection

	$\mathcal{S}$	EW(SM)	EW($\Delta_R = 1$)	$(t\bar{t}W+\text{jets})_{\text{QCD}}$	misIDℓ	S/B
pre-selection	2.8	91	183	445	476	0.091
$p_T^{\ell_1} > 100$ GeV	3.0	44	111	223	166	0.15
$m_{\ell_1\ell_2} > 125$ GeV	3.1	39	102	202	112	0.18
MET > 50 GeV	3.2	28	84	152	80	0.22
$\lvert\eta_{j_{\text{fw}}}\rvert > 1.75$	3.4	21	69	77	58	0.31
$\Delta\eta > 2$	3.5	20	67	60	49	0.36
$S_T > 500$ GeV	3.5	16	58	51	34	0.42

Table 2.5: Cut-flow for the $4j$ optimization at 13 TeV. EW stands for $(t\bar{t}Wj)_{\text{EW}}$.

requires at least 4 jets, the backgrounds $W^{\pm}W^{\pm}, WZ$ and DY should in principle be simulated with four extra partons in the matrix element, matched to the parton shower. This requires, however, a large computational effort, which goes beyond the scope of this paper. Therefore, as an estimate, we simply simulate these backgrounds with 3 additional partons at matrix element level. We find that all three processes give a very small contribution to the signal region. In particular, DY+jets is very strongly suppressed by the MET cut. The signal yields after all

	$t\bar{t}h$	$W^{\pm}W^{\pm}$	$t\bar{t}Z$	$t\bar{t}$-misIDQ	DY-misIDQ	WZ
pre-selection	233	18	105	44	16	41
all cuts	19	3	8	4	0	4

Table 2.6: Event yields for the subleading backgrounds at 13 TeV, after $4j$ pre-selection and after the full $4j$ analysis.

cuts were given in Eqs. (2.19, 2.20). The statistical uncertainty on the signal yields computed using those equations is approximately 10%. To derive the constraints on the parameters $\vec{p}$, we perform a single-bin[12] likelihood analysis, in complete analogy with Eq. (2.23), assuming the observed number of events to equal the SM prediction. We also consistently take into account the dependence of the

[12]We have verified that taking one inclusive bin instead of 6 SSL categories makes the 8 TeV bounds only slightly weaker.

subleading background $t\bar{t}Z$ on the parameters $\vec{p}$, by rescaling the yield in Table 2.6 with the ratio $\sigma_{t\bar{t}Z}(\vec{p})/\sigma^{\rm SM}_{t\bar{t}Z}$, with $\sigma_{t\bar{t}Z}$ the inclusive cross section for $pp \to t\bar{t}Z$ at 13 TeV. The resulting bounds were shown as red contours in Fig. 2.5. In addition to the 20% systematic uncertainty on the signal, we assume either no systematics on the background (solid contours), or 50% systematic uncertainty on the misIDℓ component (dotted). For comparison, we also show in dashed blue the results of the $t\bar{t}Z$ projection made in Ref. [6]. Assuming that the only deformation of the SM is a modification of the Zt_Rt_R coupling, we obtain the one-dimensional bounds reported in Eq. (2.21).

$3j$ analysis

In the $3j$ analysis, we conservatively do not make use of the forward jet that characterizes the signal, and only impose selection cuts on central jets. The pre-selection is identical to the 8 TeV analysis, except that no requirement on H_T is applied. As in the $4j$ analysis, after the pre-selection we perform a cut optimization taking the point $(\Delta_L, \Delta_R) = (0, 1)$ as signal benchmark, using the statistical significance defined in Eq. (2.24). The most effective variables in enhancing the significance are found to be $p_T^{\ell_1}, m_{\ell_1\ell_2}$, the MET and S_T. The cut-flow for the optimal cuts is in Table 2.7. After all cuts, we find a significance of 3.0 and a signal to background

	$\mathcal{S}$	EW(SM)	EW($\Delta_R = 1$)	$(t\bar{t}W{+}\text{jets})_{\rm QCD}$	misIDℓ	S/B
pre-selection	2.5	108	212	678	788	0.066
$p_T^{\ell_1} > 100$ GeV	2.9	52	129	346	258	0.12
$m_{\ell_1\ell_2} > 125$ GeV	2.9	45	117	308	170	0.14
MET > 50 GeV	3.0	32	96	229	122	0.17
$S_T > 500$ GeV	3.0	25	82	186	80	0.19

Table 2.7: Cut-flow for the $3j$ optimization at 13 TeV. EW stands for $(t\bar{t}Wj)_{\rm EW}$.

	$t\bar{t}h$	$W^{\pm}W^{\pm}$	$t\bar{t}Z$	$t\bar{t}$-misIDQ	DY-misIDQ	WZ
pre-selection	324	32	188	81	32	62
all cuts	35	12	36	10	0	16

Table 2.8: Event yields for the subleading backgrounds at 13 TeV, after $3j$ pre-selection and after the full $3j$ analysis.

ratio of ~ 0.2, to be compared with 3.5 and ~ 0.4, respectively, for the $4j$ analysis. The event yields for the subleading backgrounds are reported in Table 2.8. The DY-mis$Q$ background is very strongly suppressed by the MET cut. The signal yields after all cuts are found to be

$$N_{(t\bar{t}Wj)_{\rm EW}}(\Delta_L, \Delta_R) = 27.1 + 21.1\,\Delta_L + 240.2\,\Delta_L^2 + 3.2\,\Delta_R + 50.4\,\Delta_L\Delta_R + 58.0\,\Delta_R^2 \tag{2.25}$$

$$N_{(t\bar{t}Wj)_{\rm EW}}(\bar{c}_L, \bar{c}_R) = 27.1 - 98.4\,\bar{c}_L + 190.4\,\bar{c}_L^2 - 251.2\,\bar{c}_L^3 + 597.2\,\bar{c}_L^4 + 6.5\,\bar{c}_R - 0.5\,\bar{c}_L\bar{c}_R - 202.6\,\bar{c}_L^2\bar{c}_R + 591.2\,\bar{c}_R^2\,, \tag{2.26}$$

The statistical uncertainty on the signal yields computed using Eqs. (2.25) and (2.26) is approximately 10%. To set constraints on the parameters $\vec{p}$ we follow exactly the same procedure described for the $4j$ analysis, including taking into account the contamination due to the $t\bar{t}Z$ process. The resulting bounds are shown as green contours in Fig. 2.8.[13] If we assume that the only deformation of the SM

[13]From Fig. 2.8 we read that, in the absence of systematics on the background, the $3j$ analysis gives a stronger constraint than the $4j$ one in the $\Delta_L = 0\,,\ \Delta_R > 0$ direction. This may be surprising, considering that we chose this very direction for the optimization of the cuts, and that the $4j$ analysis reached a higher significance (3.5 versus 3.0). The effect is due to the $t\bar{t}Z$ contamination, which slightly shifts all contours, and does so more markedly for the $3j$ analysis, where the $t\bar{t}Z$ contribution to the signal region is larger.

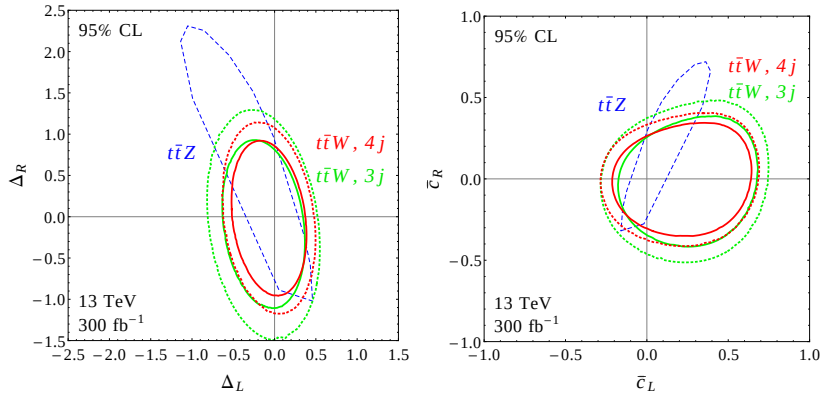

Figure 2.8: In green, the constraints on top-Z coupling deviations (left panel) and HDO coefficients (right panel) derived from our $3j$ $t\bar{t}W$ analysis at 13 TeV. The solid contour assumes no systematic uncertainty on the background, whereas the dotted one includes a 50% systematic on the misIDℓ component. For comparison, in red we show the corresponding constraints derived from the $4j$ $t\bar{t}W$ analysis, and in dashed blue the constraint obtained from the 13 TeV $t\bar{t}Z$ analysis, as derived in Ref. [6]. The red and blue contours are identical to Fig. 2.5.

is a modification of the Zt_Rt_R coupling, we find at 95% CL

$$\begin{aligned} &-0.98 < \Delta_R < 0.70 \qquad \text{or} \qquad -0.31 < \bar{c}_R < 0.22 \qquad \text{(no syst on } B\text{)}, \\ &-1.34 < \Delta_R < 1.05 \qquad \text{or} \qquad -0.42 < \bar{c}_R < 0.33 \qquad \text{(50\% syst on misID}\ell\text{)}. \end{aligned} \tag{2.27}$$

We see that in the $3j$ analysis, the deterioration of the bound due to the large systematic uncertainty on the misIDℓ background is stronger than in the $4j$ analysis, where this background is more effectively suppressed by the cuts.

2.4.4 Perturbative unitarity of the hard scattering process

As we discussed at length, the growth with the square of the energy of the $tW \to tW$ scattering amplitude is the reason behind the sensitivity of our analysis to anomalous top-Z couplings. However, this growth also implies that at sufficiently

high energy, the amplitude becomes so large that perturbative unitarity is lost, making our predictions not trustable. The scale at which this takes place can be estimated, for example, by computing the s-wave amplitude

$$a_0 = \frac{1}{16\pi s}\int_{-s}^{0} dt\mathcal{M}\,, \tag{2.28}$$

where $\mathcal{M}$ is the amplitude, and requiring that $|a_0| < 1$.[14] Considering first deviations in the Zt_Rt_R coupling, by integration of the $\mathcal{M}_{RR}$ amplitude in Eqs. (2.11, 2.12), one finds the following estimate for the cutoff scale

$$\Lambda = \frac{3\sqrt{\pi}\,v}{s_w\sqrt{|\Delta_R|}}\,, \tag{2.29}$$

which equals 2.7 TeV for $|\Delta_R| = 1$, corresponding to a BSM contribution of the same size of the SM coupling. Similarly, for deviations in the Zt_Lt_L coupling the relevant amplitude is $\mathcal{M}_{LL}$, leading to

$$\Lambda = \frac{2\sqrt{3\pi}\,v}{\sqrt{1-\frac{4}{3}s_w^2}\,\sqrt{|\Delta_L|}}\,, \tag{2.30}$$

which equals 1.8 TeV for $|\Delta_L| = 1$. To understand whether perturbative unitarity is an issue in our signal predictions, we should consider the distribution of the center-of-mass energy $\sqrt{\hat{s}}$ of the partonic hard scattering $tW \to tW$ in LHC events. However, given the topology of the signal process $pp \to t\bar{t}Wj$, it is impossible to tell on an event-by-event basis whether the hard scattering that took place was $tW \to tW$, or rather $\bar{t}W \to \bar{t}W$. Thus, to be conservative, for each event we identify $\sqrt{\hat{s}}$ with the largest of the partonic invariant masses $m(tW)$ and $m(\bar{t}W)$. Normalized distributions of this quantity are shown in Fig. 2.9. For each collider energy we show the distributions, obtained after all selection cuts, for a set of signal points that sit approximately at the edge of the exclusion region, together

[14] With this definition, perturbative unitarity in WW scattering is lost, in the absence of a Higgs boson, at the scale $\Lambda = 4\sqrt{2\pi}\,v \simeq 2.5$ TeV.

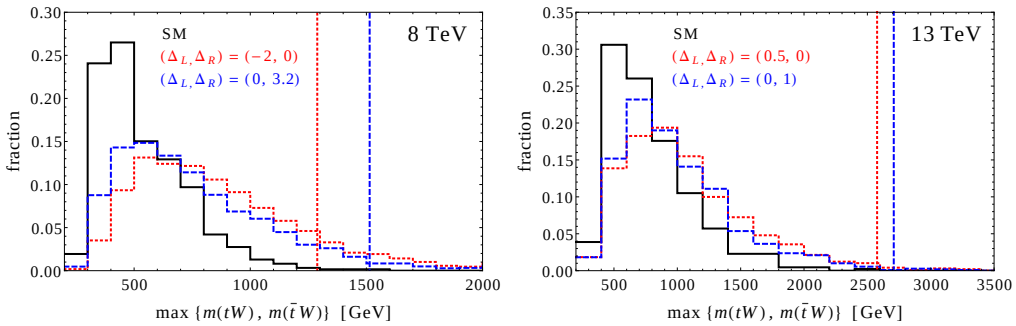

Figure 2.9: Distributions of the partonic center of mass energy, defined as the largest between $m(tW)$ and $m(\bar{t}W)$, for $(t\bar{t}Wj)_{\rm EW}$ signal events at 8 TeV (left panel) and 13 TeV (right panel). The distributions, shown for a set of representative signal points and for the SM, are obtained after application of all selection cuts. The cutoff scales corresponding to each signal point are also shown as vertical lines.

with the corresponding cutoff scales obtained from Eqs. (2.29) and (2.30). We observe that even for the very large deviations allowed by 8 TeV data, the fraction of events whose $\sqrt{\hat{s}}$ could potentially be larger than the cutoff is at most 10%. At 13 TeV, this fraction is approximately 1%. We conclude that our predictions are robustly safe from issues with perturbative unitarity.

2.5 Other processes

In this section we wish to discuss other scattering processes beyond $tW \to tW$ that involve third generation fermions and W, Z or h, where BSM deviations lead to a growth with energy. We will focus on the phenomenologically most relevant amplitudes, pointing out the deformations of the SM to which they are most sensitive to, as well as the most promising collider processes where they could be probed. While our formulas for the amplitudes are expressed in terms of general coupling deviations, in the discussion we assume that departures from the SM

can be parameterized in terms of dim-6 operators, including those proportional to $-\bar{c}_L^{(3)} = \bar{c}_L^{(1)} \equiv \bar{c}_L$, $\bar{c}_R$, and $\bar{c}_u$, and neglecting the remaining ones in Eq. (2.5). The relation between the HDO coefficients and the coupling deviations can be found in Eqs. (2.6–2.8). For all processes of the type $\psi_1 + \phi_1 \to \psi_2 + \phi_2$, with $\psi_{1,2} = \{t, b\}$ and $\phi_{1,2}$ the longitudinal $W^\pm$, Z or h, we make reference to the general form of the amplitude in Eq. (2.11).

2.5.1 $tZ \to th$

For $tZ \to th$ we find $\kappa = 1$ and

$$\begin{aligned}
A_{LL} &= c_L^h \left(1 - \tfrac{4}{3} s_w^2\right), \\
A_{RR} &= -c_R^h \tfrac{4}{3} s_w^2, \\
A_{LR} &= c_L^h + \tfrac{1}{2} c_L (c_t - c_V) - \tfrac{2}{3} s_w^2 \left[2c_L^h + (c_L - c_R)(c_t - c_V)\right], \\
A_{RL} &= -\tfrac{1}{2} c_L (c_t - c_V) - \tfrac{2}{3} s_w^2 \left[2c_R^h - (c_L - c_R)(c_t - c_V)\right].
\end{aligned} \tag{2.31}$$

This process can be probed in $pp \to t\bar{t}hj$. The leading terms of the amplitude grow as $\hat{s}$ and are controlled by the $hZtt$ interaction, which under our assumptions receives contributions from both $\bar{c}_L$ and $\bar{c}_R$: we have $A_{LL} \sim \bar{c}_L$ and $A_{RR} \sim \bar{c}_R$. As a consequence, $tZ \to th$ can be seen as complementary to $tW \to tW$ in probing these two operators, and in particular $\bar{c}_R$. However, one important difference between the $t\bar{t}Wj$ and $t\bar{t}hj$ processes is that for the former the $(t\bar{t}W{+}\text{jets})_{\text{QCD}}$ background is robustly insensitive to new physics in the top sector, whereas for the latter the main background is given by $t\bar{t}h$+jets production, which depends strongly on $c_t = 1 - \bar{c}_u$. The $t\bar{t}h$ signal has been searched for both by ATLAS [39–41] and CMS [42], with 8 TeV data implying an upper limit on the cross section of about 3 times the SM prediction. To enhance the sensitivity to $\bar{c}_L$ and $\bar{c}_R$, one may add

to the existing experimental strategy the requirement of a forward jet, as well as additional high energy cuts on the decay products of the Higgs and the tops. It is interesting to note that if an excess were found in $t\bar{t}h$+jets, in principle this could be caused either by $c_t > 1$, or by a large deviation of the Zt_Rt_R coupling.

2.5.2 $bW \to th$

For $bW^+ \to th$ we find $\kappa = \sqrt{2}$ and

$$\begin{aligned} A_{LL} &= c^h_{LL}\,, \\ A_{RR} &= c^h_{RR}\,, \\ A_{LR} &= c^h_{LL} + \tfrac{1}{2}c_{LL}(c_t - c_V), \\ A_{RL} &= c^h_{RR} + \tfrac{1}{2}c_{RR}(c_t - c_V). \end{aligned} \tag{2.32}$$

This process can be probed in $pp \to thj$. The leading terms of the amplitude grow as $\hat{s}$ and are controlled by the $hWtb$ interaction, which under our assumptions is generated only by the operator proportional to $\bar{c}_L$: we have $A_{LL} = -\bar{c}_L$ and $A_{RR} = 0$, thus the leading sensitivity is to $\bar{c}_L$. An interesting feature of the $bW \to th$ process is that the SM amplitude is strongly suppressed, due to an accidental cancellation between the diagrams with s-channel top exchange and t-channel W exchange [18]. As pointed out in Refs. [16, 17] (see also Ref. [63]), if only Higgs coupling deviations are considered, this cancellation leads to a striking sensitivity of the cross section to $A_{LR} \sim (c_t - c_V)$, which can be exploited to constrain the sign of c_t through a measurement of the thj process. Following this proposal, the CMS collaboration has performed a full analysis on 8 TeV data [64], considering the Higgs decays into $b\bar{b}$, multileptons and $\gamma\gamma$, whereas the ATLAS collaboration has published an analysis in the diphoton channel [39]. We stress that the very

strong sensitivity of thj to $(c_t - c_V)$ is mainly due to the threshold region, because of the already mentioned accidental cancellation, thus justifying why the cross section increases by more than one order of magnitude for $c_t = -c_V = -1$, even though the amplitude only grows as $\sqrt{\hat{s}}$ [17]. For more details on the experimental strategy to separate the thj signal from the background, we refer the reader to the analyses in Ref. [64]. Here we simply observe that the growth of the amplitude like $\hat{s}$ in the presence of a non-vanishing $\bar{c}_L$ suggests the application of tighter cuts on the Higgs and top decay products. In summary, thj may provide an interesting opportunity to constrain $\bar{c}_L$.

2.5.3 $bW \to tZ$

For $bW^+ \to tZ$ we have $\kappa = 1/\sqrt{2}$ and

$$\begin{aligned} A_{LL} &= c_{LL}\left[2 - c_L - c_{L^b} + \tfrac{2}{3}s_w^2(2c_L + c_{L^b} - 3)\right], \\ A_{RR} &= c_{RR}\left[2 + \tfrac{2}{3}s_w^2(2c_R + c_{R^b} - 3)\right], \\ A_{LR} &= c_{LL}\left[1 - c_{L^b} + \tfrac{2}{3}s_w^2(2c_R + c_{L^b} - 3)\right], \\ A_{RL} &= c_{RR}\left[1 - c_L + \tfrac{2}{3}s_w^2(2c_L + c_{R^b} - 3)\right]. \end{aligned} \tag{2.33}$$

This scattering can be probed at the LHC through $pp \to tZj$, which was already suggested in Refs. [6, 65] as a probe of the top-Z couplings. For the pieces that grow like $\hat{s}$ we find $A_{LL} = 2\bar{c}_L(1 - \bar{c}_L)$ and $A_{RR} = 0$, thus the leading sensitivity is to the coefficient $\bar{c}_L$. In Fig. 2.10 we show the partonic cross section for $Wb \to tZ$ scattering. We observe that the cross section is significantly affected by a non-vanishing $\bar{c}_L$, not only at large $\sqrt{\hat{s}}$ but also in the threshold region. On the contrary, $\bar{c}_R$ has a very small impact on the cross section, because its effect arises via the subleading amplitude proportional to $A_{LR} = \bar{c}_R(1 - \bar{c}_L)$, which grows only like $\sqrt{\hat{s}}$.

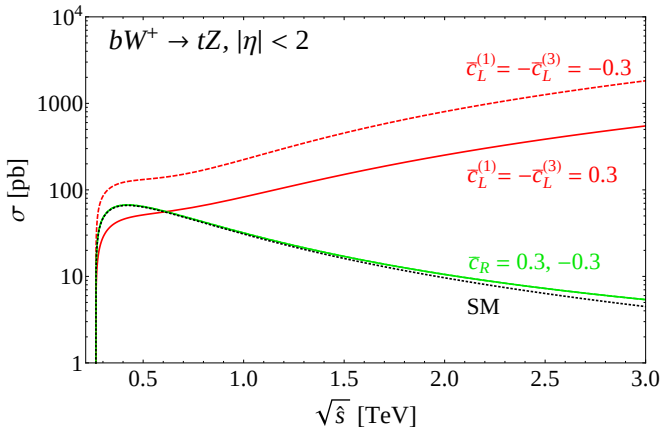

Figure 2.10: Partonic cross section for the process $bW^+ \to tZ$ as a function of the center of mass energy $\sqrt{\hat{s}}$. A pseudorapidity cut $|\eta| < 2$ has been applied to remove the contribution of the forward region, which is enhanced by the diagram with W exchange in the t-channel. At large energy, the red curves diverge like $\hat{s}$, the green curves (which are indistinguishable) tend to a constant limit, whereas the SM cross section (blue) falls off as $1/\hat{s}$.

In the SM, the cross section for tZ production at the LHC is almost as large as the one for $t\bar{t}Z$, despite the fact that the former is a b-initiated pure electroweak process [65]. This is due to the lower number of particles in the final state and the lower mass threshold. Notice that tZj gives rise to the trilepton final state, therefore in principle it could be picked up by the CMS 8 TeV $t\bar{t}Z$ search in the trilepton final state of Ref. [19]. However, the CMS event selection required at least four jets, among which at least two must be b-tagged, thus strongly suppressing the tZj contribution. In fact, in Ref. [65] jet multiplicity was studied as a potential handle to distinguish tZ from $t\bar{t}Z$ production. Based on these preliminary considerations, we conclude that tZ production has negligible sensitivity to $\bar{c}_R$, but may provide another opportunity to constrain the coefficient $\bar{c}_L$.

2.5.4 $tZ \to tZ$

Next we consider $tZ \to tZ$. We find $\kappa = 1/2$ and

$$\begin{aligned} A_{LL} &= A_{RR} = 0\,, \\ A_{LR} &= A_{RL} = (c_L^2 - c_t c_V) - \tfrac{8}{3} s_w^2 c_L (c_L - c_R) + \tfrac{16}{9} s_w^4 (c_L - c_R)^2\,. \end{aligned} \tag{2.34}$$

This process can be probed in $pp \to t\bar{t}Zj$. Differently from $tW \to tW$, however, the $tZ \to tZ$ amplitude grows only linearly with energy, the corresponding coefficients $A_{LR} = A_{RL}$ depending on a combination of $\bar{c}_L, \bar{c}_R$ and $\bar{c}_u$. As explained in Sec. 2.2, the absence of the $\hat{s}/v^2$ growth is a consequence of the symmetry structure of the $\chi\partial\chi\bar{\psi}\gamma\psi$ interactions. The sensitivity to $\bar{c}_u$ is especially interesting, because it is absent in the dominant process for $t\bar{t}Z$ production, which is of $O(g_s^2 g_w)$ and only depends on $\bar{c}_L, \bar{c}_R$. Thus the $t\bar{t}Zj$ final state may in principle provide new information on $\bar{c}_u$. The experimental strategy would rely on the trilepton final state, and the sensitivity to the $O(g_s g_w^3)$ contribution may be enhanced through a forward jet cut. Furthermore, since the amplitude grows with energy, a more stringent cut on the p_T of the Z could also be effective.

2.5.5 $t\bar{t} \to hh$

The last process we consider is $t\bar{t} \to hh$. The pieces of the amplitude that grow with energy can be written as[15]

$$\begin{pmatrix} \mathcal{M}_{LL} & \mathcal{M}_{RL} \\ \mathcal{M}_{LR} & \mathcal{M}_{RR} \end{pmatrix} = -\frac{g^2}{m_W^2} c_t^h m_t \sqrt{\hat{s}} \begin{pmatrix} 0 & 1 \\ -1 & 0 \end{pmatrix}\,, \tag{2.35}$$

where to make the notation uniform with Eq. (2.11), in $\mathcal{M}_{ij}$ the index i indicates the chirality of the top, and the index j indicates the opposite of the chirality

[15] Here we define $\hat{s} = (p_t + p_{\bar{t}})^2$.

of the antitop. This process can be probed in $pp \to t\bar{t}hh$, which was studies in detail in Ref. [66], with an emphasis on its potential role in constraining the Higgs cubic coupling. Based on the form of the amplitude in Eq. (2.35), we observe that the main sensitivity of the cross section is not to deviations in the Higgs cubic coupling, which do not lead to a growth of the amplitude with energy, but to the $h^2 t\bar{t}$ contact interaction (in turn proportional to $\bar{c}_u$), which leads to a growth like $m_t\sqrt{\hat{s}}/v^2$ of the amplitude. This conclusion is familiar from studies of the loop-induced process $gg \to hh$, which gives the largest contribution to the double Higgs production rate at the LHC and was shown to be strongly enhanced in presence of a $t\bar{t}hh$ interaction [67]. In fact, the $t\bar{t} \to hh$ amplitude can be obtained by performing an s-channel cut of $gg \to hh$. While $\bar{c}_u$ will be constrained within 15% by $t\bar{t}h$ production at LHC Run-2 [3], due to the growth of the amplitude with energy the residual effect in $pp \to t\bar{t}hh$ may be non-negligible, and potentially affect the Higgs cubic coupling constraint.

2.6 Conclusions

Progress towards an understanding of the weak scale requires testing the properties of the top quark. In natural models of electroweak symmetry breaking, the couplings of the latter generically deviate from their SM values. As long as the top couples strongly to the new physics resonances, such deformations can be large without requiring new light states. Examples of resonances are heavy vector bosons or vector-like fermions, typical of models where the Higgs arises from a strongly-interacting sector.

In this paper we proposed a new approach to measure deviations in the top

electroweak couplings, which exploits the growth with energy of certain scattering amplitudes involving tops and longitudinal gauge bosons or Higgses. This high energy behaviour can be efficiently probed at the LHC, thanks to the large center of mass energies available. As a proof of concept, we studied in detail $tW \to tW$ scattering, which diverges with the square of the energy in the presence of non-standard ttZ couplings and can be studied at the LHC in $t\bar{t}Wj$ production. By recasting an 8 TeV CMS search for $t\bar{t}W$ in the same-sign lepton final state [19], we extracted constraints on the top-Z couplings. We obtain improved limits compared to those derived from the "conventional" measurement of $t\bar{t}Z$ production, even though the analysis of Ref. [19] was not optimized for our signal. For example, considering only a deviation in the Zt_Rt_R coupling we find $-3.6 < \Delta_R < 2.4$ at 95% CL.

Having verified the effectiveness of our method, we proposed a dedicated 13 TeV analysis. We exploited the distinctive kinematic properties of the $t\bar{t}Wj$ signal, namely a tW pair with large invariant mass and a highly energetic forward jet, to suppress the background, mainly composed by $(t\bar{t}W{+}\text{jets})_{\text{QCD}}$ and misIDℓ. Assuming 300 fb^{-1} of integrated luminosity and no systematic uncertainty on the background, we find $-0.83 < \Delta_R < 0.74$ at 95% CL. In terms of the unique dim-6 operator that modifies the Zt_Rt_R coupling, this reads $-0.26 < \bar{c}_R < 0.23$. In the context of composite Higgs models with a fully composite t_R, where $\bar{c}_R \sim v^2/f^2$ with f the Goldstone-Higgs decay constant, the bound translates into $f \gtrsim 500\,\text{GeV}$.

In addition, we identified several other amplitudes in the same class that could provide further evidence of the strong connection of the top quark with the new physics sector responsible for electroweak symmetry breaking. An interesting example is the $tZ \to th$ process, which is sensitive to modifications of Zt_Rt_R and can

be probed at the LHC in $t\bar{t}hj$ production. It follows that $t\bar{t}h$+jets is sensitive to both of the two least known top couplings, namely Zt_Rt_R and htt, making it an ideal place to look for signs of BSM physics. This warrants further work, to fully exploit the opportunities offered by the LHC in testing the top-Higgs sector.

APPENDIX

2.A Electroweak Chiral Lagrangian

In the custodial invariant electroweak chiral Lagrangian the $SU(2)_L \times U(1)_Y$ SM gauge symmetry is non-linearly realized, with the Nambu-Goldstone bosons eaten by the W and Z parameterized by the 2×2 matrix

$$\Sigma(x) = \exp\left(i\sigma^a \chi^a(x)/v\right) \ , \tag{2.36}$$

where σ^a are the Pauli matrices. Such a Σ field describes the spontaneous breaking $SU(2)_L \times SU(2)_R \to SU(2)_V$, with $U(1)_Y \subset SU(2)_R$. The Higgs boson h is introduced as a singlet under the custodial $SU(2)_V$ symmetry.

The interactions of the top (and bottom) are given, at the level of one derivative, by

$$\begin{aligned}
\mathcal{L}_t^{\chi} = & \, i\bar{q}_L \gamma^\mu D_\mu q_L + i\bar{t}_R \gamma^\mu D_\mu t_R + i\bar{b}_R \gamma^\mu D_\mu b_R \\
& - \frac{y_t v}{\sqrt{2}} \bar{q}_L \Sigma P_u t_R \left(1 + \hat{c}_t \frac{h}{v} + 2\hat{c}_t^h \frac{h^2}{v^2} + \cdots\right) + \text{h.c.} \\
& - \frac{i}{2} \text{Tr}\left[\sigma^3 \Sigma^\dagger D_\mu \Sigma\right] \bar{q}_L \gamma^\mu q_L \left(\hat{c}_{L^{(1)}} + 2\hat{c}^h_{L^{(1)}} \frac{h}{v} + \cdots\right) \\
& + \frac{i}{2} \text{Tr}\left[\sigma^3 \Sigma^\dagger D_\mu \Sigma\right] \bar{q}_L \gamma^\mu \Sigma \sigma^3 \Sigma^\dagger q_L \left(\hat{c}_{L^{(2)}} + 2\hat{c}^h_{L^{(2)}} \frac{h}{v} + \cdots\right) \\
& + \frac{i}{2} \text{Tr}\left[\Sigma^\dagger \sigma^a D_\mu \Sigma\right] \bar{q}_L \gamma^\mu \sigma^a q_L \left(\hat{c}_{L^{(3)}} + 2\hat{c}^h_{L^{(3)}} \frac{h}{v} + \cdots\right) \\
& - \frac{i}{2} \text{Tr}\left[\sigma^3 \Sigma^\dagger D_\mu \Sigma\right] \bar{t}_R \gamma^\mu t_R \left(\hat{c}_R + 2\hat{c}^h_R \frac{h}{v} + \cdots\right) \\
& - \frac{i}{2} \text{Tr}\left[\sigma^3 \Sigma^\dagger D_\mu \Sigma\right] \bar{b}_R \gamma^\mu b_R \left(\hat{c}_{R^b} + 2\hat{c}^h_{R^b} \frac{h}{v} + \cdots\right) \\
& + i P_u^T \Sigma^\dagger D_\mu \Sigma P_d \, \bar{t}_R \gamma^\mu b_R \left(\hat{c}_{R^{tb}} + 2\hat{c}^h_{R^{tb}} \frac{h}{v} + \cdots\right) + \text{h.c.} \ ,
\end{aligned} \tag{2.37}$$

where the dots stand for higher order h interactions. In Eq. (2.37) we introduced $P_u = (1,0)^T$, $P_d = (0,1)^T$ as projectors onto the $Y = -1/2, +1/2$ components of

Σ respectively, and $D_\mu\Sigma = \partial_\mu\Sigma - igW^a_\mu\sigma^a\Sigma/2 + ig'B_\mu\Sigma\sigma^3/2$. From Eq. (2.36) one finds,

$$\begin{aligned}
-\frac{i}{2}\mathrm{Tr}\left[\sigma^3\Sigma^\dagger D_\mu\Sigma\right] &\overset{\Sigma=1}{=} -\frac{g}{2c_w}Z_\mu \ , \\
+\frac{i}{2}\mathrm{Tr}\left[\Sigma^\dagger\sigma^a D_\mu\Sigma\right] &\overset{\Sigma=1}{=} \frac{g}{2}W^a_\mu - \frac{g'}{2}B_\mu\delta^{a3} \ , \\
iP^T_u\Sigma^\dagger D_\mu\Sigma P_d &\overset{\Sigma=1}{=} \frac{g}{\sqrt{2}}W^+_\mu \ ,
\end{aligned} \tag{2.38}$$

in the unitary gauge $\Sigma = 1$, or equivalently at the leading order in the Nambu-Goldstone bosons χ^a. The relations between the coefficients in Eq. (2.1) and those in Eq. (2.37) trivially follow,

$$\begin{aligned}
c_L = 1 + \frac{-\hat{c}_{L^{(1)}} + \hat{c}_{L^{(2)}} + \hat{c}_{L^{(3)}}}{1 - \frac{4}{3}s^2_w} \ , \quad c_{L^b} = 1 + \frac{\hat{c}_{L^{(1)}} + \hat{c}_{L^{(2)}} + \hat{c}_{L^{(3)}}}{1 - \frac{2}{3}s^2_w} \ , \quad c_{LL} = 1 + \hat{c}_{L^{(3)}} \ , \\
c_R = 1 + \frac{\hat{c}_R}{\frac{4}{3}s^2_w} \ , \quad c_{R^b} = 1 - \frac{\hat{c}_{R^b}}{\frac{2}{3}s^2_w} \ , \quad c_{RR} = \hat{c}_{R^{tb}} \ , \quad c_t = \hat{c}_t \ ,
\end{aligned} \tag{2.39}$$

and similarly for the $\hat{c}^h_i$ coefficients. Better suited to understand the high energy behaviour of scattering amplitudes is the gauge-less limit, $g, g' \to 0$. In that case one finds

$$\begin{aligned}
-\frac{i}{2}\mathrm{Tr}\left[\sigma^3\Sigma^\dagger D_\mu\Sigma\right] &\overset{g,g'\to 0}{=} \frac{1}{v}\partial_\mu\chi_3 + \frac{1}{v^2}\big(\chi_1\partial_\mu\chi_2 - \chi_2\partial_\mu\chi_1\big) + O(\chi^3) \ , \\
+\frac{i}{2}\mathrm{Tr}\left[\Sigma^\dagger\sigma^a D_\mu\Sigma\right] &\overset{g,g'\to 0}{=} -\frac{1}{v}\partial_\mu\chi_a + \frac{1}{v^2}\epsilon_{abc}\chi_b\partial_\mu\chi_c + O(\chi^3) \ , \\
iP^T_u\Sigma^\dagger D_\mu\Sigma P_d &\overset{g,g'\to 0}{=} -\frac{\sqrt{2}}{v}\partial_\mu\chi_+ + i\frac{\sqrt{2}}{v^2}\big(\chi_3\partial_\mu\chi_+ - \chi_+\partial_\mu\chi_3\big) + O(\chi^3)
\end{aligned} \tag{2.40}$$

In a similar fashion one can write the leading interactions of the Higgs boson, at the level of two derivatives,

$$\begin{aligned}
\mathcal{L}^\chi_h = \frac{1}{2}(\partial_\mu h)^2 + \frac{v^2}{4}\mathrm{Tr}[|D_\mu\Sigma|^2]\left(1 + 2\hat{c}_V\frac{h}{v} + \cdots\right) \\
- \frac{1}{2}m^2_h h^2 - \hat{c}_3\frac{m^2_h}{2v}h^3 + \cdots \ ,
\end{aligned} \tag{2.41}$$

where the dots stand for higher order h interactions. The relation to Eq. (2.3) is given by $c_V = \hat{c}_V$ and $c_3 = \hat{c}_3$.

2.B Current and projected $t\bar{t}Z$ constraints

Here we discuss briefly the constraints derived from the $t\bar{t}Z$ process, both using 8 TeV data [19] and an existing projection to 13 TeV [6], which we used for comparison with our bounds obtained from $t\bar{t}W$.

2.B.1 8 TeV $t\bar{t}Z$ bound

The trilepton analysis in Ref. [19] was targeted at measuring the $t\bar{t}Z$ process, and thus requires, in addition to two of the leptons being compatible with a Z decay, at least 4 jets, among which at least 2 are b-tagged. To set a limit on the parameters $\vec{p}$ from that analysis, we make use of the event yields listed in Table 2 of Ref. [19] and we assume a systematic uncertainty of 50% on the total background[16]

$$L(\vec{p}\,;r) = \frac{(N_{S+B})^{N_{obs}} e^{-N_{S+B}}}{N_{obs}!} P_{0.5}(r,1) \tag{2.42}$$

where $P_\sigma(x,x_0)$ was defined in Eq. (2.23), and $N_{S+B} = rN_B + \sigma_{t\bar{t}Z}(\vec{p})\mathcal{L}\epsilon$, with $\sigma_{t\bar{t}Z}$ the inclusive cross section for $pp \to t\bar{t}Z$ at 8 TeV, $\mathcal{L} = 19.5$ fb^{-1} the integrated luminosity and ϵ the total efficiency for the SM $t\bar{t}Z$ process. The assumption of constant efficiency is justified, given that the cross section does not grow with energy for non-SM couplings. CMS finds that the contribution of $(t\bar{t}W{+}\text{jets})_{\text{QCD}}$ to the signal region is strongly subleading, therefore the sensitivity to the couplings arising from $(t\bar{t}Wj)_{\text{EW}}$ is negligible.

[16] We have verified that by assuming 50% on the total background as the only systematic uncertainty, we reproduce to good accuracy the measurement of the $t\bar{t}Z$ cross section quoted in Ref. [19]: we find 197^{+107}_{-97} fb, to be compared with 190^{+108}_{-89} fb.

2.B.2 13 TeV $t\bar{t}Z$ projection

The most recent assessment of the projected LHC sensitivity to top-Z couplings in the $pp \to t\bar{t}Z$ process was performed in Ref. [6], by making use of a signal computation at NLO in QCD. The authors focused on the trilepton final state, and to set constraints they exploited, in addition to the total cross section, the differential distribution in the azimuthal opening angle between the leptons stemming from the Z decay. Neither backgrounds nor detector effects were considered. To compare with our results we make use of their Fig. 10, where the relation $\bar{c}_L^{(1)} + \bar{c}_L^{(3)} = 0$ was assumed, and simply map the exclusion contours given there to the planes (Δ_L, Δ_R) and $(\bar{c}_L, \bar{c}_R)$ used in this paper.

2.C Fake lepton simulation

We follow Ref. [48], which proposed a method to efficiently simulate fake leptons starting from MC samples containing jets. The method exploits the relationship between the kinematics of a fake lepton and that of the jet that 'sources' it. It consists in applying to each jet an *efficiency* to generate a fake lepton, assumed to be a function of the jet p_T, and a *transfer function*, which represents a normalized probability distribution for the fraction of the jet p_T that is inherited by the fake lepton. These are parameterized as follows

$$\epsilon_{j\to\ell}(p_T^j) = \epsilon_{200}\left[1 - (1 - r_{10})\frac{200 - p_T^j/\text{GeV}}{200 - 10}\right], \tag{2.43}$$

$$\mathcal{T}_{j\to\ell}(\alpha) = \left(\frac{\sqrt{2\pi}\sigma}{2}\right)^{-1}\left[\text{erf}\left(\frac{1-\mu}{\sqrt{2}\sigma}\right) + \text{erf}\left(\frac{\mu}{\sqrt{2}\sigma}\right)\right]^{-1} e^{-\frac{(\alpha-\mu)^2}{2\sigma^2}}, \tag{2.44}$$

where $\alpha \equiv 1 - p_T^\ell/p_T^j$ is the fraction of the jet momentum that is not transferred to the fake lepton. The residual momentum is assumed to contribute to the MET.

The parameter ϵ_{200} represents the efficiency for fake lepton production at $p_T^j = 200$ GeV, whereas r_{10} sets the slope of the efficiency as function of p_T^j. The transfer function is assumed to be a Gaussian with mean μ and standard deviation σ. In our analysis, the 'source' process is $t\bar{t}+$ jets, and we will assume that fake leptons dominantly originate from heavy flavor (b) jets [19]. The parameters of the fake lepton simulation are chosen as follows. We first set, for simplicity, $r_{10} = 1$, which gives an efficiency independent of the jet p_T. We further set $\mu = 0.5$, based on the generic expectation of equal splitting of the momentum between the fake lepton and the neutrino produced in heavy flavor decays. By comparison with the H_T and $p_T^{\ell_1}$ distributions by CMS, which were obtained with a data-driven method and reported in Fig. 2 of Ref. [19], we find that $\sigma = 0.1$ gives reasonable agreement. We are thus left with only one free parameter, the global efficiency, which we fix to $\epsilon_{200} \approx 2.5 \times 10^{-4}$ to reproduce the total event yield of 12.1 quoted by CMS (see Table 2.2). A somewhat similar choice of parameters was made by the authors of Ref. [68]. We assume no significant difference occurs between fake lepton production at 8 and 13 TeV, and employ the above values of the parameters in our 13 TeV analysis.

BIBLIOGRAPHY

[1] **ATLAS** collaboration, "Observation of a new particle in the search for the Standard Model Higgs boson with the ATLAS detector at the LHC," Phys. Lett. B **716** (2012) 1, arXiv:1207.7214 [hep-ex].

[2] **CMS** collaboration, "Observation of a new boson at a mass of 125 GeV with the CMS experiment at the LHC," Phys. Lett. B **716** (2012) 30, arXiv:1207.7235 [hep-ex].

[3] S. Dawson *et al.*, "Working Group Report: Higgs Boson," 2013 Community Summer Study (Snowmass), arXiv:1310.8361 [hep-ex].

[4] U. Baur, A. Juste, L. H. Orr and D. Rainwater, "Probing electroweak top quark couplings at hadron colliders," Phys. Rev. D **71** (2005) 054013, arXiv:hep-ph/0412021.

[5] E. L. Berger, Q. H. Cao and I. Low, "Model Independent Constraints Among the Wtb, $Zb\bar{b}$, and $Zt\bar{t}$ Couplings," Phys. Rev. D **80** (2009) 074020, arXiv:0907.2191 [hep-ph].

[6] R. Röntsch and M. Schulze, "Constraining couplings of top quarks to the Z boson in $t\bar{t}+Z$ production at the LHC," JHEP **1407** (2014) 091, erratum: JHEP **1509** (2015) 132, arXiv:1404.1005 [hep-ph].

[7] M. S. Chanowitz and M. K. Gaillard, "The TeV Physics of Strongly Interacting W's and Z's," Nucl. Phys. B **261** (1985) 379.

[8] R. Contino, C. Grojean, M. Moretti, F. Piccinini and R. Rattazzi, "Strong Double Higgs Production at the LHC," JHEP **1005** (2010) 089, arXiv:1002.1011 [hep-ph].

[9] G. F. Giudice, C. Grojean, A. Pomarol and R. Rattazzi, "The Strongly-Interacting Light Higgs," JHEP **0706** (2007) 045, arXiv:hep-ph/0703164.

[10] B. Bellazzini, C. Csáki and J. Serra, "Composite Higgses," Eur. Phys. J. C **74** (2014) 5, 2766, arXiv:1401.2457 [hep-ph].

[11] G. Panico and A. Wulzer, "The Composite Nambuoldstone Higgs," Lect. Notes Phys. **913** (2016), arXiv:1506.01961 [hep-ph].

[12] B. Lillie, J. Shu and T. M. P. Tait, "Top Compositeness at the Tevatron and LHC," JHEP **0804** (2008) 087, arXiv:0712.3057 [hep-ph].

[13] A. Pomarol and J. Serra, "Top Quark Compositeness: Feasibility and Implications," Phys. Rev. D **78** (2008) 074026, arXiv:0806.3247 [hep-ph].

[14] K. Kumar, T. M. P. Tait and R. Vega-Morales, "Manifestations of Top Compositeness at Colliders," JHEP **0905** (2009) 022, arXiv:0901.3808 [hep-ph].

[15] T. Appelquist and M. S. Chanowitz, "Unitarity Bound On The Scale Of Fermion Mass Generation," Phys. Rev. Lett. **59** (1987) 2405, erratum: Phys. Rev. Lett. **60** (1988) 1589.

[16] S. Biswas, E. Gabrielli and B. Mele, "Single top and Higgs associated production as a probe of the $Ht\bar{t}$ coupling sign at the LHC," JHEP **1301** (2013) 088, arXiv:1211.0499 [hep-ph].

[17] M. Farina, C. Grojean, F. Maltoni, E. Salvioni and A. Thamm, "Lifting degeneracies in Higgs couplings using single top production in association with a Higgs boson," JHEP **1305** (2013) 022, arXiv:1211.3736 [hep-ph].

[18] F. Maltoni, K. Paul, T. Stelzer and S. Willenbrock, "Associated production of Higgs and single top at hadron colliders," Phys. Rev. D **64** (2001) 094023, arXiv:hep-ph/0106293.

[19] **CMS** collaboration, "Measurement of top quark-antiquark pair production in association with a W or Z boson in pp collisions at $\sqrt{s} = 8$ TeV," Eur. Phys. J. C **74** (2014) 9, 3060, arXiv:1406.7830 [hep-ex].

[20] J. Elias-Miro, J. R. Espinosa, E. Massó and A. Pomarol, "Higgs windows to new physics through $d = 6$ operators: constraints and one-loop anomalous dimensions," JHEP **1311** (2013) 066, arXiv:1308.1879 [hep-ph].

[21] R. D. Peccei and X. Zhang, "Dynamical Symmetry Breaking and Universality Breakdown," Nucl. Phys. B **337** (1990) 269.

[22] E. Malkawi and C. P. Yuan, "A Global analysis of the top quark couplings to gauge bosons," Phys. Rev. D **50** (1994) 4462, arXiv:hep-ph/9405322.

[23] R. Alonso, M. B. Gavela, L. Merlo, S. Rigolin and J. Yepes, "Flavor with a light dynamical 'Higgs particle'," Phys. Rev. D **87** (2013) 055019, arXiv:1212.3307 [hep-ph].

[24] C. Bernardo *et al*, "Studying the Wtb vertex structure using recent LHC results," Phys. Rev. D **90** (2014) 113007, arXiv:1408.7063 [hep-ph].

[25] J. F. Kamenik, M. Papucci and A. Weiler, "Constraining the dipole moments of the top quark," Phys. Rev. D **85** (2012) 071501, erratum: Phys. Rev. D **88** (2013) 039903, arXiv:1107.3143 [hep-ph].

[26] V. Lombardo on behalf of the **ATLAS** and **CMS** collaborations, "Diboson production cross section at LHC," arXiv:1305.3773 [hep-ex].

[27] R. S. Gupta, A. Pomarol and F. Riva, "BSM Primary Effects," Phys. Rev. D **91** (2015) 3, 035001, arXiv:1405.0181 [hep-ph].

[28] M. Geller and O. Telem, "Holographic Twin Higgs Model," Phys. Rev. Lett. **114** (2015) 191801, arXiv:1411.2974 [hep-ph].

[29] R. Barbieri, D. Greco, R. Rattazzi and A. Wulzer, "The Composite Twin Higgs scenario," JHEP **1508** (2015) 161, arXiv:1501.07803 [hep-ph].

[30] M. Low, A. Tesi and L. T. Wang, "Twin Higgs mechanism and a composite Higgs boson," Phys. Rev. D **91** (2015) 095012, arXiv:1501.07890 [hep-ph].

[31] B. Batell, S. Gori and L. T. Wang, "Higgs Couplings and Precision Electroweak Data," JHEP **1301** (2013) 139, arXiv:1209.6382 [hep-ph].

[32] K. Agashe, R. Contino, L. Da Rold and A. Pomarol, "A Custodial symmetry for $Zb\bar{b}$," Phys. Lett. B **641** (2006) 62, arXiv:hep-ph/0605341.

[33] T. M. P. Tait and C.-P. Yuan, "Single top quark production as a window to physics beyond the standard model," Phys. Rev. D **63** (2000) 014018, arXiv:hep-ph/0007298.

[34] A. Buckley *et al.*, "Global fit of top quark effective theory to data," Phys. Rev. D **92** (2015) 091501, arXiv:1506.08845 [hep-ph].

[35] J. de Blas, M. Chala and J. Santiago, "Renormalization Group Constraints on New Top Interactions from Electroweak Precision Data," JHEP **1509** (2015) 189, arXiv:1507.00757 [hep-ph].

[36] R. Barbieri, B. Bellazzini, V. S. Rychkov and A. Varagnolo, "The Higgs boson from an extended symmetry," Phys. Rev. D **76** (2007) 115008, arXiv:0706.0432 [hep-ph].

[37] J. Brod, A. Greljo, E. Stamou and P. Uttayarat, "Probing anomalous $t\bar{t}Z$ interactions with rare meson decays," JHEP **1502** (2015) 141, arXiv:1408.0792 [hep-ph].

[38] **ATLAS** and **CMS** collaborations, "Measurements of the Higgs boson production and decay rates and constraints on its couplings from a combined ATLAS and CMS analysis of the LHC pp collision data at $\sqrt{s} = 7$ and 8 TeV," ATLAS-CONF-2015-044, CMS-PAS-HIG-15-002.

[39] **ATLAS** collaboration, "Search for $H \to \gamma\gamma$ produced in association with top quarks and constraints on the Yukawa coupling between the top quark and the Higgs boson using data taken at 7 TeV and 8 TeV with the ATLAS detector," Phys. Lett. B **740** (2015) 222, arXiv:1409.3122 [hep-ex].

[40] **ATLAS** collaboration, "Search for the Standard Model Higgs boson produced in association with top quarks and decaying into $b\bar{b}$ in pp collisions at $\sqrt{s} = 8$ TeV with the ATLAS detector," Eur. Phys. J. C **75** (2015) 7, 349, arXiv:1503.05066 [hep-ex].

[41] **ATLAS** collaboration, "Search for the associated production of the Higgs boson with a top quark pair in multilepton final states with the ATLAS detector," Phys. Lett. B **749** (2015) 519, arXiv:1506.05988 [hep-ex].

[42] **CMS** collaboration, "Search for the associated production of the Higgs boson with a top-quark pair," JHEP **1409** (2014) 087, erratum: JHEP **1410** (2014) 106, arXiv:1408.1682 [hep-ex].

[43] B. Grinstein, C. W. Murphy, D. Pirtskhalava and P. Uttayarat, "Theoretical Constraints on Additional Higgs Bosons in Light of the 126 GeV Higgs," JHEP **1405** (2014) 083, arXiv:1401.0070 [hep-ph].

[44] **CMS** collaboration, "Observation of top quark pairs produced in association with a vector boson in pp collisions at $\sqrt{s} = 8$ TeV," arXiv:1510.01131 [hep-ex].

[45] **ATLAS** collaboration, "Measurement of the $t\bar{t}W$ and $t\bar{t}Z$ production cross sections in pp collisions at $\sqrt{s} = 8$ TeV with the ATLAS detector," arXiv:1509.05276 [hep-ex].

[46] W. Hollik and D. Pagani, "The electroweak contribution to the top quark forward-backward asymmetry at the Tevatron," Phys. Rev. D **84** (2011) 093003, arXiv:1107.2606 [hep-ph].

[47] F. Maltoni, M. L. Mangano, I. Tsinikos and M. Zaro, "Top-quark charge asymmetry and polarization in $t\bar{t}W$ production at the LHC," Phys. Lett. B **736** (2014) 252, arXiv:1406.3262 [hep-ph].

[48] D. Curtin, J. Galloway and J. G. Wacker, "Measuring the $t\bar{t}h$ coupling from same-sign dilepton+2b measurements," Phys. Rev. D **88** (2013) 093006, arXiv:1306.5695 [hep-ph].

[49] J. Alwall *et al.*, "The automated computation of tree-level and next-to-leading order differential cross sections, and their matching to parton shower simulations," JHEP **1407** (2014) 079, arXiv:1405.0301 [hep-ph].

[50] A. Alloul, N. D. Christensen, C. Degrande, C. Duhr and B. Fuks, "FeynRules 2.0 - A complete toolbox for tree-level phenomenology," Comput. Phys. Commun. **185** (2014) 2250, arXiv:1310.1921 [hep-ph].

[51] T. Sjostrand, S. Mrenna and P. Z. Skands, "PYTHIA 6.4 Physics and Manual," JHEP **0605** (2006) 026, arXiv:hep-ph/0603175.

[52] J. Conway, "PGS4," webpage.

[53] R. D. Ball *et al.*, "Parton distributions with LHC data," Nucl. Phys. B **867** (2013) 244, arXiv:1207.1303 [hep-ph].

[54] J. Alwall, S. de Visscher and F. Maltoni, "QCD radiation in the production of heavy colored particles at the LHC," JHEP **0902** (2009) 017, arXiv:0810.5350 [hep-ph].

[55] F. Maltoni, D. Pagani and I. Tsinikos, "Associated production of a top-quark pair with vector bosons at NLO in QCD: impact on $t\bar{t}H$ searches at the LHC," arXiv:1507.05640 [hep-ph].

[56] M. Czakon, P. Fiedler and A. Mitov, "Total Top-Quark Pair-Production Cross Section at Hadron Colliders Through $O(\alpha_S^4)$," Phys. Rev. Lett. **110** (2013) 252004, arXiv:1303.6254 [hep-ph].

[57] LHC Higgs Cross Section Working Group, "Handbook of LHC Higgs Cross Sections: 3. Higgs Properties," arXiv:1307.1347 [hep-ph].

[58] **CMS** collaboration, "Performance of Electron Reconstruction and Selection with the CMS Detector in Proton-Proton Collisions at $\sqrt{s} = 8$ TeV," JINST **10** (2015) 06, P06005, arXiv:1502.02701 [physics.ins-det].

[59] S. Frixione, V. Hirschi, D. Pagani, H.-S. Shao and M. Zaro, "Electroweak and QCD corrections to top-pair hadroproduction in association with heavy bosons," JHEP **1506** (2015) 184, arXiv:1504.03446 [hep-ph].

[60] M. Aliev *et al.*, "HATHOR: HAdronic Top and Heavy quarks crOss section calculatoR," Comput. Phys. Commun. **182** (2011) 1034, arXiv:1007.1327 [hep-ph].

[61] LHC Higgs Cross Section Working Group, webpage.

[62] M. Backović, T. Flacke, S. J. Lee and G. Perez, "LHC Top Partner Searches Beyond the 2 TeV Mass Region," JHEP **1509** (2015) 022, arXiv:1409.0409 [hep-ph].

[63] S. Biswas, E. Gabrielli, F. Margaroli and B. Mele, "Direct constraints on the top-Higgs coupling from the 8 TeV LHC data," JHEP **1307** (2013) 073, arXiv:1304.1822 [hep-ph].

[64] **CMS** collaboration, "Search for the associated production of a Higgs boson with a single top quark in proton-proton collisions at $\sqrt{s} = 8$ TeV," arXiv:1509.08159 [hep-ex].

[65] J. Campbell, R. K. Ellis and R. Röntsch, "Single top production in association with a Z boson at the LHC," Phys. Rev. D **87** (2013) 114006, arXiv:1302.3856 [hep-ph].

[66] C. Englert, F. Krauss, M. Spannowsky and J. Thompson, "Di-Higgs phenomenology in $t\bar{t}hh$: The forgotten channel," Phys. Lett. B **743** (2015) 93, arXiv:1409.8074 [hep-ph].

[67] R. Gröber and M. Mühlleitner, "Composite Higgs Boson Pair Production at the LHC," JHEP **1106** (2011) 020, arXiv:1012.1562 [hep-ph].

[68] E. Izaguirre and B. Shuve, "Multilepton and Lepton Jet Probes of Sub-Weak-Scale Right-Handed Neutrinos," Phys. Rev. D **91** (2015) 093010, arXiv:1504.02470 [hep-ph].

CHAPTER 3

PROBING A SLEPTON HIGGS ON ALL FRONTIERS

3.1 Introduction

The LHC collaborations have recently discovered the Higgs boson at around 125 GeV [1, 2], but have yet to find any of the particles which should have appeared below the TeV scale as required to solve the hierarchy problem [3]. This suggests that if supersymmetry (SUSY) is present at the TeV scale, it deviates from its most naive implementations. There are many suggestions as to how Nature could be supersymmetric but still avoid the bounds applied by the LHC. In particular, there has been a lot of interest in substituting the R-parity of the Minimal Supersymmetric Standard Model (MSSM) for a continuous R-symmetry, ($U(1)_R$) [4, 5] (see [12–16, 16–19, 19–21, 23, 24, 26, 28–33] for recent work in this direction).

One interesting feature of imposing a $U(1)_R$ symmetry is that it allows the ordinary down-type Higgs to be in a supermultiplet with one of the charged-lepton doublets,

$$H \equiv (H, \ell_L) \tag{3.1}$$

and still avoid phenomenological bounds. This intriguing possibility has been discussed in several recent papers: see [16, 19, 27] for model building, [28] for stop phenomenology, and [29] for a suggested explanation of the recent $eejj, e\nu jj$ excess [30, 31] as well as further discussion on light squark phenomenology. For the purpose of this work we will focus on the possibility that the Higgs doublet is identified with the selectron doublet, though much of our discussion will be more general. This is motivated in section 3.2 as it naturally explains the smallness of the electron mass.

While it is more economical to construct SUSY models where the Higgs is identified with a slepton, usually this causes phenomenological difficulties due to violation of lepton number. In particular, the Kähler potential generates electroweak-scale Dirac masses between the partner neutrino (defined as the neutral fermionic component of L_e) and the gauginos. As a result the partner neutrino generically becomes too heavy. This problem can be avoided by introducing a global symmetry to forbid Majorana neutralino masses, and adding additional adjoint chiral superfields as Dirac partners of the gauginos. This ensures a massless physical neutralino that can be identified with the neutrino. However, due to the smallness of neutrino masses, it is important that the symmetry be preserved under electroweak symmetry breaking. This requires that the global symmetry be an R-symmetry such that the neutrino be charged under the $U(1)_R$ but still leave the Higgs uncharged.

One may wonder why there aren't additional constraints from the many experiments probing lepton flavor number violation. This is because these models generically only have lepton number violation for one flavor (in our case the electron). The stringent limits from lepton number changing processes rely on violation of at least two lepton flavor numbers (most notably $\mu \to e\gamma$, which requires muon and electron number violation).

In this work we explore how Higgs-as-slepton models can be further probed in several different ways. A generic feature of these models is a mixing between the electron doublet and the gauginos, resulting in the physical electron doublet no longer equal to the corresponding gauge eigenstate. This mixing puts bounds on the size of the wino and bino masses. Previous papers have emphasized the corresponding bounds from the high energy frontier through neutral and charged

current universality measurements. In this work we explore the limits from low energy measurements of G_F. We find these to be more stringent then the high energy constraints for bounds on the bino masses and competitive with bounds on the wino masses. Furthermore, we look at the discovery potential of the future e^+e^- collider program. Intriguingly, we find that such a machine has the potential to probe this variant of supersymmetry up to $\mathcal{O}(10\text{ TeV})$.

Another aspect of the model which we will examine is the breaking of R-symmetry through Planck-scale effect, naturally generating a small parameter in the theory. This is responsible for generating neutrino masses which would otherwise be zero, but may also lead to effects such as proton decay.

Experimentally, there has recently been significant development in the neutrino sector. The differences in the squares of the neutrino masses and the three neutrino mixing angles have been measured [32]. Having the Higgs be part of a supermultiplet with the lepton has crucial implications in terms of neutrino phenomenology, the consequences of which we will explore. Planck-scale suppression of R-symmetry breaking effects lead to naturally small neutrino masses. Assuming this is the only source of neutrino masses, we find that in order to obtain the large mixing angles measured by neutrino oscillation experiments, the model typically requires a low cutoff scale of at most $\mathcal{O}(10\text{ TeV})$. In other words, a generic minimal supersymmetric model with the Higgs playing the role of a slepton requires a low ultraviolet (UV) completion scale.

In addition to contributing to neutrino masses, R-symmetry breaking can also lead to proton decay if the gravitino mass is very heavy. Neutrino mass measurements suggests a gravitino mass range between $\mathcal{O}(10\text{ eV}) - \mathcal{O}(10\text{ keV})$ assuming generic gravity-mediated R-breaking. With such masses the model could have

rapid proton decay which restricts the possible UV completions of the model.

This paper is structured as follows. We begin by outlining general properties of the Higgs-as-slepton models in Sec. 3.2. We then proceed to study the constraints on gaugino masses from the lepton-gaugino mixing in Sec. 3.3. Phenomenological implications on future e^+e^- colliders are covered in Sec. 3.4. Implications of the lepton mixing angles on these models are discussed in Sec. 3.5. We move on to bounds on the gravitino mass from proton decay and neutrino mass measurements in Sec. 3.6. We conclude in Sec. 3.7 with a summary of our main results.

3.2 The basics of Higgs-as-slepton models

We consider the most minimal version of the Higgs-as-slepton model from a bottom-up perspective, in which the only additional fields added to the Higgs-less Standard Model (SM) and their supersymmetric partners are the Dirac partners of the gauginos. Table 7.1 lists the superfields and their gauge and $U(1)_R$ representations. As mentioned earlier we have chosen the Higgs to be in L_e. In places where we generalize our discussion to other choices of lepton flavor, this will be stated in the text. The R-charges are chosen so that left-handed (LH) and right-handed (RH) quarks and leptons form R-symmetric Dirac pairs, and that the Higgs vacuum expectation value (VEV) does not break R-symmetry.

Note that we keep B and L as free parameters, and thus they are not identified with the usual baryon and lepton numbers. Based on our assignments, the quarks have R-charges B, the muon and tau $-L$, while the electron always carries R-charge -1. Moreover, the normalization of L and B is not determined such that different normalization result in different models with different phenomenology.

	$(SU(3)_C, SU(2)_L)_Y$	$U(1)_R$
$H \equiv L_e$	$(1,2)_{-1/2}$	0
E_e^c	$(1,1)_1$	2
$L_{\mu,\tau}$	$(1,2)_{-1/2}$	$1-L$
$E_{\mu,\tau}^c$	$(1,1)_1$	$1+L$
$Q_{1,2,3}$	$(3,2)_{1/6}$	$1+B$
$U_{1,2,3}^c$	$(\bar{3},1)_{-2/3}$	$1-B$
$D_{1,2,3}^c$	$(\bar{3},1)_{1/3}$	$1-B$
$W^{a\alpha}$	$(8,1)_0 + (1,3)_0 + (1,1)_0$	1
Φ^a	$(8,1)_0 + (1,3)_0 + (1,1)_0$	0

Table 3.1: Superfields in the minimal low energy model with the Higgs doublet identified with the selectron doublet. The $U(1)_R$ charges are parameterized with two unknown variables L and B, which gives the most general assignment consistent with the requirement of the existence of Yukawas, R-charge conservation after electroweak symmetry breaking, and supersymmetry. The $U(1)_R$ in the table refers to the scalar component of the superfield.

We learn that B and L are parameters that determine the R-charge of the quarks and the second- and third-generation lepton superfields. No significant change in phenomenology arises from different choices of B, except for $B = 1/3$ or 1 which lead to rapid proton decay and are hence forbidden (see Sec. 3.6). Therefore, in our discussion we only consider the generic B case. On the other hand, viable models can be built for several choices of L. In particular we will consider the $L = -1$, $L = 0$, $L = 1$ and the generic L case, that is $L \neq -1, 0, 1$. Each of these four choices result in distinct lepton phenomenology and hence can be regarded as a separate model.

For a generic assignment of B and L, the superpotential consistent with the symmetries is

$$\mathcal{W} = \sum_{i,j=1}^{3} y_{d,ij} H Q_i D_j^c + \sum_{i,j\in\{\mu,\tau\}} y_{e,ij} H L_i E_j^c \,. \tag{3.2}$$

For the $B = 1/3$ or $L = 1$ cases there are extra terms, but we do not discuss them here. In the case $L = 1$, the details of which can be found in [19, 28].

The Higgs-as-slepton model faces a number of difficulties and here we discuss two of them. First is the fact that supersymmetry forbids a mass term for the up-type quarks. This problem can be solved by introducing non-renormalizable SUSY-breaking Kähler terms suppressed by a UV cutoff scale, Λ,

$$\int d^4\theta \frac{X^\dagger}{M} \frac{H^\dagger Q U}{\Lambda} \,, \tag{3.3}$$

where M is the R-symmetric mediation scale and X is the spurion whose vacuum expectation value $\langle F_X \rangle$ corresponds to the SUSY breaking scale. Perturbativity of the couplings requires the cutoff scale to be at most 4π TeV. Thus the model requires a low-scale UV completion. In principle, one can avoid this by introducing an additional pair of Higgs doublets [16, 19], which then allows top masses to be generated by the tree-level superpotential. However, as we will show in section 3.5, reproducing the correct lepton mixing angles also requires a low cutoff if we assume neutrino masses arise from generic R-breaking. This requirement holds even with the additional Higgs doublets. The second problem is that the superpotential cannot provide a mass term for the fermion component of the $H = L_e$ doublet (related to the left-handed electron field) since $HH = 0$. Again, this can be resolved by generating a mass in an analogous way [33],

$$\int d^4\theta \frac{X^\dagger X}{M^2} \frac{H D^\alpha H D_\alpha E_3}{\Lambda^2} \,, \tag{3.4}$$

where D_α is the superspace derivative. If the electron doublet is the Higgs partner, then this provides a natural explanation for the smallness of the electron mass, hence motivating our original choice.

One of the most important consequences of having the Higgs as a slepton is the mixing between the electroweak gauginos and the Higgs fermionic superpartner. This puts generic constraints on such models. The Kähler potential generates weak

scale Dirac mass terms given by

$$\int d^4\theta H^\dagger e^V H \supset -\frac{gv}{\sqrt{2}} e_L \tilde{W}^+ - \frac{gv}{2}\nu_e \tilde{W}^0 + \frac{g'v}{2}\nu_e \tilde{B}^0 \,, \tag{3.5}$$

where, g, g' are the $SU(2)_L$ and $U(1)_Y$ coupling constants and $v \simeq 246$ GeV is the vacuum expectation value of the Higgs. The Dirac wino and bino masses, $M_{\tilde{W}}$ and $M_{\tilde{B}}$, are of order of the soft R-symmetric SUSY-breaking scale $M_{\rm soft} \equiv \langle F_X \rangle / M$. This implies a mixing of order of the ratio of the electroweak scale to the soft R-symmetric scale, which we quantify using the small parameter

$$\epsilon \equiv \frac{gv}{2M_{\tilde{W}}} = \frac{m_W}{M_{\tilde{W}}}, \tag{3.6}$$

where m_W is the mass of the W boson. The above implies that the mass of the gauginos must be high. As discussed in the following, the upper bounds on ϵ are $\mathcal{O}0.1$. The mixing can also depend on the size of the non-renormalizable operators arising at the scale Λ. These contributions are model dependent and will be assumed to be negligible. We have also neglected any R-symmetry breaking effects, although we will need to include them when discussing neutrino masses and proton decay later. We also assume that $|M_{\tilde{W}}^2 - M_{\tilde{B}}^2| \gg m_W^2$. While the mixing between the winos and the binos is modified should we relax this assumption, it turns out to have no significant effects on the phenomenology considered in our work. With the above assumptions, and working to $\mathcal{O}(\epsilon^2)$ the mass eigenstates are

$$\chi^-_{1,L} = \left(1 - \epsilon^2\right) e^-_L - \sqrt{2}\epsilon \psi^-_{\tilde{W}} \qquad \chi^{c,+}_{1,R} = e^{c,+}_R \tag{3.7}$$

$$\chi^-_{2,L} = \left(1 - \frac{1}{2}\epsilon^2\right) \psi^-_{\tilde{W}} + \sqrt{2}\epsilon e^-_L \qquad \chi^{c,+}_{2,R} = \tilde{W}^+ \tag{3.8}$$

$$\chi^-_{3,L} = \tilde{W}^- \qquad \chi^{c,+}_{3,R} = \tilde{\psi}^+ \tag{3.9}$$

$$\chi^0_{1,L} = \left(1 - \frac{1}{2}\epsilon^2\left(1 + \alpha^2 t_w^2\right)\right)\nu_e - \epsilon\psi_{\tilde{W}} + \epsilon\alpha t_w \psi_{\tilde{B}} \tag{3.10}$$

$$\chi^0_{2,L} = \left(1 - \frac{1}{2}\epsilon^2\right)\psi_{\tilde{W}} + \epsilon\nu_e + \epsilon^2\frac{\alpha t_w}{1-\alpha}\psi_{\tilde{B}} \qquad \chi^{c,0}_{2,R} = \tilde{W}^0 + \epsilon^2\frac{\alpha^2 t_w}{1-\alpha^2}\tilde{B} \tag{3.11}$$

$$\chi^0_{3,L} = \left(1 - \frac{2}{1}\epsilon^2\alpha^2 t_w^2\right)\psi_{\tilde{B}} - \epsilon\alpha t_w \nu_e - \epsilon^2\frac{\alpha^3 t_w}{1-\alpha^2}\psi_{\tilde{W}} \quad \chi^{c,0}_{3,R} = \tilde{B} - \epsilon^2\frac{\alpha^2 t_w}{1-\alpha^2}\tilde{W}^0 \tag{3.12}$$

where t_w denotes the tangent of the Weak mixing angle, and $\alpha \equiv M_{\tilde{W}}/M_{\tilde{B}}$. (For details on the mixing matrices and diagonalization, see appendix 3.A.)

3.3 Limits on gaugino-electron doublet mixing

Previous works have shown that the strongest constraints on the model arise from the mixing between the gaugino and the electron doublet [16, 27]. The bounds from neutral current universality have been emphasized (with a mention of the weak charged-current universality bounds in Ref. [27]). Charged-current interactions also provide a different set of constraints through non-standard neutrino interactions (NSI) [34–39]. In this section we compute the neutral-current bounds in our general framework and compare the results with additional bounds from NSI. Note that at tree-level neutral current effects can only constrain the wino masses since this arises from mixing of the electrons in the Zee interaction, while charged current measurements are affected by both electron and neutrino mixing in the $We\nu$, yielding bounds on both the wino and bino masses.

We start by computing the electron neutral current. Definitions of the mixing matrices $U_{C,L}$, $U_{C,R}$ and $U_{N,L}$ used here are provided in Appendix 3.A. The

interaction is given by

$$\Delta\mathcal{L} = \frac{g}{c_w}\Bigg[\left(c_w^2 - |(U_{C,R})_{11}|^2\right) (\chi_{1,R}^{c,+})^\dagger \bar{\sigma}^\mu Z_\mu \chi_{1,R}^{c,+} - \left(c_w^2 - \frac{1}{2}|(U_{C,L})_{11}|^2\right) (\chi_{1,L}^-)^\dagger \bar{\sigma}^\mu Z_\mu \chi_{1,L}^- \Bigg]. \tag{3.13}$$

Keeping only terms to $\mathcal{O}(\epsilon^2)$, this gives

$$\Delta\mathcal{L} = \frac{g}{c_w}\left[-s_w^2 (\chi_{1,R}^{c,+})^\dagger \bar{\sigma}^\mu \chi_{1,R}^{c,+} - \left(\frac{1}{2} - s_w^2\right)(\chi_{1,L}^-)^\dagger \bar{\sigma}^\mu \chi_{1,L}^-\right] Z_\mu - \frac{g}{c_w}\epsilon^2 (\chi_{1,L}^-)^\dagger \bar{\sigma}^\mu Z_\mu \chi_{1,L}^-, \tag{3.14}$$

from which we obtain the axial current coupling of the Z to fermions

$$g_A = g_A^{SM}\left[1 + 2\epsilon^2\right], \qquad g_A^{SM} = \frac{g}{2c_w}, \tag{3.15}$$

where g_A^{SM} is the SM value of the axial coupling. (Bounds on the vector current are much weaker and hence irrelevant for this discussion.) Experimentally the bounds on the axial current are [32],

$$\left|\frac{\delta g_A^e}{g_A^e}\right| \approx 1.2 \times 10^{-3} \quad (90\%\ \text{CL}). \tag{3.16}$$

This stringent bound applies only to the wino mass. Bounds on the bino mass arise from modifications of the charged current. The left-handed electron charged current are described by

$$\Delta\mathcal{L} = g\left((U_{N,L})_{21}^*(U_{C,L})_{21} + \frac{1}{\sqrt{2}}(U_{N,L})_{11}^*(U_{C,L})_{11}\right) W_\mu (\chi_{1,R}^{c,+})^\dagger \bar{\sigma}^\mu \chi_{1,L}^0 \tag{3.17}$$

$$= \frac{g}{\sqrt{2}}\left(1 + \frac{\epsilon^2}{2}\left(1 - \alpha^2 t_w^2\right)\right) W_\mu (\chi_{1,R}^{c,+})^\dagger \bar{\sigma}^\mu \chi_{1,L}^0 . \tag{3.18}$$

Ref. [27] computed the charged current universality constraints from τ decays. This corresponds to the limit [40],

$$\frac{|\delta g|}{g^{SM}} \lesssim 2.6 \times 10^{-3} \quad (90\%\ \text{CL}). \tag{3.19}$$

There are more stringent constraints arising from NSI interactions. The most stringent constraint, in models where the Cabibbo-Kobayashi-Maskawa (CKM) matrix is assumed to be unitary, arise from taking the ratio of G_F measured in two different ways. The first is through beta- and Kaon- decays and the second (and more precise) through muon decay. If the CKM is unitary then these should be equal to each other and the ratio gives the bound [34],

$$\frac{|\delta g|}{g^{SM}} \lesssim 4.0 \times 10^{-4} \quad (90\% \text{ CL}) \,. \tag{3.20}$$

This limit, as well as the one from the neutral current, are presented in figure 3.1. We see that while neutral current interactions place a stronger constraint on the wino mass than NSI, it does not constrain the bino mass. Meanwhile, the NSI bounds on the bino mass are generally weaker than on the wino mass due to a t_w suppression in the bino mixing with the neutrino. Combining the NSI and neutral current bounds, we can put a constraint on the bino mass of $M_{\tilde{B}} \gtrsim 1.2$ TeV. This is more stringent than the existing universality constraint of about 500 GeV [27].

3.4 Discovery potential at an e^+e^- collider

The Higgs-as-slepton model generates deviations of the SM couplings in the electron interactions through modifications of pure SM couplings and from additional interactions with the gauginos. This leads us to expect significant discovery potential at an e^+e^- collider. In this section we consider different $2 \to 2$ processes that will deviate from their SM predictions. In the following we keep terms to $\mathcal{O}(\epsilon^2)$ and we ignore all non-renormalizable corrections arising at the scale Λ. In particular we consider, $e^+e^- \to W^+W^-, ZZ, hZ$. The relevant Feynman diagrams are

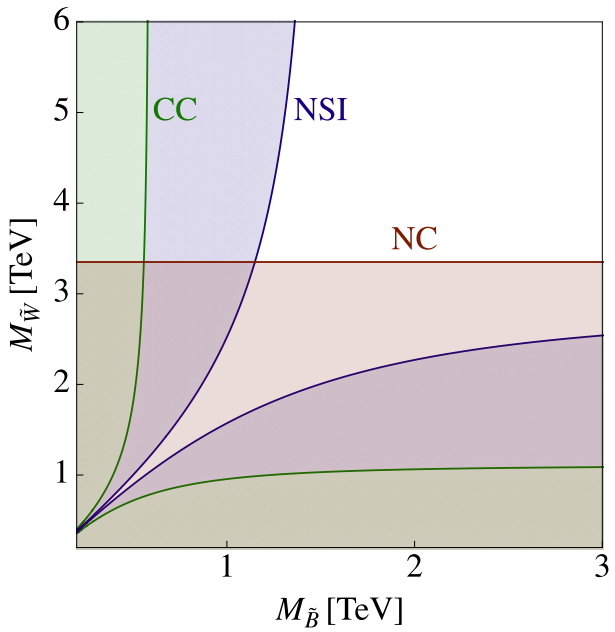

Figure 3.1: Current limits on the bino and wino masses. The regions in blue are excluded by NSI constraints and depend on both the bino and wino mass, while the region in red is ruled out by neutral current constraints. The limits from charged current universality are shown in green.

displayed in figure 3.1. Naively one would expect to also have $e^+e^- \to hh$ arising from chargino exchange, however these turn out not to arise at tree level up to $\mathcal{O}(\epsilon^4)$ due to angular momentum conservation suppressing s-wave production. We use the Feynman rules detailed in Appendix 3.A to compute the cross-sections.

To study projections at a future collider we use the condition that the significance, that we take to be $S/\sqrt{B}$, where S is the signal and B is the background, is larger than 1.645 (corresponding to a 90% confidence interval),

$$\frac{\mathcal{L} \times \delta\sigma}{\sqrt{\mathcal{L} \times \sigma^{SM}}} > 1.645\,, \tag{3.21}$$

where $\mathcal{L}$ is the luminosity of the collider and $\delta\sigma \equiv \sigma^{BSM} - \sigma^{SM}$. We expect this to be a reasonable estimate due to the controlled environment offered by a lepton collider, leading to negligible backgrounds.

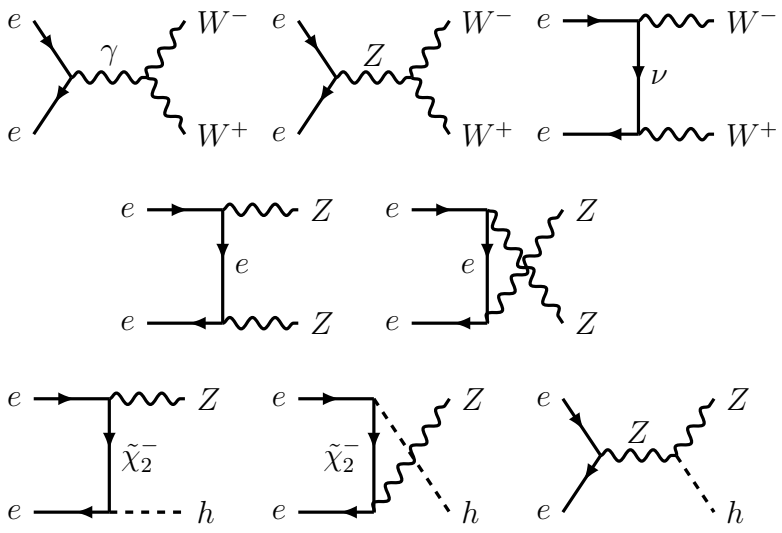

Figure 3.1: Feynman diagrams for the $2 \to 2$ processes that we consider in this work. The top row shows $e^+e^- \to W^+W^-$, the middle row represents $e^+e^- \to ZZ$, and the bottom process is $e^+e^- \to Zh$. We use $\tilde{\chi}_2^-$ to denote the Dirac spinor $\left(\chi_{2,L}^-, (\chi_{2,R}^{c,+})^\dagger\right)$.

One subtlety is the cross-section diverges for small t, or equivalently small $|\eta|$, due to a Rutherford singularity. In order to remove sensitivity to this divergence we cut off the phase space integration at $|\eta| = 2$. To avoid this complication in our expressions, we quote the differential $d(\delta\sigma)/dt$ for each process.

3.4.1 $e^+e^- \to W^+W^-$

We begin by computing the effects to $e^+e^- \to W^+W^-$ scattering. The Feynman diagrams which contribute up to $\mathcal{O}(\epsilon^2)$ are shown in figure 3.1. Note that there are no diagrams with virtual charginos or neutralinos since adding these requires paying the price of additional ϵ's in the vertices. The only modifications to the SM cross-section are from deviations in the Zee couplings. The effects considered here are a close analog to deviations considered in $tW \to tW$ scattering at the LHC from

anomalous Ztt couplings [41]. The cross-sections are straightforward to compute but the expressions are complicated without making some approximations. For simplicity we only quote the result to lowest order in m_V^2/s ($V = h, Z$, or W), though in producing the figures we use the full expressions. The result for the signal is

$$\frac{d(\delta\sigma)}{dt} = \frac{1}{4}\frac{\beta}{32\pi s}\left\{\frac{2e^4}{s_w^4}\frac{\left(\frac{1}{2}-s_w^2-\alpha^2\right)}{\alpha^2}\frac{(-t)}{M_{\tilde{W}}^2}\frac{s+t}{s}+\mathcal{O}\left(\frac{m_V^2}{s},\frac{s^2}{M_{\tilde{W}}^4}\right)\right\}, \qquad (3.22)$$

where $\beta \equiv \sqrt{1-4m_W^2/s}$ is the velocity of either W boson, s_w is the sine of the weak mixing angle, $s \equiv (p_{e^-}+p_{e^+})^2$, $t \equiv (p_{W^-}+p_{W^+})^2$ and $\alpha = m_Z/m_W$.

3.4.2 $e^+e^- \to ZZ$

Next we consider $e^+e^- \to ZZ$ scattering, depicted in figure 3.1. As for W^+W^-, the chargino-exchange diagrams only arise at higher orders in ϵ. Also in this process the deviation from the SM is in the Zee coupling, but, unlike in the W^+W^- case the total cross-section does not grow with energy but is roughly constant. The difference of the energy scaling between ZZ and W^+W^- production can be traced back to the algebra of $SU(2)$ or equivalently the fact that there doesn't exist a triple gauge coupling ZZZ in the model. The signal is,

$$\frac{d(\delta\sigma)}{dt} = \frac{1}{2}\frac{1}{4}\frac{\beta}{32\pi s}\left\{\frac{2e^4}{s_w^4 c_w^4}\left(1-2s_w^2\right)^2\frac{m_W^2}{M_{\tilde{W}}^2}\frac{s^2+2st+2t^2}{t(s+t)}+\mathcal{O}\left(\frac{m_V^4}{s^2},\frac{s^2}{M_{\tilde{W}}^4}\right)\right\}, \qquad (3.23)$$

where here $\beta \equiv \sqrt{1-4m_Z^2/s}$ gives the speed of one of the Z bosons.

Note that for $e^+e^- \to ZZ$ the deviation of the coupling is factorizable as the two diagrams (see figure 3.1) have the same dependence on the anomalous coupling. Thus the new physics contribution is just a rescaling of the SM cross-section.

3.4.3 $e^+e^- \to hZ$

Another interesting channel at a lepton collider is hZ production. The Feynman diagrams are shown in figure 3.1 with the beyond the SM (BSM) effects entering from chargino exchange as well as modifications to the Zee coupling. Since the $\tilde{\chi}_2 he$ vertex does not have an ϵ suppression, these diagrams are still of $\mathcal{O}(\epsilon^2)$. The signal is,

$$\frac{d(\delta\sigma)}{dt} = \frac{1}{4}\frac{\beta}{32\pi s}\left\{\frac{e^4}{s_w^4 c_w^2}\left(\frac{1}{2} - s_w^2\right)\frac{(-t)}{M_{\tilde{W}}^2}\frac{s+t}{s} + \mathcal{O}\left(\frac{m_V^2}{s^2}, \frac{s^2}{M_{\tilde{W}}^4}\right)\right\}, \tag{3.24}$$

where

$$\beta \equiv \sqrt{1 - m_Z^2/E_Z^2}, \qquad E_Z \equiv \frac{\sqrt{s}}{2}\left(1 + \frac{m_Z^2}{s} - \frac{m_h^2}{s^2}\right) \tag{3.25}$$

such that β denotes the speed of the Z boson. The signal is roughly the same as that of W^+W^- production, however the SM cross-section of hZ is significantly smaller due to the relatively small hZZ vertex. This makes deviations easier to identify, increasing its sensitivity to new physics.

Figure 3.2 compares the reach of the different channels as a function of luminosity for a 1 TeV linear collider. The reach at such a collider is striking. A 300fb^{-1} collider can probe wino masses up to $M_{\tilde{W}} \sim 5.4$ TeV, $M_{\tilde{W}} \sim 2.3$ TeV, and $M_{\tilde{W}} \sim 11.5$ TeV for W^+W^-, ZZ, and hZ respectively. The scale probed by hZ is impressive, exploring physics well beyond the TeV scale. Furthermore, correlated excesses in all these channels would be a smoking-gun for the model. These projections highlight the promising opportunities offered by an e^+e^- collider in testing Higgs-as-slepton models.

Lastly, we note that three body production channels can likely be used to probe the model further. In particular, modifications to hhZ production (important for measuring the Higgs-trilinear coupling) are also affected at $\mathcal{O}(\epsilon^2)$. We leave the

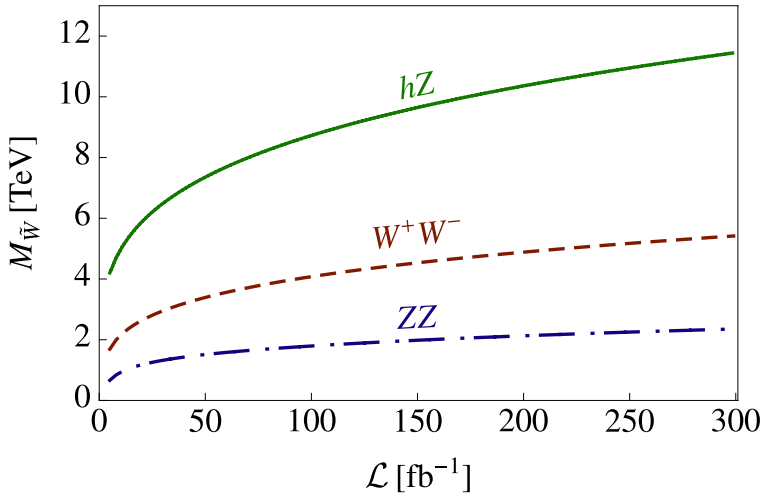

Figure 3.2: The potential reach from $e^+e^- \to VV$ at a future lepton collider as a function of luminosity. The hZ deviations are by far the largest as they scale quickly with energy and have suppressed SM contributions compared to W^+W^-.

study of these channels for future work.

3.5 U_{PMNS} and the need for a TeV-scale cutoff

We next discuss the neutrinos sector in Higgs-as-slepton models. For a generic choices of L, that is, $L \neq 0, 1, -1$, the $U(1)_R$ symmetry forbids neutrino masses. Thus, all neutrino masses are $U(1)_R$-breaking, which can naturally explain the hierarchy between neutrinos and the rest of SM fermions masses. (Exceptions occur in the case $L = 0, -1$, which we will address later.) One extra ingredient in the model is that since it singles out one neutrino flavor to be the Higgs superpartner, this can lead to suppression of the mixing between the Higgs-partner neutrino with the other two neutrino flavors, with obvious implications for the Pontecorvo-Maki-Nakagawa-Sakata (PMNS) matrix, U_{PMNS}. A large suppression of one or more of the mixing angles would be inconsistent with measured values of the $|\theta_{12}| \approx 0.6$,

$|\theta_{23}| \approx 0.7$ and $|\theta_{13}| \approx 0.15$ [32].

In this section, we show that for generic gravity-mediated $U(1)_R$-breaking, consistency with the measured mixing angles requires that the cutoff-scale Λ be less than $\mathcal{O}(10$ TeV), so that non-renormalizable contributions to the neutrino mass matrix be of comparable sizes to that from mixing-induced contributions involving gaugino soft masses. This turns out to be the case regardless of the choice of L. It is interesting to note that the upper-bound on the cutoff scale is similar to the one required for generating a large enough top quark mass, despite the two phenomena being unrelated. While not the focus of this work, we also briefly discuss neutrino mixing in the Higgs-as-slepton model with two additional Higgs doublets (in principle this can replace the UV cutoff needed to produce the top mass). We find that such models also generically require a low energy cutoff, except for particular choices of L.

3.5.1 $L \neq -1, 0, 1$

We establish our analysis framework using the $L \neq -1, 0, 1$ case as an example. We first derive the 3×3 neutrino mass matrix from the full neutralino mass matrix, which we then use to obtain the mixing angles required to diagonalize the neutrino mass matrix. We assume generic gravity mediation and we estimate the sizes of the matrix elements using a spurion analysis, assuming $\mathcal{O}(1)$ coefficients and including non-renormalizable contributions involving the cutoff Λ. Measured values of the mixing angles then translate to bounds on Λ.

To provide a useful picture of the mass scales involved, we refer to Sec. 3.6, where we find that the gravitino mass should be $m_{3/2} \sim \mathcal{O}(10$ eV $-$ 100 eV) in

order to provide the correct neutrino masses. This is much smaller than the $U(1)_R$-symmetric soft mass scale which, as we discussed above, are of the order of few TeVs.

Neutrino mass matrix

In Sec. 3.3 and 3.4, where we studied electroweak precision and collider phenomenology, the main effects came from the mixing between the Higgs-partner neutrinos and the gauginos. Therefore, it was convenient to ignore $U(1)_R$-breaking masses and work with Dirac mass matrices, even for the neutralinos. However, since we are now interested in the mixing between neutrino flavors, the $U(1)_R$-breaking masses play an important role and so it is more useful to work with a Majorana mass matrix instead.

We begin with the tree-level 7×7 neutralino Majorana mass matrix in the interaction basis $\{\nu_e, \nu_\mu, \nu_\tau, \tilde{B}, \tilde{W}^0, \psi_{\tilde{B}}, \psi^0_{\tilde{W}}\}$. We first diagonalize the matrix only with respect to the $U(1)_R$-symmetric terms, from which we find that three of the eigenvectors $\{\nu'_e, \nu_\mu, \nu_\tau\}$ do not have $U(1)_R$-symmetric masses, where ν'_e is given to order $\mathcal{O}(\epsilon)$ by

$$\nu'_e \simeq \nu_e + \epsilon t_w \alpha \psi_{\tilde{B}} - \epsilon \psi_{\tilde{W}^0}. \tag{3.26}$$

These three eigenvectors can still have $U(1)_R$-breaking masses. The associated 3×3 block of the transformed 7×7 neutralino Majorana mass matrix is (the origin of the terms is derived below)

$$M_\nu \equiv \begin{array}{c} \\ \nu'_e \\ \nu_\mu \\ \nu_\tau \end{array} \begin{array}{c} \begin{array}{ccc} \nu'_e & \nu_\mu & \nu_\tau \end{array} \\ \begin{pmatrix} c_{\psi_{\tilde{W}}} + t_w^2 \alpha^2 c_{\psi_{\tilde{B}}} + \epsilon' c_{ee} & \epsilon' c_{e\mu} & \epsilon' c_{e\tau} \\ \epsilon' c_{\mu e} & \epsilon' c_{\mu\mu} & \epsilon' c_{\mu\tau} \\ \epsilon' c_{\tau e} & \epsilon' c_{\tau\mu} & \epsilon' c_{\tau\tau}, \end{pmatrix} \end{array} \epsilon^2 m_{3/2} \tag{3.27}$$

where

$$\epsilon' \equiv \frac{2M_{\tilde{W}}^2}{g^2\Lambda^2}. \tag{3.28}$$

ϵ' can be roughly interpreted as the ratio of the soft mass scales to the cutoff scale of the model. Therefore, a small ϵ' implies a high cutoff scale, while an $\mathcal{O}(1)$ ϵ' implies a low cutoff scale only slightly above the sparticle masses.

The overall factor of $\epsilon^2 m_{3/2}$ can be understood from the fact that the neutrino masses break both $U(1)_R$ and electroweak symmetry. We now explain the origin of the various mass terms. The first two terms in $(M_\nu)_{ee}$ arise from the fact that ν_e' contains $\psi_{\tilde{B}}$ and $\psi^0_{\tilde{W}}$, which in turn are involved in the soft $U(1)_R$-breaking neutralino mass terms

$$\int d^4\theta \frac{X^\dagger}{M_{\rm Pl}} \left(\frac{c_{\psi_{\tilde{B}}}}{2} \Phi_{\tilde{B}} \Phi_{\tilde{B}} + \frac{c_{\psi_{\tilde{W}}}}{2} \Phi_{\tilde{W}} \Phi_{\tilde{W}} \right) \supset m_{3/2} \left(\frac{c_{\psi_{\tilde{B}}}}{2} \psi_{\tilde{B}} \psi_{\tilde{B}} + \frac{c_{\psi_{\tilde{W}}}}{2} \psi^0_{\tilde{W}} \psi^0_{\tilde{W}} \right) , \tag{3.29}$$

where $c_{\psi_{\tilde{B}}}$ and $c_{\psi_{\tilde{W}}}$ are arbitrary $\mathcal{O}(1)$ coefficients since we have assumed generic gravity mediation. As for the other matrix elements, they can be generated by non-renormalizable operators of the form

$$\int d^4\theta \frac{X^\dagger}{M_{\rm Pl}\Lambda^2} \frac{1}{2} c_{ij} \left(L_e^\dagger e^V L_i \right) \left(L_e^\dagger e^V L_j \right) \supset \frac{M_{\tilde{W}}^2}{\Lambda^2} \frac{c_{ij}}{g^2} \epsilon^2 m_{3/2} \nu_i \nu_j \, , \tag{3.30}$$

where $i, j \in \{e, \mu, \tau\}$, and we have again assumed c_{ij} to be $\mathcal{O}(1)$. Note that we have replaced v^2 by $\frac{4M_{\tilde{W}}^2}{g^2}\epsilon^2$ to make the ϵ-dependence manifest.

In principle, one should also take into account loop contributions to M_ν. Generically, we expect the contribution to $(M_\nu)_{ee}$ to be of order $(\epsilon^2 m_{3/2})/(16\pi^2)$, which is a loop factor smaller than the first two tree-level terms and can hence be systematically ignored. For the other matrix elements, the loop contributions cannot be achieved with a single soft $U(1)_R$-breaking insertion (the soft terms cannot supply the required number of units of $U(1)_R$-breaking for these elements), and so require

an insertion of a nonrenormalizable operator, in which case they are also a loop factor smaller than the corresponding tree-level terms. Since we will show that agreement with the measured $U_{\rm PMNS}$ requires a low TeV-scale cutoff Λ, these loop contributions are definitely much smaller than the corresponding tree-level non-renormalizable contributions and so it is consistent to ignore the former without affecting the validity of our final results.

Finally, we argue that M_ν should in fact be regarded as the 3×3 neutrino mass matrix. The neutrino mass matrix is obtained by block-diagonalizing the transformed 7×7 neutralino mass matrix, this time with respect to the $U(1)_R$-breaking masses. However, since the four other transformed states have masses $M_{\tilde{W}}$ or $M_{\tilde{B}}$, the remaining "transformation angles" required for block-diagonalization are at most of $\mathcal{O}(\frac{\epsilon^2 m_{3/2}}{M_{\tilde{W}}})$ or $\mathcal{O}(\frac{\epsilon^2 m_{3/2}}{M_{\tilde{B}}})$. This implies that the basis $\{\nu'_e, \nu_\mu, \nu_\tau\}$ is very close to the actual basis required for block-diagonalization, and also that the resulting "corrections" to M_ν are at most $\mathcal{O}(\frac{\epsilon^4 m_{3/2}}{M_{\tilde{W}}} m_{3/2})$ or $\mathcal{O}(\frac{\epsilon^4 m_{3/2}}{M_{\tilde{B}}} m_{3/2})$ and hence negligible.

Reproducing U_{PMNS}

To obtain the mixing angles in $U_{\rm PMNS}$, we need to find the transformations that diagonalize the charged-lepton and neutrino mass matrices. We first consider the charged-lepton sector. Unlike the neutrinos, the charged-lepton masses are dominated by $U(1)_R$-symmetric contributions. Therefore, the 3×3 charged-lepton Dirac mass matrix is block-diagonal between the electron and the other lepton flavors to a very good approximation since mass terms of the form $e'_L \mu^c_R$, $e'_L \tau^c_R$, $\mu_L e'^c_R$ and $\tau_L e'^c_R$ are $U(1)_R$-breaking and hence much smaller. Therefore, we are completely justified in choosing the lepton flavor basis to coincide with the charged-lepton

mass basis, since the required transformation does not involve the Higgs-partner generation. This means that the PMNS mixing angles are entirely determined by the neutrino sector.

We now consider the neutrinos. We first assume that we can have a high cutoff scale so that $\epsilon' \ll 1$ in which case the neutrino mass matrix takes the form

$$M_\nu \sim \begin{array}{c} \\ \nu'_e \\ \nu_\mu \\ \nu_\tau \end{array} \begin{array}{c} \begin{array}{ccc} \nu'_e & \nu_\mu & \nu_\tau \end{array} \\ \begin{pmatrix} \mathcal{O}(1) & \mathcal{O}(\epsilon') & \mathcal{O}(\epsilon') \\ \mathcal{O}(\epsilon') & \mathcal{O}(\epsilon') & \mathcal{O}(\epsilon') \\ \mathcal{O}(\epsilon') & \mathcal{O}(\epsilon') & \mathcal{O}(\epsilon') \end{pmatrix} \end{array} \epsilon^2 m_{3/2}\,. \tag{3.31}$$

We find that the neutrino mass eigenstate ν_1 (associated most closely with ν'_e) is much heavier than ν_2 and ν_3, and that both mixing angles θ_{12} and θ_{13} are of order ϵ' and hence small. These observations are inconsistent with experimental measurements, implying that we cannot have $\epsilon' \ll 1$. Rather, a $\mathcal{O}(1)$ ϵ' is preferred. In the best-case scenario, allowing for fluctuations in $\mathcal{O}(1)$ coefficients, we place a lower bound of $\epsilon' \gtrsim \mathcal{O}(0.1)$, which in turn implies that

$$\Lambda \lesssim \mathcal{O}\left(\frac{\sqrt{20}}{g} M_{\tilde{W}}\right)\,. \tag{3.32}$$

For $M_{\tilde{W}} \sim$ TeV the required cutoff scale is $\mathcal{O}(10\text{ TeV})$. This ensures that the non-renormalizable contributions to M_ν are comparable to the mixing-induced gaugino soft-term contributions to $(M_\nu)_{ee}$ which is required to have large neutrino mixing angles and a mass hierarchy consistent with measurements. Note that it is possible to evade the mass hierarchy issue associated with $\epsilon' \ll 1$ by choosing a different lepton generation for the Higgs (e.g. the choice τ is consistent with normal hierarchy), but the problems associated with the mixing angles remain.

Finally, we recall that in order to generate the top mass in the Higgs-as-slepton model we require $\Lambda \lesssim \mathcal{O}(10\,\text{TeV})$. It is interesting to note that both the top mass

and neutrino mixing, that are unrelated physical phenomena, both point towards an $\mathcal{O}(10\text{ TeV})$ upper bound for the cutoff scale.

3.5.2 $L = 1$

Now we consider the case with $L = 1$ where there are two main differences with respect to the general case discussed above. The first is the fact that in the neutrino sector, the loop contributions to all the M_ν matrix elements can now be generated by a single soft $U(1)_R$-breaking insertion (whereas this is only true for $(M_\nu)_{ee}$ when $L \neq 1$). Nevertheless, being at least one loop factor smaller than the soft-mass contribution to $(M_\nu)_{ee}$, they are still too small to replace the need for a low cutoff scale Λ.

The second effect is more important; in the charged-lepton sector, the mass terms $e'_L\mu^c_R$, $e'_L\tau^c_R$, $\mu_L e'^c_R$ and $\tau_L e'^c_R$ are no longer $U(1)_R$-breaking, so the charged-lepton Dirac mass matrix isn't diagonal anymore. If we choose the flavor basis to be the charged-lepton mass basis, it is no longer guaranteed that the Higgs be associated with a single flavor, i.e. all the sneutrinos can in principle get VEVs. On the other hand, such a scenario is inconsistent with bounds on lepton-flavor violating processes such as $\mu \to e\gamma$ [32]. For example, if all the sneutrinos get VEVs, the W and Z gauge coupling vertices will then mix the gauginos with all three charged-lepton mass eigenstates such that a W/Z-gaugino loop can induce $\mu \to e\gamma$. Therefore, any successful implementation of the $L = 1$ scenario requires that the sneutrino VEVs be suppressed for two of the generations, which, returning to our original flavor basis, suggests that the Dirac mass matrix should again be approximately block-diagonal. (Note that this also implies that the $L = 1$ model is less favorable than the generic L model due to the need for the sneutrino VEV

suppression in the other two generations.)

Therefore, we conclude that these differences do not affect our conclusion of the need for a TeV-scale cutoff. We note that the same conclusion was made in [19] in the context of a Two Higgs Doublet Model (2HDM) extension of the Higgs-as-slepton model. As a result, the authors introduced a right-handed Dirac neutrino as a low-scale UV completion, which is analogous to our idea of a cutoff scale Λ.

The above discussion is only valid for generic gravity mediated $U(1)_R$-breaking. As discussed in [19], anomaly mediation does not generate soft mass terms of the form $\psi_{\tilde{W}^0}\psi_{\tilde{W}^0}$ and $\psi_{\tilde{B}}\psi_{\tilde{B}}$, so in fact the neutrino mass matrix can be entirely dominated by loop contributions without any constraints on Λ.

3.5.3 $L = 0$

For $L = 0$, before imposing any additional symmetry, the non-renormalizable contributions to $\nu_\mu\nu_\mu$, $\nu_\mu\nu_\tau$ and $\nu_\tau\nu_\tau$ are no longer $U(1)_R$-breaking. As a result, two of the neutrinos become too heavy. Therefore, for such a choice to work, one needs to impose an additional global $U(1)$ lepton number symmetry on L_μ and L_τ [16], assumed to be broken at some flavor scale M_f. At this scale we get an R-conserving but lepton symmetry-violating operator,

$$\int d^4\theta \frac{X^\dagger}{M_f\Lambda^2}\frac{1}{2}c_{ij}\left(L_e^\dagger e^V L_i\right)\left(L_e^\dagger e^V L_j\right) \supset \alpha' \frac{M_{\tilde{W}}^2}{\Lambda^2}\frac{c_{ij}}{g^2}\epsilon^2 m_{3/2}\nu_i\nu_j \quad (i,j \in \{\mu,\tau\})\,, \tag{3.33}$$

where $\alpha' \equiv M_{\rm Pl}/M_f \geq 1$. Note that we have assumed that the M_f-scale mediators can also mediate SUSY-breaking, due to the involvement of the spurion X. Otherwise, we should either replace one of the Λ by M, or replace M_f by $M_{\rm Pl}$,

whichever gives the lower overall suppression. As a result, M_ν now takes the form

$$M_\nu \sim \begin{array}{c} \\ \nu'_e \\ \nu_\mu \\ \nu_\tau \end{array} \begin{array}{c} \begin{array}{ccc} \nu'_e & \nu_\mu & \nu_\tau \end{array} \\ \begin{pmatrix} \mathcal{O}(1) & \mathcal{O}(\epsilon') & \mathcal{O}(\epsilon') \\ \mathcal{O}(\epsilon') & \mathcal{O}(\alpha'\epsilon') & \mathcal{O}(\alpha'\epsilon') \\ \mathcal{O}(\epsilon') & \mathcal{O}(\alpha'\epsilon') & \mathcal{O}(\alpha'\epsilon') \end{pmatrix} \end{array} \epsilon^2 m_{3/2}. \tag{3.34}$$

There are two scenarios that result in the neutrino mixings angles, θ_{12} and θ_{13}, that are very small, which we would like to avoid. The first is if $\epsilon' \ll 1$, and the second if $\alpha'\epsilon' \gg 1$. To avoid both scenarios, we require that $\epsilon' \gtrsim 0.1$ and $\alpha'\epsilon' \lesssim 10$ (or equivalently $\alpha' \lesssim 100$). The first constraint again corresponds to a low TeV-scale cutoff as was found in the previous cases. The second constraint corresponds to $M_f \gtrsim M_{\rm Pl}/100$ or, in other words, that we need the flavor scale cutoff to be close to the Planck scale so that the $U(1)_R$-symmetric neutrino masses do not become too large. Therefore, the lepton number symmetry should be broken very close to the Planck scale. Yet, we note that this conclusion assumes that M_f-scale mediators can also mediate SUSY-breaking, and is not valid otherwise.

3.5.4 $L = -1$

Next, we consider the $L = -1$ case. While less obvious than the $L = 0$ case, we also have the problem of two of the neutrinos becoming too heavy. This can seen from the fact that ν_e, $\psi_{\tilde{W}^0}$ and $\psi_{\tilde{B}}$ have $U(1)_R$-charges -1, while ν_μ, ν_τ, $\tilde{W}^0$ and $\tilde{B}$ have $U(1)_R$-charges $+1$, so there can be three massive Dirac pairs at the $U(1)_R$-symmetric level, leaving only one massless neutralino. More specifically, one can

come up with $U(1)_R$-symmetric mass terms such as

$$\begin{aligned}&\int d^4\theta \frac{X^\dagger}{M}\left(c_{\tilde{B}i}\frac{\Phi_{\tilde{B}}L_e^\dagger e^V L_i}{\Lambda}+c_{\tilde{W}i}\frac{\Phi^a_{\tilde{W}}L_e^\dagger e^V\tau^a L_i}{\Lambda}+c_{ei}\frac{\left(L_e^\dagger e^V L_e\right)\left(L_e^\dagger e^V L_i\right)}{\Lambda^2}\right)\\ &\supset \frac{M_{\rm Pl}}{M}m_{3/2}\left(\frac{\sqrt{2}M_{\tilde{W}}}{g\Lambda}c_{\tilde{B}i}\epsilon\psi_{\tilde{B}}\nu_i+\frac{M_{\tilde{W}}}{\sqrt{2}g\Lambda}c_{\tilde{W}i}\epsilon\psi_{\tilde{W}^0}\nu_i+\frac{M^2_{\tilde{W}}}{g^2\Lambda^2}c_{ei}\epsilon^2\nu_e\nu_i\right),\end{aligned} \tag{3.35}$$

for $i\in\{\mu,\tau\}$, leading to large neutrino masses. Note that $\frac{M_{\rm Pl}}{M}m_{3/2}$ gives the soft $U(1)_R$-symmetric scale.

As in the $L=0$ case, one way to resolve this issue is to introduce an additional $U(1)$ lepton symmetry on L_μ and L_τ, both of which are broken at the flavor scale M_f. As a result, all instances of M in the above equation should be replaced by M_f. Assuming M_f to be large and hence the above terms to be much smaller than the original $U(1)_R$-symmetric masses, we can then follow the previous procedure to obtain the neutrino mass matrix. In other words, we first diagonalize the full 7×7 Majorana mass matrix with respect to the original $U(1)_R$-symmetric terms, following which we block-diagonalize with respect to the remaining lepton symmetry-breaking and/or $U(1)_R$-breaking terms. We find that M_ν now takes the form

$$M_\nu\sim \begin{array}{c} \\ \nu'_e \\ \nu_\mu \\ \nu_\tau \end{array}\begin{array}{c} \begin{array}{ccc}\nu'_e & \nu_\mu & \nu_\tau\end{array} \\ \begin{pmatrix}\mathcal{O}(1) & \mathcal{O}(\alpha'\epsilon') & \mathcal{O}(\alpha'\epsilon') \\ \mathcal{O}(\alpha'\epsilon') & \mathcal{O}(\epsilon') & \mathcal{O}(\epsilon') \\ \mathcal{O}(\alpha'\epsilon') & \mathcal{O}('\epsilon') & \mathcal{O}(\epsilon')\end{pmatrix}\end{array}\epsilon^2 m_{3/2}. \tag{3.36}$$

Again, there are two scenarios that lead to small neutrino mixing(s) which we want to avoid. The first is if $\epsilon'\ll 1$, leading to one or two small angles depending on the size of $\alpha'\epsilon'$. The second is if $\alpha'\epsilon'\gg 1$, leading to one small angle. Therefore, just as in the $L=0$ case, we again see that we require both a low cutoff-scale Λ, and a lepton number-breaking scale M_f close to the Planck scale. Note that the

constraints here are slightly weaker since the suppression may now occur only for one mixing angle, which can be identified with the smallest measured angle θ_{13}.

3.5.5 2HDM Higgs-as-slepton model

Finally, we discuss the 2HDM Higgs-as-slepton model (see appendix 3.B for a summary of the differences), where we will only consider the $L \neq -1, 0, 1$ case for brevity. The 2HDM model may be one possible UV completion of the Higgs-as-sneutrino model [27], completing the model to a much higher scale since the top quark can now gain mass from the up-type Higgs (although the electron mass still has to come from non-renormalizable operators). We now show that the requirement of lepton mixing angles forces also the 2HDM model to have a much lower UV completion scale than one might expect.

The analysis follows the same procedure as before, although it is now complicated by the fact that there are two additional neutralinos, one associated with the up-type Higgs $\tilde{h}_u^0$, and another with the electroweak doublet required for anomaly cancellation $\tilde{r}_d^0$ (these correspond to the superfields H_u and R_d). Also, there are now additional soft $U(1)_R$-breaking terms that can contribute to the neutrino mass matrix via mixing. For instance, we can now have

$$\int d^4\theta \frac{X^\dagger}{M_{\rm Pl}} c_i L_i H_u \supset c_i m_{3/2} \nu_i \tilde{h}_u^0 \tag{3.37}$$

where $i \in \{e, \mu, \tau\}$. This enters the neutrino mass matrix since ν_e' now also contains a $\tilde{h}_u^0$ component. Finally, being a 2HDM model, there is also a $\tan\beta \equiv v_u/v_d$ dependence (where $v_u(v_d)$ is the vacuum expectation value of $h_u(h_d)$).

We find that the neutrino mass matrix takes the form

$$M_\nu \sim \begin{array}{c} \\ \nu'_e \\ \nu_\mu \\ \nu_\tau \end{array} \begin{array}{c} \begin{array}{ccc} \nu'_e & \nu_\mu & \nu_\tau \end{array} \\ \begin{pmatrix} \mathcal{O}(c_\beta^2) + \mathcal{O}(c_\beta s_\beta) + \mathcal{O}(\epsilon') & \mathcal{O}(c_\beta s_\beta) + \mathcal{O}(\epsilon') & \mathcal{O}(c_\beta s_\beta) + \mathcal{O}(\epsilon') \\ \mathcal{O}(c_\beta s_\beta) + \mathcal{O}(\epsilon') & \mathcal{O}(\epsilon') & \mathcal{O}(\epsilon') \\ \mathcal{O}(c_\beta s_\beta) + \mathcal{O}(\epsilon') & \mathcal{O}(\epsilon') & \mathcal{O}(\epsilon') \end{pmatrix} \end{array} \epsilon^2 m_{3/2} \tag{3.38}$$

where $c_\beta \equiv \cos\beta$ and $s_\beta \equiv \sin\beta$. If we assume that $c_\beta s_\beta \sim \mathcal{O}(1)$ or $c_\beta^2 \sim \mathcal{O}(1)$, then we again find one or two mixing angles with size $\mathcal{O}(\epsilon')$. Therefore, we see that even in the 2HDM model, we still need a low cutoff scale in order to reproduce the PMNS matrix. In general the constraint is slightly weaker than before due to the β dependence. This is a non-trivial result since the 2HDM version can otherwise have a much higher cutoff scale given that the top quark mass can be generated by H_u rather than through nonrenormalizable operators. On the other hand, if $t_\beta \gg 1$, we expect both $c_\beta s_\beta$ and c_β^2 to be small, in which case the constraints on the cutoff scale can be less stringent depending on the size of t_β. In particular, for large t_β the required cutoff scale is,

$$\Lambda \lesssim \sqrt{\frac{20}{g^2} t_\beta} M_{\tilde{W}} \,, \tag{3.39}$$

raising the cutoff by a factor of $\sqrt{t_\beta}$.

We note that the above conclusion is invalid for the case $L = 0$, since in this specific case the $\mathcal{O}(\epsilon')$ terms in the lower right 2×2 block are then replaced by $\mathcal{O}(\alpha'\epsilon')$. A small ϵ' can be compensated by a large α' to give large mixing angles. In other words, a larger cutoff-scale Λ can be compensated for by a smaller flavor scale M_f.

3.6 Neutrino masses, proton decay and the gravitino mass

The $U(1)_R$ symmetry in Higgs-as-slepton models serves two important roles: to forbid neutrino masses (as long as the gauginos have separate Dirac mass partners $\psi_{\tilde{G}}$, $\psi_{\tilde{W}}$ and $\psi_{\tilde{B}}$) as well as to forbid superpotential and soft terms that might have otherwise led to rapid proton decay. However, since neutrino masses are small but nonzero, we require explicit breaking of the $U(1)_R$ symmetry, possibly through gravity mediation to account for this smallness. In particular, this implies a relation between the neutrino masses and the gravitino mass $m_{3/2} \approx \langle F_X \rangle / M_{\rm Pl}$, the details of which depends on whether the breaking is through generic "Planck-scale" gravity mediation or through anomaly mediation. The $U(1)_R$-breaking may also introduce proton decay channels, which lead to upper bounds on the gravitino mass $m_{3/2}$. It is hence of interest to discuss the bounds on $m_{3/2}$ from the neutrino mass spectrum and from proton decay. In this section we restrict our attention to the case of generic gravity mediation, since the proton decay channels we consider below do not arise in anomaly mediation despite the $U(1)_R$-breaking.

3.6.1 Bounds from neutrino masses

We have already discussed neutrino masses in Sec. 3.5 and so we will only briefly review the relevant points. If $L \neq -1, 0$, then all neutrino masses involve $U(1)_R$-breaking and hence scale with the gravitino mass $m_{3/2}$. In particular, for generic gravity mediation, we have shown that the Majorana mass for the Higgs-partner neutrino is given by $\sim \epsilon^2 m_{3/2}$. This arises mainly from the mixing of the neutrino with $\psi_{\tilde{B}}$ and $\psi^0_{\tilde{W}}$ and is generally larger than loop-induced masses. We use this to set the mass scale of the heaviest neutrino, since all other terms in the neutrino

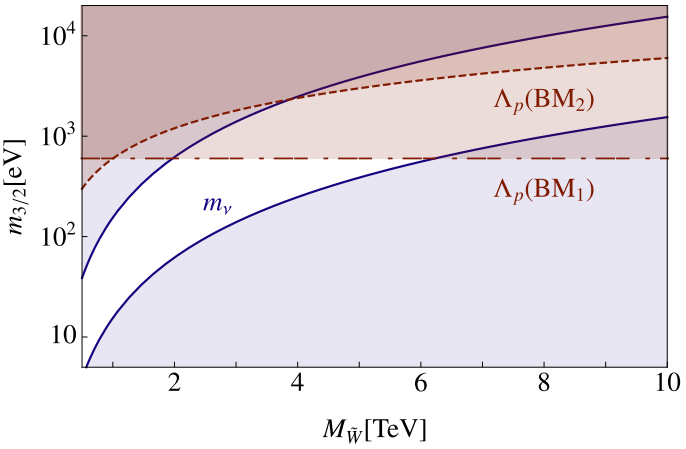

Figure 3.1: The excluded gravitino mass range. The limits in blue correspond to constraints from the neutrino mass scale while the limits in red are from proton lifetime measurements. The constraints from the proton lifetime are dependent on the $m_{\tilde{s}_R}$,$m_{\tilde{g}}$, and we include two benchmark scenarios. BM$_1$ is for $m_{\tilde{s}_R} = M_{\tilde{g}} =$ 1 TeV while BM$_2$ is for $m_{\tilde{s}_R} = 1$ TeV, $M_{\tilde{g}} = M_{\tilde{W}}$.

mass matrix are expected to be of the same order so as to explain the large mixing angles in $U_{\rm PMNS}$. Even for the cases $L = 0$ and $L = -1$, while some of the neutrino mass terms are $U(1)_R$-symmetric, we require them to be suppressed by some flavor scale M_f close to the Planck scale so that these mass terms are comparable to the mixing-induced term above.

Mass hierarchy measurements from neutrino oscillation experiments require the heaviest neutrino mass to be at least around 0.1 eV, while cosmology and spectroscopy experiments place an upper bound of around 1 eV [32]. Together, this implies the following bounds on the gravitino mass:

$$\left(\frac{0.1}{\epsilon}\right)^2 10\,\text{eV} \lesssim m_{3/2} \lesssim \left(\frac{0.1}{\epsilon}\right)^2 100\,\text{eV}. \tag{3.40}$$

Note that the bounds are dependent on the wino mass through ϵ. The allowed values of the gravitino mass are shown in Fig. 3.1 as a function of the wino mass, with the excluded region shown in blue.

3.6.2 Upper bounds from proton decay

After generic gravity-mediated $U(1)_R$-breaking, various operators appear that can give rise to proton decay. For example, we now have $a_{ijk}U^c_{Ri}D^c_{Rj}D^c_{Rk}$ in the superpotential, which comes from

$$\mathcal{L} \supset \int d^4\theta A_{ijk}\frac{X^\dagger}{M_{\rm Pl}\Lambda}U^c_{Ri}D^c_{Rj}D^c_{Rk}, \tag{3.41}$$

so $a_{ijk} = (m_{3/2}/\Lambda)A_{ijk}$, where A_{ijk} are $\mathcal{O}(1)$ coefficients. In conjunction with $y_{d,ij}L_1Q_{Li}D^c_{Rj} \equiv y_{d,ij}H_dQ_{Li}D^c_{Rj}$ already present in the $U(1)_R$-symmetric superpotential, this gives rise to tree-level proton decay, familiar from the R-parity violating MSSM. Remember that we have already excluded the $B = 1$ scenario, in which $a_{ijk}U^c_{Ri}D^c_{Rj}D^c_{Rk}$ is $U(1)_R$-symmetric and hence a_{ijk} is entirely unsuppressed, leading to rapid proton decay.

Another possibility is the one-loop proton decay channels shown in Fig. 3.2, which requires soft trilinear terms $b_{ijk}\tilde{u}^c_{Ri}\tilde{d}^c_{Rj}\tilde{d}^c_{Rk}$, as well as the soft Majorana mass $m_{\tilde{g}}$ and $m_{\psi_{\tilde{g}}}$ for the gluinos and their Dirac partners. The latter are always $U(1)_R$-breaking, so we expect that $m_{\tilde{g}} = c_{\tilde{g}}m_{3/2}$ and $m_{\psi_{\tilde{g}}} = c_{\psi_{\tilde{g}}}m_{3/2}$, where $c_{\tilde{g}}$ and $c_{\psi_{\tilde{g}}}$ are $\mathcal{O}(1)$ coefficients. For $B \neq 1/3$, the trilinear terms are also $U(1)_R$-breaking, so we expect that $b_{ijk} = B_{ijk}m_{3/2}$ where B_{ijk} are $\mathcal{O}(1)$ coefficients. For $B = 1/3$ however, the trilinear terms do not break $U(1)_R$ symmetry, so b_{ijk} should instead be of order the $U(1)_R$-symmetric soft mass scale.

We first consider the one-loop proton decay channels since, as we will see later, they are less dependent on the UV completion than the tree-level ones. For convenience, we work in the basis where the flavor eigenstates of $d_{L,i}, d^c_{R,i}$, and $u_{R,i}$ coincide with the mass eigenstates (otherwise we would have additional CKM matrix contributions, which would of course simplify to the same final result), so for

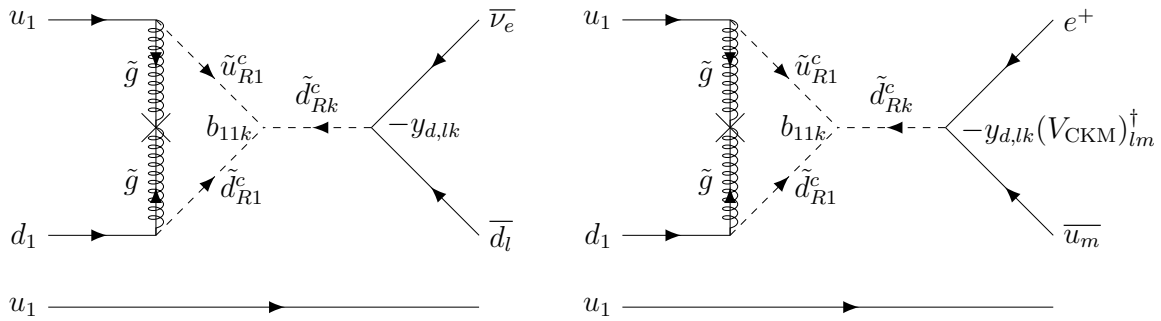

Figure 3.2: One-loop proton decay channels arising from soft trilinear scalar terms $\tilde{u}^c_{Ri}\tilde{d}^c_{Rj}\tilde{d}^c_{Rk}$ and the Majorana gluino mass. All indices here label mass eigenstates. The cross indicates a Majorana gluino mass insertion. There is a similar set of diagrams involving the Majorana mass of the gluino Dirac partner.

instance $y_{d,ij} = \sqrt{2}m_{d,i}\delta_{ij}/v$, where $m_{d,i}$ are the down-type quark masses. We also assume that the quark and squark mass basis are exactly aligned to simplify the index assignments in Fig. 3.2. Relaxing this assumption complicates the analysis but is not expected to significantly affect our main results. Antisymmetry of b_{ijk} under exchange of j and k (due to $SU(3)$ contraction) further implies that $k = 2$ or 3, while kinematic considerations implies $l = 1$ or 2 in the left diagram and $m = 1$ in the right diagram. For an electron-sneutrino Higgs, we find two decay channels: $uud \to u\bar{s}\bar{\nu}$ ($p \to K^+\,\bar{\nu}$) is the dominant decay channel, while $uud \to u\bar{u}e^+$ ($p \to \pi^0\,e^+$) is subdominant due to CKM suppression, despite having a slight phase space enhancement. (Note that the current bounds on either decay channels are comparable [42, 43].) Since the dominant decay channel is to the neutrino rather than the charged lepton, the subsequent analysis remains valid in the case of a muon- or tau-sneutrino Higgs.

We now focus on the dominant one-loop channel. Integrating out the gluinos and squarks gives us the standard dimension-6 proton decay operator $\bar{d^c}\bar{u^c}q_L l_L/\Lambda_p^2$. For simplicity we assume that the gluinos are somewhat heavier than the squarks (as is typical in R-symmetric models due to the supersoft mechanism [44]) and

that $m_{\tilde{g}} \approx m_{\psi_{\tilde{g}}}$. We find that

$$\frac{1}{\Lambda_p^2} \sim \frac{g_s^2}{16\pi^2} \frac{m_{\tilde{g}} b_{112} m_s / v_H}{M_{\tilde{s}_R}^2 M_{\tilde{g}}^2}, \tag{3.42}$$

where g_s is the QCD gauge coupling, m_s the strange quark mass, $M_{\tilde{s}_R}$ the mass of the RH strange squark, and $M_{\tilde{g}}$ Dirac gluino mass. We would like to convert the current lower bound of $\Lambda_p \gtrsim \mathcal{O}(10^{15})\,\text{GeV}$ [43] to an upper bound on $m_{3/2}$. For $B \neq 1/3$, we find that

$$m_{3/2} \lesssim \left(\frac{1}{c_{\tilde{g}} B_{112}}\right)^{1/2} \left(\frac{M_{\tilde{s}_R}}{1\,\text{TeV}}\right) \left(\frac{M_{\tilde{g}}}{1\,\text{TeV}}\right) \times 0.6\,\text{keV}. \tag{3.43}$$

We see that for coefficients of order $\mathcal{O}(1)$ and sparticle masses of order $\mathcal{O}(1)\,\text{TeV}$, we require a gravitino mass of less than $\mathcal{O}(1)\,\text{keV}$. In Fig. 3.1, we compare this to the bounds from neutrino masses for different benchmarks of squark and gluino masses. We see in general that the two bounds still remain compatible.

For $B = 1/3$, we instead have

$$m_{3/2} \lesssim \frac{1}{c_{\tilde{g}}} \left(\frac{1\,\text{TeV}}{b_{112}}\right) \left(\frac{M_{\tilde{s}_R}}{1\,\text{TeV}}\right)^2 \left(\frac{M_{\tilde{g}}}{1\,\text{TeV}}\right)^2 \times 4 \times 10^{-7}\,\text{eV}. \tag{3.44}$$

The bound is much stronger in this case, which is not surprising since $U(1)_R$-breaking now only enters once through the Majorana mass insertion and not the trilinear terms. In fact, this bound clearly conflicts with the bounds from neutrino masses, indicating that $B = 1/3$ is incompatible with generic gravity-mediated $U(1)_R$-breaking.

Now we move on to the the tree-level channel. Integrating out the squarks to obtain the dimension-6 proton decay operator, we find that

$$\frac{1}{\Lambda_p^2} \sim \frac{a_{112} m_s / v_H}{M_{\tilde{s}_R}^2}, \tag{3.45}$$

which translates to a bound of

$$m_{3/2} \lesssim \frac{1}{A_{112}} \left(\frac{M_{\tilde{s}_R}}{1\,\text{TeV}}\right)^2 \left(\frac{\Lambda}{10\,\text{TeV}}\right) \times 3 \times 10^{-8}\,\text{eV}. \tag{3.46}$$

This bound is in conflict with the neutrino mass measurements. This suggests either that the $U(1)_R$-breaking is non-generic, or that we require a non-trivial UV completion such that instead of a suppression by $M_{\rm Pl}\Lambda$ in the tree-level operator, we have an $M_{\rm Pl}^2$ suppression. In this case we replace Λ in the above bound by $M_{\rm Pl}$, from which we get

$$m_{3/2} \lesssim \frac{1}{A_{112}} \left(\frac{M_{\tilde{s}_R}}{1\,\text{TeV}} \right)^2 \times 6\,\text{MeV}. \tag{3.47}$$

which is now consistent with the neutrino constraints and in fact weaker than that from the previous one-loop channel.

To summarize, we have obtained upper bounds on the gravitino mass $m_{3/2}$ from tree-level and one-loop proton decay channels, assuming generic gravity-mediated $U(1)_R$-breaking. Bounds from both channels are consistent with the bounds from the neutrino mass spectrum, provided that $B \neq 1/3$ and that the tree-level non-renormalizable operator is entirely Planck-scale suppressed. The latter condition implies the need for non-trivial UV completions such that the lighter mass scales M or Λ do not enter in the denominator of the tree-level operator, while the suppression is entirely due to M_{Pl}. Finally, we emphasize that our entire discussion hinges on the assumption of generic gravity mediation. If $U(1)_R$-breaking is non-generic, certain $\mathcal{O}(1)$ coefficients may be suppressed or even forbidden.

3.7 Conclusions

Supersymmetric models with the Higgs as a slepton are interesting alternatives to the MSSM. These models have two distinctive features: an R-symmetry which must be broken by gravity and a mixing of the Higgs superpartner lepton with the electroweakinos. These properties allow us to place general bounds on such

models from several different frontiers. In this work, we have studied a variety of such constraints, which we summarize below.

Previous work has pointed out constraints from neutral and charged current universality on the mixing of the electron with the gauginos. These bounds are stringent for the wino, $M_{\tilde{W}} \gtrsim 3.3$ TeV, but weaker for the bino, $M_{\tilde{B}} \gtrsim 500$ GeV. We revisited these bounds in our framework and compare them to complementary bounds from low energy probes, which are much more stringent for the bino, $M_{\tilde{B}} \gtrsim 1.2$ TeV and competitive for the wino mass, $M_{\tilde{W}} \gtrsim 2.8$ TeV. We then moved to study the probing power a future e^+e^- machine. We find large deviations from SM predictions leading to spectacular reach for such a collider. In particular, for an integrated luminosity of 300fb^{-1} and a center of mass energy of 1 TeV, we estimate the potential to probe winos with masses up to 11.5 TeV in the $e^+e^- \to hZ$ channel.

Higgs-as-slepton models also offer a novel explanation for the smallness of neutrino masses, arising from spontaneous breaking of the $U(1)_R$-symmetry due to gravity. We explore the ability of such models to reproduce the neutrino mass spectrum and the measured mixing angles. Typically, we find that the models must be UV-completed at a low scale of at most $\mathcal{O}(10\,\text{TeV})$ in order to reproduce the large measured mixing angles. Interestingly, this is in agreement with the scale required to give a sufficiently large top mass. For the choices $L = 0$ and -1 (where L parameterizes the R-charge of the non-Higgs-partner leptons), some neutrino mass terms are not R-breaking and hence small neutrino masses require an additional lepton number symmetry, assumed to be broken at a scale M_f. We find that, under certain assumptions, constraints on the mixing angles also force M_f to be close to the Planck scale.

Lastly, R-breaking will also generically lead to tree-level proton decay rates inconsistent with experiment. This puts a restriction on the type of models which can UV complete the model. Furthermore, we study loop contributions to proton decay which will be present regardless of the UV completion. We find that these restrict the viable range for the gravitino mass to within the range $\mathcal{O}(10\,\mathrm{eV}) - \mathcal{O}(1\mathrm{keV})$, which is consistent with the predictions from neutrino mass measurements. It may be interesting to study the implications of such a gravitino mass range on observational cosmology, but we will defer this to future work.

The possibility that the Higgs is the superpartner of the electron is an intriguing alternative to standard supersymmetric extensions of the Standard Model. Future tests at the LHC, lepton colliders, low energy experiments, and of the neutrino mixing patterns each provide an avenue to discover this variant of supersymmetry.

APPENDIX

3.A Feynman rules

In this appendix, we derive the couplings for Yukawa and gauge interactions in the chargino and neutralino mass basis. The mixing matrices used here are derived prior to introducing any $U(1)_R$-breaking.

3.A.1 Mixing matrices

The chargino and neutralino mass matrices are given by

$$\mathcal{M}_C \equiv \begin{array}{c} \\ e_L^- \\ \psi_{\tilde{W}}^- \\ \tilde{W}^- \end{array} \begin{array}{c} \begin{array}{ccc} e_R^{c,+} & \tilde{W}^+ & \psi_{\tilde{W}}^+ \end{array} \\ \begin{pmatrix} \mathcal{O}(\epsilon_{\rm NR}) & \frac{gv}{\sqrt{2}} & 0 \\ \mathcal{O}(\epsilon_{\rm NR}) & M_{\tilde{W}} & 0 \\ 0 & 0 & M_{\tilde{W}} \end{pmatrix} \end{array}, \qquad \mathcal{M}_N \equiv \begin{array}{c} \\ \nu_{e,L} \\ \psi_{\tilde{W}}^0 \\ \psi_{\tilde{B}} \end{array} \begin{array}{c} \begin{array}{cc} \tilde{W}^0 & \tilde{B} \end{array} \\ \begin{pmatrix} \frac{gv}{2} & -\frac{g'v}{2} \\ M_{\tilde{W}} & \mathcal{O}(\epsilon_{\rm NR}) \\ \mathcal{O}(\epsilon_{\rm NR}) & M_{\tilde{B}} \end{pmatrix} \end{array}, \tag{3.48}$$

where $\mathcal{O}(\epsilon_{\rm NR})$ denotes any non-renormalizable contributions suppressed by the scale Λ. While we usually neglect them in our calculations unless specified, we include them here to distinguish them from terms which are identically zero due to $U(1)_R$ symmetry.

The chargino mass eigenstates are denoted by

$$\begin{aligned}
&\begin{pmatrix} \chi^-_{1,L} \\ (\chi^{c,+}_{1,R})^\dagger \end{pmatrix} \text{ or } \begin{pmatrix} e^{-\prime}_L \\ (e^{c,+\prime}_R)^\dagger \end{pmatrix} : \quad \text{mass} \sim \mathcal{O}(\epsilon_{\rm NR}), \\
&\begin{pmatrix} \chi^-_{2,L} \\ (\chi^{c,+}_{2,R})^\dagger \end{pmatrix} : \qquad\qquad\quad \text{mass} \approx M_{\tilde{W}}, \\
&\begin{pmatrix} \chi^-_{3,L} \\ (\chi^{c,+}_{3,R})^\dagger \end{pmatrix} : \qquad\qquad\quad \text{mass} \approx M_{\tilde{W}},
\end{aligned} \tag{3.49}$$

and the neutralino mass eigenstates by

$$\begin{aligned}
&\chi^0_{1,L} \text{ or } \nu'_{e,L} : \quad \text{mass} = 0 \\
&\begin{pmatrix} \chi^0_{2,L} \\ (\chi^{c,0}_{2,R})^\dagger \end{pmatrix} : \quad \text{mass} \approx M_{\tilde{W}}, \\
&\begin{pmatrix} \chi^0_{3,L} \\ (\chi^{c,0}_{3,R})^\dagger \end{pmatrix} : \quad \text{mass} \approx M_{\tilde{B}},
\end{aligned} \tag{3.50}$$

where we have arranged the Weyl fermions into Dirac pairs wherever appropriate.

We denote the unitary transformations between the interaction and mass basis by the matrices $U_{C,L}$, $U_{C,R}$, $U_{N,L}$ and $U_{N,R}$, defined as

$$\begin{aligned}
&\begin{pmatrix} e^-_L \\ \psi^-_{\tilde{W}} \\ \tilde{W}^- \end{pmatrix} = U_{C,L} \begin{pmatrix} \chi^-_{1,L} \\ \chi^-_{2,L} \\ \chi^-_{3,L} \end{pmatrix}, \quad \begin{pmatrix} e^{c,+}_R \\ \tilde{W}^+ \\ \psi^+_{\tilde{W}} \end{pmatrix} = U_{C,R} \begin{pmatrix} \chi^{c,+}_{1,R} \\ \chi^{c,+}_{2,R} \\ \chi^{c,+}_{3,R} \end{pmatrix}, \\
&\begin{pmatrix} \nu_{e,L} \\ \psi^0_{\tilde{W}} \\ \psi_{\tilde{B}} \end{pmatrix} = U_{N,L} \begin{pmatrix} \chi^0_{1,L} \\ \chi^0_{2,L} \\ \chi^0_{3,L} \end{pmatrix}, \quad \begin{pmatrix} \tilde{W}^0 \\ \tilde{B} \end{pmatrix} = U_{N,R} \begin{pmatrix} \chi^{c,0}_{1,R} \\ \chi^{c,0}_{2,R} \\ \chi^{c,0}_{3,R} \end{pmatrix}.
\end{aligned} \tag{3.51}$$

Note that $\chi^{c,0}_{1,R}$ does not correspond to any fields present in the model and has been introduced simply for notational convenience.

Assuming $|M_{\tilde{W}} - M_{\tilde{B}}| > m_W$, we find that

$$
\begin{aligned}
U_{C,L} &= \begin{pmatrix} \mathcal{O}(1) & \mathcal{O}(\epsilon) & 0 \\ \mathcal{O}(\epsilon) & \mathcal{O}(1) & 0 \\ 0 & 0 & 1 \end{pmatrix} \xrightarrow{\mathcal{O}(\epsilon^2),\mathcal{O}(\epsilon^0_{\rm NR})} \begin{pmatrix} 1-\epsilon^2 & \sqrt{2}\epsilon & 0 \\ -\sqrt{2}\epsilon & 1-\epsilon^2 & 0 \\ 0 & 0 & 1 \end{pmatrix}, \\
U_{C,R} &= \begin{pmatrix} \mathcal{O}(1) & \mathcal{O}(\epsilon_{\rm NR}) & 0 \\ \mathcal{O}(\epsilon_{\rm NR}) & \mathcal{O}(1) & 0 \\ 0 & 0 & 1 \end{pmatrix} \xrightarrow{\mathcal{O}(\epsilon^2),\mathcal{O}(\epsilon^0_{\rm NR})} \begin{pmatrix} 1 & 0 & 0 \\ 0 & 1 & 0 \\ 0 & 0 & 1 \end{pmatrix}, \\
U_{N,L} &= \begin{pmatrix} \mathcal{O}(1) & \mathcal{O}(\epsilon) & \mathcal{O}(\epsilon) \\ \mathcal{O}(\epsilon) & \mathcal{O}(1) & \mathcal{O}(\epsilon^2) \\ \mathcal{O}(\epsilon) & \mathcal{O}(\epsilon^2) & \mathcal{O}(1) \end{pmatrix} \xrightarrow{\mathcal{O}(\epsilon^2),\mathcal{O}(\epsilon^0_{\rm NR})} \begin{pmatrix} 1-\epsilon^2\frac{1}{2}\left(1+\alpha^2 t_w^2\right) & \epsilon & -\epsilon\alpha t_w \\ -\epsilon & 1-\frac{1}{2}\epsilon^2 & -\frac{\epsilon^2\alpha^3 t_w}{1-\alpha^2} \\ \epsilon\alpha t_w & \frac{\epsilon^2\alpha t_w}{1-\alpha^2} & 1-\epsilon^2\frac{1}{2}\alpha^2 t_w^2 \end{pmatrix}, \\
U_{N,R} &= \begin{pmatrix} 0 & \mathcal{O}(1) & \mathcal{O}(\epsilon^2) \\ 0 & \mathcal{O}(\epsilon^2) & 1 \end{pmatrix} \xrightarrow{\mathcal{O}(\epsilon^2),\mathcal{O}(\epsilon^0_{\rm NR})} \begin{pmatrix} 0 & 1 & -\frac{\epsilon^2\alpha^2 t_w}{1-\alpha^2} \\ 0 & \frac{\epsilon^2\alpha^2 t_w}{1-\alpha^2} & 1 \end{pmatrix},
\end{aligned}
\tag{3.52}
$$

where $\epsilon \equiv m_W/M_{\tilde{W}} = gv/(2M_{\tilde{W}})$, $\alpha \equiv M_{\tilde{W}}/M_{\tilde{B}}$ and $t_w \equiv \tan\theta_w = g'/g$.

3.A.2 Couplings for Yukawa interactions

The Yukawa interactions between the charginos/neutralinos and the Higgs arise from the Kähler potential of the Higgs/electron supermultiplet. The chargino couplings are given by

$$
\begin{aligned}
\mathcal{L} &\supset -g\frac{h}{\sqrt{2}} e_L^- \tilde{W}^+ \\
&= -\frac{g}{\sqrt{2}} h (U_{C,L})_{1i} (U_{C,R})_{2j} \chi^-_{i,L} \chi^-_{j,L}.
\end{aligned}
\tag{3.53}
$$

To $\mathcal{O}(\epsilon)$ and ignoring $\mathcal{O}(\epsilon_{\rm NR})$, this simplifies to

$$
\mathcal{L} \supset -\frac{g}{\sqrt{2}} h \left(\chi^-_{1,L} \chi^{c,+}_{2,R} + \sqrt{2}\epsilon \chi^-_{2,L} \chi^{c,+}_{2,R} \right). \tag{3.54}
$$

The neutralino couplings are given by

$$\begin{aligned}\mathcal{L} &\supset -g\frac{h}{2}\nu_{e,L}\tilde{W}^0 + g'\frac{h}{2}\nu_{e,L}\tilde{B} \\ &= -g\frac{h}{2}(U_{N,L})_{1i}\left[(U_{N,R})_{1j} - t_w(U_{N,L})_{2j}\right]\chi^0_{i,L}\chi^{c,0}_{j,R}.\end{aligned} \tag{3.55}$$

To $\mathcal{O}(\epsilon)$ and ignoring $\mathcal{O}(\epsilon_{\rm NR})$, this simplifies to

$$\mathcal{L} \supset -g\frac{h}{2}\left(\chi^0_{1,L} + \epsilon\chi^0_{2,L} - t_w\frac{M_{\tilde{W}}}{M_{\tilde{B}}}\epsilon\chi^0_{3,L}\right)\left(\chi^{c,0}_{1,R} - t_w\chi^{c,0}_{2,R}\right). \tag{3.56}$$

3.A.3 Couplings for gauge interactions

We begin with the gauge interactions in the interaction basis:

$$\begin{aligned}\mathcal{L} \supset\ & g\begin{pmatrix}(\tilde{W}^+)^\dagger & (\tilde{W}^0)^\dagger & (\tilde{W}^-)^\dagger\end{pmatrix}\begin{pmatrix}W^0_\mu & -W^+_\mu & 0\\ -W^-_\mu & 0 & +W^+_\mu\\ 0 & +W^-_\mu & -W^0_\mu\end{pmatrix}\bar{\sigma}^\mu\begin{pmatrix}\tilde{W}^+\\ \tilde{W}^0\\ \tilde{W}^-\end{pmatrix} \\ & + g\begin{pmatrix}(\psi^+_{\tilde{W}})^\dagger & (\psi^0_{\tilde{W}})^\dagger & (\psi^-_{\tilde{W}})^\dagger\end{pmatrix}\begin{pmatrix}W^0_\mu & -W^+_\mu & 0\\ -W^-_\mu & 0 & +W^+_\mu\\ 0 & +W^-_\mu & -W^0_\mu\end{pmatrix}\bar{\sigma}^\mu\begin{pmatrix}\psi^+_{\tilde{W}}\\ \psi^0_{\tilde{W}}\\ \psi^-_{\tilde{W}}\end{pmatrix} \\ & + g\begin{pmatrix}(\nu_{e,L})^\dagger & (e^-_L)^\dagger\end{pmatrix}\begin{pmatrix}\frac{W^0_\mu}{2} & \frac{W^+_\mu}{\sqrt{2}}\\ \frac{W^-_\mu}{\sqrt{2}} & -\frac{W^0_\mu}{2}\end{pmatrix}\bar{\sigma}^\mu\begin{pmatrix}\nu_{e,L}\\ e^-_L\end{pmatrix} \\ & - \frac{g'}{2}\begin{pmatrix}(\nu_{e,L})^\dagger & (e^-_L)^\dagger\end{pmatrix}B_\mu\bar{\sigma}^\mu\begin{pmatrix}\nu_{e,L}\\ e^-_L\end{pmatrix} \\ & + g'(e^{c,+}_R)^\dagger B_\mu\bar{\sigma}^\mu e^{c,+}_R.\end{aligned} \tag{3.57}$$

For clarity, we separate this into a few parts before converting to the mass basis.

Charged current interactions

The couplings to W_μ^+ are given by

$$\begin{aligned}\mathcal{L} \supset \; & gW_\mu^+ \Bigg\{ (U_{N,R})^*_{1,i} (\chi^{c,0}_{i,R})^\dagger \bar{\sigma}^\mu \chi^-_{3,L} - (U_{C,R})^*_{2,i} (U_{N,R})_{1j} (\chi^{c,+}_{i,R})^\dagger \bar{\sigma}^\mu \chi^{c,0}_{j,R} \\ & + \left[(U_{N,L})^*_{2i} (U_{C,L})_{2j} + \frac{1}{\sqrt{2}} (U_{N,L})^*_{1i} (U_{C,L})_{1j} \right] (\chi^0_{i,L})^\dagger \bar{\sigma}^\mu \chi^-_{j,L} \\ & - (U_{C,R})^*_{3i} (U_{N,L})_{2j} (\chi^{c,+}_{i,R})^\dagger \bar{\sigma}^\mu \chi^0_{j,L} \Bigg\}. \end{aligned} \tag{3.58}$$

We have used the fact that $\tilde{W}^-$ doesn't mix with e_L^- nor $\psi^-_{\tilde{W}}$ (due to $U(1)_R$ symmetry) to eliminate one of the mixing matrices in the first term. To $\mathcal{O}(\epsilon)$ and ignoring $\mathcal{O}(\epsilon_{\rm NR})$, this simplifies to

$$\begin{aligned}\mathcal{L} \supset \; & gW_\mu^+ \Big[(\chi^{c,0}_{2,R})^\dagger \bar{\sigma}^\mu \chi^-_{3,L} - (\chi^{c,+}_{2,R})^\dagger \bar{\sigma}^\mu \chi^{c,0}_{2,R} + \frac{1}{\sqrt{2}} (\chi^0_{1,L})^\dagger \bar{\sigma}^\mu \chi^-_{1,L} \\ & - \frac{1}{\sqrt{2}} \epsilon (\chi^0_{2,L})^\dagger \bar{\sigma}^\mu \chi^-_{1,L} + (\chi^0_{2,L})^\dagger \bar{\sigma}^\mu \chi^-_{2,L} + \epsilon (\chi^{c,+}_{3,R})^\dagger \bar{\sigma}^\mu \chi^0_{1,L} - (\chi^{c,0}_{3,R})^\dagger \bar{\sigma}^\mu \chi^0_{2,L} \Big]. \end{aligned} \tag{3.59}$$

Note that the $V-A$ violating term $(\chi^{c,+}_{1,R})^\dagger \bar{\sigma}^\mu \chi^0_{1,L}$ does not appear, even when we include higher powers of ϵ as well as $\mathcal{O}(\epsilon_{\rm NR})$. This is not surprising since such a term violates $U(1)_R$ symmetry.

Neutral current interactions

We first consider neutral current interactions with the neutralinos, given by

$$\begin{aligned}\mathcal{L} \supset & \frac{g}{c_w} Z_\mu \frac{1}{2} (\nu_{e,L})^\dagger \bar{\sigma}^\mu \nu_{e,L} \\ = & \frac{g}{c_w} Z_\mu \frac{1}{2} (U_{N,L})^*_{1i} (U_{N,L})_{1j} (\chi^0_{i,L})^\dagger \bar{\sigma}^\mu \chi^0_{j,L}. \end{aligned} \tag{3.60}$$

There are no couplings to the photon as expected. To $\mathcal{O}(\epsilon)$ and ignoring $\mathcal{O}(\epsilon_{\rm NR})$, this simplifies to

$$\mathcal{L} \supset \frac{g}{c_w} Z_\mu \frac{1}{2} \left\{ (\chi^0_{1,L})^\dagger \bar{\sigma}^\mu \chi^0_{1,L} + \left[\epsilon (\chi^0_{1,L})^\dagger \bar{\sigma}^\mu \chi^0_{2,L} - t_w \frac{M_{\tilde{W}}}{M_{\tilde{B}}} \epsilon (\chi^0_{1,L})^\dagger \bar{\sigma}^\mu \chi^0_{3,L} + \text{h.c.} \right] \right\}. \tag{3.61}$$

Now we move on to the charginos. The couplings to the photon are given by

$$\begin{aligned} \mathcal{L} \supset \; & eA_\mu \Big[(e^{c,+}_R)^\dagger \bar{\sigma}^\mu e^{c,+}_R + (\tilde{W}^+)^\dagger \bar{\sigma}^\mu \tilde{W}^+ + (\psi^+_{\tilde{W}})^\dagger \bar{\sigma}^\mu \psi^+_{\tilde{W}} \\ & - (e^-_L)^\dagger \bar{\sigma}^\mu e^-_L - (\psi^-_{\tilde{W}})^\dagger \bar{\sigma}^\mu \psi^-_{\tilde{W}} - (\tilde{W}^-)^\dagger \bar{\sigma}^\mu \tilde{W}^- \Big] \\ = \; & eA_\mu \left[(\chi^{c,+}_{i,R})^\dagger \bar{\sigma}^\mu \chi^{c,+}_{i,R} - (\chi^-_{i,L})^\dagger \bar{\sigma}^\mu \chi^-_{i,L} \right]. \end{aligned} \tag{3.62}$$

The couplings are universal as expected since $U(1)_{\rm EM}$ is unbroken.

The couplings to Z_μ are given by

$$\begin{aligned} \mathcal{L} \supset \; & \frac{g}{c_w} Z_\mu \left[(\tilde{W}^+)^\dagger \bar{\sigma}^\mu \tilde{W}^+ - (\tilde{W}^-)^\dagger \bar{\sigma}^\mu \tilde{W}^- + (\psi^+_{\tilde{W}})^\dagger \bar{\sigma}^\mu \psi^+_{\tilde{W}} - (\psi^-_{\tilde{W}})^\dagger \bar{\sigma}^\mu \psi^-_{\tilde{W}} - \frac{1}{2} (e^-_L)^\dagger \bar{\sigma}^\mu e^-_L \right] \\ & - \frac{g}{c_w} s_w^2 Z_\mu \Big[(e^{c,+}_R)^\dagger \bar{\sigma}^\mu e^{c,+}_R + (\tilde{W}^+)^\dagger \bar{\sigma}^\mu \tilde{W}^+ + (\psi^+_{\tilde{W}})^\dagger \bar{\sigma}^\mu \psi^+_{\tilde{W}} \\ & - (e^-_L)^\dagger \bar{\sigma}^\mu e^-_L - (\psi^-_{\tilde{W}})^\dagger \bar{\sigma}^\mu \psi^-_{\tilde{W}} - (\tilde{W}^-)^\dagger \bar{\sigma}^\mu \tilde{W}^- \Big] \\ = \; & \frac{g}{c_w} Z_\mu \Bigg\{ \left[(U_{C,R})^*_{2i} (U_{C,R})_{2j} + (U_{C,R})^*_{3i} (U_{C,R})_{3j} \right] (\chi^{c,+}_{i,R})^\dagger \bar{\sigma}^\mu \chi^{c,+}_{j,R} \\ & - \left[\frac{1}{2} (U_{C,L})^*_{1i} (U_{C,L})_{1j} + (U_{C,L})^*_{2i} (U_{C,L})_{2i} + (U_{C,L})^*_{3i} (U_{C,L})_{3i} \right] (\chi^-_{i,L})^\dagger \bar{\sigma}^\mu \chi^-_{j,L} \Bigg\} \\ & - \frac{g}{c_w} s_w^2 Z_\mu \left[(\chi^{c,+}_{i,R})^\dagger \bar{\sigma}^\mu \chi^{c,+}_{i,R} - (\chi^-_{i,L})^\dagger \bar{\sigma}^\mu \chi^-_{i,L} \right]. \end{aligned} \tag{3.63}$$

This comprises of a non-universal part related to mixing between different $SU(2)_L$ representations and a universal part related to Q. Using unitarity of $U_{C,L}$ and $U_{C,R}$, this can be written more succinctly as

$$\begin{aligned} \mathcal{L} \supset \; & \frac{g}{c_w} Z_\mu \Big[(1 - s_w^2) (\chi^{c,+}_{i,R})^\dagger \bar{\sigma}^\mu \chi^{c,+}_{i,R} + (-1 + s_w^2) (\chi^-_{i,L})^\dagger \bar{\sigma}^\mu \chi^-_{i,L} \Big] \\ & + \frac{g}{c_w} Z_\mu \Big[- (U_{C,R})^*_{1i} (U_{C,R})_{1j} (\chi^{c,+}_{i,R})^\dagger \bar{\sigma}^\mu \chi^{c,+}_{j,R} + \frac{1}{2} (U_{C,L})^*_{1i} (U_{C,L})_{1j} (\chi^-_{i,L})^\dagger \bar{\sigma}^\mu \chi^-_{i,L} \Big]. \end{aligned} \tag{3.64}$$

	$(SU(3)_C, SU(2)_L)_Y$	$U(1)_R$
$H_d \equiv L_e$	$(1,2)_{-1/2}$	0
E_e^c	$(1,1)_1$	2
$L_{\mu,\tau}$	$(1,2)_{-1/2}$	$1-L$
$E_{\mu,\tau}^c$	$(1,1)_1$	$1+L$
$Q_{1,2,3}$	$(3,2)_{1/6}$	$1+B$
$U_{1,2,3}^c$	$(\bar{3},1)_{-2/3}$	$1-B$
$D_{1,2,3}^c$	$(\bar{3},1)_{1/3}$	$1-B$
$W^{a\alpha}$	$(8,1)_0+(1,3)_0+(1,1)_0$	1
Φ^a	$(8,1)_0+(1,3)_0+(1,1)_0$	0
H_u	$(1,2)_{1/2}$	0
R_d	$(1,2)_{-1/2}$	2

Table 3.B.1: Superfields and their gauge and $U(1)_R$ representations for the 2HDM version of the Higgs-as-sneutrino model.

To $\mathcal{O}(\epsilon)$ and ignoring $\mathcal{O}(\epsilon_{\rm NR})$, this simplifies to

$$\begin{aligned}\mathcal{L} \supset\ & \frac{g}{c_w} Z_\mu \left[(1-s_w^2)(\chi_{i,R}^{c,+})^\dagger \bar{\sigma}^\mu \chi_{i,R}^{c,+} + (-1+s_w^2)(\chi_{i,L}^-)^\dagger \bar{\sigma}^\mu \chi_{i,L}^-\right] \\ & + \frac{g}{c_w} Z_\mu \left\{ -(\chi_{1,R}^{c,+})^\dagger \bar{\sigma}^\mu \chi_{1,R}^{c,+} + \frac{1}{2}(\chi_{1,L}^-)^\dagger \bar{\sigma}^\mu \chi_{1,L}^- + \left[\sqrt{2}\epsilon (\chi_{1,L}^-)^\dagger \bar{\sigma}^\mu \chi_{2,L}^- + \text{h.c.}\right]\right\}. \end{aligned} \tag{3.65}$$

3.B Two Higgs Doublet Model

Here we briefly review the Higgs-as-slepton model with two additional Higgs doublets, H_u, R_d. The H_u can then be used to provide a mass to the top quark, while R_d is needed for anomaly cancellation. Table 3.B.1 lists the superfields and their gauge and $U(1)_R$ representations. The most general superpotential consistent with the symmetries (assuming $B \neq 1/3$ and $L \neq 1$) is

$$\begin{aligned}\mathcal{W} = & \sum_{i,j=1}^{3} y_{d,ij} H_d Q_i D_j^c + \sum_{i,j\in\{\mu,\tau\}} y_{e,ij} H_d L_i E_j^c + \sum_{i,j=1}^{3} y_{u,ij} H_u Q_i U_j^c \\ & + \mu H_u R_d + \lambda_S H_u \Phi_{\tilde{B}} R_d + \lambda_T H_u \Phi_{\tilde{W}} R_d \,. \end{aligned} \tag{3.66}$$

$\tilde{h}_u$ and $\tilde{r}_d$ are now additional neutralinos and charginos which mix with the gaugino and the Higgs-partner lepton. Unlike in the model with the single Higgs doublet, the top quark mass can arise from an $H_u QU$ term, removing the need for a low UV cutoff.

For the purpose of deriving the neutrino mass matrix in Sec. 3.5.5, after diagonalising the R-symmetric terms in the 9×9 neutralino mass matrix, we now have

$$\nu_e' \simeq \nu_e + \left(\frac{M_{\tilde{W}}}{M_{\tilde{B}}} t_w\right) c_\beta \epsilon \, \psi_{\tilde{B}} - c_\beta \epsilon \, \psi^0_{\tilde{W}} + \left(\frac{M_{\tilde{W}}}{\mu} \frac{\lambda_T}{\sqrt{2} g} - \frac{M^2_{\tilde{W}}}{M_{\tilde{B}} \mu} \frac{\sqrt{2} \lambda_S t_w}{g}\right) c_\beta s_\beta \epsilon^2 \, \tilde{h}^0_u. \tag{3.67}$$

In contrast to the 1HDM case, ν_e' now contains a $\tilde{h}^0_u$ component, and some of the coefficients depend on c_β and s_β. The $\tilde{h}^0_u$ component induces the $\nu_e' \nu_\mu$ and $\nu_e' \nu_\tau$ terms in the neutrino mass matrix through the R-breaking mass terms $\tilde{h}^0_u \nu_\mu$ and $\tilde{h}^0_u \nu_\tau$.

BIBLIOGRAPHY

[1] **ATLAS** Collaboration, G. Aad et al., *Observation of a new particle in the search for the Standard Model Higgs boson with the ATLAS detector at the LHC*, *Phys. Lett.* **B716** (2012) 1–29, [arXiv:1207.7214].

[2] **CMS** Collaboration, S. Chatrchyan et al., *Observation of a new boson at a mass of 125 GeV with the CMS experiment at the LHC*, *Phys. Lett.* **B716** (2012) 30–61, [arXiv:1207.7235].

[3] N. Craig, *The State of Supersymmetry after Run I of the LHC*, in *Beyond the Standard Model after the first run of the LHC Arcetri, Florence, Italy, May 20-July 12, 2013*, 2013. arXiv:1309.0528.

[4] L. Randall and N. Rius, *The Minimal U(1)-R symmetric model revisited*, *Phys. Lett.* **B286** (1992) 299–306.

[5] L. J. Hall and L. Randall, *U(1)-R symmetric supersymmetry*, *Nucl. Phys.* **B352** (1991) 289–308.

[6] G. D. Kribs, E. Poppitz, and N. Weiner, *Flavor in supersymmetry with an extended R-symmetry*, *Phys.Rev.* **D78** (2008) 055010, [arXiv:0712.2039].

[7] K. Benakli and M. Goodsell, *Dirac Gauginos in General Gauge Mediation*, *Nucl.Phys.* **B816** (2009) 185–203, [arXiv:0811.4409].

[8] S. D. L. Amigo, A. E. Blechman, P. J. Fox, and E. Poppitz, *R-symmetric gauge mediation*, *JHEP* **0901** (2009) 018, [arXiv:0809.1112].

[9] K. Benakli, *Dirac Gauginos: A User Manual*, *Fortsch.Phys.* **59** (2011) 1079–1082, [arXiv:1106.1649].

[10] K. Benakli, M. D. Goodsell, and A.-K. Maier, *Generating mu and Bmu in models with Dirac Gauginos*, *Nucl.Phys.* **B851** (2011) 445–461, [arXiv:1104.2695].

[11] M. Heikinheimo, M. Kellerstein, and V. Sanz, *How Many Supersymmetries?*, *JHEP* **1204** (2012) 043, [arXiv:1111.4322].

[12] R. Davies and M. McCullough, *Small neutrino masses due to R-symmetry breaking for a small cosmological constant*, *Phys.Rev.* **D86** (2012) 025014, [arXiv:1111.2361].

[13] P. Kumar and E. Ponton, *Electroweak Baryogenesis and Dark Matter with an approximate R-symmetry*, *JHEP* **1111** (2011) 037, [arXiv:1107.1719].

[14] R. Fok, G. D. Kribs, A. Martin, and Y. Tsai, *Electroweak Baryogenesis in R-symmetric Supersymmetry*, *Phys.Rev.* **D87** (2013), no. 5 055018, [arXiv:1208.2784].

[15] J. Kalinowski, *R-symmetric supersymmetric Higgs bosons at the LHC*, *Acta Phys.Polon.* **B42** (2011) 1419–1426.

[16] C. Frugiuele and T. Gregoire, *Making the Sneutrino a Higgs with a $U(1)_R$ Lepton Number*, *Phys. Rev.* **D85** (2012) 015016, [arXiv:1107.4634].

[17] S. Chakraborty and S. Roy, *Higgs boson mass, neutrino masses and mixing and keV dark matter in an $U(1)_R-$ lepton number model*, *JHEP* **1401** (2014) 101, [arXiv:1309.6538].

[18] Y. Morita, H. Nakano, and T. Shimomura, *Neutrino Mass and Proton Decay in a $U(1)_R$ Symmetric Model*, *PTEP* **2013** (2013) 053B02, [arXiv:1212.4304].

[19] E. Bertuzzo and C. Frugiuele, *Fitting Neutrino Physics with a $U(1)_R$ Lepton Number*, *JHEP* **05** (2012) 100, [arXiv:1203.5340].

[20] J. Kalinowski, *Higgs bosons of R-symmetric supersymmetric theories*, *PoS* **EPS-HEP2011** (2011) 265.

[21] P. Diener, J. Kalinowski, W. Kotlarski, and D. Stckinger, *Higgs boson mass and electroweak observables in the MRSSM*, *JHEP* **1412** (2014) 124, [arXiv:1410.4791].

[22] S. J. De Lope Amigo, *R-symmetry, Gauge Mediation and Decaying Dark Matter*. PhD thesis, Toronto U., 2011.

[23] G. D. Kribs and N. Raj, *Mixed Gauginos Sending Mixed Messages to the LHC*, *Phys.Rev.* **D89** (2014), no. 5 055011, [arXiv:1307.7197].

[24] K. Benakli, M. D. Goodsell, and F. Staub, *Dirac Gauginos and the 125 GeV Higgs*, *JHEP* **1306** (2013) 073, [arXiv:1211.0552].

[25] C. Csaki, J. Goodman, R. Pavesi, and Y. Shirman, *The $m_D - b_M$ problem of*

Dirac gauginos and its solutions, *Phys. Rev.* **D89** (2014), no. 5 055005, [arXiv:1310.4504].

[26] R. Fok and G. D. Kribs, *μ to e in R-symmetric Supersymmetry*, *Phys.Rev.* **D82** (2010) 035010, [arXiv:1004.0556].

[27] F. Riva, C. Biggio, and A. Pomarol, *Is the 125 GeV Higgs the superpartner of a neutrino?*, *JHEP* **02** (2013) 081, [arXiv:1211.4526].

[28] S. Chakraborty, A. Datta, K. Huitu, S. Roy, and H. Waltari, *Light top squarks in $U(1)_R$-lepton number model with a right handed neutrino and the LHC*, arXiv:1508.01875.

[29] J. Berger, J. A. Dror, and W. H. Ng, *Sneutrino Higgs models explain lepton non-universality in $eejj, e\nu jj$ excesses*, *JHEP* **09** (2015) 156, [arXiv:1506.08213].

[30] **CMS** Collaboration, V. Khachatryan et al., *Search for heavy neutrinos and* W *bosons with right-handed couplings in proton-proton collisions at $\sqrt{s} = 8$ TeV*, *Eur. Phys. J.* **C74** (2014), no. 11 3149, [arXiv:1407.3683].

[31] **CMS Collaboration** Collaboration, *Search for Pair-production of First Generation Scalar Leptoquarks in pp Collisions at $\sqrt{s} = 8$ TeV*, Tech. Rep. CMS-PAS-EXO-12-041, CERN, Geneva, 2014.

[32] **Particle Data Group** Collaboration, K. A. Olive et al., *Review of Particle Physics*, *Chin. Phys.* **C38** (2014) 090001.

[33] A. K. Grant and Z. Kakushadze, *Higgs as a slepton*, *Phys. Lett.* **B465** (1999) 108–112, [hep-ph/9906556].

[34] C. Biggio, M. Blennow, and E. Fernandez-Martinez, *General bounds on non-standard neutrino interactions*, *JHEP* **08** (2009) 090, [arXiv:0907.0097].

[35] S. Davidson, C. Pena-Garay, N. Rius, and A. Santamaria, *Present and future bounds on nonstandard neutrino interactions*, *JHEP* **03** (2003) 011, [hep-ph/0302093].

[36] J. Barranco, O. G. Miranda, C. A. Moura, and J. W. F. Valle, *Constraining non-standard neutrino-electron interactions*, *Phys. Rev.* **D77** (2008) 093014, [arXiv:0711.0698].

[37] T. Ohlsson, *Status of non-standard neutrino interactions*, *Rept. Prog. Phys.* **76** (2013) 044201, [arXiv:1209.2710].

[38] A. Bolanos, O. G. Miranda, A. Palazzo, M. A. Tortola, and J. W. F. Valle, *Probing non-standard neutrino-electron interactions with solar and reactor neutrinos*, *Phys. Rev.* **D79** (2009) 113012, [arXiv:0812.4417].

[39] **Super-Kamiokande** Collaboration, G. Mitsuka et al., *Study of Non-Standard Neutrino Interactions with Atmospheric Neutrino Data in Super-Kamiokande I and II*, *Phys. Rev.* **D84** (2011) 113008, [arXiv:1109.1889].

[40] W. Loinaz, N. Okamura, S. Rayyan, T. Takeuchi, and L. C. R. Wijewardhana, *The NuTeV anomaly, lepton universality, and nonuniversal neutrino gauge couplings*, *Phys. Rev.* **D70** (2004) 113004, [hep-ph/0403306].

[41] J. A. Dror, M. Farina, E. Salvioni, and J. Serra, *Strong tW Scattering at the LHC*, arXiv:1511.03674.

[42] **Super-Kamiokande** Collaboration, H. Nishino et al., *Search for Proton Decay via $p \to e^+\pi^0$ and $p \to \mu^+\pi^0$ in a Large Water Cherenkov Detector*, *Phys. Rev. Lett.* **102** (2009) 141801, [arXiv:0903.0676].

[43] **Super-Kamiokande** Collaboration, K. Abe et al., *Search for proton decay via $p \to \nu K^+$ using 260 kiloton.year data of Super-Kamiokande*, *Phys. Rev.* **D90** (2014), no. 7 072005, [arXiv:1408.1195].

[44] P. J. Fox, A. E. Nelson, and N. Weiner, *Dirac gaugino masses and supersoft supersymmetry breaking*, *JHEP* **08** (2002) 035, [hep-ph/0206096].

CHAPTER 4

ANGULAR DISTRIBUTIONS AS LIFETIME PROBES

4.1 Introduction

Measuring the lifetime of new particles is a powerful method to probe Beyond Standard Model (BSM) theories. While the first run at the LHC did not yield any BSM particles, we still hope to find such states. If new particles are found with short lifetimes or equivalently large widths, $\Gamma \gtrsim 1\,\text{GeV}$, then their widths can be measured directly. If these particles live much longer, $\Gamma \lesssim 10^{-4}\,\text{eV}$, then we can measure their lifetimes using a displaced vertex. However, there is currently no technique to measure particle lifetimes in the "problematic region,"

$$10^{-4}\,\text{eV} \lesssim \Gamma \lesssim 1\,\text{GeV}\,. \tag{4.1}$$

This may not be an issue as many BSM theories do not predict any particles with lifetimes in this region. Nevertheless, there are many well motivated BSM theories with particles in the problematic region, such as, Z'-mediated Supersymmetry Breaking models (e.g. the Wino next-to-lightest supersymmetric particle (NLSP)) [1], split SUSY (e.g the neutralino with a large neutralino mass) [2], Gauge-mediated broken SUSY (e.g. the NLSP with breaking scale $\lesssim 10^6\,\text{GeV}$), SUSY with a heavy scalar mass scale (e.g. gluino with heavy scalar mass $\lesssim 10^4\,\text{TeV}$) [3, 4], Dynamic R-parity violating models (e.g. the gluino as the lightest supersymmetric particle with large gluino mass) [5], minimal flavor violation models (e.g. the stop except for very small values of $\tan\beta$) [6, 7], and GUTS in warped extra dimensions(e.g. next-to-lightest Z_3 charged particles) [8].

The problem of how to probe lifetimes in the problematic region was discussed

in detail in Ref. [9], where a new technique to measure the lifetime of a hypothetical top-like particle was suggested. This hypothetical, but generic, particle has the same quantum numbers as the top, but its mass and width are kept as unknowns. In this paper we apply the principles introduced in [9] to experiments that can be done at the LHC and future colliders. We often refer to our hypothetical particle as a top or t quark while we really mean a top-like quark with a longer lifetime than the top.

We briefly discuss the general principles of the method here and leave the details to Ref. [9]. Consider producing a top-like particle with spin up. After a short time, of order $1/\Lambda_{QCD}$, the colored particle forms a hadron through hadronization, with mesons forming about 90% of the time [10] (in our discussion we focus on meson production and decay, though adding in baryons is straightforward [9]). Since the hyperfine splitting is small compared to Λ_{QCD}, after hadronization the system is in its QCD ground state without resolving the hyperfine splitting. That is, it produces an incoherent mix,

$$50\%\ |{+}{+}\rangle \oplus 50\,\%\ |{+}{-}\rangle\ , \tag{4.2}$$

where $\oplus$ denote an incoherent sum and the state $|{+}{+}\rangle$ ($|{+}{-}\rangle$) denotes a meson with top spin up and the light degree of freedom with spin up (down). Excluding decays, the mass eigenstates of the system are given by the triplet and singlet state which we denote by $T(s, m_s)$ ($s = 0, 1$ is the spin and m_s is the spin along the quantization axis). These states are related to the earlier ones by

$$|{+}{+}\rangle = T(1,1), \qquad |{+}{-}\rangle = \frac{T(1,0) + T(0,0)}{\sqrt{2}}\,. \tag{4.3}$$

One source of depolarization is due to the triplet state decaying into the singlet with a lifetime that we denote by $1/\Delta\Gamma$. Another source is due to the top that is initially in the $|{+}{-}\rangle$ state, which oscillates between a spin up and spin down with a

timescale of $1/\Delta m$ where Δm is the mass splitting between the triplet and singlet states. The third timescale involved is the weak decay width of the top quark, $1/\Gamma$. The calculation of Δm and $\Delta\Gamma$ is discussed in [9], and for our discussion we assume them to be known. Then, the idea is to measure an observable that is sensitive to the polarization of the top quarks. The amount of depolarization gives us the sensitivity to Γ.

We use as our observable the spin of the top projected onto a quantization axis. The average spin in this direction of a collection of tops as a function of time, excluding top quark decay, is given by

$$\mathrm{pol}(t) \equiv \frac{\langle s\rangle\,(t)}{\langle s\rangle\,(0)} = \frac{1}{2}\left(e^{-\Delta\Gamma t} + \cos\Delta m t\right). \tag{4.4}$$

Note that this is the spin projection for the top-like quarks, not the mesons themselves. We have access to the spin of the tops through their decay products. Since we do not have good enough time resolution to measure $\mathrm{pol}(t)$ directly, what we measure is the time integrated value multiplied by the exponential probability density function:

$$r \equiv \int dt\Gamma e^{-\Gamma t}\frac{\langle s\rangle\,(t)}{\langle s\rangle\,(0)} = \frac{1}{2}\left(\frac{1}{1+x^2} + \frac{1}{1+y}\right), \tag{4.5}$$

where we defined,

$$x \equiv \frac{\Delta m}{\Gamma}, \qquad y \equiv \frac{\Delta\Gamma}{\Gamma}. \tag{4.6}$$

(note that [9], contains an error and defines $y \equiv \Delta\Gamma/2\Gamma$ while it should be defined as the above.) A plot of r as a function of Γ is shown in Fig. 4.1.

By finding r we can deduce the value of Γ. In principle this can be done to any precision. However, by looking at the structure of $r(\Gamma)$, it is clear that in practice, we can only split the problematic region into three different regions. In region I, where the lifetime is short the decaying particles do not feel the hadronization,

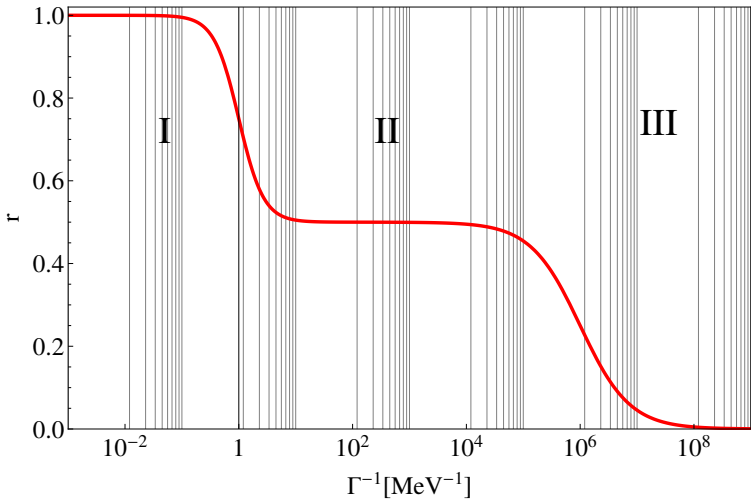

Figure 4.1: r as a function of the lifetime for $\Delta\Gamma = 1\,\text{eV}$ and $\Delta m = 1\,\text{MeV}$. Particles with lifetimes in regions I , II, and III have different levels of depolarization prior to decay. By measuring r we have a direct measurement of the lifetime.

as is the case for the real top quark [11]. In region II the top lost half its initial polarization due to oscillation at the time of decay. In region III the top has lost all its polarization prior to its decay due to oscillation and to decay of the triplet into the singlet state. Due to staircase structure of $r(\Gamma)$, the uncertainties of a on our input parameters, Δm and $\Delta\Gamma$, have a very small impact on the results.

At this point all the basic physics is set, the big question left is how to practically measure this effect. We cannot create exotic particles, trap them, polarize them, and measure their angular momentum. Instead we propose a method to make use of current detectors available at the LHC. One potential concern in this study is that we are completely reliant on our ability to produce polarized particles. While not simple, this turns out to be straightforward and has been shown to be feasible at the LHC in the SM in both single top production [12] and di-top channels [13] due to its chiral nature. A second challenge is measuring the polarization itself. The spin of each particle is unattainable at the LHC, but the angular distributions can be measured. For a review of such methods, see, for

example, [14–16]. For a chiral theory the angles of the decay products depend on the polarization of the parent particle. Thus depolarization effects will appear in the angular distributions, and in particular, a forward backward asymmetry. This, in turn, will enable us to probe the lifetime. Our idea is therefore, to define a forward backwards asymmetry that changes as a function of r and thus can be used to extract the lifetime.

In this work our emphasis is on studying a working example for the lifetime measurement. While depending on the specific particle production and decay channel the details will change, the ideas will should be the same. Furthermore, we do not attempt a full study with semi-realistic detector simulation but leave such investigation for future studies.

4.2 The General Formalism

We are now in a position to make our discussion more explicit. Consider a general process shown in Fig. 4.1 in which a top is produced and decays in the absence of hadronization. We assume the width of the top is much less than its mass (as is the case for any particle for which this method is valid) and work far from the top production threshold. We can now write the square of the matrix element for production and decay of a single top quark in an arbitrary channel as (for a discussion on these methods with regards to the top quark see e.g. [17]),

$$|\mathcal{M}|^2 = \frac{\pi\delta\left(t^2 - m^2\right)}{m\Gamma} \sum_{\lambda,\lambda'} \rho\left(\lambda,\lambda'\right)\Gamma\left(\lambda,\lambda'\right) \,, \tag{4.7}$$

where λ and λ' label the spin of the top quark and

$$\rho\left(\lambda,\lambda'\right) \equiv \mathcal{M}_\rho(\lambda)\mathcal{M}_\rho(\lambda') \,, \qquad \Gamma\left(\lambda,\lambda'\right) \equiv \mathcal{M}_\Gamma(\lambda)\mathcal{M}_\Gamma(\lambda') \,. \tag{4.8}$$

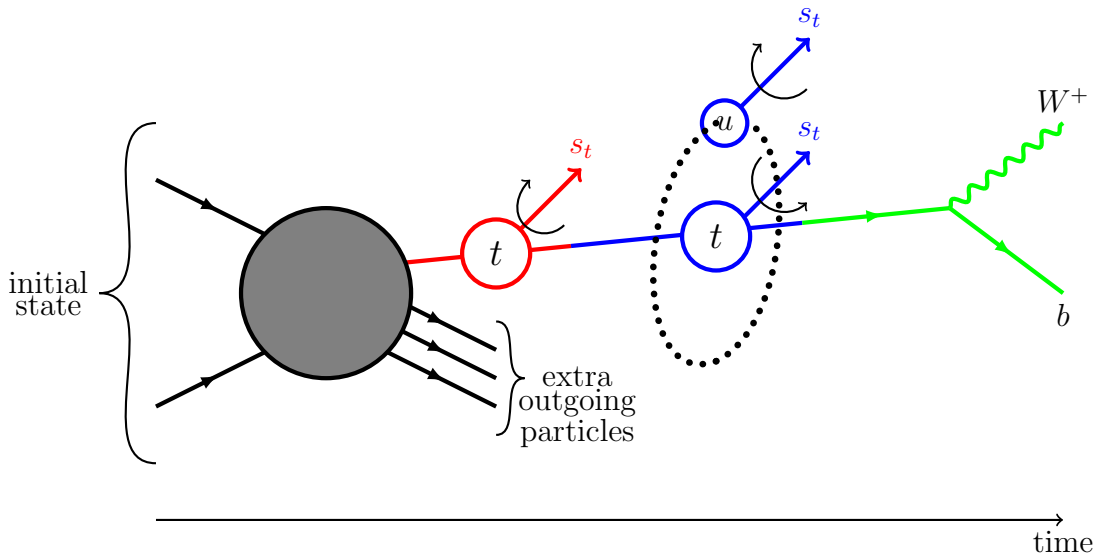

Figure 4.1: (color online). A general process considered here. Two particles combine producing a top-like quark [red], which hadronizes [blue] and subsequently decays [green] after a time t. A $\bar{u}$ quark is chosen as the light degree of freedom, though it can be any light quark. s_t denotes our chosen spin quantization axis. The interaction between the spin of the $\bar{u}$ and t may provide a spin flip in the top as shown.

Here we define $\mathcal{M}_\rho(\lambda)[\mathcal{M}_\Gamma(\lambda)]$ as the production [decay] amplitude of a top with spin λ. Further, in this work we denote a particles 4-momenta with their symbol and m is the top quark mass. ρ and Γ are known as the spin density and decay matrices respectively.

A complete treatment with general couplings requires the calculation of each element in these matrices, which take into account the interference terms between spin up and spin down tops that are being produced. These interference terms can result in complicated expressions for the full cross-section in single top production, see, for example, [18]. However, a powerful simplification can be made if the tops come out highly polarized. In this case, the outgoing particles are roughly pure spin states and interference terms are small. This requires a clever choice of spin quantization axis, instead of the helicity basis. The idea to consider a different spin

basis has been successful in the ditop channel in maximizing polarization [13, 19]. Finding the appropriate basis to minimize correlations is non-trivial but has been done for the s-channel single top production using general couplings [20,21]. While deviating from the helicity basis makes the results more difficult to interpret it greatly simplifies the calculation. By choosing such a basis we are diagonalizing the spin density matrix, ρ. In that basis the results are also independent of the off-diagonal elements of the decay matrix, Γ, see Eq. (4.7). While here we consider only the s-channel, a polarization vector that diagonalizes the spin density matrix can be found for a variety of different channels [20,22,23]. With this simplification the cross-section without hadronization can be approximated by [24],

$$d\sigma = \sigma_{\uparrow}\frac{d\Gamma_{\uparrow}}{\Gamma} + \sigma_{\downarrow}\frac{d\Gamma_{\downarrow}}{\Gamma}\,, \tag{4.9}$$

where σ_{λ} is the cross-section for producing a top of spin λ and $d\Gamma_{\lambda}$ is the differential rate of the decay of such a top.

Hadronization, however, modifies this equation. So far we have assumed a spin up top stays spin up while a spin down stays spin down. Instead, we can think of the particles having an effective decay distribution given by

$$\frac{d\Gamma_{\uparrow}}{\Gamma} \longrightarrow \frac{d\Gamma_{\uparrow}^{eff}}{\Gamma} = P(t)\frac{d\Gamma_{\uparrow}}{\Gamma} + [1-P(t)]\frac{d\Gamma_{\downarrow}}{\Gamma}\,, \tag{4.10}$$

$$\frac{d\Gamma_{\downarrow}}{\Gamma} \longrightarrow \frac{d\Gamma_{\downarrow}^{eff}}{\Gamma} = [1-P(t)]\frac{d\Gamma_{\uparrow}}{\Gamma} + P(t)\frac{d\Gamma_{\downarrow}}{\Gamma}\,, \tag{4.11}$$

where $P(t)$ is the probability a spin up (down) top will remain spin up (down) after a time t.

In principle the problem is solved. We can define a forward backward asymmetry from this expression that will be dependent on the hadronization. However, this is currently very abstract. In order to make progress we need four ingredients,

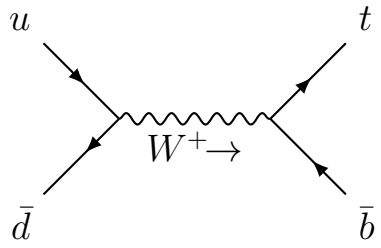

Figure 4.1: The s-channel processes we consider for top-like quark production.

1. A spin quantization axis such that interference terms between producing spin up and spin down top-like quarks are negligible.
2. The top production cross-section into spin up and spin down, $\sigma_\uparrow$ and $\sigma_\downarrow$.
3. The probability that a spin up top will stay spin up, $P(t)$.
4. The top decay distributions for a spin up and spin down top, $d\Gamma_\uparrow/\Gamma$ and $d\Gamma_\downarrow/\Gamma$.

4.3 t Quark Production

Consider top-like quark produced from the s-channel process shown in Fig. 4.1. In order to calculate the production cross-section of the hypothetical top quark we need to settle on a particular model. While we take the up-down vertex to be a Standard Model vertex, we consider a general vector coupling between the t and b

$$\mathcal{L}_{int} = \frac{g_W}{\sqrt{2}} W_\mu \, t \, \bar{b} \, \gamma^\mu \left(P_L f_L + P_R f_R \right) , \qquad P_{R,L} \equiv (1 \pm \gamma^5)/2 \, . \tag{4.12}$$

In the Standard Model (SM) for the real top we have $f_L = 1$ and $f_R = 0$. For our technique to work, the couplings need to be chiral, that is, $f_L \neq f_R$. Note that the above expression is not the most general possible coupling as we could have a derivative term vertex. While such terms could have been included, they add unnecessary complications without any more insight into the problem.

We are now ready to calculate the production cross-sections of the top-like quark. We find the amplitude for spin up and spin down decay separately using the spinor helicity method (for reviews see for example [25–27]). We introduce two massless momenta,

$$t_{1,2} \equiv \frac{t \pm m\, s_t}{2}\,, \tag{4.13}$$

where s_t is its spin quantization axis. We also use standard notations [25],

$$|p\pm\rangle \equiv u_\pm(p) = v_\mp = P_{R,L}u(p)\,, \qquad \langle p\pm| \equiv \bar{u}_\pm(p) = \bar{v}_\mp(p) = \bar{u}(p)P_{L,R}\,, \tag{4.14}$$

with,

$$\langle pq\rangle \equiv \bar{u}_-(p)_+(q)\,, \qquad [pq] \equiv \bar{u}_+(p)u_-(q)\,. \tag{4.15}$$

We denote the amplitude for top production by $\mathcal{M}_{\lambda_{\bar{b}}\lambda_t}$ where λ_i denotes the spin of particle i (the spin of the up and anti-down quarks is fixed by the chirality of the vertex). The amplitudes for this process in spinor helicity notation are given by:

$$\mathcal{M}_{-+} = f_L 2\Delta \left[u\bar{b}\right] \left\langle t_2 \bar{d}\right\rangle \frac{[t_1 t_2]}{m}, \tag{4.16}$$

$$\mathcal{M}_{++} = f_R 2\Delta \left[t_1 u\right] \left\langle \bar{d}\,\bar{b}\right\rangle, \tag{4.17}$$

$$\mathcal{M}_{--} = f_L 2\Delta \left[u\bar{b}\right] \left\langle t_1 \bar{d}\right\rangle, \tag{4.18}$$

$$\mathcal{M}_{+-} = f_R 2\Delta \left[t_2 u\right] \left\langle \bar{d}\,\bar{b}\right\rangle \frac{\langle t_1 t_2\rangle}{m}, \tag{4.19}$$

where we define

$$\Delta \equiv \frac{g_W^2 V_{ud}}{2(s - M_W^2 + iM_W\Gamma_W)}\,. \tag{4.20}$$

Here we denote M_W and Γ_W as the mass and width of the W boson respectively. We have kept only the W and top masses and sent the other masses to zero.

The total amplitude for top production is

$$\overline{|\mathcal{M}|^2} = \frac{N_c}{2^2}\left(|\mathcal{M}_{-+} + \mathcal{M}_{--}|^2 + |\mathcal{M}_{++} + \mathcal{M}_{+-}|^2\right)\,. \tag{4.21}$$

The interference terms are given by

$$\mathcal{M}^*_{--}\mathcal{M}_{-+} = 4\,|\Delta|^2\,|f_L|^2\,\langle \bar{b}u\rangle\,\left[u\,\bar{b}\right]\,\left[\bar{d}\,t_1\right]\,\langle t_2\,\bar{d}\rangle\,\frac{[t_1\,t_2]}{m} + h.c.\,, \tag{4.22}$$

$$\mathcal{M}^*_{++}\mathcal{M}_{+-} = 4\,|\Delta|^2\,|f_R|^2\,\left[\bar{b}\,\bar{d}\right]\,\langle \bar{d}\,\bar{b}\rangle\,\langle u\,t_1\rangle\,[t_2\,u]\,\frac{\langle t_1\,t_2\rangle}{m} + h.c.\,. \tag{4.23}$$

A general spin axis that minimizes the interference terms, proposed in [20], for any values of f_L and f_R is given by

$$s_t^\mu = A\Big\{\,|f_L|^2\left[(u\cdot\bar{b})(\bar{d}\cdot t)t^\mu - (u\cdot\bar{b})\bar{d}\right] + |f_R|^2\left[(\bar{d}\cdot\bar{b})(u\cdot t)t^\mu - (\bar{d}\cdot\bar{b})m^2u^\mu\right]\Big\}\,, \tag{4.24}$$

where A is a constant chosen such that $s^2 = -1$. In the limit of small $|f_R|$, the vector is given by

$$s_t^\mu = \frac{1}{m}\left(\frac{m^2}{\bar{d}\cdot t}\bar{d}^\mu - t^\mu\right)\,. \tag{4.25}$$

Choosing s_t^μ as the quantization axis sets $\left[\bar{d}\,t_1\right] = 0$ and eliminates the interference term in (4.22) that is proportional to $|f_L|^2$, while it keeps the one in (4.23) that is proportional to $|f_R|^2$. Since we are assuming $|f_R|$ to be small, the interference terms are small, justifying the choice of quantization axis. Furthermore, the interference terms are suppressed by m/E and thus are unimportant at high energies. For these reasons we eliminate such terms from the discussion and keep only diagonal terms in the spin density matrix. In practice, the effects of the interference terms can always be estimated and included in the systematic uncertainties.

The total cross-sections are

$$\sigma_\uparrow = \frac{s-m^2}{32\pi s^2}\Delta^2 N_c\Big\{\,|f_L|^2\,\frac{1}{3}\left(2s^2 - m^2s - m^4\right) + |f_R|^2\left(\frac{2m^2s^2}{s-m^2}\log\frac{s}{m^2} - 2m^2s\right)\Big\}\,, \tag{4.26}$$

$$\sigma_\downarrow = \frac{s-m^2}{32\pi s^2}\Delta^2 N_c\,|f_R|^2\left\{\frac{1}{3}\left(2s^2 + 5m^2s - m^4\right) - \frac{2m^2s^2}{s-m^2}\log\frac{s}{m^2}\right\}\,. \tag{4.27}$$

The sum of these two agrees with the results of Ref. [28]. Note that $\sigma_\uparrow$ and $\sigma_\downarrow$ depend of the choice of the quantization axis, but their sum does not. In the limit

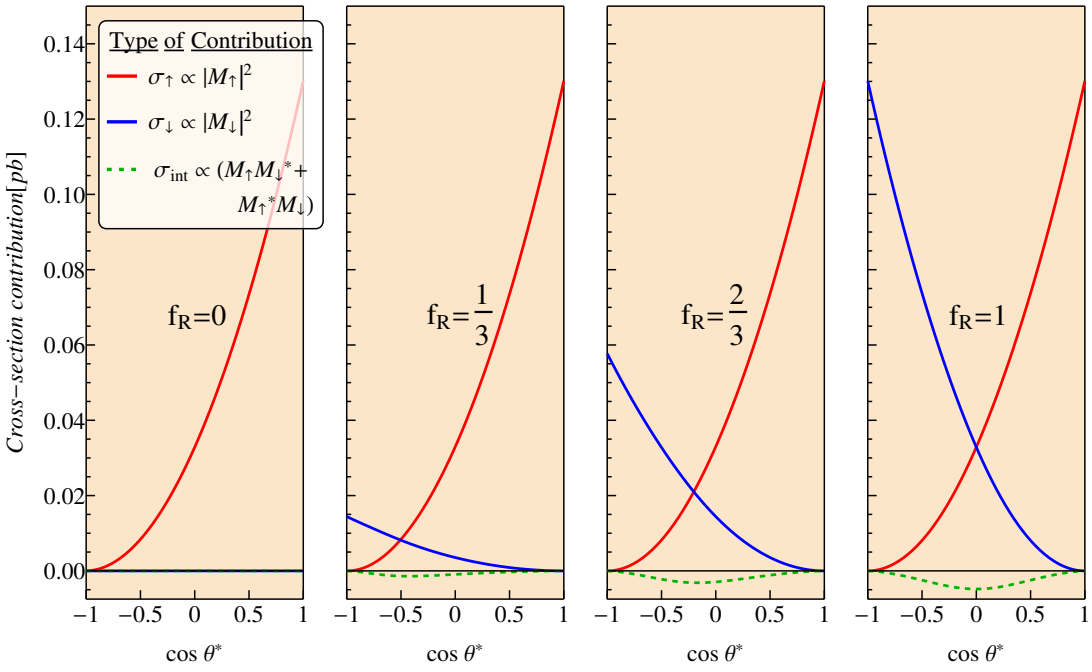

Figure 4.2: (color online). The contribution to the top-like quark production cross-section of all the terms including the interference terms (σ_{int}), which are dropped in the final results. Here we use the general coupling polarization vector with $f_L = 1$, vary f_R, and take $M_W = 80.4\,\text{GeV}, \Gamma_W = 2.1\,\text{GeV}, m = 300\,\text{GeV}$, and $\sqrt{s} = 1\,\text{TeV}$. Clearly, the interference terms are much smaller than the dominant cross-section contributions.

that $|f_R|^2 \to 0$ the tops come out 100% polarized as in the SM [29]. This shows another advantage of using the spin axis direction chosen earlier, since the larger the polarization, the better our resolution.

The different contributions to the total cross-section using the general spin vector given in Eq. (4.24) with $f_L = 1$ and different values of f_R are shown in Fig. 4.2. The interference terms (shown in dashed green) are clearly much smaller then the dominant spin up top production cross-section, even for a non-negligible choice of f_R. This is a consequence of the choice of spin basis. As expected, in the $f_R \to 0$ these terms vanish.

4.4 Decay distribution

To calculate the decay distribution we use the same model as above. We calculate the distributions for the spin up and spin down top decays separately. As before, we denote the amplitudes as $\mathcal{M}_{\lambda_{\bar{b}}\lambda_t}$ where λ_i denotes the spin of particle i. The amplitudes for the decays are:

$$\mathcal{M}_{--} = \frac{g_W}{\sqrt{2}} f_L \langle b - | \not{\epsilon} | t_1 - \rangle \ , \tag{4.28}$$

$$\mathcal{M}_{-+} = \frac{g_W}{\sqrt{2}} f_L \langle b - | \not{\epsilon} | t_2 - \rangle \frac{\langle t_2 t_1 \rangle}{m} , \tag{4.29}$$

$$\mathcal{M}_{+-} = \frac{g_W}{\sqrt{2}} f_R \langle b + | \not{\epsilon} | t_2 + \rangle \frac{[t_2 t_1]}{m} , \tag{4.30}$$

$$\mathcal{M}_{++} = \frac{g_W}{\sqrt{2}} f_R \langle b + | \not{\epsilon} | t_1 + \rangle \ , \tag{4.31}$$

where we have neglected all masses but the top quark and W boson masses. We denote $\not{\epsilon} \equiv \epsilon_\mu \gamma^\mu$ where ϵ_μ is the polarization vector of the external W boson.

The amplitude squared for the decay distribution for a spin-up and spin-down top quark are (we omit the color factor as its taken care of in the top production cross-sections)

$$\overline{|\mathcal{M}_\uparrow|^2} \equiv \left(|\mathcal{M}_{-+}|^2 + |\mathcal{M}_{++}|^2 \right) , \qquad \overline{|\mathcal{M}_\downarrow|^2} \equiv \left(|\mathcal{M}_{--}|^2 + |\mathcal{M}_{+-}|^2 \right) . \tag{4.32}$$

These give the decay distributions,

$$\frac{1}{\Gamma} \frac{d\Gamma_\uparrow}{d \cos\theta^*} = \frac{1}{2} \left(1 - \alpha \cos\theta^* \right) , \qquad \frac{1}{\Gamma} \frac{d\Gamma_\downarrow}{d \cos\theta^*} = \frac{1}{2} \left(1 + \alpha \cos\theta^* \right) , \tag{4.33}$$

where

$$\alpha \equiv \left(\frac{|f_L|^2 - |f_R|^2}{|f_L|^2 + |f_R|^2} \right) \times \left(\frac{m^2 - 2M_W^2}{m^2 + M_W^2} \right) \tag{4.34}$$

and θ^* is the angle between the spin quantization axis of the t quark, defined in Eq. (4.25), and the direction of b quark. This expression agrees with Ref. [30]. In

the final result we do not have any cross terms proportional to $|f_R|\,|f_L|$. This is a consequence of taking the massless limit for the bottom quark.

Note that θ^* is an observable. It is the angle between the axis that we quantize the spin of the top quark and the momenta of the b quark in the top rest frame. Of course, the number of particles moving into different angles in the center of mass frame is independent of the choice of quantization axis. However, depending on this choice, the values of $\sigma_\uparrow$ and $\sigma_\downarrow$ change with θ^* to leave the center of mass variables invariant. By measuring the angles that the b quark is emitted in the center of mass frame one can calculate θ^*. For simplicity we express our results in terms of this angle.

Eq. (4.33) shows that a $1-\alpha\cos\theta^*$ distribution is characteristic of a spin up top decay while a $1+\alpha\cos\theta^*$ distribution is characteristic of a spin down top decay. We will soon see the effect of having both such decays and the interaction between the two. We also see that we need a chiral theory. In a parity conserving theory we have $f_L = f_R$ and hence $\alpha = 0$. In this case we have the same distribution for a spin up and spin down top and they cannot be differentiated. Since we will use angular correlations to probe the lifetime of the decaying particles, the method fails in this case.

4.5 Lifetime Measurement

We are now in position to find the effective distribution. Using Eqs. (4.10), (4.11), and (4.33) we write

$$\frac{d\Gamma^{eff}_{\uparrow,\downarrow}}{d\cos\theta^*} = \frac{1}{2}\left[1 \mp (2P(t)-1)\alpha\cos\theta^*\right] . \tag{4.35}$$

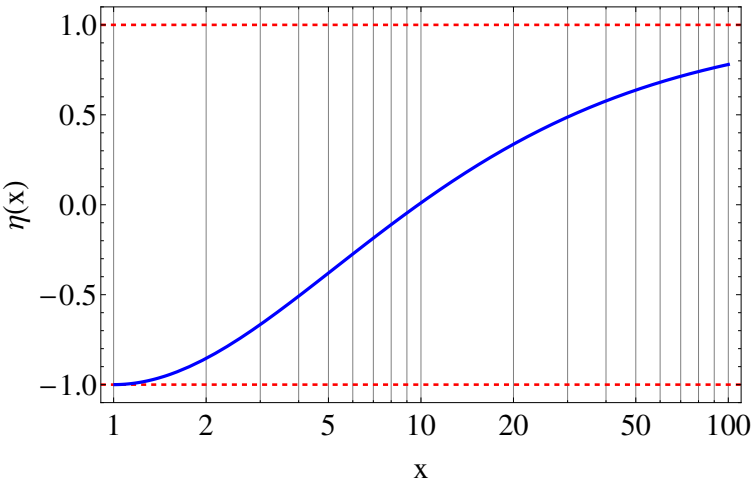

Figure 4.1: η as a function of center of mass energy. η at low energies is -1 but rapidly increases to 1 at larger energies.

The key dynamic quantity is $2P(t) - 1$. Now note that the polarization of a set of tops given in Eq. (4.4) is related to the probability of a spin up top remaining spin up after a time t by (if a top is measured spin up it contributions $+1/2$ to the net angular momentum and if a top is measured spin down it contributes $-1/2$ to the net angular momentum),

$$\frac{\langle s\rangle\,(t)}{\langle s\rangle\,(0)} = \frac{1}{1/2}\left\{\frac{1}{2}P(t) - \frac{1}{2}(1 - P(t))\right\} = 2P(t) - 1\,. \tag{4.36}$$

So the dynamics are indeed controlled by the average polarization.

Top-like quarks come out with two opposing distributions. Depending on how many tops decay with spin up compared to the number coming out with spin down we have a $1-\alpha\cos\theta^*$ or a $1+\alpha\cos\theta^*$ dominated distribution. The average angular momentum of the set of tops, which oscillates as a function of time, determines the net distribution. Inserting the effective decay distributions into (4.9), we can

write the distribution of b quarks at different angles θ^* and times t,

$$\begin{aligned}\frac{d\sigma(t)}{d\cos\theta^* dt} &= \Gamma e^{-\Gamma t}\frac{1}{2}\left\{\sigma_\uparrow\left(1-\frac{\langle s\rangle(t)}{\langle s\rangle(0)}\alpha\cos\theta^*\right)+\sigma_\downarrow\left(1+\frac{\langle s\rangle(t)}{\langle s\rangle(0)}\alpha\cos\theta^*\right)\right\}, \\ &= \Gamma e^{-\Gamma t}\left(\sigma_\uparrow+\sigma_\downarrow\right)\frac{1}{2}\left(1-\frac{\sigma_\uparrow-\sigma_\downarrow}{\sigma_\uparrow+\sigma_\downarrow}\alpha\frac{\langle s\rangle(t)}{\langle s\rangle(0)}\cos\theta^*\right), \end{aligned} \tag{4.37}$$

Here we have multiplied this dynamic cross-section by the probability density that a top quark lives until a time t. A more careful treatment of how to add the time dependence is given in Appendix 4.A. In the case of equal spin up and spin down production we lose the sensitivity to the lifetime.

Thus far the discussion has been quite general and did not involve any specific channel. While the results do depend on the production cross-section, and in particular how polarized the production channel is, the details of the particular production channel have little importance. We now specialize to the s-channel by using Eqs. (4.26) and (4.27) and integrate over all time. This gives the distribution of outgoing b quarks,

$$\frac{1}{\sigma}\frac{d\sigma}{d\cos\theta^*}=\frac{1}{2}\left\{1-\left(\frac{|f_L|^2-\eta(s/m^2)\,|f_R|^2}{|f_L|^2+|f_R|^2}\alpha\right)r\cos\theta^*\right\}, \tag{4.38}$$

where

$$\eta(x)\equiv\frac{(2x^3+9x^2-12x+1)-12x^2\log(x)}{(x-1)^2(2x+1)}, \tag{4.39}$$

such that $-1\leq\eta(x)\leq 1$ but its exact value has little impact on the results. It is shown for different energies in Fig. 4.1. Using this we can extract r and hence the lifetime of the particle. Eq. (4.38) is our main result. We have the angular dependence as a function of time.

We are now in position to define a simple observable, a time integrated forward-backward asymmetry. We look at the total number of b quarks at all times produced in different angles and define

$$a_{fb}\equiv\frac{N_b(\cos\theta^*>0)-N_b(\cos\theta^*<0)}{N_b(\cos\theta^*>0)+N_b(\cos\theta^*<0)}=\left(\frac{\sigma_\uparrow-\sigma_\downarrow}{\sigma_\uparrow+\sigma_\downarrow}\right)\alpha\times r\,. \tag{4.40}$$

Specializing to the s-channel gives,

$$a_{fb} = \left\{ \frac{|f_L|^2 - \eta(s/m^2)\,|f_R|^2}{|f_L|^2 + |f_R|^2} \; \frac{|f_L|^2 - |f_R|^2}{|f_L|^2 + |f_R|^2} \; \frac{2M_W^2 - m^2}{2M_W^2 + m^2} \right\} \times r\,. \tag{4.41}$$

In the limit of $|f_L|^2 \gg |f_R|^2$, the dependence on η drops out and we have the particularly simple result,

$$a_{fb} = \left\{ \frac{2M_W^2 - m^2}{2M_W^2 + m^2} \right\} \times r\,. \tag{4.42}$$

4.6 LHC, ILC, and future work

The method discussed above requires collisions between $\bar{d}$ and u to produce top quarks. This is not an ideal channel to produce top-like quarks at the LHC, which is dominated by pair productions from gluons, followed by the valence quarks, u and d [31]. However, at small momentum fractions, the number of sea quarks is significant and the s channel discussed above is certainly feasible. Of course, if the top-like particle is heavy, single top-like production will be the dominate production mechanism. Moreover, also in the SM there are some simple and calculable alternatives to top-like production with significant polarization, including the tW^- associated production and the dominant Wg fusion [29]. Since the tW^- associated production suffers from either CKM suppression or requires a b from the sea, it is suppressed. This makes the Wg fusion process, which uses a gluon and an up quark as the initial state, the most promising channel at the LHC with regards to measuring single top-like quark lifetimes in this way.

The ILC is planned to have incoming beams with up to 80% polarization for one beam and 30% for the other [32]. While the discussion above focused on unpolarized initial states, having polarized incoming particles can increase the

polarization of the top-like quarks [33], yielding a better precision for the lifetime measurement technique we suggested. Of course, the channel discussed above is irrelevant for the ILC, which will collide electrons and positrons. Nevertheless, there exist both single top [34] and ditop production channels [13,33] which can be used instead. While the references listed assume a SM coupling, any new physics coupling to top-like quarks that are chiral would yield similar results.

In this paper we presented two observables that can be measured at a collider and are sensitive to the lifetime. The differential cross-section given in Eq. (4.38) and a forward-backward asymmetry, a_{fb}, derived from this cross-section given in Eq. (4.41). a_{fb} has the advantage of being particularly intuitive and emphasizes the importance of parity violation in our calculations. For low statistics this is the best measure to use. On the other hand, the forward backward asymmetry removes some of the information embedded in the cross-section. Eventually when more data is accumulated fitting to the outgoing quark distribution would yield more precise estimate of the lifetime.

In this paper we have focused on single top production and decay. However, the most common channel to study top production is through the ditop production channel. As before, there exists an appropriate choice of polarization vectors that minimizes the interference terms [35]. Extending the lifetime measurement technique to this channel should be straightforward and likely more precise as typically the ditop channel contains many more events. A last requirement before particle lifetimes can be measured with the techniques presented here is to run simulations to test it.

To conclude, we implemented a new technique to measure lifetimes of top-like particles with lifetimes in the "problematic region" where current experiments

cannot access. The complications associated with the calculations can be greatly reduced by choosing an appropriate spin basis that both maximizes polarization and eliminates extra terms. We arrive at a simple forward-backward asymmetry that is directly proportional to a quantity which characterizes the average angular momentum of top-like particles, r. This value is a function of the lifetime and its measurement allows direct access to the lifetime.

APPENDIX

4.A The Dynamic Cross-section

Consider a sample of tops at a time t. Assume that initially the sample is completely polarized. The number of top quarks that are alive between t and $t + \Delta t$ is

$$N(t) = N_0 \left(e^{-\Gamma t} - e^{-\Gamma(t+\Delta t)} \right) . \tag{4.43}$$

The initial number of particles is given by

$$N_0 = \mathcal{L} \int d\sigma \, , \tag{4.44}$$

where $\mathcal{L}$ is the luminosity of the beam. The number of spin up tops which decayed between time $t, t + \Delta t$ is

$$dN_{decayed} = \left(\mathcal{L} \int d\sigma \right) \left(e^{-\Gamma t} - e^{-\Gamma(t+\Delta t)} \right) P(t) \, , \tag{4.45}$$

where we denoted $P(t)$ as the probability that a spin up top will remain spin up at a time t (neglecting its decay probability).

The total number of spin up tops which decayed is given by

$$N_{dec} = \sum_t \left(\mathcal{L} \int d\sigma \right) \left(\frac{e^{-\Gamma t} - e^{-\Gamma(t+\Delta t)}}{\Delta t} \right) \Delta t P(t) \, , \tag{4.46}$$

where the sum is over all possible times. Taking the $\Delta t \to 0$ limit we have

$$N_{dec} = \int dt \left(\mathcal{L} \int d\sigma \right) \Gamma e^{-\Gamma t} P(t) \, . \tag{4.47}$$

For every decaying top quark there is a corresponding b quark that is emitted at some angle. Adding in a factor for the distribution of bottom quarks. The total number of b quarks arriving at the detector is

$$N_{t_\uparrow \to t_\uparrow \to bW} = \int_0^\infty \left[\mathcal{L} \int d\sigma \right] \left[dt \Gamma e^{-\Gamma t} \right] \left[P(t) \right] \left[\int \frac{1}{\Gamma} \frac{d\Gamma_\uparrow}{d \cos\theta^*} d\cos\theta^* \right] , \tag{4.48}$$

where in brackets we have denoted the process we considered, producing spin up tops which remain spin up and decay.

Now switching this to a differential cross-section,

$$\frac{d\sigma_{t_\uparrow \to t_\uparrow \to bW}}{d\Omega d\cos\theta^* dt} = \frac{d\sigma(u\bar{d} \to \bar{b}t_\uparrow)}{d\Omega}\left[\Gamma e^{-\Gamma t}\right]\left[P(t)\right]\left[\frac{1}{\Gamma_t}\frac{d\Gamma_\uparrow}{d\cos\theta^*}\right], \tag{4.49}$$

where $d\Omega$ is the solid angle associated with top production. This calculation was done for one case where a spin up top was produced and stayed spin up when it decayed. Including all four cases,

$$\begin{aligned} u\bar{d} \to t_\uparrow &\xrightarrow{had} t_\uparrow \to bW \qquad & u\bar{d} \to t_\downarrow &\xrightarrow{had} t_\uparrow \to bW \\ u\bar{d} \to t_\downarrow &\xrightarrow{had} t_\downarrow \to bW \qquad & u\bar{d} \to t_\uparrow &\xrightarrow{had} t_\uparrow \to bW \end{aligned} \tag{4.50}$$

and integrating over $d\Omega$ gives,

$$\begin{aligned} \frac{d\sigma(t)}{d\cos\theta^* dt} = \Gamma e^{-\Gamma t}\Bigg\{ &\Big[\sigma_\uparrow P(t) + \sigma_\downarrow(1-P(t))\Big]\frac{d\Gamma_\uparrow}{d\cos\theta^*} \\ &+ \Big[\sigma_\downarrow P(t) + \sigma_\downarrow(1-P(t))\Big]\frac{d\Gamma_\downarrow}{d\cos\theta^*}\Bigg\}, \end{aligned} \tag{4.51}$$

which is equivalent to Eq. (4.37) once the differential distribution is added.

BIBLIOGRAPHY

[1] P. Langacker, G. Paz, L.-T. Wang, and I. Yavin, *Aspects of Z'-mediated supersymmetry breaking*, *Phys. Rev. D* **77** (Apr, 2008) 085033, [arXiv:0801.3693].

[2] N. Arkani-Hamed, S. Dimopoulos, G. Giudice, and A. Romanino, *Aspects of split supersymmetry*, *Nucl. Phys. B* **709** (2005) 3–46, [hep-ph/0409232].

[3] R. Sato, S. Shirai, and K. Tobioka, *Gluino decay as a probe of high scale supersymmetry breaking*, *JHEP* **11** (2012) 041, [arXiv:1207.3608].

[4] N. Arkani-Hamed and S. Dimopoulos, *Supersymmetric unification without low energy supersymmetry and signitures for fine-tuning at the LHC*, *JHEP* **0506** (2005) 73, [hep-th/0405159v2].

[5] C. Csaki, E. Kuflik, and T. Volansky, *Dynamical R-parity violation*, *pre-print* (2013) [arXiv:1309.5957].

[6] C. Csaki, Y. Grossman, and B. Heidenreich, *MFV SUSY: A natural theory for R-parity violation*, *Phys. Rev. D.* **85** (2012) 095009, [arXiv:1111.1239].

[7] E. Nikolidakis and C. Smith, *Minimal flavor violation, seesaw, and R-partiy*, *Phys. Rev. D.* **77** (2008) 015021, [arXiv:0710.3129].

[8] K. Agashe and G. Servant, *Baryon number in warped GUTs: Model building and (dark matter related) phenomenology*, *JCAP* **0502** (2005) 002, [hep-ph/0411254].

[9] Y. Grossman and I. Nachshon, *Hadronization, spin, and lifetimes*, *JHEP* **0807** (2008) 016, [arXiv:0803.1787].

[10] P. Chliapnikov, *Hyperfine splitting in light-flavour hadron production at LEP*, *Phys. Lett. B.* **462** (1999) 341–353.

[11] I. Bigi, Y. Dokshitzer, V. Khoze, J. Kühn, and P. Zerwas, *Production and decay properties of ultra-heavy quarks*, *Phys. Lett. B* **181** (1986) 157–163.

[12] ATLAS, *Search for $\mathcal{CP}$ violation in single top quark events in pp collisions at $\sqrt{s}$ = 7 TeV with the ATLAS detector*, Tech. Rep. ATLAS-CONF-2013-032, CERN, Geneva, Mar, 2013.

[13] G. Mahlon and S. Parke, *Angular correlations in top quark pair production and decay at hadron colliders*, *Phys. Rev. D* **53** (1996) 4886–4896, [hep-ph/9512264].

[14] I. Yavin and L. Wang, *Spin measurements in cascade decays at the LHC*, *JHEP* **0704** (2007) 032, [hep-ph/0605296].

[15] G. Moortgat-Pick, K. Rolbiecki, and J. Tattersall, *Early spin determination at the LHC?*, *Phys. Lett. B* **699** (2011) 158–163, [arXiv:1102.0293].

[16] F. Boudjema and R. Singh, *A model independent spin analysis of fundamental particles using azimuthal asymmetries*, *JHEP* **0907** (2009) 028, [arXiv:0903.4705].

[17] R. Godbole, S. Rindani, and R. Singh, *Lepton distribution as a probe of new physics in production and decay of the t quark and its polarization*, *JHEP* **0612** (2006) 021, [hep-ph/0605100].

[18] S. Rindani and P. Sharma, *Probing anomolous tbW couplings in single-top production using top polarization at the large hadron collider*, *JHEP* **1111** (2011) 082, [arXiv:1107.2597].

[19] S. Parke and Y. Shadmi, *Spin correlations in top-quark pair production at e^+e^- colliders*, *Phys. Lett. B* **387** (1996) 199–206, [hep-ph/9606419].

[20] D. Espriu and J. Manzano, *A study of top polarization in single-top production at the LHC*, *Phys. Rev. D* **66** (2002) 114009, [hep-ph/0209030].

[21] B. Grzadkowski and Z. Hioki, *Decoupling of anomalous top-quark-decay vertices in angular distribution of secondary particles*, *Phys. Lett. B* **557** (2003) 55–59, [hep-ph/0208079].

[22] D. Espriu and J. Manzano, *Measuring effective electroweak couplings in single top productiona at the LHC*, *Phys. Rev. D* **65** (2002) 073005, [hep-ph/0107112].

[23] G. Mahlon and S. Parke, *Single top quark production at the LHC: Understanding spin*, *Phys. Rev. B* **476** (2000) 323–330, [hep-ph/9912458].

[24] S. Kawasaki, T. Shirafuji, and S. Tsai, *Productions and decays of short-lived particles in e^+e^- collding beam experiments*, *Prog. Theor. Phys.* **49** (1973) 1656–1678.

[25] T. Nasuno, *Spin Correlations in Top Quark Production at e^+e^- Linear Colliders*. PhD thesis, Hiroshima University, 1999. hep-ph/9906252.

[26] H. Elvang and Y. Huang, *Scattering amplitudes*, arXiv:1308.1697.

[27] V. Andreev, *Spinor techniques for massive fermions with arbitrary polarization*, *Phys. Rev. D* **62** (2001) 014029, [hep-ph/0101140].

[28] C.-R. Chen, F. Larios, and C.-P. Yuan, *General analysis of single top production and W helicity in top decay*, *Phys. Lett. B.* **631** (2005) 126–132, [hep-ph/0503040].

[29] G. Mahlon, *Observing spin correlations in single top production and decay*, 2000. hep-ph/0011349. Talk presented at the Thinkshop2 on Top-Quark Physics.

[30] M. Najafabadi, *Secondary particles spectra in the decay of a polarized top quark with anomalous tWb couplings*, *J. Phys. G* **34** (2007) 39–46, [hep-ph/0601155].

[31] J. Campbell, J. Huston, and W. Stirling, *Hard interactions of quarks and gluons: a primer for LHC physics*, *Rept. Prog. Phys.* **70** (2007) 89, [hep-ph/0611148].

[32] A. Roeck et al., *From the LHC to future colliders*, *Eur. Phys. J. C* **66** (2010) 525–583, [arXiv:0909.3240].

[33] D. Asner, A. Hoang, et al., *Top quark precision physics at the international linear collider*, arXiv:1307.8265.

[34] F. Penunuri, F. Larios, and A. Bouzas, *QCD corretion to single top production at the ILC*, *Phys. Rev. D* **83** (2011) 077501, [arXiv:1102.1417].

[35] B. Grzadkowski and Z. Hioki, *Angular distributions of leptons in general ttbar production and decay*, *Phys. Lett. B* **529** (2002) 82–86, [hep-ph/0112361].

CHAPTER 5

NEW CONSTRAINTS ON LIGHT VECTORS COUPLED TO ANOMALOUS CURRENTS

5.1 Introduction:

Recent years have seen a resurgence of interest in the possibility of extending the Standard Model (SM) by including relatively light and very weakly coupled states [1, 14]. New light vectors are a popular candidate, having been proposed for purposes including addressing experimental anomalies at low energies [21, 35, 37, 40, 46, 50], explaining puzzles such as baryon stability [26], or acting as a mediator to a dark sector [8, 16, 25].

In this paper, we will consider light vectors with dimension-4 couplings to SM states. Unless the SM current that a vector couples to is conserved (i.e. the electromagnetic (EM) or $B-L$ current), there are (energy/vector mass)^2 processes involving the longitudinal mode of the new vector. These make the SM + vector effective field theory (EFT) non-renormalisable, requiring a cutoff at some scale $\propto$ (vector mass / vector coupling). For a light, weakly coupled new vector, such energy-enhanced processes can be the dominant production mechanism in high-energy experiments, and can place strong constraints on its coupling.

For models in which the SM current is broken by tree-level processes — e.g. axial currents are broken by fermion masses — such constraints have been considered in a number of works [19, 34, 40, 41].[1] In this Letter, we point out they can also apply if a light vector X couples to a current that is conserved at tree level, but

[1] In accompanying work [33], we identify processes which place stronger constraints on vectors coupling to tree-level non-conserved SM currents.

broken by the chiral anomaly (within the SM + X EFT), such as the SM baryon number current. These loop-level, but (energy/vector mass)^2 enhanced, processes can place significantly stronger constraints on light X than existing constraints.

The only way to avoid such processes is for the UV completion to introduce extra electroweak symmetry breaking, which generally runs into strong experimental constraints. Conversely, cancelling the anomalies with new heavy fermions, that obtain their masses from a SM-singlet vacuum expectation value (VEV), always results in enhanced longitudinal X emission, as we show and exploit in the rest of this Letter.

5.2 Anomalous amplitudes:

We will use the SM baryon number current as our prototypical example — a light vector coupled to this current has been considered in many papers over the past decades, e.g. [20, 26, 27, 29, 35, 47, 51]. Within the SM, the baryon number current is conserved at tree level, but violated by the chiral anomaly, which gives a divergence [9]

$$\partial^\mu J_\mu^{\text{baryon}} = \frac{\mathcal{A}}{16\pi^2}\left(g^2 W^a_{\mu\nu}(\tilde{W}^a)^{\mu\nu} - g'^2 B_{\mu\nu}\tilde{B}^{\mu\nu}\right) \tag{5.1}$$

where $\mathcal{A} = 3/2$, and $\tilde{B}^{\mu\nu} \equiv \frac{1}{2}\epsilon^{\mu\nu\sigma\rho}B_{\sigma\rho}$ etc. If a new light vector X is coupled to the baryon number current, then the SM + X EFT is non-renormalisable, and must be UV-completed at a scale $\lesssim \frac{4\pi m_X}{g_X}/\left(\frac{3g^2}{16\pi^2}\right)$ [49], where g_X and m_X are the coupling strength and mass of X, respectively.

In the simplest such UV completions, the anomalies are cancelled by introducing new fermions with chiral couplings to X, and vectorial couplings to the

SM gauge bosons. For example, the mixed anomalies can be cancelled with one weak doublet of Dirac fermions, with $(Y, X_A) = (-\frac{1}{2}, -3)$, and a weak singlet with $(Y, X_A) = (-1, 3)$, where Y and X_A are the hypercharge and axial X charge respectively [22, 32]. The XXX anomaly can then be cancelled by an additional SM-singlet fermion, and all of the new fermions can obtain heavy masses from a SM-singlet VEV.

Anomaly cancellation ensures that the theory is well-behaved at very high energies. However, as reviewed in [8, 33], triangle diagram amplitudes have both a fermion-mass-independent 'anomalous' piece, and a piece that depends on the mass of the fermions in the loop. The mass-dependent parts of longitudinal triangle amplitudes are proportional to the fermion's axial coupling; since X has vectorial couplings to SM fermions, we obtain

$$-(p+q)_\mu \mathcal{M}^{\mu\nu\rho} = \frac{1}{2\pi^2}\epsilon^{\nu\rho\lambda\sigma} p_\lambda q_\sigma g_X g'^2 \times \sum_f 2m_f^2 I_{00}(m_f, p, q) X_{A,f} Y_f^2 \tag{5.2}$$

$$\mathcal{M}^{\mu\nu\rho} \equiv \sum_{f, f_{\rm SM}}$$

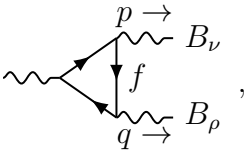

,

where f ($f_{\rm SM}$) runs over heavy (SM) fermions; the 'anomalous' parts have cancelled between the new fermions and the SM fermions, and the mass-dependent 'scalar integral' term I_{00} is [8]

$$I_{00}(m_f, p, q) \equiv \int_0^1 dx \int_0^{1-x} dy \, \frac{1}{D(x, y, p, q)}\,, \tag{5.3}$$
$$D \equiv y(1-y)p^2 + x(1-x)q^2 + 2xy\, p\cdot q - m_f^2$$

For $m_f^2 \gg p^2, q^2, p\cdot q$ we have $I_{00} \simeq -1/2m_f^2$. Anomaly cancellation requires that $2\sum_f X_f Y_f^2 = \mathcal{A}$. Consequently, if the external momenta on the triangle are

small compared to the masses of the new heavy fermions, then we have a total longitudinal amplitude of

$$-(p+q)_\mu \mathcal{M}^{\mu\nu\rho} \simeq \frac{1}{4\pi^2}\epsilon^{\nu\rho\lambda\sigma} p_\lambda q_\sigma g_X g'^2 \mathcal{A} \tag{5.4}$$

up to a relative error $\mathcal{O}(\{p^2, q^2, p\cdot q\}/m_f^2)$.

This result is independent of the particulars of the heavy fermion sector, and is precisely the result we would have obtained by adopting a 'covariant' [8, 33] SM-gauge-group-preserving regularisation scheme within the SM + X EFT. As we review below, this is because the lack of extra electro-weak symmetry breaking (EWSB) in the UV theory determines the behaviour in the EFT.

The amplitudes for XWW triangles will have similar behaviour, with g' replaced by g. An additional feature is that, since $SU(2)_L$ is non-abelian, there are anomalous $XWWW$ box diagrams. These have an analogous story of fermion mass dependence in the UV theory.

5.3 Low-energy theory and UV completions:

Other classes of UV completions can give different results for low-energy triangle amplitudes. This is corresponds to the fact that the SM + X EFT generically includes dimension-4 Wess-Zumino (WZ) terms,

$$\begin{aligned}\mathcal{L} \supset\ & C_B g_X g'^2 \epsilon^{\mu\nu\rho\sigma} X_\mu B_\nu \partial_\rho B_\sigma \\ & + C_W g_X g^2 \epsilon^{\mu\nu\rho\sigma} X_\mu W^a_\nu D_\rho W^a_\sigma \,,\end{aligned} \tag{5.5}$$

Since X has purely vectorial couplings to SM fermions, we must have $C_B = -C_W \equiv C_{\mathrm{WZ}}$ to avoid breaking the EM gauge symmetry. The coefficient of the WZ terms

is determined by the UV theory (with the appropriate numerical value also determined by the regularisation scheme chosen for the anomalous diagrams [33]). For example, in a 'SM-covariant' regularisation scheme for the EFT, $C_{\mathrm{WZ}} = 0$ corresponds to the UV theory introducing no extra EWSB, as per the example above. The key point is that there is no choice for C_{WZ} that preserves both $U(1)_X$ and the SM gauge groups [49].

At the other extreme, the UV theory may preserve $U(1)_X$ by breaking the SM gauge groups — in the EFT, this corresponds to the WZ term cancelling longitudinal X amplitudes from SM fermion triangles. For example, we could cancel the anomalies by introducing new, heavy SM-chiral fermions, which obtain their masses through large Yukawa couplings with the SM Higgs. Once the new fermions are integrated out, this introduces extra EWSB into the low-energy theory [30,31], analogously to integrating out the top quark in the SM (after which the photon remains massless, even though the fermion content is anomalous). As reviewed in [33], this possibility is strongly constrained by electroweak precision tests and collider experiments. If the current LHC run sees no deviations from the SM, it would be fairly robustly ruled out. Variations on this scenario, employing an enlarged EWSB sector, may be slightly more viable, but also inevitably introduce dangerous new physics at the electroweak scale.

Intermediate scenarios, in which the EFT breaks $U(1)_X$ and the SM EW group, are also possible. If, in the UV theory, the SM-breaking contributions to the anomaly-cancelling heavy fermion masses are small compared to their total mass, then the WZ coefficient in the low-energy EFT will be approximately that expected from a SM-preserving theory, up to $(m_{\mathrm{EWSB}}/m_f)^2$ corrections [33]. Conversely, if the new fermions obtain most of their mass from a EWSB-breaking VEV, there

will be strong experimental constraints, analogous to those mentioned above for new SM-chiral fermions.

It should be noted that such constraints rely on the existence of new, SM-chiral states, which have effects (such as electroweak precision observables) unsuppressed by the small coupling g_X. There may be more exotic UV completions, without anomaly-cancelling fermions, which are experimentally viable; within the low-energy theory, the effects of the SM-breaking WZ terms are all suppressed by g_X, and if this is small enough, may not be problematic. While the rest of this Letter will work under the assumption of a SM-preserving low-energy EFT, this caveat should be kept in mind.

Another possible complication is that the new 'UV' degrees of freedom do not necessarily have to be heavier than all of the SM states. For example, if the anomalies are cancelled by SM-vector-like fermions, then collider constraints only require that they have masses $\gtrsim 90\,\mathrm{GeV}$ [32] (for a baryon number vector). As per equation 5.3, this would introduce extra momentum dependence into triangle amplitudes with EW-scale external momenta. For sufficiently small m_X/g_X, even lighter new states would be required; however, such large g_X will generally be constrained more directly.

5.4 Axion-like behaviour:

By the usual Goldstone boson equivalence arguments, the $1/m_X$-enhanced parts of amplitudes involving longitudinal X are approximately equal to those for the corresponding Goldstone (pseudo)scalar, φ. In our case, the processes which are not suppressed by m_X all come from the anomalous couplings computed above.

In the φ theory, we can integrate by parts to write the interactions within the low-energy theory as

$$\begin{aligned}
&\frac{\mathcal{A}}{16\pi^2}\frac{g_X\varphi}{m_X}(g^2W^a\tilde{W}^a - g'^2B\tilde{B}) = \\
&\frac{\mathcal{A}}{16\pi^2}\frac{g_X\varphi}{m_X}\Big(g^2(W^+\tilde{W}^- + W^-\tilde{W}^+) \\
&\quad + gg'(\cot\theta_w - \tan\theta_w)Z\tilde{Z} + 2gg'Z\tilde{F}) \\
&\quad - ieg^2\tilde{F}^{\mu\nu}(W^+_\mu W^-_\nu - W^+_\nu W^-_\mu) + \ldots\Big)
\end{aligned} \tag{5.6}$$

where we have suppressed indices, and the dots correspond to further terms of the form AW^+W^- and ZW^+W^-.[2]

Since there is no two-photon anomalous coupling, longitudinal emission processes involving sub-EW-scale momenta are suppressed. Consequently, the relatively most important effects of the anomalous couplings arise either in high-energy collisions — for example, on-shell Z decay at LEP — or in virtual processes which can be dominated by large loop momenta, such as rare meson decays.

5.5 $Z \to \gamma X$ decays:

If $m_X < m_Z$, then the $\varphi Z\tilde{F}$ coupling in (5.6) gives rise to $Z \to \gamma X$ decays, with width

$$\Gamma_{Z\to\gamma X} \simeq \frac{\mathcal{A}^2}{384\pi^5}g_X^2 g^2 g'^2\frac{m_Z^3}{m_X^2} \tag{5.7}$$

corresponding to a branching ratio

$$\frac{\Gamma_{Z\to\gamma X}}{\Gamma_Z} \simeq 10^{-7}\mathcal{A}^2\left(\frac{\text{TeV}}{m_X/g_X}\right)^2 \tag{5.8}$$

[2] the $WWWW$ terms from $W^a_{\mu\nu}(\tilde{W}^a)^{\mu\nu}$ cancel, reflecting the lack of pentagon anomalies for an abelian vector [24]

If X decays invisibly, then LEP searches for single photons at half the Z energy [4,5] limit this branching ratio to be $\lesssim 10^{-6}$. The bounds for SM decays of X are less stringent [6, 7, 10], though the large number of Z bosons produced at hadron colliders should allow enhanced sensitivity to rare Z decays, as we discuss later.

5.6 FCNCs:

The couplings of X to quarks, and the anomalous XWW coupling, lead to flavour changing neutral current (FCNC) interactions between quarks. These effects can be summarised by integrating out EW-scale states to obtain an effective interaction,

$$\mathcal{L} \supset g_{Xd_id_j} X_\mu \bar{d}_j \gamma^\mu \mathcal{P}_L d_i + \text{h.c.} + \ldots \tag{5.9}$$

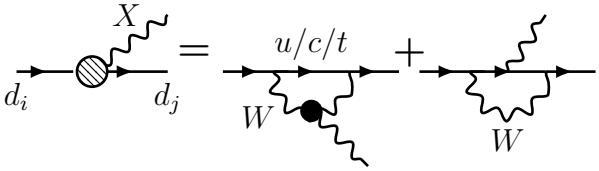

where we have taken a down-type FCNC for illustration, and have omitted other, higher-loop-order diagrams (as well as X emission from external quark legs). The solid XWW vertex indicates the sum of WZ terms and fermion triangles (within a UV theory, it would simply be the sum over triangles). If X is coupled to a fully-conserved current, then $g_{Xd_id_j} = 0$, and the effective interaction is higher-dimensional; if X is coupled to a tree-level conserved current (as we consider here), then only the anomalous XWW coupling contributes to $g_{Xd_id_j}$.

In the calculation of $g_{d_id_jX}$, while each individual diagram is divergent, these divergences cancel in the sum over virtual quark generations, by CKM unitarity. As a result, the integral is dominated by momenta $\sim m_t$, and higher-dimensional

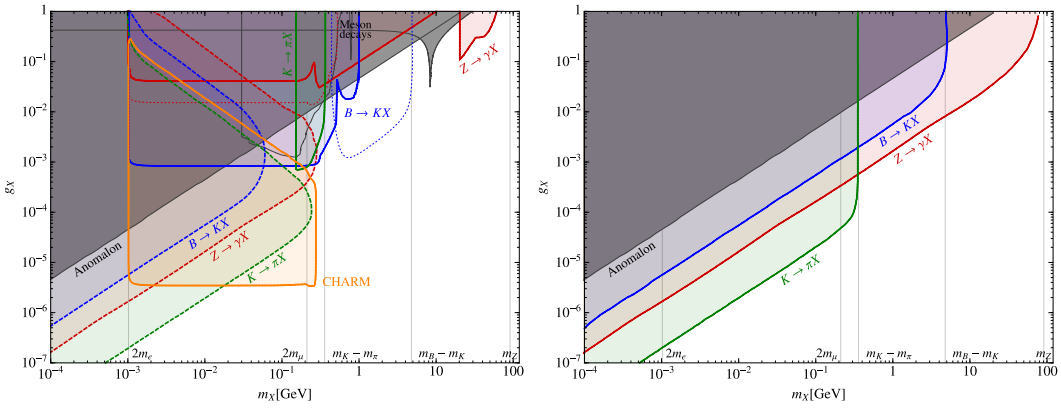

Figure 5.1: *Left panel:* Constraints on a vector X coupling to baryon number, assuming a kinetic mixing with the SM photon $\epsilon \sim eg_X/(4\pi)^2$, and no additional invisible X decay channels. Colored regions with solid borders indicate constraints from visible decays, dashed borders correspond to missing energy searches, and dotted borders denote projections based on current expected sensitivities. The gray regions indicate constraints from the previous literature. The new constraints come from searches for $K \to \pi X$ (green) [12,15,17], $B \to KX$ (blue) [2,18,38,45], $Z \to X\gamma$ (red) [4–7,10], and very displaced decays at the CHARM proton beam dump experiment [23]. For the latter, the enhanced $K \to \pi X$ decays result in larger X production than computed in naive analyses [13,36]. The 'anomalon' line shows the approximate region in which anomaly-cancelling fermions would be light enough to have been detected [32]. The other gray constraints are from ϕ and η decays [51], and Υ decays [26] (left to right). *Right panel:* As above, but with the assumption that X dominantly decays invisibly.

couplings suppressed by the cutoff scale will give sub-leading contributions (in the UV theory, the masses of the UV fermions in triangles will be much larger than the external momenta of these triangles). The coefficient of the effective vertex is

$$\begin{aligned} g_{Xd_id_j} &= -\frac{3g^4\mathcal{A}}{(16\pi^2)^2} g_X \sum_{\alpha\in\{u,c,t\}} V_{\alpha i}V^*_{\alpha j} F\left(\frac{m_\alpha^2}{m_W^2}\right) + \dots \\ &\simeq -\frac{3g^4\mathcal{A}}{(16\pi^2)^2} g_X V_{ti}V^*_{tj} F\left(\frac{m_t^2}{m_W^2}\right) + \dots , \end{aligned} \tag{5.10}$$

where

$$F(x) \equiv \frac{x(1+x(\log x - 1))}{(1-x)^2} \simeq x \quad (\text{for } x \ll 1) \tag{5.11}$$

Compared to these effective FCNC vertices, other effective flavour-changing operators are higher-dimensional, and so are suppressed by more powers of g_X/m_X

and/or $1/m_W^2$. Thus, despite equation 5.10 representing a 2-loop contribution (within the UV theory), it is able to dominate over 1-loop $d_i d_j X$ processes. For example, in the $B \to KX$ decay, we have

$$\mathcal{M}^{2-\text{loop}}/\mathcal{M}^{1-\text{loop}} \propto g^2/(16\pi^2) \times (m_t/m_X)^2 \tag{5.12}$$

which, for m_X light enough to be emitted in the decay, is $\gg 1$.[3] Competing SM FCNC processes are also suppressed; for example, the $bs\gamma$ vertex is of the form $\propto \frac{m_b}{m_W^2} F_{\mu\nu} \bar{b}_L \sigma^{\mu\nu} s_L$ [44] (since the photon couples to a conserved current), while 4-fermion vertices are suppressed by at least G_F.

If m_X is light enough, then FCNC meson decays via an on-shell longitudinal X become possible, and are enhanced by $(\text{energy}/m_X)^2$, in addition to being lower-dimensional than other effective flavour-changing processes. Most directly, the bsX and sdX vertices result in $B \to K^{(*)}X$ and $K \to \pi X$ decays, giving new flavour-changing meson decays that can place strong constraints on the coupling of X. This is in exact analogy to the FCNC processes discussed in [39], for axion-like particles with a coupling to $W^a \tilde{W}^a$.

5.7 Experimental constraints:

The left panel of Figure 5.1 shows a selection of experimental bounds on the coupling of a baryon number vector ($\mathcal{A} = 3/2$); for consistency with other literature [51], we assume a loop-suppressed kinetic mixing with the photon, $\epsilon = e g_X/(4\pi)^2$. As the figure illustrates, the anomalous bounds, derived in this work, are significantly stronger than existing bounds across a wide mass range.

[3] The $\propto m_X^2$ (rather than $\propto m_X$) relative suppression of 1-loop emission comes from angular momentum conservation in the pseudoscalar $\to$ pseudoscalar + vector decay; for $B \to K^* X$ decays, we would have $\mathcal{M}^{2-\text{loop}}/\mathcal{M}^{1-\text{loop}} \propto m_t^2/(m_X m_b)$ instead.

In particular, they constrain couplings significantly smaller than those at which we might expect the anomaly-cancelling fermions to have been observed at colliders [32], showing that our assumption of separation of scales can be valid. These improved bounds rule out some models of phenomenological interest. For example, [35] proposes a baryon number vector model to account for the claimed evidence of a new particle in ^{8}Be decays [43], with the anomalies being cancelled by heavy fermions that are vectorial under the SM. Their fiducial parameters of $m_X \simeq 17\,\mathrm{MeV}$, $g_X \simeq 6 \times 10^{-4}$ (and a large kinetic mixing $\epsilon \simeq -10^{-3}$) result in $\mathrm{Br}(B \to K^* X) \simeq 2 \times 10^{-4}$ from the anomalous XWW coupling, well above the experimental bound of $\Delta\mathrm{Br}(B \to K^* e^+ e^-) \lesssim 10^{-6}$ [18].

Figure 5.1 (right) shows the constraints that arise if X has a significant branching ratio to invisible states (e.g. light dark matter, or additional neutrino species). For example, one light Dirac fermion χ with X-charge of 1 and $2m_\chi < m_X$ will result in an invisible branching fraction of $\gtrsim 30\%$. The constraints from missing energy searches are strong, and limit the discovery prospects for light dark matter coupled through such a mediator at neutrino experiments [11].

5.8 Future searches:

At $m_X \lesssim$ GeV, the enhanced rate of $K \to \pi X$ and $B \to KX$ decays means that future proton beam dump experiments such as SHIP [13] will be more sensitive than projected in existing analyses. At higher masses, the enhanced $B \to KX$ rate motivates searches for bumps in the invariant mass spectrum of $B \to K +$ hadronic decays. For example, the $B \to K\omega$ decay is detected as a peak in the $m_{3\pi}$ distribution of $B \to K\pi^+\pi^-\pi^0$ decays, with branching ratio error $\sim 10^{-6}$ [28];

a similar search could be performed at other invariant masses.

For $Z \to \gamma X$ decays, the large number of Zs produced at hadron colliders would likely allow leptonic $Z \to \gamma(X \to l^+l^-)$ decays to be probed down to $\mathcal{O}(10^{-5})$ branching ratios or better [3, 42]. This would be especially helpful in constraining models of other anomalous vectors — for example, those with purely right-handed couplings [21], which result in $XZ\gamma$ anomalous couplings, but no XWW coupling.

5.9 Conclusions:

In this Letter, we have pointed out the phenomenological consequences of energy-enhanced longitudinal mode production, for light vectors coupling to anomalous SM currents. Such models have been considered for a variety of purposes in previous literature, but anomalous processes were overlooked. Taking the example of a light vector coupled to baryon number, we showed that anomalous production can place stronger coupling constraints over a wide mass range. In forthcoming work [33], we discuss these points in more depth, and also derive improved constraints on vectors coupled to SM currents that are broken by tree-level processes.

BIBLIOGRAPHY

[1] *Fundamental Physics at the Intensity Frontier*, 2012.

[2] R. Aaij et al. Differential branching fraction and angular analysis of the $B^+ \to K^+\mu^+\mu^-$ decay. *JHEP*, 02:105, 2013.

[3] T. A. Aaltonen et al. First Search for Exotic Z Boson Decays into Photons and Neutral Pions in Hadron Collisions. *Phys. Rev. Lett.*, 112:111803, 2014.

[4] P. Abreu et al. Search for neutral heavy leptons produced in Z decays. *Z. Phys.*, C74:57–71, 1997. [Erratum: Z. Phys.C75,580(1997)].

[5] M. Acciarri et al. Search for new physics in energetic single photon production in e^+e^- annihilation at the Z resonance. *Phys. Lett.*, B412:201–209, 1997.

[6] P. D. Acton et al. A Measurement of photon radiation in lepton pair events from Z0 decays. *Phys. Lett.*, B273:338–354, 1991.

[7] B. Adeva et al. Search for narrow high mass resonances in radiative decays of the Z0. *Phys. Lett.*, B262:155–162, 1991.

[8] S. Adler. Perturbation theory anomalies. In S. Deser, M. Grisaru, and H. Pendleton, editors, *Lectures on Elementary Particles and Quantum Field Theory, vol. 1*, pages 3–164. MIT Press, 1970.

[9] S. L. Adler. Axial vector vertex in spinor electrodynamics. *Phys. Rev.*, 177:2426–2438, 1969.

[10] O. Adriani et al. Isolated hard photon emission in hadronic Z0 decays. *Phys. Lett.*, B292:472–484, 1992.

[11] A. A. Aguilar-Arevalo et al. Dark Matter Search in a Proton Beam Dump with MiniBooNE. *Submitted to: Phys. Rev. Lett.*, 2017.

[12] A. Alavi-Harati et al. Search for the rare decay K(L) to pi0 e+ e-. *Phys. Rev. Lett.*, 93:021805, 2004.

[13] S. Alekhin et al. A facility to Search for Hidden Particles at the CERN SPS: the SHiP physics case. *Rept. Prog. Phys.*, 79(12):124201, 2016.

[14] J. Alexander et al. Dark Sectors 2016 Workshop: Community Report. 2016.

[15] V. V. Anisimovsky et al. Improved measurement of the K+ to pi+ nu anti-nu branching ratio. *Phys. Rev. Lett.*, 93:031801, 2004.

[16] N. Arkani-Hamed, D. P. Finkbeiner, T. R. Slatyer, and N. Weiner. A Theory of Dark Matter. *Phys. Rev.*, D79:015014, 2009.

[17] A. V. Artamonov et al. New measurement of the $K^+ \to \pi^+ \nu\bar{\nu}$ branching ratio. *Phys. Rev. Lett.*, 101:191802, 2008.

[18] B. Aubert et al. Direct CP, Lepton Flavor and Isospin Asymmetries in the Decays $B \to K^{(*)}\ell^+\ell^-$. *Phys. Rev. Lett.*, 102:091803, 2009.

[19] V. Barger, C.-W. Chiang, W.-Y. Keung, and D. Marfatia. Constraint on parity-violating muonic forces. *Phys. Rev. Lett.*, 108:081802, 2012.

[20] B. Batell, P. deNiverville, D. McKeen, M. Pospelov, and A. Ritz. Leptophobic Dark Matter at Neutrino Factories. *Phys. Rev.*, D90(11):115014, 2014.

[21] B. Batell, D. McKeen, and M. Pospelov. New Parity-Violating Muonic Forces and the Proton Charge Radius. *Phys. Rev. Lett.*, 107:011803, 2011.

[22] P. Batra, B. A. Dobrescu, and D. Spivak. Anomaly-free sets of fermions. *J. Math. Phys.*, 47:082301, 2006.

[23] F. Bergsma et al. Search for Axion Like Particle Production in 400-GeV Proton - Copper Interactions. *Phys. Lett.*, B157:458–462, 1985.

[24] A. Bilal. Lectures on Anomalies. 2008.

[25] C. Boehm and P. Fayet. Scalar dark matter candidates. *Nucl. Phys.*, B683:219–263, 2004.

[26] C. D. Carone and H. Murayama. Possible light U(1) gauge boson coupled to baryon number. *Phys. Rev. Lett.*, 74:3122–3125, 1995.

[27] C. D. Carone and H. Murayama. Realistic models with a light U(1) gauge boson coupled to baryon number. *Phys. Rev.*, D52:484–493, 1995.

[28] V. Chobanova et al. Measurement of branching fractions and CP violation parameters in $B \to \omega K$ decays with first evidence of CP violation in $B^0 \to \omega K^0_S$. *Phys. Rev.*, D90(1):012002, 2014.

[29] P. Coloma, B. A. Dobrescu, C. Frugiuele, and R. Harnik. Dark matter beams at LBNF. *JHEP*, 04:047, 2016.

[30] E. D'Hoker and E. Farhi. Decoupling a Fermion in the Standard Electroweak Theory. *Nucl. Phys.*, B248:77, 1984.

[31] E. D'Hoker and E. Farhi. Decoupling a Fermion Whose Mass Is Generated by a Yukawa Coupling: The General Case. *Nucl. Phys.*, B248:59–76, 1984.

[32] B. A. Dobrescu and C. Frugiuele. Hidden GeV-scale interactions of quarks. *Phys. Rev. Lett.*, 113:061801, 2014.

[33] J. Dror, R. Lasenby, and M. Pospelov. *in preparation.*

[34] P. Fayet. Constraints on Light Dark Matter and U bosons, from psi, Upsilon, K+, pi0, eta and eta-prime decays. *Phys. Rev.*, D74:054034, 2006.

[35] J. L. Feng, B. Fornal, I. Galon, S. Gardner, J. Smolinsky, T. M. P. Tait, and P. Tanedo. Particle Physics Models for the 17 MeV Anomaly in Beryllium Nuclear Decays. 2016.

[36] S. Gardner, R. J. Holt, and A. S. Tadepalli. New Prospects in Fixed Target Searches for Dark Forces with the SeaQuest Experiment at Fermilab. *Phys. Rev.*, D93(11):115015, 2016.

[37] S. N. Gninenko and N. V. Krasnikov. The Muon anomalous magnetic moment and a new light gauge boson. *Phys. Lett.*, B513:119, 2001.

[38] J. Grygier et al. Search for $\boldsymbol{B \to h\nu\bar{\nu}}$ decays with semileptonic tagging at Belle. 2017.

[39] E. Izaguirre, T. Lin, and B. Shuve. A New Flavor of Searches for Axion-Like Particles. 2016.

[40] Y. Kahn, M. Schmitt, and T. M. P. Tait. Enhanced rare pion decays from a model of MeV dark matter. *Phys. Rev.*, D78:115002, 2008.

[41] S. G. Karshenboim, D. McKeen, and M. Pospelov. Constraints on muon-specific dark forces. *Phys. Rev.*, D90(7):073004, 2014. [Addendum: Phys. Rev.D90,no.7,079905(2014)].

[42] V. Khachatryan et al. Study of Final-State Radiation in Decays of Z Bosons Produced in *pp* Collisions at 7TeV. *Phys. Rev.*, D91(9):092012, 2015.

[43] A. J. Krasznahorkay et al. Observation of Anomalous Internal Pair Creation in Be8 : A Possible Indication of a Light, Neutral Boson. *Phys. Rev. Lett.*, 116(4):042501, 2016.

[44] M. Misiak et al. Estimate of $\mathcal{B}(\bar{B} \to X_s\gamma)$ at $O(\alpha_s^2)$. *Phys. Rev. Lett.*, 98:022002, 2007.

[45] C. Patrignani et al. Review of Particle Physics. *Chin. Phys.*, C40(10):100001, 2016.

[46] M. Pospelov. Secluded U(1) below the weak scale. *Phys. Rev.*, D80:095002, 2009.

[47] M. Pospelov. Neutrino Physics with Dark Matter Experiments and the Signature of New Baryonic Neutral Currents. *Phys. Rev.*, D84:085008, 2011.

[48] M. Pospelov, A. Ritz, and M. B. Voloshin. Secluded WIMP Dark Matter. *Phys. Lett.*, B662:53–61, 2008.

[49] J. Preskill. Gauge anomalies in an effective field theory. *Annals Phys.*, 210:323–379, 1991.

[50] D. Tucker-Smith and I. Yavin. Muonic hydrogen and MeV forces. *Phys. Rev.*, D83:101702, 2011.

[51] S. Tulin. New weakly-coupled forces hidden in low-energy QCD. *Phys. Rev.*, D89(11):114008, 2014.

CHAPTER 6

CODECAYING DARK MATTER

6.1 Introduction

The nature of dark matter (DM) is one of the most important open questions in physics. The possibility that dark matter is a thermal relic with mass around the weak scale is intriguing, but has been under significant experimental pressure from direct detection [1–3] and at the LHC [4]. This motivates the study of models which are not constrained by these searches, but can still be discovered by indirect detection, where limits are weaker and have made rapid progress in recent years [5].

Mechanisms for thermal dark matter freezeout usually rely on the DM remaining in chemical and thermal equilibrium with the Standard Model (SM) bath while non-relativistic, which leads to depletion of DM through Boltzmann suppression. In this work we consider the possibility that part of the dark sector decays out of equilibrium with the SM. This delays the exponential suppression of the DM density well beyond the point where the DM candidate becomes non-relativistic.

The mechanism, which we refer to as *Co-Decaying Dark Matter*, has the following properties:

1. The dark sector has decoupled from the SM before it becomes non-relativistic.
2. The lightest dark sector particle decays into the SM out of equilibrium.
3. The dark sector contains additional particles that are (approximately) degenerate with the decaying particle, and remain in chemical and thermal

equilibrium with it until freezeout. One or more of these particles are DM candidates.

Co-decaying DM will be a generic feature of large dark sectors in which the lightest state decays. To illustrate the idea, we will focus on the simplified case of two degenerate dark sector particles: A will be the DM candidate, and B will be the decaying state, with sizable annihilations $AA \to BB$.

After the dark sector decouples from the SM bath, the A and B comoving entropy density is conserved, and their number density does not exponentially deplete when they become non-relativistic (in contrast to the Weakly Interacting Massive Particle (WIMP)). Instead, the exponential suppression is delayed until the B's begin decaying:

$$n_A \sim n_B \propto e^{-\Gamma_B t} \simeq e^{-\frac{1}{2}\Gamma_B/H}\,, \tag{6.1}$$

where $n_{A,B}$ is the number density, Γ_B is the decay rate of the B particle, and H is the Hubble parameter. The A population tracks the B population until the $AA \to BB$ process cannot keep up with the expansion of the universe. At this point the A population freezes out and the B's continue to decay. The relic density of A is then set by both the annihilation rate, $\langle\sigma v\rangle$, as well as the B decay rate, Γ_B. A schematic illustration of the timeline for co-decaying DM is shown in Fig. 6.1.

The delay in the starting point of exponential suppression from the temperature in which DM becomes non-relativistic to the temperature at which B-decay begins, causes freezeout to occur at later times than the WIMP. The DM relic density has less time to redshift to today, and therefore, must have a smaller density at freezeout. In order to match the observed DM relic abundance a larger annihilation cross-section is required. This leads to a boosted indirect detection signal relative

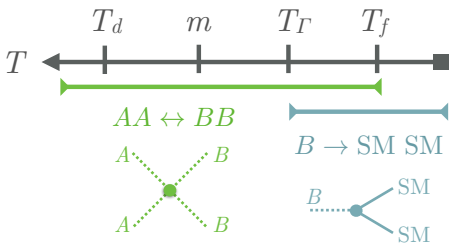

Figure 6.1: Co-decay dark matter timeline. At T_d the SM and dark sector decouple; at T_Γ the decay of B's begin to deplete the dark sector density; and at T_f the $AA \leftrightarrow BB$ process freezes out, resulting in a relic abundance for the A particles.

to WIMP models.

Previous work on multi-component dark sectors where interactions within the dark sector are necessary to get the correct dark matter relic abundance is extensive. Some examples including co-annihilating [6, 7], Secluded [8], SIMP [9, 10], Cannibalizing [11–16] and Forbidden [6, 17] DM. Additionally, models of particle decays affecting the relic abundance have been considered in [16, 18–27]. The freezeout mechanism of co-decaying DM is unique, with differing phenomenology. Furthermore, we emphasize that while we are mainly interested in the implications on dark matter, the dynamics studied here have a broad impact and can take place for any thermal relic.

In this Letter we study the co-decaying DM mechanism. We present an intuitive estimate of the relic density and check the results numerically using the Boltzmann equations. The constraints and signals of co-decaying DM are described, with a significant enhancement in the indirect detection signature. We conclude by presenting an explicit model realizing the phenomena.

6.2 Freezeout and Relic Abundance

The DM relic abundance can be solved in the standard sudden freezeout approximation, when $AA \to BB$ annihilations effectively stop:

$$n_{A,f}\langle\sigma v\rangle_f = H_f \implies \Omega_A = \frac{s_0}{\rho_c}\frac{\sqrt{g_{\star,m}}}{\sqrt{g_{\star,f}}}\frac{mH_m}{s_m}\frac{x_f}{\langle\sigma v\rangle_f}. \tag{6.2}$$

Here m is the DM mass, $x_i = m/T_i$, s is the entropy density of the SM bath, and the subscripts m and f denote quantities at temperatures $T = m$ and freezeout, respectively[1]. Note that Eq. (6.2) is identical to the standard WIMP scenario. However, for co-decaying DM, we will see that $x_f \gg 1$, leading to a boosted annihilation cross section relative to the standard WIMP case, where $x_f \simeq 20$.

We now compute the SM and dark sector temperatures at freezeout. To this end, we study the temperature evolution of the dark sector through the three stages depicted in Fig. 6.1: from the time of decoupling of the dark sector from the SM (T_d), to the onset of the B decay (T_Γ), and until freezeout of the $AA \to BB$ annihilations (T_f). We use the d, Γ, and f subscripts throughout to denote quantities evaluated at these stages, respectively, and primes to denote dark sector (total $A + B$) quantities.

At high temperatures, A and B decouple from the SM plasma when relativistic. The entropy densities in each sector are separately conserved until the decay of B begins, and therefore

$$s'_\Gamma = \frac{s'_d}{s_d} s_\Gamma \equiv \xi s_\Gamma \,, \tag{6.3}$$

The dark sector number density at the onset of decay, roughly when $\Gamma_B \simeq H_\Gamma$, is

[1] Throughout this section we will neglect the differences in effective entropy degrees of freedom $g_{\star s}$ and effective energy degrees of freedom $g_\star$.

given by the second law of thermodynamics for non-relativistic particles:

$$n'_\Gamma = \frac{T'_\Gamma}{m - \mu'_\Gamma + \frac{5}{2}T'_\Gamma}\xi s_\Gamma \,, \tag{6.4}$$

where μ' is the chemical potential of A and B.

While the $AA \leftrightarrow BB$ process is fast, the A density matches the B density. Taking the number of degrees of freedom in A and B to be equal (which we will assume throughout the paper for simplicity), the total dark sector density at the time of $AA \leftrightarrow BB$ freezeout is

$$n'_f a_f^3 = n'_\Gamma a_\Gamma^3 e^{-\frac{1}{2}\Gamma_B(t_f - t_\Gamma)} \simeq \frac{\xi s_\Gamma a_\Gamma^3}{x'_\Gamma - \frac{\mu'}{T'_\Gamma} + \frac{5}{2}} e^{-\frac{1}{4}\frac{\Gamma_B}{H_f}} \,. \tag{6.5}$$

where a is the cosmic scale factor. The A abundance is hence depleted through the decay of B particles. Using Eq. (6.2) with Eq. (6.5), the temperature at freezeout is given by

$$x_f \simeq \frac{2}{\sqrt{\Gamma_B/H_m}} \log^{1/2} \frac{\frac{2}{\sqrt{\pi}}\frac{s_m}{H_m}\xi\sigma}{x_f\sqrt{x'_f}x'_\Gamma(1 - \frac{\mu'_\Gamma}{m} + \frac{5}{2x'_\Gamma})} \,, \tag{6.6}$$

where $n_{A,f} = \frac{1}{2}n'_f$ and for brevity we have dropped ratios of $g_\star$. Here we have taken

$$\langle\sigma v\rangle = \frac{4}{\sqrt{\pi}}\frac{\sigma}{\sqrt{x'}} \tag{6.7}$$

for $x' \gg 1$ and s-wave scattering, where σ is the $2 \to 2$ cross-section at threshold. (For reference, note that the observed relic density for a WIMP would require $\sigma \simeq 10^{-36}$ cm^2.) Since Γ_B/H_m may be as small as 10^{-18} (see Fig. 6.1), x_f may be as large as 10^8.

The chemical potential and dark temperature will depend on whether number changing processes are active in the A, B system, e.g., $3 \to 2$ processes. Without number changing processes, the comoving entropy and number densities are separately conserved in the dark sector between decoupling and decay ($s'_\Gamma/s_\Gamma = s'_d/s_d$

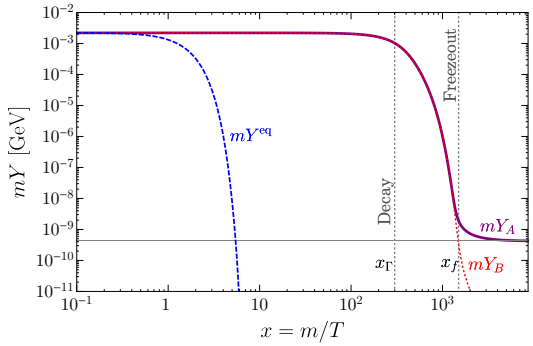

Figure 6.1: Yields ($Y \equiv n/s$) as a function of SM temperature without cannibalism for a benchmark point $g_A = g_B = 1$, $m = 1$ GeV, $\sigma = 1 \times 10^{-30}$ cm^2, $\Gamma_B = 6 \times 10^{-23}$ GeV. The (**purple**/solid) and (**red**/dotted) lines show the yield for A and B particles, respectively. For comparison, the (**blue**/dashed) line shows the yield assuming the DM was in chemical and thermal equilibrium. For this choice of parameters $x_\Gamma \simeq 300$, while freezeout occurs at $x_f \simeq 1500$. The dark temperature at freezeout is $x'_f \simeq 5 \times 10^6$.

and $n'_\Gamma/s_\Gamma = n'_d/s_d$). This decreases the dark temperature relative to the SM temperature, while inducing a chemical potential:

$$x'_\Gamma \simeq \frac{1}{3.7}\left(\frac{g_{\star,d}}{g_{\star,\Gamma}}\right)^{\frac{2}{3}} x_\Gamma^2, \quad \frac{\mu'_\Gamma}{m} \simeq 1 - \frac{3}{2x'_\Gamma} \quad \text{(w/o canb)}, \tag{6.8}$$

In contrast, if number changing processes are active, cannibalization can occur [15]. The SM temperature decreases exponentially relative to the dark sector, while the chemical potential is held fixed ($\mu' = 0$). Using conservation of comoving entropy in the hidden sector, one finds

$$x'_\Gamma \simeq \log \frac{x_\Gamma^3}{3.\,\xi\, x_\Gamma'^{1/2} g_{\star,\Gamma}}, \quad \frac{\mu'_\Gamma}{m} = 0 \quad \text{(w canb)}. \tag{6.9}$$

In both cases, the dark temperature at freezeout is redshifted from the temperature at decay,

$$x'_f \simeq x'_\Gamma \left(\frac{a_f}{a_\Gamma}\right)^2 \sim x'_\Gamma \left(\frac{x_f}{x_\Gamma}\right)^2. \tag{6.10}$$

Note that the dark matter will have a large energy density before it decays, and may come to dominate the energy density of the universe. When the DM decays,

it will release a significant amount of entropy and reheat the SM bath. However, since the reheating occurs before DM freezeout, the entropy dump does not dilute the DM relic abundance. The most important effects are a delay in the start of the decay and a modification to the final relationship in Eq. (6.10). These effects are taken into account in the numerical solutions to the Boltzmann equations and in computing the viable parameter space.

Combining Eqs. (6.2) and (6.6) to (6.10), the relic abundance in the absence of cannibalization and when cannibalization is active throughout is:

$$\frac{\Omega_A}{\Omega_{\rm DM}} \simeq \left(\frac{10^{-36}}{\sigma/{\rm cm}^2}\right) \times \begin{cases} \left(\dfrac{m}{\rm GeV}\right)\left(\dfrac{10^{-18}}{\Gamma_B/m}\right) & \text{(w/o canb)}, \\ \left(\dfrac{m}{\rm GeV}\right)^{\frac{1}{2}}\left(\dfrac{10^{-17}}{\Gamma_B/m}\right)^{\frac{1}{2}} & \text{(w canb)}. \end{cases} \tag{6.11}$$

where we have taken, $g_{\star,\,d} = 106.75$, and $\Omega_{\rm DM} = 0.27$ [28]. Here and throughout we will take the entropy density ratio at decoupling, defined in Eq. (6.3), to be $\xi = (g_A + g_B)/g_{\star,\,d} \simeq 0.02$.

Generically in any given model, one expects number changing self-interactions to be present, which leads to some amount of cannibalization. Additionally, in much of parameter space cannibalization can shut off before decays begin. Therefore, a realistic scenario will likely be between the two limiting cases in Eq. (6.11).

6.3 Boltzmann equations

We now present a numerical study of co-decaying dark matter. To track the number densities of A and B as well as the dark temperature T', 3 different equations are

required:

$$\begin{aligned}
\dot{n}_A + 3Hn_A &= -\langle\sigma v\rangle(n_A^2 - n_B^2)\,, \\
\dot{n}_{A+B} + 3Hn_{A+B} &= -\left(\langle\Gamma_B\rangle_{T'} n_B - \langle\Gamma_B\rangle_T n_T^{\rm eq}\right)\,, \\
\dot{\rho}_{A+B} + 3H(\rho_{A+B} + P_{A+B}) &= -m\Gamma_B\left(n_B - n_T^{\rm eq}\right)\,,
\end{aligned} \tag{6.12}$$

where $\langle\Gamma_B\rangle_{T(T')}/\Gamma_B = m\langle E_B^{-1}\rangle_{T(T')}$ is the thermally averaged inverse boost factor over the DM (SM) phase-space distributions. Time derivatives can be related to derivatives of the SM temperature T using the Friedman equation and second law of thermodynamics,

$$\begin{aligned}
H^2 &\equiv \left(\frac{\dot{a}}{a}\right)^2 = \frac{8\pi G}{3}(\rho + \rho')\,, \\
a\frac{d}{da}(s\,a^3) &= \frac{1}{T}\frac{d(\rho\,a^4)}{da} = \frac{m\Gamma_B}{HT}\left(n_B - n_T^{\rm eq}\right)a^3\,,
\end{aligned} \tag{6.13}$$

where G is the gravitational constant.

If number-changing processes in the dark sector are present, such as $3 \to 2$ processes, then there are additional terms in the number density equations of the form

$$-\left\langle\sigma v^2\right\rangle_{ijk\to lm}\left(n_i n_j n_k - n_l n_m n^{\rm eq}\right), \tag{6.14}$$

where n_i can be n_A or n_B.

The Boltzmann equations, Eq. (6.12), are straightforward to solve numerically, and the results for a benchmark point are given in Fig. 6.1. As shown, the dark sector does not follow the equilibrium distribution; instead it undergoes exponential decay at a later time. When the dark matter becomes non-relativistic ($x \simeq 1$), the co-moving number density remains constant, until decay begins ($x \simeq x_\Gamma$). The A density matches the B density until freezeout ($x \simeq x_f$) , where the DM candidate A decouples, while B continues to decay. For smaller Γ_B, the co-moving number density remains constant for longer and the decays will begin later. Depending

on the size of Γ_B, the cross section needed to decouple at the correct time, and match the observed relic abundance, can be orders of magnitude larger than those of the WIMP scenario. The solutions to the Boltzmann equations match well the analytic estimates given by Eq. (6.11).

6.4 Signatures and constraints

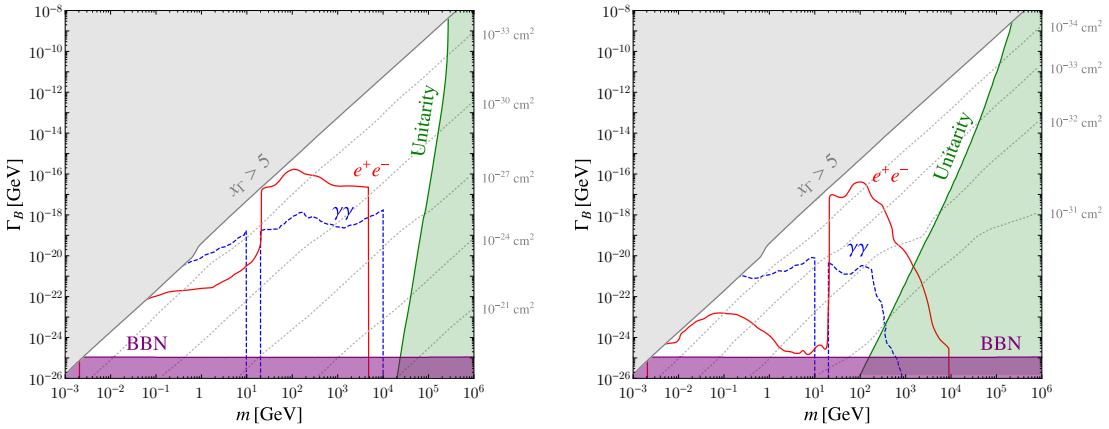

Figure 6.1: The viable parameter space for co-decaying dark matter assuming no cannibalization (**Left**), and a cannibalizing dark sector (**Right**). The central white region shows the range of validity of the model. The different regions show constraints from $N_{\rm eff}$ (**purple**); DM decays out of equilibrium (**gray**); unitarity constraints (**green**); and indirect detection assuming decays into e^+e^- (**red**/solid) or $\gamma\gamma$ (**blue**/dashed), excluding the region below the curve. The gap in the $\gamma\gamma$ limit between $10-20$ GeV is due to thresholds used in the two recasts. The **light gray** dotted lines represent contours of constant σ with values indicated on the right.

We now discuss the signatures and constraints of co-decaying dark matter , whose parameter space is characterized by m, Γ_B, and σ. The viable parameter space is summarized in Fig. 6.1, where the dotted gray lines represent contours of constant σ. As expected by the rough estimate in Eq. 6.11, the cross section contours are much more widely spaced without cannibalization than without.

First, the co-decay setup requires B to decay out of equilibrium; otherwise the dark matter candidate will be Boltzmann suppressed when it becomes non-relativistic, effectively reducing to the WIMP scenario. This corresponds to $x_\Gamma \gtrsim 1$, though requiring that the DM does not re-thermalize with the SM imposes $x_\Gamma \gtrsim 5$. This is depicted by the gray shaded area in Fig. 6.1.

Next we consider constraints on N_{eff} [29, 30]. This gives the rough condition that the DM decays before big bang nucleosynthesis (BBN), $\Gamma_B \gtrsim H_{m_e}$. This is depicted by the shaded purple regions in Fig. 6.1.

Unitarity places constraints on the size of the thermally averaged cross section. The requirement of unitarity is given for s-wave scattering by [31],

$$\langle \sigma v \rangle_f \leq \frac{4\pi \langle v^{-1} \rangle_f}{m^2} \quad \Longrightarrow \quad \sigma \lesssim \frac{\pi\sqrt{2}}{m^2} x'_f \,, \tag{6.15}$$

where $\langle v^{-1} \rangle_f \simeq \sqrt{2x'_f/\pi}$ is the thermally averaged inverse velocity. The severity of the bound is dependent on whether or not the dark sector is cannibalizing. Without cannibalization, fixing the relic density corresponds to $\sigma \propto 1/\Gamma_B$ and $x'_f \propto 1/\Gamma_B$, and thus the unitarity bound is roughly Γ_B-independent. On the other hand, with cannibalization, $\sigma \propto 1/\sqrt{\Gamma_B}$ and x'_f is only log-dependent on Γ_B, and the unitarity bound reads:

$$\frac{m}{100 \text{ TeV}} \lesssim \begin{cases} 1 & \text{(w/o canb)}, \\ 100 \left(\frac{\Gamma_B}{\text{GeV}}\right)^{1/6} & \text{(w/ canb)}\,. \end{cases} \tag{6.16}$$

These relations are modified for small Γ by matter-domination effects. The resulting unitarity bounds are shown in the green shaded regions in Fig. 6.1.

Since co-decaying DM is decoupled from the SM, it is difficult to discover using direct detection or direct production. The signature from indirect detection is, however, enhanced with respect to WIMP candidates due to the large thermally

averaged cross section. This makes indirect detection a powerful tool to probe co-decaying DM.

We map the current constraints from telescope and satellite data on the (m, Γ_B) parameter space, using the analyses of Refs. [32, 33].The constraint on our four-body final state from two-body final states analyzed in [32, 33] are obtained by rescaling the mass and cross-section limits appropriately. For illustration, we plot the full constraints from B decays into only e^+e^- (red, solid) or into only $\gamma\gamma$ (blue, dashed) in Fig. 6.1, excluding the region below the curves.

Lastly we note that co-decaying dark matter is not constrained by the Cosmic Microwave Background, since the thermally averaged cross-sections is always velocity suppressed.

The combined allowed parameter space is shown in Fig. 6.1, without cannibalization (left-panel) and with cannibalization (right-panel). We learn that co-decaying dark matter can occur over a broad range of DM masses, spanning an MeV up to hundreds of TeV, and decay rates spanning many orders of magnitude.

6.5 Mass splitting

Thus far, we focused on degenerate dark sector particles, which can result from an underlying symmetry. However, a realistic model may include symmetry-breaking effects, which can lift the degeneracy. It is then important to understand the effect of mass-splittings on the co-decaying DM framework. We leave a detailed study of the phenomenology of co-decays with mass splittings to future work [34] and highlight the expected features here.

If $m_A > m_B$, the co-decay mechanism remains conceptually unchanged. However, for mass splitting $\mathcal{O}(\%)$ or more, the parameter space to produce the observed relic abundance can differ significantly. To understand this, consider s-wave annihilation, which can proceed as zero temperature in the presence of mass-splittings. Comparing the annihilation rates at large x', we have

$$\langle \sigma v \rangle_{m_A > m_B} \simeq \frac{\sqrt{\pi x'}}{2} \langle \sigma v \rangle_{m_A = m_B} \tag{6.17}$$

for fixed matrix-element. Since freezeout occurs for $x' \gg 1$, obtaining the observed relic abundance requires σ smaller than in the degenerate case.

If $m_A < m_B$, then annihilations proceed off the exponential tail of A's velocity distribution, $\langle \sigma v \rangle_{AA \to BB} \propto e^{-2\Delta x'}$,, where $\Delta \equiv (m_B - m_A)/m_A$. This exponential suppression of the cross-section significantly alters the parameters required to produce the correct relic density.

6.6 Model

Having described the general framework, we now present a simple model where co-decay can drive dark matter freezeout. Consider a dark $\mathrm{SU}(2)_D$ gauge theory with coupling g_D, and a dark Higgs doublet Φ_D,

$$\mathcal{L} \supset D^\mu \Phi_D^\dagger D_\mu \Phi_D - \frac{1}{4} F_D^{a,\mu\nu} F^a_{D,\mu\nu} - \lambda_D \left(\Phi_D^\dagger \Phi_D - \frac{v_D^2}{2} \right)^2 , \tag{6.18}$$

The dark Higgs' VEV, $v_D/\sqrt{2}$, spontaneously breaks $\mathrm{SU}(2)_D$. All three dark gauge bosons acquire masses $m_D = \frac{1}{2} g_D v_D$, while the dark Higgs boson, h_D, gains a mass $m_{h_D} = \sqrt{2\lambda_D} v_D$. The stability and degeneracy of the gauge bosons are ensured by an unbroken SU(2) custodial symmetry. We take $m_{h_D} \gg m_D$, which decouples the dark Higgs.

We introduce a dimension-six operator, which explicitly breaks the custodial symmetry down to U(1),

$$\mathcal{L} \supset \frac{(\Phi_D^\dagger D^\mu \Phi_D)(\Phi^\dagger D_\mu \Phi)}{\Lambda^2}\,, \tag{6.19}$$

where Φ is the SM Higgs doublet. This can be generated by integrating out heavy fermions charged under both $\mathrm{SU}(2)_D$ and the SM gauge symmetry, $\mathrm{SU}(2)_L$. This operator mixes the gauge boson $Z_D \equiv W_D^3$ and the Z boson, decaying Z_D to the SM.The remaining gauge bosons $W_D^\pm \equiv (W_D^1 \mp i W_D^2)/\sqrt{2}$ are stable since they are the lightest particles charged under the unbroken U(1) custodial symmetry.

The $W_D^\pm$ are stable and play the role of A, while the nearly-degenerate Z_D plays the role of B. For $m_D \sim$ GeV and $\Lambda \sim 10$'s TeV, negligible mass differences between $W_D^\pm$ and Z_D are generated, and corrections to electroweak precision observables are small. Number-changing processes, e.g., $Z_D Z_D Z_D \to W_D^+ W_D^-$, are large and cannibalization effects must be taken into account.

This model can be mapped onto the constraints of the previous sections using

$$\sigma = \frac{688}{3}\frac{\alpha_D^2}{m_D^2}\,, \qquad \Gamma_{Z_D} = \frac{1}{48\pi^2}\frac{m_D^5}{\Lambda^4}|g|^2\,, \tag{6.20}$$

where $|g|^2 \equiv \sum_i |g_i|^2\,(|g_V^i|^2 + |g_A^i|^2)$, g_V (g_A) is the vector (axial) coupling of the fermion i to the Z-boson.

Lastly, we comment on further model building directions. To build a viable model one needs a approximate symmetry to achieve degeracy between the lightest dark states, but whose breaking induces a decay into the SM. In this section we considered the possibility that a remnant of a broken SU(2) gauge symmetry protects the masses, however interesting alternatives include flavor symmetries or supersymmetry, both of which could play a role in a larger framework. Depending

on the type of symmetry used to ensure the degenaracy, this may or may not induce significant cannibalization.

BIBLIOGRAPHY

[1] P. Cushman *et al.*, Working Group Report: WIMP Dark Matter Direct Detection, in *Proceedings, 2013 Community Summer Study on the Future of U.S. Particle Physics: Snowmass on the Mississippi (CSS2013): Minneapolis, MN, USA, July 29-August 6, 2013*, 2013, 1310.8327.

[2] LUX, D. S. Akerib *et al.*, Phys. Rev. Lett. **116**, 161301 (2016), 1512.03506.

[3] XENON, E. Aprile *et al.*, JCAP **1604**, 027 (2016), 1512.07501.

[4] A. Askew, S. Chauhan, B. Penning, W. Shepherd, and M. Tripathi, Int. J. Mod. Phys. **A29**, 1430041 (2014), 1406.5662.

[5] J. Buckley *et al.*, Working Group Report: WIMP Dark Matter Indirect Detection, in *Proceedings, Community Summer Study 2013: Snowmass on the Mississippi (CSS2013): Minneapolis, MN, USA, July 29-August 6, 2013*, 2013, 1310.7040.

[6] K. Griest and D. Seckel, Phys. Rev. **D43**, 3191 (1991).

[7] M. J. Baker *et al.*, JHEP **12**, 120 (2015), 1510.03434.

[8] M. Pospelov, A. Ritz, and M. B. Voloshin, Phys. Lett. **B662**, 53 (2008), 0711.4866.

[9] Y. Hochberg, E. Kuflik, T. Volansky, and J. G. Wacker, Phys. Rev. Lett. **113**, 171301 (2014), 1402.5143.

[10] Y. Hochberg, E. Kuflik, H. Murayama, T. Volansky, and J. G. Wacker, Phys. Rev. Lett. **115**, 021301 (2015), 1411.3727.

[11] D. Pappadopulo, J. T. Ruderman, and G. Trevisan, Phys. Rev. **D94**, 035005 (2016), 1602.04219.

[12] E. Kuflik, M. Perelstein, N. R.-L. Lorier, and Y.-D. Tsai, Phys. Rev. Lett. **116**, 221302 (2016), 1512.04545.

[13] N. Bernal and X. Chu, JCAP **1601**, 006 (2016), 1510.08527.

[14] N. Bernal, X. Chu, C. Garcia-Cely, T. Hambye, and B. Zaldivar, JCAP **1603**, 018 (2016), 1510.08063.

[15] E. D. Carlson, M. E. Machacek, and L. J. Hall, Astrophys. J. **398**, 43 (1992).

[16] M. Farina, D. Pappadopulo, J. T. Ruderman, and G. Trevisan, (2016), 1607.03108.

[17] R. T. D'Agnolo and J. T. Ruderman, Phys. Rev. Lett. **115**, 061301 (2015), 1505.07107.

[18] J. L. Feng, A. Rajaraman, and F. Takayama, Phys. Rev. Lett. **91**, 011302 (2003), hep-ph/0302215.

[19] M. Kaplinghat, Phys. Rev. **D72**, 063510 (2005), astro-ph/0507300.

[20] M. Farina, JCAP **1511**, 017 (2015), 1506.03520.

[21] T. Moroi and L. Randall, Nucl. Phys. **B570**, 455 (2000), hep-ph/9906527.

[22] B. S. Acharya, G. Kane, S. Watson, and P. Kumar, Phys. Rev. **D80**, 083529 (2009), 0908.2430.

[23] L. J. Hall, K. Jedamzik, J. March-Russell, and S. M. West, JHEP **03**, 080 (2010), 0911.1120.

[24] A. Berlin, D. Hooper, and G. Krnjaic, Phys. Lett. **B760**, 106 (2016), 1602.08490.

[25] D. E. Morrissey, D. Poland, and K. M. Zurek, JHEP **07**, 050 (2009), 0904.2567.

[26] T. Cohen, D. J. Phalen, A. Pierce, and K. M. Zurek, Phys. Rev. **D82**, 056001 (2010), 1005.1655.

[27] P. Bandyopadhyay, E. J. Chun, and J.-C. Park, JHEP **06**, 129 (2011), 1105.1652.

[28] Planck, P. A. R. Ade *et al.*, Astron. Astrophys. **594**, A13 (2016), 1502.01589.

[29] E. Di Valentino, S. Gariazzo, M. Gerbino, E. Giusarma, and O. Mena, Phys. Rev. **D93**, 083523 (2016), 1601.07557.

[30] C. Boehm, M. J. Dolan, and C. McCabe, JCAP **1308**, 041 (2013), 1303.6270.

[31] K. Griest and M. Kamionkowski, Phys. Rev. Lett. **64**, 615 (1990).

[32] R. Essig, E. Kuflik, S. D. McDermott, T. Volansky, and K. M. Zurek, JHEP **11**, 193 (2013), 1309.4091.

[33] G. Elor, N. L. Rodd, T. R. Slatyer, and W. Xue, JCAP **1606**, 024 (2016), 1511.08787.

[34] J. A. Dror, E. Kuflik, and W. H. Ng, (2016), to appear.

CHAPTER 7

SNEUTRINO HIGGS MODELS EXPLAIN LEPTON NON-UNIVERSALITY IN CMS EXCESSES

7.1 Introduction

The Standard Model (SM) of particle physics is among the most successful models ever devised, yet it leaves open several puzzles that should be resolved by a more complete description of nature. A well-motivated, broad class of models based on supersymmetry (SUSY) has the potential to resolve one or more of the outstanding puzzles of the SM, including the hierarchy problem, the nature of dark matter, the mechanism of baryogenesis, and the running of gauge couplings to a unified value. From a phenomenological point of view, however, there are several issues with models based on SUSY. In particular, the naive implementation of natural R-parity conserving MSSM requires a light spectrum of color-charged particles to which the experiments at the Large Hadron Collider (LHC) should have sensitivity, yet no hints of SUSY have been seen in the "standard candle" channels with Missing Transverse Energy [1]. Furthermore, a Higgs boson with mass 125 GeV is not generically reconciled with a natural spectrum of superpartners [2]. Both of these tensions hint at the possibility that, if natural SUSY describes our universe, then it may have an alternative structure.

The lack of observation at colliders has lead to the introduction of many variations of supersymmetry such as R-parity violating (RPV) [3–11] and R-symmetric supersymmetry [12–22, 22–33]. Constraints on SUSY, even in the context of RPV models, are already quite stringent [34–36]. These constraints are somewhat less restrictive in models with R-symmetric models due to the requirement of Dirac

gauginos [37]. In particular, this prevents same-sign lepton signatures that would be smoking gun indicators of physics Beyond the SM (BSM). An additional intriguing feature of such models is that they allow for the Higgs field to be identified with the superpartner of a left-handed electron [22, 38, 39][1]. In this unique framework, traditional LLE^c and LQD^c RPV effects are present but necessarily suppressed by the smallness of the Yukawa couplings. However, RPV effects appear due to a mixing between the electron doublet and the gauginos (such mixing has been previously used to put constraints of possible sneutrino VEVs [40]). Since the electron is singled out as the Higgs partner, such models have non-standard lepton flavor structure leading in general to an abundance of electrons in the final state. Furthermore as we will show, the requirement of nearly massless neutrinos requires the introduction of an R-symmetry.

The CMS experiment has recently seen hints of potential BSM physics at the $\sim 2.5\sigma$ level in three separate searches that appear to single out the first generation of leptons. Two of these analyses were optimized to look for pair production of leptoquarks. In one case, the leptoquarks decay to an $eejj$ final state, while in the other they decay to an $e\nu jj$ final state [41]. Both showed excesses hinting at a roughly 650 GeV leptoquark, at the 2.4σ and 2.6σ levels respectively. The excesses are not consistent with the only decay modes of the leptoquarks being ej and νj [41, 42]. The third search was optimized for a W_R decaying to an $eejj$ final state and saw a 2.8σ local excess for a resonance near 2.1 TeV [43]. However, the distributions of the excess do not appear to be consistent with those of a W_R [43]. Its important to note that the leptoquark searches did not see an excess in its high leptoquark mass bins. While not emphasized in earlier work, this puts serious limitations on new BSM signals attempting to explain the excess. No excesses

[1] In general this can be any lepton, but as we will discuss in section 7.2, the electron is the most natural choice.

were observed in the corresponding channels with muons [43, 44].

Several models have been constructed in order to explain this excess. Many of these models are supersymmetric in nature [45–50] (see [42, 51–61] for non-supersymmetric explanations). The vast majority of them do not attempt to explain the puzzling flavor structure of the observed excesses, but merely choose certain couplings to be larger then others. Standard tools for suppressing flavor-violating processes such as minimal flavor violation (MFV) [21] cannot explain a different coupling for the first and second generations. In MFV, such non-universal terms in the Lagrangian are suppressed by m_μ/m_τ. Furthermore, due to the presence of a heavy resonance, these models often predict an excess in the searches for higher mass leptoquarks, which has not been observed in the data.

In this paper, we investigate the possibility that supersymmetric models with the Higgs as a sneutrino could explain the excesses seen by CMS. The lepton flavor structure is naturally obtained within the context of such models. The complex SUSY spectrum yields a rich variety of decay modes, suppressing the number of events seen in individual channels and allowing such models to evade many constraints. Overall, this class of models provides a good fit for the current data, while making several new and testable predictions for the upcoming run of the LHC. The role of the leptoquarks in the model is played by a left-handed first-generation squark with R-parity violating decays, while the heavier ~ 2 TeV resonance is explained by gluino-squark production. The masses that give the best fit are an up squark mass of 810 GeV and a gluino mass of 1790 GeV. In addition to accounting for the excesses observed by CMS, this model addresses the lack of an excess when the set of cuts is optimized for higher mass leptoquarks. The model considered in this paper addresses this potential issue by softening the

"leptoquark" spectrum with additional jets, as proposed in [60].

The remainder of this paper is structured as follows. In Section 2, we review the minimal model with the Higgs as a sneutrino. We determine a set of parameters of this model that provide a good fit to the current CMS data in Section 3. We then conclude discussing current bounds on the model and provide additional predictions.

7.2 Model with Higgs as a slepton

7.2.1 Overview

To illustrate the main ideas behind the Higgs-as-slepton model [38], we begin by attempting to construct a supersymmetric Standard Model that is more minimal than the MSSM. One can identify the SM Higgs doublet H with a slepton doublet $\tilde{L}_a$, since they are both in the same gauge representation $(1,2)_{-1/2}$. The model then requires two fewer doublet chiral superfields than the MSSM. However, a major issue arises from the fact that the Kähler potential generates electroweak-scale Dirac masses between the partner leptons $L_a \equiv (\nu_a, l_a^-)$ and the Winos and Binos:

$$\mathcal{L} \supset -\frac{g v_H}{\sqrt{2}} l_a^- \tilde{W}^+ - \frac{g v_H}{2} \nu_a \tilde{W}^0 + \frac{g' v_H}{2} \nu_a \tilde{B} + \text{h.c.} \tag{7.1}$$

This leads to neutrino masses that are too large.

One way around this difficulty is to first impose a $U(1)_R$ symmetry, with R-charge zero for the slepton doublet $\tilde{L}_a$ and -1 for the partner lepton doublet L_a. The $U(1)_R$ symmetry remains unbroken when $\tilde{L}_a$ acquires a VEV, and can

	$SU(3)_C \times SU(2)_L \times U(1)_Y$	$U(1)_R$
$H \equiv L_3$	$(1,2)_{-1/2}$	0
E_3^c	$(1,1)_1$	2
$L_{1,2}$	$(1,2)_{-1/2}$	$1-L$
$E_{1,2}^c$	$(1,1)_1$	$1+L$
$Q_{1,2,3}$	$(3,2)_{1/6}$	$1+B$
$U_{1,2,3}^c$	$(\bar{3},1)_{-2/3}$	$1-B$
$D_{1,2,3}^c$	$(\bar{3},1)_{1/3}$	$1-B$
$W^{a\alpha}$	$(8,1)_0 + (1,3)_0 + (1,1)_0$	1
Φ^a	$(8,1)_0 + (1,3)_0 + (1,1)_0$	0

Table 7.1: Superfields and their gauge and $U(1)_R$ representations in the Higgs-as-slepton model.

still forbid Majorana masses for all $U(1)_R$-charged neutralinos. By introducing adjoint chiral superfields Φ and SUSY-breaking Dirac gaugino masses, one of the neutralino mass eigenstates becomes massless. This massless neutralino is mainly comprised of ν_a and can be identified with the "physical" neutrino.

We now present the details of the model. Table 7.1 lists all the superfields and their gauge and $U(1)_R$ representations. With the CMS excesses in mind, we have chosen the first-generation leptons to partner the Higgs. This will give rise to experimental signatures specific to the electron, without the need to tweak any lepton couplings. B and L are arbitrary parameters that determine the $U(1)_R$ representations of the quark and the 2nd- and 3rd-generation lepton superfields.

The most general superpotential consistent with the symmetries (assuming $B \neq 1/3$ and $L \neq 1$) is

$$\mathcal{W} = \sum_{i,j=1}^{3} y_{d,ij} H Q_i D_j^c + \sum_{i=1}^{2} y_{e,i} H L_i E_i^c. \tag{7.2}$$

We have chosen to work in the mass basis of the charged leptons. The superpotential does not generate up-type quark masses due to the absence of an up-type Higgs superfield H_u. The same is true for the electron mass, since the required

term HHE_3^c is identically zero. Both can be generated by SUSY-breaking Kähler terms of the form [38]

$$\int d^2\theta d^2\bar{\theta} \frac{X^\dagger}{M} \frac{H^\dagger Q_i U_j^c}{\Lambda} \tag{7.3}$$

and

$$\int d^2\theta d^2\bar{\theta} \frac{X^\dagger X}{M^2} \frac{H D^\alpha H D_\alpha E_e^c}{\Lambda^2} \tag{7.4}$$

that are suppressed by a Λ cutoff scale. This also provides a natural explanation for the smallness of the electron mass, hence further motivating our decision to partner the first-generation leptons with the Higgs.

The $U(1)_R$ symmetry forbids mixing between left-handed and right-handed squarks, so the squark phenomenology differs from that of the MSSM [25]. This also simplifies our subsequent analysis of squark production and decay since the squark mass eigenstates are then either left- or right-handed.

We note that the terms in the superpotential can also be interpreted as RPV terms of the form $L_3 Q_i D_j^c$ and $L_3 L_i E_j^c$. Therefore, experimental bounds on RPV coefficients [63] can be applied to the superpotential Yukawas $y_{d,ij}$ and $y_{e,ij}$, which are in turn determined by the SM fermion masses and mixings. We find that these bounds are satisfied by the model for the choices of squark masses to be used in later sections.

While we assume the model described above in this work, our results are largely independent of the detailed mechanism giving the up-type quark and electron masses. Alternative models which introduce additional chiral superfields are also possible [22, 39] and can also produce similar signatures.

7.2.2 Chargino and neutralino mass matrices and mixing

The chargino and neutralino Dirac mass matrices are given by

$$\mathcal{M}_C = \begin{array}{c} \\ \tilde{W}^- \\ \psi^-_{\tilde{W}} \\ e^-_L \end{array} \begin{array}{c} \begin{array}{ccc} \tilde{W}^+ & \psi^+_{\tilde{W}} & e^{c+}_R \end{array} \\ \begin{pmatrix} 0 & M_{\tilde{W}} & 0 \\ M_{\tilde{W}} & 0 & 0 \\ \frac{gv_H}{\sqrt{2}} & 0 & 0 \end{pmatrix} \end{array}, \quad \mathcal{M}_N = \begin{array}{c} \\ \psi_{\tilde{B}} \\ \psi^0_{\tilde{W}} \\ \nu_e \end{array} \begin{array}{c} \begin{array}{cc} \tilde{B} & \tilde{W}^0 \end{array} \\ \begin{pmatrix} M_{\tilde{B}} & 0 \\ 0 & M_{\tilde{W}} \\ -\frac{g'v_H}{2} & \frac{gv_H}{2} \end{pmatrix} \end{array} \tag{7.5}$$

We have neglected the masses from Λ-suppressed SUSY-breaking terms such as electron masses, since they are much smaller than the present terms and hence not expected to play an important role. To order $\epsilon \equiv gv_H/(2M_{\tilde{W}}) = m_W/M_{\tilde{W}}$, the chargino 4 component mass eigenstates are:

$$\chi^-_1 = \begin{pmatrix} -\sqrt{2}\epsilon\psi^-_{\tilde{W}} + e^-_L \\ e^-_R \end{pmatrix}, \quad \chi^-_2 = \begin{pmatrix} \tilde{W}^- \\ \psi^{+\,c}_{\tilde{W}} \end{pmatrix}, \quad \chi^-_3 = \begin{pmatrix} \psi^-_{\tilde{W}} + \sqrt{2}\epsilon e^-_L \\ \tilde{W}^{+\,c} \end{pmatrix} \tag{7.6}$$

with mass eigenvalues $m_{\chi^-_1} = 0$ and $m_{\chi^-_2} = m_{\chi^-_3} = M_{\tilde{W}}$. The mass eigenstates for the neutralinos are[2] :

$$\chi^0_1 = \begin{pmatrix} \frac{g'}{g}\frac{M_{\tilde{W}}}{M_{\tilde{B}}}\epsilon\psi_{\tilde{B}} - \epsilon\psi^0_{\tilde{W}} + \nu_e \\ 0 \end{pmatrix}, \quad \chi^0_2 = \begin{pmatrix} \psi^0_{\tilde{W}} + \epsilon\nu_e \\ \tilde{W}^{0\,c} \end{pmatrix}, \quad \chi^0_3 = \begin{pmatrix} \psi_{\tilde{B}} - \frac{g'}{g}\frac{M_{\tilde{W}}}{M_{\tilde{B}}}\epsilon\nu_e \\ \tilde{B}^c \end{pmatrix} \tag{7.7}$$

with mass eigenvalues $m_{\chi^0_1} = 0$, $m_{\chi^0_2} = M_{\tilde{W}}$ and $m_{\chi^0_3} = M_{\tilde{B}}$.

χ^-_1 can be identified with the physical electron, and χ^0_1 with the "physical" electron neutrino, before PMNS mixing. We note that the gauge couplings of the

[2]We have assumed here that $\left|M^2_{\tilde{W}} - M^2_{\tilde{B}}\right| \gg m^2_W$. In the converse case where $\left|M^2_{\tilde{W}} - M^2_{\tilde{B}}\right| \ll m^2_W$, the actual heavy neutralino eigenstates are linear superpositions of χ^0_2 and χ^0_3 above, with mixings given by the Weinberg angle θ_W. Nonetheless, this does not affect any of our subsequent results on the partial widths.

physical gauginos and first-generation leptons to $W^{\pm}$ and Z are affected by the $O(\epsilon)$ mixing. One consequence is that the eeZ coupling is modified, hence violating lepton flavour universality. This allows us to place a lower bound of $\sim 2\,\mathrm{TeV}$ on the Dirac chargino mass $M_{\tilde{W}}$ [38]. Another consequence is that the modified gauge couplings mix the physical gauginos and leptons, thus providing a channel for the gauginos to decay completely to SM particles, e.g. $\chi_2^0 \to \chi_1^- W^+$. Should the squarks be lighter than the gauginos, which we assume in the rest of this work, virtual cascades such as $\tilde{d}_L \to d\,\overline{\chi_2^0}^* \to d\,\overline{\chi_1^-}\,W^-$ may also become important decay channels for the first-generation squarks, as we will see below.

7.2.3 First-generation left-handed squark decays

In MSSM with RPV, supersymmetric particles can decay completely to SM particles through channels generated by RPV superpotential and soft SUSY-breaking terms. While this is also true for the Higgs-as-slepton model, there are new decay channels due to the mixing of physical gauginos and leptons by the modified gauge couplings. A typical diagram for the new channel is shown in Fig. 7.1. The new channels are especially important for first-generation squarks compared to the standard RPV channels, due to the smallness of the Yukawas in the latter [38]. The approximate partial widths of these channels for first-generation LH squarks are shown in Table 7.2. Fig. 7.2 compares the partial widths of the mixing-induced and standard RPV channels for $\tilde{d}_L$ decay, from which we see that the former is dominant except for very large values of $M_{\tilde{W}}$.

Supersymmetric particles (and the Higgs) can also decay into SM particles + the gravitino, which is the lightest supersymmetric particle (LSP) in the model. The decay occurs via goldstino interaction terms fixed by supersymmetry, with

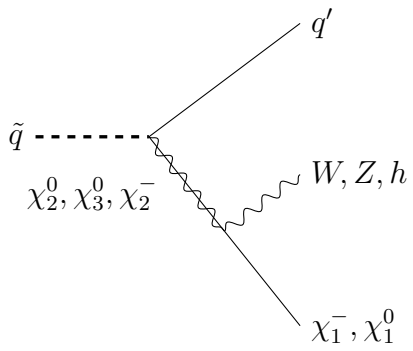

Figure 7.1: Mixing-induced decay channels in which a supersymmetric particle $\tilde{q}_L$ decays completely to SM particles.

Decay channel	Partial width$\Gamma, /(\frac{1}{6144\pi^3})$
$\tilde{u}_L \to d\,\overline{\chi_1^-}\,h^0$	$m_{\tilde{u}}^5 g^4/M_{\tilde{W}}^4 \times 1/2$
$\tilde{u}_L \to d\,\overline{\chi_1^-}\,Z$	$m_{\tilde{u}}^5 g^4/M_{\tilde{W}}^4 \times 1/2$
$\tilde{d}_L \to u\,\overline{\chi_1^0}\,W^-$	$m_{\tilde{d}}^5 g^4/M_{\tilde{W}}^4$
$\tilde{u}_L \to u\,\overline{\chi_1^-}\,W^-$	$m_{\tilde{u}}^5 \left[g'^2 Y_Q/M_{\tilde{B}}^2 + g^2/(2M_{\tilde{W}}^2)\right]^2$
$\tilde{d}_L \to d\,\overline{\chi_1^0}\,h^0$	$m_{\tilde{d}}^5 \left[g'^2 Y_Q/M_{\tilde{B}}^2 + g^2/(2M_{\tilde{W}}^2)\right]^2 \times 1/2$
$\tilde{d}_L \to d\,\overline{\chi_1^0}\,Z$	$m_{\tilde{d}}^5 \left[g'^2 Y_Q/M_{\tilde{B}}^2 + g^2/(2M_{\tilde{W}}^2)\right]^2 \times 1/2$
$\tilde{u}_L \to u\,\overline{\chi_1^0}\,h^0$	$m_{\tilde{u}}^5 \left[g'^2 Y_Q/M_{\tilde{B}}^2 - g^2/(2M_{\tilde{W}}^2)\right]^2 \times 1/2$
$\tilde{u}_L \to u\,\overline{\chi_1^0}\,Z$	$m_{\tilde{u}}^5 \left[g'^2 Y_Q/M_{\tilde{B}}^2 - g^2/(2M_{\tilde{W}}^2)\right]^2 \times 1/2$
$\tilde{d}_L \to d\,\overline{\chi_1^-}\,W^-$	$m_{\tilde{d}}^5 \left[g'^2 Y_Q/M_{\tilde{B}}^2 - g^2/(2M_{\tilde{W}}^2)\right]^2$

Table 7.2: Partial widths for the mixing-induced decay channels. Here χ_1^- and χ_1^0 refer to the physical electron and electron neutrino. Y_Q is the hypercharge of the LH quark doublet. The decay channels have been arranged such that the approximate isospin symmetry from the Goldstone boson equivalence theorem is obvious.

partial widths that typically scale as $m_{\rm sp}^5/(m_{3/2}M_{\rm Pl})^2$, where $m_{\rm sp}$ is the sparticle mass, $m_{3/2}$ the gravitino mass and $M_{\rm Pl}$ the Planck scale [38]. However, as long as the gravitino mass is not too small ($m_{3/2} \gg 1\,\text{eV}$), these decays are expected to be sub-dominant and can hence be neglected. For the rest of this work, we assume all first-generation squarks to decay via the mixing-induced decay channels.

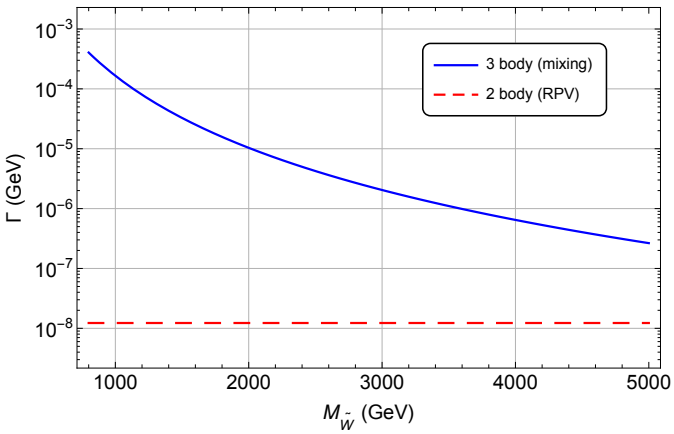

Figure 7.2: Partial widths of $\tilde{d}_L$ for mixing-induced and standard RPV decay channels, assuming $m_{\tilde{d}} = 810\,\text{GeV}$ and $M_{\tilde{B}} = M_{\tilde{W}}$. The mixing-induced channel dominates over the range of $M_{\tilde{W}}$ considered.

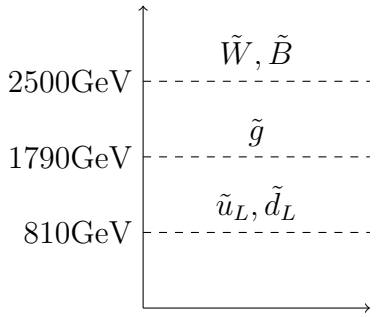

Figure 7.1: The spectrum of our benchmark point. All other fields are decoupled.

7.3 Simulation and Results

In this section, we estimate the contribution of the above model to the CMS leptoquark and W_R searches. The spectrum and production channels of interest are depicted in figures 7.1 and 7.2.

The model predictions are calculated at tree level using Madgraph [64], Pythia 6.4 [40] for showering and hadronization, and PGS [41] for detector simulation. The model files were created using Feynrules [67]. To estimate the next-to-leading order (NLO effects we scaled the cross-sections by their corresponding K-factors

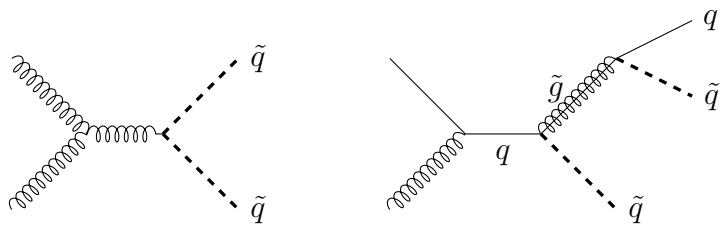

Figure 7.2: Sample production mechanisms for disquark and single gluino production channels. Squarks decay through the 3 body decay shown in figure 7.1.

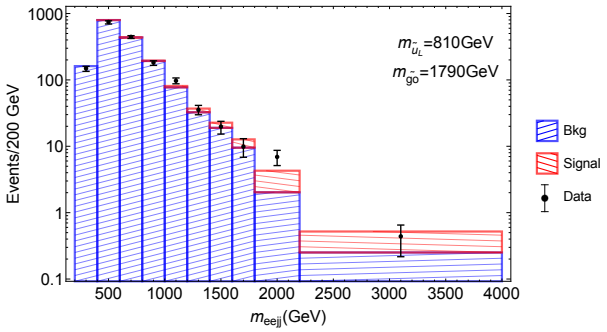

Figure 7.3: The m_{eejj} prediction for our model after applying cuts used in the W_R search. The background and relevant cuts were taken from [43].

calculated using Prospino 2.1 [68]. While Prospino was designed for the MSSM we do not expect significant deviations in the calculations of K-factors.

The W_R search distribution is shown in figure 7.3. We reproduce the invariant mass distribution of the two leading electrons and two leading jets. We also applied all the relevant cuts detailed by CMS in Ref. [43], the most restrictive requiring the invariant mass of the electrons be greater then 200GeV.

The single gluino production dominates the high mass peak, while the disquark channel contributes broadly to the bins between $1 - 2$ TeV. The broad feature is a consequence of a many-body structure of the decay which, and as pointed out in [60], is useful to evade bounds by the CMS leptoquark search without introducing multiple decay channels. We emphasize that in our model we satisfy both properties of the signal. Firstly, no signal is found in corresponding muon channels

as only the electron doublet mixes with the other neutralinos and charginos in this framework. Secondly, the events are dominated by opposite-sign electrons. This is guaranteed by the imposed R symmetry for which an electron and positron have opposite charges.

Next we reproduce the leptoquark (LQ) searches in this framework. In the LQ search a sequence of more stringent cuts are applied, optimized for different mass leptoquarks. In the $eejj$ channel, the main discriminating variables are S_T (the scalar sum of p_T of two leading electrons and jets), m_{ee} (invariant mass of the two electrons), and m_{ej}^{min} (the minimum of the electron-jet invariant mass of the four possible combinations for $eejj$). In the $e\nu jj$ channel, the main discriminating variables are S_T, E_T^{miss}, and m_{ej}. Typically models that predict large m_{eejj} (in order to explain the W_R excess) will also produce large S_T (and m_{ej}^{min} unless they arise from a very light LQ). In general, this leads to expected excess in the heavy LQ mass cut range. Thus it is important to check the predictions of any model attempting to explain the flavor violating anomalies in these high mass bins.

The corresponding cuts for each LQ mass can be found in [41] (see tables 2 and 3). Here we plot the difference between the data and the SM background as a function of LQ mass cut. The results are shown in Fig. 7.4. Each bin is a fraction of the events in the lower LQ mass cut bin and thus the bins are highly correlated. We see moderate agreement of our signal with the observed counts. We are able to explain the excess in the $\sim$ 650GeV region, but see small excess in the higher mass cuts for $eejj$. The excess in the high mass range is a general characteristic of trying to explain both the W_R and LQ searches. Note that the excess is $\mathcal{O}(5)$ events instead of $\mathcal{O}(10)$ which were found in the W_R search. This is a consequence of the large number of jets increasing the effectiveness of the S_T cut.

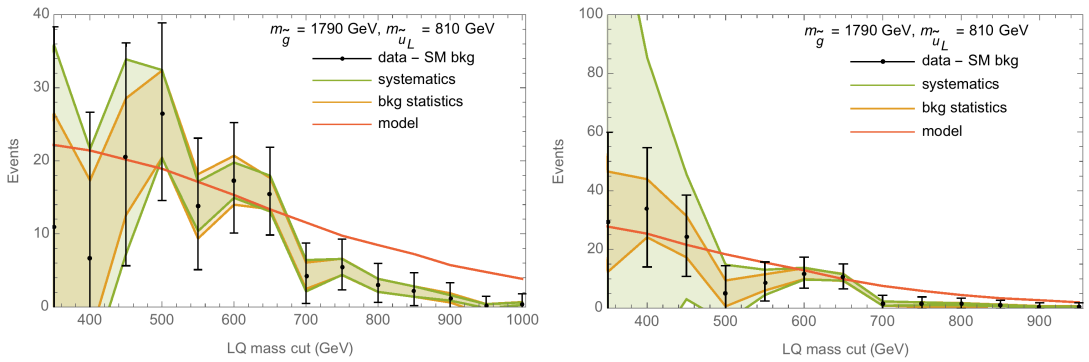

(a) $eejj$ search (b) $e\nu jj$ search

Figure 7.4: Bin-by-bin background-subtracted events for the LQ searches. Each bin count is a subset of the previous bin and hence the bins are highly correlated. The model shows some tension with the data at high LQ mass cuts.

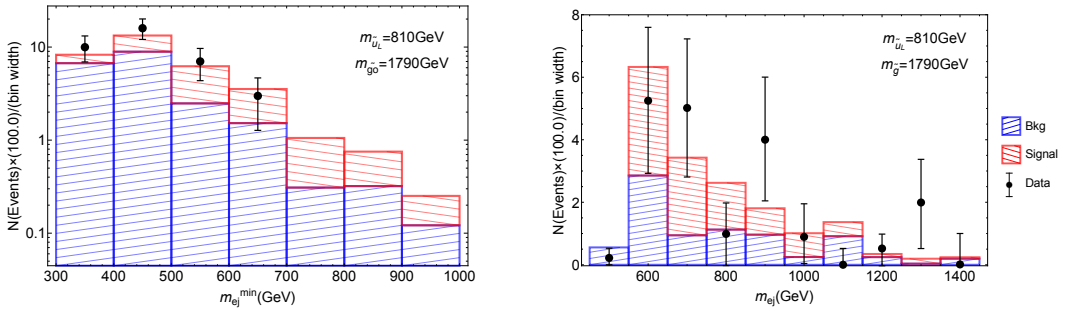

(a) $eejj$ search (figure 5 in [41]) (b) $e\nu jj$ search (figure 8 in [41])

Figure 7.5: The CMS leptoquark search plots.

To further check the kinematic properties of the model we compare our m_{ej}^{min} and m_{ej} distributions at the 650 GeV mass cut point. The results for both searches are shown in figure 7.5. In both the $eejj$ and $e\nu jj$ channel we see good agreement between the model and experiment. The broad feature of the plots is again a consequence of the many jet signal and is necessary to get the right kinematic spread in the LQ invariant mass distributions.

This framework has two characteristic features - many electrons in the final state and many jets. Due to their limited background, we expect the most stringent bounds on our model arise from multilepton searches [69, 70]. The model produces

more than 2 leptons if each squark decays into an electron and additional leptons arise from vector boson decays. We now roughly estimate the number of expected events in the multilepton searches. The NLO cross section for squark-squark and squark-gluino production at our mass point is 5.7 fb. At $\mathcal{L} \sim 20$ fb^{-1} this corresponds to about 115 events. The probability of both squarks producing electrons (as opposed to neutrinos) is about 1/4. Furthermore, the probability of at least one of the vector bosons decaying leptonically is between 11 and 40% depending on whether there is a WW, WZ, or ZZ is in the final state. This suggests $5 - 10$ events with 3 or more leptons. However, these events don't contain any genuine E_T^{miss} or b-tagged jets, both of which are powerful discrimating variables in such searches. This makes the signal hard to detect, even in a multilepton search. Thus we conclude the model is safe from current multilepton bounds, though we expect sensitivity with more data at higher energies.

7.4 Discussion and Conclusions

In this paper, we have explored the phenomenology of a class of SUSY models in which the Higgs is a sneutrino. Such models could account for excesses seen in the CMS experiment, while accounting for the observed kinematics and flavor structure in a natural way.

As with most SUSY models, several correlated observables are expected. While the detailed spectrum and branching fractions are model-dependent, these models have a few generic predictions. Most reliably, there should be correlated excesses in multi-lepton searches. Since the decay of hadronic sparticles necessarily proceeds via electroweakinos, the decays will generally feature leptons, possibly in

large numbers and with a preference for electrons. These excesses would come with some missing energy from neutrinos, but decays without neutrinos are certainly possible. The flavor structure of these excesses would again be striking, featuring more electrons than muons or taus. The scales of $\lesssim 1600$ GeV from $\tilde{q}\tilde{q}^*$, $\lesssim 2400$ GeV from $\tilde{q}\tilde{g}$, and $\lesssim 3600$ GeV from $\tilde{g}\tilde{g}$ would also feature in the total invariant (transverse) mass distribution.

The remaining signals are highly dependent on the more weakly coupled or heavier elements of the spectrum. The constraints on sleptons and electroweakinos remain weak after Run 1 of the LHC, but searches for signatures of new electroweak states are a vital part of Run 2 that can only be fully exploited at high luminosity. Such particles with mass $\mathcal{O}(100$ GeV) could be in the spectrum and would decay primarily to elecrtoweak bosons, electrons, and neutrinos.

The first run of the LHC has seen a remarkable confirmation of the SM with few searches finding excesses beyond the 2σ level. On the other hand, several searches that have seen excesses indicate similar final states with electrons and jets, as well as large energy scales of ~ 650 GeV and ~ 2 TeV. If such excesses are the first hints of a new state beyond the SM, then Run 2 will bring striking and nearly immediate discoveries, as the sensitivity to physics at ~ 2 TeV is vastly superor to that in the first run.

BIBLIOGRAPHY

[1] N. Craig, *The State of Supersymmetry after Run I of the LHC*, arXiv:1309.0528.

[2] L. J. Hall, D. Pinner, and J. T. Ruderman, *A Natural SUSY Higgs Near 126 GeV*, *JHEP* **1204** (2012) 131, [arXiv:1112.2703].

[3] E. Nikolidakis and C. Smith, *Minimal Flavor Violation, Seesaw, and R-parity*, *Phys.Rev.* **D77** (2008) 015021, [arXiv:0710.3129].

[4] C. Csaki, Y. Grossman, and B. Heidenreich, *MFV SUSY: A Natural Theory for R-Parity Violation*, *Phys.Rev.* **D85** (2012) 095009, [arXiv:1111.1239].

[5] B. Bhattacherjee, J. L. Evans, M. Ibe, S. Matsumoto, and T. T. Yanagida, *Natural supersymmetrys last hope: R-parity violation via UDD operators*, *Phys.Rev.* **D87** (2013), no. 11 115002, [arXiv:1301.2336].

[6] C. Csaki and B. Heidenreich, *A Complete Model for R-parity Violation*, *Phys.Rev.* **D88** (2013) 055023, [arXiv:1302.0004].

[7] R. Franceschini and R. Mohapatra, *New Patterns of Natural R-Parity Violation with Supersymmetric Gauged Flavor*, *JHEP* **1304** (2013) 098, [arXiv:1301.3637].

[8] G. Krnjaic and Y. Tsai, *Soft RPV Through the Baryon Portal*, *JHEP* **1403** (2014) 104, [arXiv:1304.7004].

[9] A. Monteux, *Natural, R-parity violating supersymmetry and horizontal flavor symmetries*, *Phys.Rev.* **D88** (2013) 045029, [arXiv:1305.2921].

[10] L. Di Luzio, M. Nardecchia, and A. Romanino, *Framework for baryonic R-parity violation in grand unified theories*, *Phys.Rev.* **D88** (2013), no. 11 115008, [arXiv:1305.7034].

[11] C. Csaki, E. Kuflik, and T. Volansky, *Dynamical R-Parity Violation*, *Phys.Rev.Lett.* **112** (2014) 131801, [arXiv:1309.5957].

[12] G. D. Kribs, E. Poppitz, and N. Weiner, *Flavor in supersymmetry with an extended R-symmetry*, *Phys.Rev.* **D78** (2008) 055010, [arXiv:0712.2039].

[13] K. Benakli and M. Goodsell, *Dirac Gauginos in General Gauge Mediation*, *Nucl.Phys.* **B816** (2009) 185–203, [arXiv:0811.4409].

[14] S. D. L. Amigo, A. E. Blechman, P. J. Fox, and E. Poppitz, *R-symmetric gauge mediation*, *JHEP* **0901** (2009) 018, [arXiv:0809.1112].

[15] K. Benakli, *Dirac Gauginos: A User Manual*, *Fortsch.Phys.* **59** (2011) 1079–1082, [arXiv:1106.1649].

[16] K. Benakli, M. D. Goodsell, and A.-K. Maier, *Generating mu and Bmu in models with Dirac Gauginos*, *Nucl.Phys.* **B851** (2011) 445–461, [arXiv:1104.2695].

[17] M. Heikinheimo, M. Kellerstein, and V. Sanz, *How Many Supersymmetries?*, *JHEP* **1204** (2012) 043, [arXiv:1111.4322].

[18] R. Davies and M. McCullough, *Small neutrino masses due to R-symmetry breaking for a small cosmological constant*, *Phys.Rev.* **D86** (2012) 025014, [arXiv:1111.2361].

[19] P. Kumar and E. Ponton, *Electroweak Baryogenesis and Dark Matter with an approximate R-symmetry*, *JHEP* **1111** (2011) 037, [arXiv:1107.1719].

[20] R. Fok, G. D. Kribs, A. Martin, and Y. Tsai, *Electroweak Baryogenesis in R-symmetric Supersymmetry*, *Phys.Rev.* **D87** (2013), no. 5 055018, [arXiv:1208.2784].

[21] J. Kalinowski, *R-symmetric supersymmetric Higgs bosons at the LHC*, *Acta Phys.Polon.* **B42** (2011) 1419–1426.

[22] C. Frugiuele and T. Gregoire, *Making the Sneutrino a Higgs with a $U(1)_R$ Lepton Number*, *Phys. Rev. D.* (2011).

[23] S. Chakraborty and S. Roy, *Higgs boson mass, neutrino masses and mixing and keV dark matter in an $U(1)_R-$ lepton number model*, *JHEP* **1401** (2014) 101, [arXiv:1309.6538].

[24] Y. Morita, H. Nakano, and T. Shimomura, *Neutrino Mass and Proton Decay in a $U(1)_R$ Symmetric Model*, *PTEP* **2013** (2013) 053B02, [arXiv:1212.4304].

[25] C. Frugiuele, T. Gregoire, P. Kumar, and E. Ponton, *"$L = R$" - $U(1)_R$ lepton number at the LHC*, *JHEP* **05** (2013) 012, [arXiv:1210.5257].

[26] J. Kalinowski, *Higgs bosons of R-symmetric supersymmetric theories*, *PoS* **EPS-HEP2011** (2011) 265.

[27] J. Kalinowski, *Phenomenology of R-symmetric supersymmetry*, *Acta Phys.Polon.* **B42** (2011) 2425–2432.

[28] P. Diener, J. Kalinowski, W. Kotlarski, and D. Stckinger, *Higgs boson mass and electroweak observables in the MRSSM*, *JHEP* **1412** (2014) 124, [arXiv:1410.4791].

[29] S. J. De Lope Amigo, *R-symmetry, Gauge Mediation and Decaying Dark Matter*, .

[30] G. D. Kribs and N. Raj, *Mixed Gauginos Sending Mixed Messages to the LHC*, *Phys.Rev.* **D89** (2014), no. 5 055011, [arXiv:1307.7197].

[31] K. Benakli, M. D. Goodsell, and F. Staub, *Dirac Gauginos and the 125 GeV Higgs*, *JHEP* **1306** (2013) 073, [arXiv:1211.0552].

[32] C. Csaki, J. Goodman, R. Pavesi, and Y. Shirman, *The $m_D - b_M$ problem of Dirac gauginos and its solutions*, *Phys.Rev.* **D89** (2014), no. 5 055005, [arXiv:1310.4504].

[33] R. Fok and G. D. Kribs, *μ to e in R-symmetric Supersymmetry*, *Phys.Rev.* **D82** (2010) 035010, [arXiv:1004.0556].

[34] M. Asano, K. Rolbiecki, and K. Sakurai, *Can R-parity violation hide vanilla supersymmetry at the LHC?*, *JHEP* **1301** (2013) 128, [arXiv:1209.5778].

[35] Z. Han, A. Katz, M. Son, and B. Tweedie, *Boosting searches for natural supersymmetry with R-parity violation via gluino cascades*, *Phys.Rev.* **D87** (2013), no. 7 075003, [arXiv:1211.4025].

[36] J. Berger, M. Perelstein, M. Saelim, and P. Tanedo, *The Same-Sign Dilepton Signature of RPV/MFV SUSY*, *JHEP* **1304** (2013) 077, [arXiv:1302.2146].

[37] P. J. Fox, A. E. Nelson, and N. Weiner, *Dirac gaugino masses and supersoft supersymmetry breaking*, *JHEP* **0208** (2002) 035, [hep-ph/0206096].

[38] F. Riva, C. Biggio, and A. Pomarol, *Is the* $125\,GeV$ *Higgs the superpartner of the neutrino?*, *Journal of High Energy Physics* (2012).

[39] C. Frugiuele and T. Gregoire, *Fitting Neutrino Physics with a* $U(1)_R$ *Lepton Number*, *JHEP* (2012).

[40] D. Brahm, L. J. Hall, and S. D. H. Hsu, *Ruling out large sneutrino vacuum expectation values*, *Phys. Rev. D* **42** (1990) 1860–1862.

[41] **CMS** Collaboration, C. Collaboration, *Search for Pair-production of First Generation Scalar Leptoquarks in pp Collisions at sqrt s = 8 TeV*, .

[42] Y. Bai and J. Berger, *Coloron-assisted Leptoquarks at the LHC*, *Phys.Lett.* **B746** (2015) 32–36, [arXiv:1407.4466].

[43] **CMS Collaboration** Collaboration, V. Khachatryan et al., *Search for heavy neutrinos and W bosons with right-handed couplings in proton-proton collisions at* $\sqrt{s} = 8$ *TeV*, arXiv:1407.3683.

[44] **CMS Collaboration** Collaboration, *Search for Pair-production of Second generation Leptoquarks in 8 TeV proton-proton collisions.*, Tech. Rep. CMS-PAS-EXO-12-042, CERN, Geneva, 2013.

[45] E. J. Chun, S. Jung, H. M. Lee, and S. C. Park, *Stop and Sbottom LSP with R-parity Violation*, *Phys.Rev.* **D90** (2014), no. 11 115023, [arXiv:1408.4508].

[46] B. Allanach, S. Biswas, S. Mondal, and M. Mitra, *Resonant slepton production yields CMS* $eejj$ *and* ep_Tjj *excesses*, *Phys.Rev.* **D91** (2015), no. 1 015011, [arXiv:1410.5947].

[47] S. Biswas, D. Chowdhury, S. Han, and S. J. Lee, *Explaining the lepton non-universality at the LHCb and CMS within a unified framework*, *JHEP* **1502** (2015) 142, [arXiv:1409.0882].

[48] B. Allanach, S. Biswas, S. Mondal, and M. Mitra, *Explaining a CMS* $eejj$ *Excess With* $\mathcal{R}-$*parity Violating Supersymmetry and Implications for Neutrinoless Double Beta Decay*, *Phys.Rev.* **D91** (2015), no. 1 011702, [arXiv:1408.5439].

[49] M. Dhuria, C. Hati, R. Rangarajan, and U. Sarkar, *Explaining the CMS* $eejj$

and e missing p_T jj *excess and leptogenesis in superstring inspired* E_6 *models*, *Phys.Rev.* **D91** (2015), no. 5 055010, [arXiv:1501.04815].

[50] B. A. Ovrut, A. Purves, and S. Spinner, *The Minimal SUSY* $B - L$ *Model: From the Unification Scale to the LHC*, arXiv:1503.01473.

[51] B. A. Dobrescu and Z. Liu, *A* W' *boson near 2 TeV: predictions for Run 2 of the LHC*, arXiv:1506.06736.

[52] B. A. Dobrescu, *Leptophobic boson signals with leptons, jets and missing energy*, arXiv:1506.04435.

[53] C. Englert, P. Harris, M. Spannowsky, and M. Takeuchi, *Unitarity-controlled resonances after Higgs discovery*, arXiv:1503.07459.

[54] B. Allanach, A. Alves, F. S. Queiroz, K. Sinha, and A. Strumia, *Interpreting the CMS* $\ell^+\ell^- jj\not{E}_T$ *Excess with a Leptoquark Model*, arXiv:1501.03494.

[55] J. L. Evans and N. Nagata, *Signatures of Leptoquarks at the LHC and Right-handed Neutrinos*, arXiv:1505.00513.

[56] J. Gluza and T. Jelinski, *Heavy neutrinos and the* $pp \to lljj$ *CMS data*, arXiv:1504.05568.

[57] M. Dhuria, C. Hati, R. Rangarajan, and U. Sarkar, *Falsifying leptogenesis for a TeV scale* $W_R^\pm$ *at the LHC*, arXiv:1503.07198.

[58] M. Dhuria, C. Hati, R. Rangarajan, and U. Sarkar, *The* $eejj$ *Excess Signal at the LHC and Constraints on Leptogenesis*, arXiv:1502.01695.

[59] F. S. Queiroz, K. Sinha, and A. Strumia, *Leptoquarks, Dark Matter, and Anomalous LHC Events*, *Phys.Rev.* **D91** (2015), no. 3 035006, [arXiv:1409.6301].

[60] B. A. Dobrescu and A. Martin, *Interpretations of anomalous LHC events with electrons and jets*, *Phys.Rev.* **D91** (2015), no. 3 035019, [arXiv:1408.1082].

[61] M. Heikinheimo, M. Raidal, and C. Spethmann, *Testing Right-Handed Currents at the LHC*, *Eur.Phys.J.* **C74** (2014), no. 10 3107, [arXiv:1407.6908].

[62] G. D'Ambrosio, G. Giudice, G. Isidori, and A. Strumia, *Minimal flavor violation: An Effective field theory approach*, *Nucl.Phys.* **B645** (2002) 155–187, [hep-ph/0207036].

[63] R. Barbier et al., *R-parity violating supersymmetry*, *Phys. Rep.* **420** (2005) 1–202, [hep-ph/0406039].

[64] J. A. et al, *Madgraph 5: going beyond*, arXiv:1106.0522.

[65] T. Sjostrand, *Pythia 6.4 physics and manual*, hep-ph/0603175.

[66] J. Conway, *Pretty good simulation*, .

[67] A. Alloul, N. D. Christensen, C. Degrande, C. Duhr, and B. Fuks, *FeynRules 2.0 - A complete toolbox for tree-level phenomenology*, *Comput.Phys.Commun.* **185** (2014) 2250–2300, [arXiv:1310.1921].

[68] W. Beenakker, R. Hopker, and M. Spira, *PROSPINO: A Program for the production of supersymmetric particles in next-to-leading order QCD*, hep-ph/9611232.

[69] **CMS** Collaboration, C. Collaboration, *Search for supersymmetry in pp collisions at sqrt(s) = 8 TeV in events with three leptons and at least one b-tagged jet*, .

[70] **ATLAS** Collaboration, G. Aad et al., *Search for supersymmetry at $\sqrt{s}$=8 TeV in final states with jets and two same-sign leptons or three leptons with the ATLAS detector*, *JHEP* **1406** (2014) 035, [arXiv:1404.2500].

CHAPTER 8

NOVEL KINEMATICS FROM A CUSTODIALLY PROTECTED DIPHOTON RESONANCE

8.1 Introduction

The recent observation of an excess in the diphoton channel around 750 GeV invariant mass by ATLAS and CMS at $\sqrt{s} = 13$ TeV [1, 2] has generated much interest in models with a heavy scalar resonance, ϕ, that decays to two photons. Most explanations proposed so far are considering loop induced resonance production, typically via heavy vector-like quarks (VLQ) charged under the Standard Model (SM). Otherwise, tree-level decays to SM particles would naturally dominate the branching ratio of ϕ, either leading to a diphoton rate too small to explain the excess or a production rate of two SM particles with large invariant mass that is excluded by existing measurements.

In this paper, we propose a novel tree-level production mechanism where ϕ arises from the decay of a VLQ. The VLQs can be singly produced due to their mixing with the SM quarks, while the resonance is protected by the $\mathrm{SU}(2)_L \times \mathrm{SU}(2)_R$ custodial symmetry. In order to have significant mixing between the VLQs and the light quarks without modifying the $Zq\bar{q}$ couplings predicted by the SM, we introduce VLQs in a bidoublet representation of the custodial symmetry, while the resonance ϕ is part of a triplet under $\mathrm{SU}(2)_R$. The model has several advantages and new features:

- It is one of the few viable examples of tree-level production consistent with the excess signal rate, existing experimental constraints, and the kinematic

distributions of the diphoton background events.

- The ratio of production rates between 13 and 8 TeV is different than gluon or quark fusion. Depending on the model the ratio can be as large as about 7 (vs. 4.7 for gluon fusion), eliminating the tension with the 8 TeV diphoton searches.
- The custodial symmetry protects the resonance from the leading one-loop decays to hh, WW, and gg, while allowing decays to $\gamma\gamma$. The suppression of the hh decay is particularly significant since in most models this coupling will arise at tree-level, making it difficult to reconcile with the expectantly large diphoton branching ratio and unobserved hh decays. The $\gamma\gamma$ (as well as ZZ and $Z\gamma$) decay width is nonvanishing due to the explicit breaking of the custodial symmetry from gauging the $\mathrm{U}(1)_Y$ subgroup of $\mathrm{SU}(2)_R$.
- The custodial symmetry also forbids one-loop gluon fusion production, explaining the dominance of the tree-level production via a decay of a VLQ.

The scenario where ϕ is produced primarily from the decay of singly-produced VLQs has not been considered in the diphoton excess literature, although some authors have considered production of ϕ through a cascade decay of a heavier parent particle (e.g., [3–10]). Furthermore, several authors have pointed out the potential to measure VLQ top or bottom partners decaying to ϕ [11–13]. However, to explain the bulk of the excess signal through a decay of pair-produced top or bottom partners would require couplings at their perturbative limits to achieve large enough $\gamma\gamma$ rate and to explain why the VLQ decay process dominates over gluon fusion [5]. Moreover, pair production of two VLQs per event would give several hard jets in the event in addition to the diphoton, which is inconsistent with the kinematic distributions of events in the excess region. The tree-level production

mechanism presented in this paper avoids these problems. Interestingly, it has been pointed out in [14] that a top partner need not be a mass eigenstate but rather could be a mixture of top and charm-like mass eigenstates raising the possibility that the vector-like quarks which mix with light quarks could also play a role in solving the little hierarchy problem.

This paper is organized as follows. In Sec. 8.2, we introduce a motivated model consistent with low energy flavor constraints in which a bidoublet of vector-like quarks with $m_V \gtrsim m_\phi$ mix with the light-SM quarks. In Sec. 8.3 we discuss the production and decays of the new particles and find that the model can easily accommodate the current excess in the diphoton data without tension from existing searches, both from the 8 TeV searches sensitive to the 750 GeV resonance as well as searches sensitive to VLQs. Furthermore, we compare the kinematic distributions of our signal and the diphoton background, finding that, depending on the splitting between the VLQ and the scalar, the distributions can be challenging to distinguish without additional data.

8.2 Custodial symmetry and light quark mixing

In this section, we present a model in which the resonance is a decay product of an electroweak produced VLQ from the dominant t-channel process shown in figure 8.1. Single production of VLQs requires a large mixing angle between the light quarks and VLQs. One would naively expect such mixing to yield large corrections to the $Zq\bar{q}$ couplings, which are strongly constrained by electroweak precision observables. However, we can protect the Z couplings via the custodial symmetry by using a bidoublet representation V for the VLQs [15]. In addition,

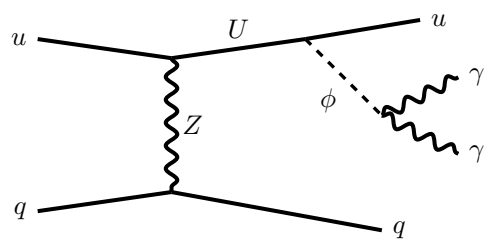

Figure 8.1: The dominant production of the diphoton excess from a decaying VLQ (U). In addition to the resonance, there are two additional jets. The p_T of the jets (and hence the visibility of the signal) is strongly dependent on the mass of the VLQ.

we introduce the $\mathrm{SU}(2)_R$ triplet, Φ, whose neutral component (which we denote by ϕ) will play the role of the 750 GeV resonance. This model is an example of a custodially symmetric model commonly considered in composite Higgs and extra dimensional models [14, 16–23].

8.2.1 Field content and mixing

We organize the fields into irreducible representations of $\mathrm{SU}(3)_C \times \mathrm{SU}(2)_L \times \mathrm{SU}(2)_R \times \mathrm{U}(1)_X$ in Table 8.1, where the $\mathrm{SU}(2)_R$ is a global symmetry and the fermions are left-handed Weyl spinors. Hypercharge is embedded in $\mathrm{SU}(2)_R \times \mathrm{U}(1)_X$ as $Y = T_R^3 + X$. The SM quarks are taken to be singlets under $\mathrm{SU}(2)_R$ and we represent the Higgs doublet as a bifundamental, $\mathcal{H} = (\epsilon H^*, H)$.

Four VLQs form the bidoublet,

$$V \equiv \begin{pmatrix} U_1 & X \\ D & U_2 \end{pmatrix}, \; \overline{V} \equiv \begin{pmatrix} \overline{U}_1 & \overline{D} \\ \overline{X} & \overline{U}_2 \end{pmatrix}. \tag{8.1}$$

The charges of the new quarks are $Q_{U_1} = Q_{U_2} = 2/3$, $Q_D = -1/3$, and $Q_X = 5/3$.

The Lagrangian for the VLQs (not including the terms coupling to the scalar

Field	$SU(3)_C$	$SU(2)_L$	$SU(2)_R$	$U(1)_X$
Φ	**1**	**1**	**3**	0
V	**3**	**2**	**2**	$+2/3$
$\overline{V}$	$\bar{\mathbf{3}}$	**2**	**2**	$-2/3$
$\mathcal{H}$	**1**	**2**	**2**	0
Q	**3**	**2**	**1**	$+1/6$
$\overline{u}$	$\bar{\mathbf{3}}$	**1**	**1**	$-2/3$

Table 8.1: The representations of relevant fields. The new vector-like quarks are in a single bidoublet V, and the 750 GeV resonance is the neutral component of Φ. The Higgs and the light quarks have the usual SM assignments. All fermionic fields are left-handed Weyl spinors.

Φ) is

$$\mathcal{L}_{VLQ} = m_V \mathrm{Tr}\left[\overline{V}V\right] - \lambda_V \mathrm{Tr}\left[\mathcal{H}^\dagger V\right]\overline{u}^{(0)} + h.c.\,, \tag{8.2}$$

where the (0) superscript denotes the quark fields in the SM mass basis of the up-type sector (the basis of diagonal SM Yukawa couplings). We assume the VLQs only mix with a single generation of right-handed up-type quark, however in appendix 8.A.4 we also consider a different $U(1)_X$ charge for V and the case of mixing with one generation of right-handed down-type quark. Note that we have made an important assumption regarding alignment: the bidoublet V couples to the up-type quark in the mass basis of the SM. This assumption is to avoid low energy flavor constraints from flavor changing neutral currents but is not a crucial ingredient for the collider phenomenology that follows.

The down-type quark masses are unaffected by the new VLQs. One flavor of the up-type quarks can mix significantly with the new VLQs through the off-diagonal mass matrix:

$$\begin{pmatrix} u^{(0)} & U_1 & U_2 \end{pmatrix} \begin{pmatrix} \lambda_u v/\sqrt{2} & 0 & 0 \\ -\lambda_V v/\sqrt{2} & m_V & 0 \\ -\lambda_V v/\sqrt{2} & 0 & m_V \end{pmatrix} \begin{pmatrix} \overline{u}^{(0)} \\ \overline{U}_1 \\ \overline{U}_2 \end{pmatrix} + h.c. \tag{8.3}$$

where λ_u is the Yukawa of the up-type quark. From here on, we assume the mixing is with the up or charm quark and neglect the up-type quark mass. The mass eigenstates (u, U, and $\tilde{U}$) are related to the gauge eigenstates by:

$$\begin{pmatrix} \overline{u}^{(0)} \\ \overline{U}_1 \\ \overline{U}_2 \end{pmatrix} = \begin{pmatrix} 1 & 0 & 0 \\ 0 & 1/\sqrt{2} & -1/\sqrt{2} \\ 0 & 1/\sqrt{2} & 1/\sqrt{2} \end{pmatrix} \begin{pmatrix} c_\theta & -s_\theta & 0 \\ s_\theta & c_\theta & 0 \\ 0 & 0 & 1 \end{pmatrix} \begin{pmatrix} \overline{u} \\ \overline{\tilde{U}} \\ \overline{U} \end{pmatrix} \qquad (8.4)$$
$$\begin{pmatrix} u^{(0)} \\ U_1 \\ U_2 \end{pmatrix} = \begin{pmatrix} 1 & 0 & 0 \\ 0 & 1/\sqrt{2} & -1/\sqrt{2} \\ 0 & 1/\sqrt{2} & 1/\sqrt{2} \end{pmatrix} \begin{pmatrix} u \\ \tilde{U} \\ U \end{pmatrix}$$

where $s_\theta \equiv \sin\theta$ and $c_\theta \equiv \cos\theta$ with

$$s_\theta = \frac{\lambda_V v}{m_{U^+}}\,, \qquad (8.5)$$

where $v \simeq 246$ GeV is the vacuum expectation value of the Higgs, and the masses of the VLQs are $m_{U^-} = m_D = m_\chi = m_V$ and $m_{U^+} = \sqrt{m_V^2 + \lambda_V^2 v^2}$. The down-sector does not experience any mixing, i.e. X and D are mass eigenstates.

The mixing, parameterized by s_θ, leads to couplings between a generation of SM quarks, SM gauge bosons, and the VLQs (derived in more detail in appendix 8.A):

$$\mathcal{L}_{EW} = -\frac{e s_\theta}{2 c_w s_w} Z_\mu \overline{u}^\dagger \bar{\sigma}^\mu \overline{U} - \frac{g s_\theta}{2} W_\mu^- (\overline{u}^\dagger \bar{\sigma}^\mu \overline{D} + \overline{X}^\dagger \bar{\sigma}^\mu \overline{u}) + h.c.\,, \qquad (8.6)$$

where s_w (c_w) is the sine (cosine) of the Weinberg angle and g (e) is the SU(2)$_L$ (QED) coupling constant. If the mixing angle is sufficiently large, these couplings can result in electroweak production of single VLQs (U, D, or X) which can dominate over the VLQ pair production cross section. Notice that only U, which will be responsible for the production of the diphoton resonance, couples to an up-type quark and the Z. $\tilde{U}$ is not produced by electroweak interactions in this

model. This is because only the linear combination $\overline{U}_1+\overline{U}_2$ mixes with the up-type quark, which is a necessary feature for the protection of the $Zq\bar{q}$ coupling in this model.

8.2.2 Consequences of a custodial triplet

The 750 GeV diphoton resonance ϕ is embedded in an $\mathrm{SU}(2)_R$ triplet scalar Φ as follows.

$$\Phi = \begin{pmatrix} \phi/\sqrt{2} & \phi_+ \\ \phi_- & -\phi/\sqrt{2} \end{pmatrix} \tag{8.7}$$

This allows for a coupling of Φ to the VLQs of the form

$$\mathcal{L}_\Phi = \sqrt{2} y_\phi \mathrm{Tr}\left[\overline{V}\Phi V\right] + h.c. \tag{8.8}$$

$$= y_\phi \phi \left(U_1\overline{U}_1 - U_2\overline{U}_2 + X\overline{X} - D\overline{D}\right) + h.c. + ... \tag{8.9}$$

$$= y_\phi \phi \left(-s_\theta U\bar{u} - \tilde{U}\overline{U} - c_\theta U\overline{\tilde{U}} + X\overline{X} - D\overline{D}\right) + h.c. + ... \tag{8.10}$$

where the ellipses refer to terms involving the charged components of Φ. The relative minus sign between the $U_1\overline{U}_1$ and $U_2\overline{U}_2$ terms gives rise to the coupling of ϕ to U and the SM up quark (as opposed to a coupling to $\tilde{U}$) which is responsible for the production of the resonance.

These interactions will generate couplings of ϕ to SM dibosons, such as gg, WW, hh etc. via triangle diagrams with the VLQs. However, in the limit of exact custodial symmetry, these amplitudes are forbidden. For example, the operator $\Phi\, G^{\mu\nu,A}G^A_{\mu\nu}$ has no custodially invariant contraction because the gluon field strength tensor G is a custodial singlet. Furthermore, the Higgs coupling to the

scalar vanishes since (using $\mathcal{H}\mathcal{H}^\dagger \propto \mathbb{1}$),

$$\mathrm{Tr}\left[\mathcal{H}^\dagger \Phi \mathcal{H}\right] \propto \mathrm{Tr}\,\Phi = 0\,. \tag{8.11}$$

In practice, the vanishing of the amplitudes is a consequence of cancellations of the contributions due to different VLQs running in the loop, which contain important relative minus signs as a consequence of the custodial symmetry.

The loop amplitudes for ϕ therefore require the insertion of $\mathrm{SU}(2)_R$ violating interactions. The largest such couplings in the SM are the third generation Yukawas, however in the flavor alignment limit these couplings will not directly affect the diphoton resonance sector since we assume mixing is not occurring with the third generation up-type quark. The dominant source of custodial symmetry breaking in this sector will therefore be the embedding of the hypercharge gauge group within the T_3^R generator of $\mathrm{SU}(2)_R$, and so it is to be expected that the leading loop amplitude will be that coupling ϕ to hypercharge gauge bosons, $\phi\, B^{\mu\nu} B_{\mu\nu}$. Indeed, the one-loop contributions to this operator do not cancel among the VLQs due to their differing hypercharges. The other loop amplitudes will be generated at higher order and are suppressed by an additional factor $\sim \alpha/4\pi c_w^2$ compared to their naive sizes. These two-loop contributions can induce a mixing angle between ϕ and the Higgs of order $\sim (v/16\pi^2 m_\phi)\,(\alpha/4\pi c_w^2)$ (where m_ϕ denotes the mass of the resonance), however this is much too small to induce sizable decays to $t\bar{t}$. Direct couplings of ϕ to the up-type quarks can also arise at two-loops but is suppressed by a Yukawa coupling, making it negligible. We verify the effects of custodial symmetry breaking explicitly in 8.A.3. This custodial protection mechanism generates a natural hierarchy between the decays of the resonance to diphotons and its decays to gg, WW, hh, and also suppresses the gluon fusion production of ϕ.

We now briefly compare this to a scenario in which the diphoton resonance is assumed to be a custodial singlet S with couplings

$$\mathcal{L}_S = y_S S \,\mathrm{Tr}\left[\overline{V}V\right] + h.c. \tag{8.12}$$

$$= y_S S \left(U_1\overline{U}_1 + U_2\overline{U}_2 + D\overline{D} + X\overline{X}\right) + h.c. \tag{8.13}$$

$$= y_S S \left(s_\theta \tilde{U}\overline{u} + U\overline{U} + c_\theta \tilde{U}\overline{\tilde{U}} + D\overline{D} + X\overline{X}\right) + h.c. \tag{8.14}$$

In this case, the only S-quark-VLQ coupling involves $\tilde{U}$, which does not couple to SM gauge bosons and therefore cannot be produced via VLQ single production. $\tilde{U}$ is pair-produced and can decay $\tilde{U} \to Su$, however the rate for pair production is subdominant to electroweak production of U and insufficient to explain the excess. Furthermore, this singlet does not exhibit custodial protection, which is a consequence of the couplings in eq. 8.13 adding constructively rather than destructively.

8.3 Diphoton cross section

Above we presented a model in which ϕ can be produced as a decay product of a singly produced VLQ (we will assume $m_V > m_\phi$ throughout). The dominant production mechanism for the diphoton resonance is depicted in figure 8.1.[1] In this section, we demonstrate that the $\gamma\gamma$ rate is sufficient to explain the diphoton excess while avoiding constraints from existing VLQ searches and electroweak precision tests. We consider two variations of the model, one where the VLQs mix with the up quark and another with the VLQs mixing with the charm quark.

[1]Secondary production modes from UZ production, pair production of VLQs, and direct ϕZ production mediated by a VLQ make up 10-30% of inclusive diphoton cross section. We explore the size of different contributions in Sec. 8.4.2, but since the size of the subdominant modes is highly dependent on the detailed parameters of the model, we only include the dominant production when studying the inclusive diphoton rate and kinematics.

Since the $\gamma\gamma$ final state arises from a decay chain, the inclusive cross section into $\gamma\gamma$ is given in the narrow width approximation by

$$\sigma_{\gamma\gamma} = \sigma(pp \to U\bar{u}, \bar{U}u) \times \mathrm{Br}(U \to \phi u) \times \mathrm{Br}(\phi \to \gamma\gamma). \tag{8.15}$$

Each of these contributions has different dependence on the relevant parameters of the model, y_ϕ and s_θ. The production cross section of the VLQs, $\sigma(pp \to U\bar{u}, \bar{U}u)$, is proportional to s_θ^2 but is independent of y_ϕ.

8.3.1 Branching ratios

The complete formulae for the branching ratios of ϕ and U are given in appendix 8.A.2. We summarize the results here. U has two decay channels, $U \to Zj$ and $U \to \phi j$ with the dominant decay being Zj. This results in the branching ratio of $U \to u\phi$ ranging between 1-10%, proportional to y_ϕ^2 and independent of the mixing angle. ϕ has competing decays between a 3-body tree-level decay and loop-induced 2-body decays. The only tree-level decay of ϕ is to $Zu\bar{u}$ through an off-shell U with a rate is proportional to $s_\theta^4 y_\phi^2$, making it highly sensitive to the mixing angle. ϕ has additional loop-induced decays into $\gamma\gamma$, $Z\gamma$, and ZZ. These decays arise from gauging hypercharge resulting in the relative ratios,

$$\Gamma_{\gamma\gamma} \,:\, \Gamma_{\gamma Z} \,:\, \Gamma_{ZZ} = 1 \,:\, 2\tan^2\theta_w \,:\, \tan^4\theta_w\,. \tag{8.16}$$

The loop-induced rates are largely independent of the mixing, proportional to y_ϕ^2.[2]

The leading branching ratios of ϕ are shown in figure 8.1 for a benchmark point relevant in the case of up-mixing with $s_\theta = 0.1$ (left) and charm-mixing

[2]We have checked that non-zero mixing has at most a 10% effect on the loop-induced rates in the region of parameter space we are interested in. Furthermore, these effects will not have any bearing on the size of the $\gamma\gamma$ rate and thus we ignore these effects in our analysis.

	y_ϕ	s_θ
u_R benchmark	0.7	0.1
c_R benchmark	2	0.3

Table 8.1: Benchmark points for the up quark and charm quark mixing models. For the u_R model, there are more stringent constraints on the mixing angle though a larger production cross section.

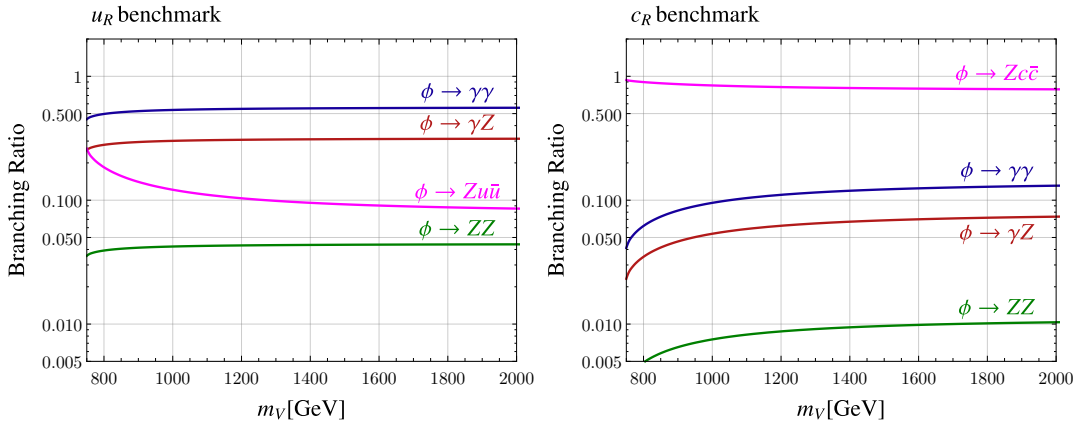

Figure 8.1: The different branching ratios for ϕ. The loop-induced decays to $\gamma\gamma$, γZ, and ZZ always compete with the 3-body decay. At large mixing, the 3-body decay is the preferred decay mode, however for small-mixing, the loop-induced decays (which are roughly independent of the mixing) dominate. **Left:** The branching ratios for the u_R benchmark point (small-mixing). **Right:** The branching ratios for the c_R benchmark (large-mixing).

with $s_\theta = 0.3$ (right). A couple comments on the choice of benchmark points (displayed in Table 8.1) are in order. First, regarding the size of the mixing angle, we have provided constraints on the allowed mixing angle for electroweak produced VLQs in appendix 8.B, obtained by reinterpreting the constraints from direct LHC searches on light quark composite partner models [14]. For the up-quark mixing, the mixing angle is experimentally constrained to be $s_\theta \lesssim 0.12$, while for charm mixing, the constraints are much weaker with $s_\theta \lesssim 0.5$. Larger mixing angles are allowed for the case of charm mixing since the electroweak production cross section of the VLQs are suppressed by the charm parton distribution function.

8.3.2 The inclusive cross section

Depending on the size of mixing, the inclusive cross section for diphoton production scales differently with the mixing angle. There are two distinct regimes, large and small mixing angles. If the mixing angle is large, then the dominant decay of ϕ is through the 3-body decay. In this case the branching ratio into diphotons is $\propto 1/s_\theta^4$ giving an inclusive cross section

$$\sigma_{\gamma\gamma} \propto \frac{y_\phi^2}{s_\theta^2} \quad \text{(large mixing)}\,. \tag{8.17}$$

For small mixing, the 3-body ϕ decay is heavily suppressed making the diphoton rate the dominant mode, i.e. $\mathrm{Br}(\phi \to \gamma\gamma) \approx 1$, independent of y_ϕ or s_θ. In this case, the inclusive cross section scales as

$$\sigma_{\gamma\gamma} \propto y_\phi^2 s_\theta^2 \quad \text{(small mixing)}\,. \tag{8.18}$$

The transition between the two regimes occurs around $s_\theta \sim 0.2$, and this is the point where the cross section is maximized. Due to the constraints, the up mixing case is always in the small mixing scenario while the charm can be either the large or small mixing regimes. For our chosen benchmark point, the charm scenario corresponds to large mixing.

To reproduce the excess, we simulate the production of ϕ at leading order using a custom FeynRules model [25] with MadGraph5 [26]. To roughly estimate the size of next-to-leading order (NLO) effects, we compute the production cross section with an additional jet, finding that it makes up about 50% of the leading order cross section. This suggests an NLO K-factor of about 1.5, and we use this correction throughout. We compute the diphoton rate using equation 8.15 and the branching ratios given in appendix 8.A.2. Figure 8.2 shows the inclusive diphoton

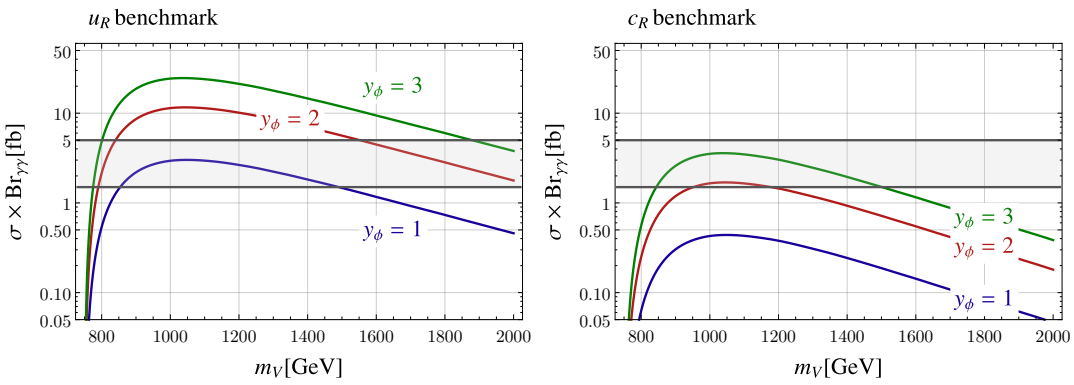

Figure 8.2: The inclusive cross section into $\gamma\gamma$ as a function of VLQ mass and varying the values of y_ϕ. In gray we show the rough cross section necessary to explain the excess with a narrow width $(1.5 - 5$ fb) [24]. **Left:** The cross section for the u_R benchmark point. **Right:** The cross section for the c_R benchmark point.

production cross section for different VLQ masses and values of y_ϕ for the two benchmark points.

We see in the left of figure 8.2 that we need $y_\phi \sim 0.7$ to get enough cross section to explain the excess in the up quark variation of the model. Larger Yukawa couplings are required in the charm-mixing benchmark point, requiring $y_\phi \sim 2$ to achieve the minimum cross section needed to explain the excess.

As with many models explaining the diphoton excess, such Yukawa couplings can lead to non-perturbativity of the model before the GUT scale. The up-mixing benchmark becomes non-perturbative at around 100 TeV, although there is some parameter space where the coupling remains perturbative beyond the GUT scale. The charm-mixing model is more problematic given the Yukawa coupling runs to its perturbative limit at a few TeV, putting into question the validity of our analysis. However, this problem can be easily overcome by adding additional flavors of bidoublets (these may or may not mix with the SM quarks) which feed into the running, but also boost the diphoton decay rate as the square of the

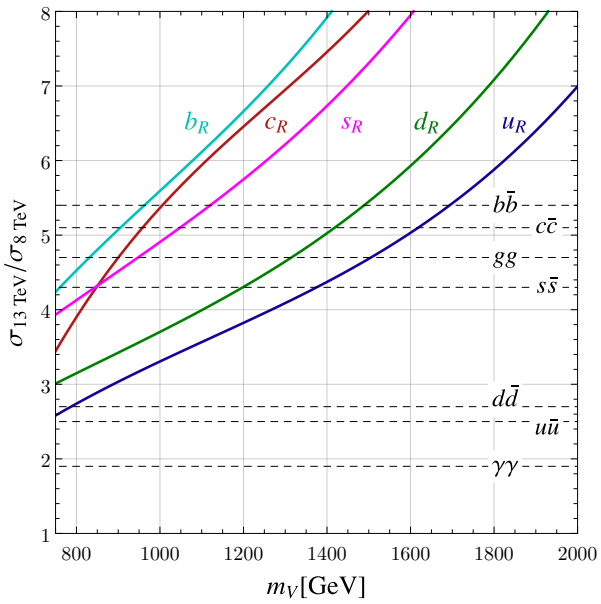

Figure 8.3: The ratio of $\sqrt{s} = 13$ to 8 TeV cross section of the up-mixing signal (blue) and charm-mixing signal (red). We have included the scaling properties of the down-type version of this model where the down (green), strange (pink), or bottom (light blue) quark mix with VLQs. The scaling of other proposed production processes are shown as dashed lines and were taken from [3].

number of flavors allowing for much smaller couplings, and a much higher scale of strong coupling.

8.3.3 Eliminating tension with 8 TeV data

One of the puzzling features of the 13 TeV diphoton excess is its seemingly large cross section compared to cross section limits from 8 TeV searches. A 750 GeV resonance is not ruled out by Run I searches but, depending on the production mechanism and width, may be in tension with Run I limits [24, 27]. Thus to reproduce the excess, it is important to have sufficiently large scaling, r, defined as the ratio of the cross section at 13 TeV to that at 8 TeV. We compute the scaling for our model as a function of the VLQ mass (the scaling is independent of the

couplings) and assuming the K-factor is constant from 8 to 13 TeV. The results are shown in figure 8.3 alongside the scaling of other proposed models, including gluon fusion, $q\bar{q}$ production [28], and photon fusion [29–31]. The up-mixing model inherits the scaling from the $u\bar{u}$ production at $m_V \sim 750$ GeV but grows with the mass of the VLQ due to the higher center-of-mass energy. For heavy VLQ masses near 1500 GeV, the scaling is comparable to gluon fusion. The charm variation of the model, however, scales much better due to the parton distribution function of the charm in the initial state. For VLQ masses nearly degenerate with m_ϕ (800 GeV $\lesssim m_V \lesssim$ 1000 GeV) for which the extra jet from the U decay is relatively soft, the scaling is as large as for $b\bar{b}$ production. For larger masses, the charm-mixing scenario has $r \gtrsim 7$, but in this region of parameter space, the ϕ would be accompanied by a high-p_T jet in the final state (we explore the plausibility of this scenario in Sec. 8.4). We conclude that, depending on the mass of the VLQ, our signal can achieve larger cross section scaling from 8 to 13 TeV than any proposed model of single resonance production.

For simplicity, we have only considered mixing with up-type quarks. It is possible to construct a similar model in which new VLQs mix with the down-type quarks. The terms in the Lagrangian responsible for production of a down-type variation of this model are presented in appendix 8.A.4. We include the scaling properties of production from down, strange, and bottom quark mixing in figure 8.3. The bottom quark mixing scenario has the largest ratio of 13 to 8 TeV cross section, while the down and strange quark scenarios interpolate between the scaling of the up and charm scenarios.

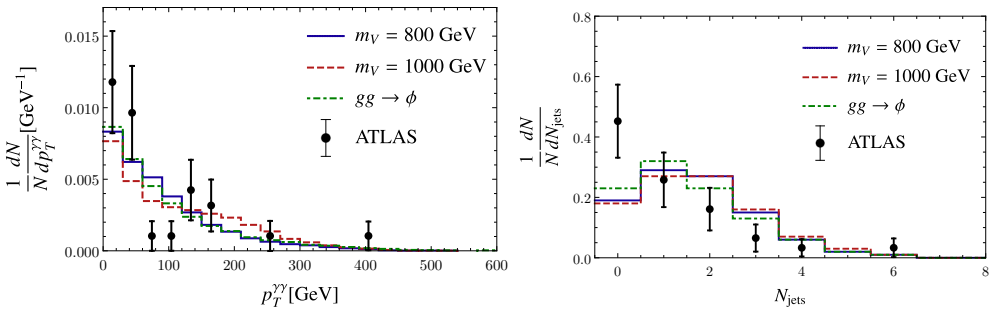

Figure 8.1: The kinematic distributions of the sum of the signal and background for vector-like quark mass of 800 (blue) and 1000 GeV (red) compared to the distributions observed by ATLAS (black) with 3.2 fb^{-1} of data. We also provide gluon fusion kinematics (green) for comparison. The N_{jets} and $p_T^{\gamma\gamma}$ distributions for the background and observed events are obtained from the slides presented by ATLAS [32].

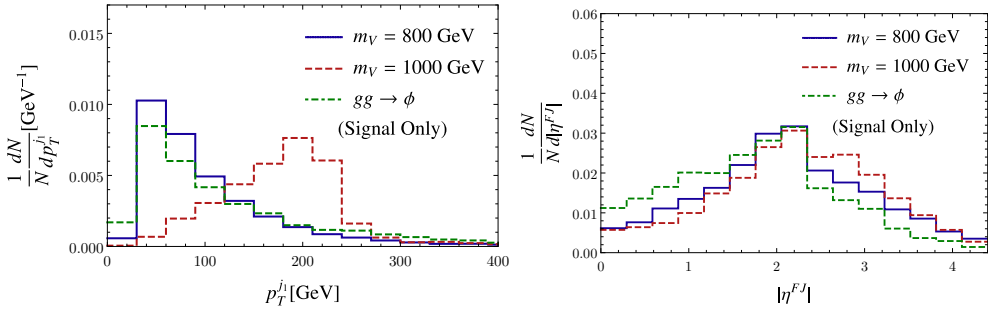

Figure 8.2: The leading-jet p_T and forward jet pseudorapidity distributions of the signal for vector-like quark mass of 800 (blue) and 1000 GeV (red) along with a gluon fusion signal (green) for comparison. For VLQs almost degenerate with the resonance, the signal is difficult to differentiate from the QCD background or a resonance produced via gluon fusion since these events also contain soft, forward jets from initial state radiation.

8.4 Kinematics

8.4.1 Comparing with ATLAS

In addition to the diphoton resonance signature at $m_{\gamma\gamma} \sim 750$ GeV, our signal has two additional jets, with one of the jets typically in the forward direction. AT-

LAS and CMS have remarked that events in the excess region are consistent with the background kinematics. Furthermore, ATLAS has recently provided kinematic distributions of the excess events [32] for the number of jets, N_{jets} (ATLAS defined a jet using $p_T^j > 25$ GeV for $\eta < 2.4$ and $p_T^j < 50$ GeV for $\eta < 4.4$), and the transverse momentum of the $\gamma\gamma$ resonance, $p_T^{\gamma\gamma}$. Furthermore, ATLAS provided estimates for the expected SM diphoton background from simulations. The distributions are provided for the region 700 GeV $< m_{\gamma\gamma} <$ 840 GeV and with the requirements on the leading and subleading photon energies $E_T^{\gamma_1} > 0.4 m_{\gamma\gamma}$ and $E_T^{\gamma_2} > 0.3 m_{\gamma\gamma}$. In this bin, ATLAS found a total of 34 events, about 10 of which are diphoton excess candidates.

To compare the compatibility of the kinematics of the excess with our signal we simulate our signal using a combination of MadGraph5, Pythia 8.2 [33], and Delphes 3 [43] making use of the NNPDF2.3LO parton distribution functions [35]. To compare with the distributions observed by ATLAS, we perform a weighted sum of our signal and the background estimates provided by ATLAS

$$N = rN_{sig} + (1 - r)N_{bkg}. \tag{8.19}$$

This is done for each bin and we take $r \approx 10/34$. We also simulate gluon fusion at leading order and perform this procedure in order to compare our signal with the kinematics of single production. By comparing the distributions in figure 8.1, we conclude that although our signal has two extra jets in the final state, the distributions for N_{jets} and $p_T^{\gamma\gamma}$ are consistent with the data provided by ATLAS (as is also the case for the gluon fusion signal). Furthermore, the mass of the VLQ has only a mild effect on these distributions since the number of jets from the hard process is independent of m_V. The signal does have distinctive features in other distributions, however, and we explore these features in the next section.

8.4.2 Additional signatures

Our signal predicts observable jet signatures that can be used to discern this process from background events or from other resonance production mechanisms. In particular, we expect a forward jet as well as one central jet with higher p_T, depending on m_V. The distributions for the p_T of the leading jet ($p_T^{j_1}$) and the absolute value of the pseudorapidity of the most forward jet ($|\eta^{FJ}|$) for the signals with $m_V = 800$ and 1000 GeV are shown in figure 8.2 along with the gluon fusion signal for comparison. Note that ATLAS and CMS did not provide the background or observed kinematic distributions for these observables, so we did not combine the background and the signal in these plots.

The distributions have some distinctive characteristics. Firstly, we see that for small splitting $p_T^{j_1}$ is peaked around zero since, at these splittings, the central jet, which will typically be the leading jet, has low p_T. However, for larger splitting the distribution has a kinematic edge with the end-point at the splitting between the VLQ and the resonance. This is prototypical of a jet arising from a heavy particle decay to a second heavy particle. Interestingly, such a distribution can suggest the mass of the VLQ. The forward jet in the event is most easily probed using its pseudorapidity. The distribution has a dip at $\eta \approx 2.4$ as a consequence of the cuts used by ATLAS for the jet definition (see above). As expected, the signal has a jet with large η, however this is also true of the dominant background, $\gamma\gamma$. In this background, jets are emitted from the initial state and hence tend to be in the forward region. This can result in the feature being well hidden inside the SM background of the searches.

In addition to the features of the dominant production mode, there are secondary production modes of the excess. In principle, one may expect that any of

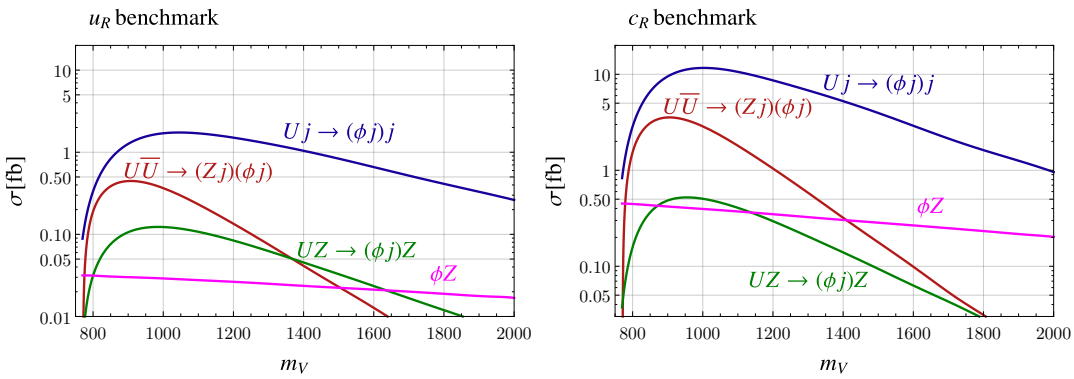

Figure 8.3: The cross sections for the different production modes at our benchmark points. We see that production through single VLQ dominates with the secondary production modes providing up to 10-30% corrections on the inclusive diphoton cross section.

the VLQs could decay into the resonance, but this is not the case. Due to the custodial structure of the model, only U couples to the resonance and a SM quark (see equation 8.10), and hence its the only single VLQ production mode. However, there are three subdominant modes which can contribute significantly to the cross section, single VLQ production through $pp \to UZ, \overline{U}Z$, QCD pair production of VLQs through $pp \to U\overline{U}$, and direct production of the resonance through a t-channel VLQ, $pp \to \phi Z$. The cross section composition depends strongly on the choice of mixing angle and mass of the VLQ. The various contributions to the total cross section as a function of the mass for our benchmark points are shown at leading order in figure 8.3 (for simplicity we do not apply K-factors when comparing between these different channels). We conclude that the additional production modes make up 10-30% of the inclusive diphoton cross section for reasonable choices of parameters. With more statistics, excesses in these subleading channels could be used to differentiate our signal.

Lastly we note that in principle the charged scalars, which are almost degenerate with ϕ, can also be observed as they are singly produced by a similar

mechanism as ϕ. However, the loop-induced decays to WZ and $W\gamma$ both vanish in the custodial limit, rendering their 3-body decays dominant in almost all of parameter space. These 3-body decays could be probed, but such studies are likely less sensitive then other searches.

8.5 Conclusions

We have presented a model describing a 750 GeV diphoton resonance arising from a custodial triplet which is produced as a decay product of a singly-produced VLQ. Our model has novel kinematics compared to other proposed production mechanisms and eliminates the tension from the 8 TeV diphoton searches while maintaining consistency with the kinematic distributions in the excess region. With additional statistics, our signal could be confirmed by the presence of a forward jet in the diphoton events or as a kinematic edge in the leading-jet p_T distributions if the VLQ mass is significantly heavier than 800 GeV. The scalar resonance enjoys custodial protection, explaining the dominance of the $\gamma\gamma$ decay rate over WW, hh, and dijet decays.

Additional signatures of the model include a corresponding excess in the $Z\gamma$ and ZZ channels with fixed rates with respect to the $\gamma\gamma$ rate. Furthermore, searches for single production of VLQs in Run II will probe deep into the viable parameter space of this model.

We now note some interesting model building possibilities which we leave for future studies. First, in this work we focus on the case where the new scalar arises from an $\mathrm{SU}(2)_R$ triplet but is uncharged under $\mathrm{SU}(2)_L$. However, many of the benefits enjoyed by this model are present in similar representation choices, in

particular if ϕ is a $(\mathbf{3},\mathbf{1})$ or $(\mathbf{3},\mathbf{3})$ under $(\mathrm{SU}(2)_L, \mathrm{SU}(2)_R)$. These models also forbid gluon fusion and the tree-level production mechanism can dominate. Another interesting possibility is if the VLQs are related to the the top sector, as one might expect in a composite Higgs model, and the custodial symmetry is broken explicitly by the top Yukawa. Such a breaking can induce ϕ production through gluon fusion, perhaps in a controlled manner such that the decays to hh as well as decays to W^+W^- are still suppressed. Finally, we comment on some ways to further reduce the size of the Yukawas. In this work we focused on a single flavor of VLQ for simplicity. However, if there are additional flavors (with or without mixing to the other SM quarks), this can greatly enhance the diphoton decay rate, reducing the size of Yukawas necessary to reproduce the excess. An additional possibility is if $\mathrm{SU}(2)_R$ is gauged. In this case, the additional gauge bosons will propagate in the diphoton loop giving a significant enhancement to the diphoton rate.

APPENDIX

8.A Model details

8.A.1 Couplings

In this section, we derive the couplings relevant for the model between the quarks and the vector-like quarks, beginning with the Z couplings. The Z boson interactions with the up-type quarks in the interaction basis are given by (we define $\not{Z} \equiv \bar{\sigma}^\mu Z_\mu$) [3]

$$\mathcal{L}_Z = \frac{e}{c_w s_w}\left\{\frac{2}{3}s_w^2\overline{u}^{(0)\,\dagger}\not{Z}\overline{u}^{(0)} + \left(\frac{1}{2}+\frac{2}{3}s_w^2\right)\overline{U}_1^\dagger\not{Z}\overline{U}_1 + \left(-\frac{1}{2}+\frac{2}{3}s_w^2\right)\overline{U}_2^\dagger\not{Z}\overline{U}_2\right\} \tag{8.20}$$

$$= \frac{e}{s_w c_w}\boldsymbol{\mathcal{U}}^{(0)\dagger}\begin{pmatrix} \frac{2}{3}s_w^2 & 0 & 0 \\ 0 & \frac{1}{2}+\frac{2}{3}s_w^2 & 0 \\ 0 & 0 & -\frac{1}{2}+\frac{2}{3}s_w^2 \end{pmatrix}\not{Z}\boldsymbol{\mathcal{U}}^{(0)}\,, \quad \boldsymbol{\mathcal{U}}^{(0)} \equiv \begin{pmatrix} \overline{u}^{(0)} \\ \overline{U}_1 \\ \overline{U}_2 \end{pmatrix}. \tag{8.21}$$

Notice that we can split the coupling matrix into two pieces,

$$\frac{2}{3}s_w^2\begin{pmatrix} 1 & 0 & 0 \\ 0 & 1 & 0 \\ 0 & 0 & 1 \end{pmatrix} + \frac{1}{2}\begin{pmatrix} 0 & 0 & 0 \\ 0 & 1 & 0 \\ 0 & 0 & -1 \end{pmatrix}. \tag{8.22}$$

The first matrix is diagonal and commutes with the rotation to the mass basis while the second matrix yields new couplings between the VLQs and the quarks

[3] Note that U_1 is the upper component of an $\mathrm{SU}(2)_L$ doublet, while U_2 is the lower component of a second doublet.

upon moving to the mass basis. Performing the rotation (the rotation matrices are given in eq. 8.4) gives,

$$\mathcal{L}_Z = \frac{e}{c_w s_w}\left\{\frac{1}{2}\boldsymbol{\mathcal{U}}^\dagger \begin{pmatrix} 0 & 0 & -s_\theta \\ 0 & 0 & -c_\theta \\ -s_\theta & -c_\theta & 0 \end{pmatrix} \not{Z}\boldsymbol{\mathcal{U}} + \frac{2}{3}s_w^2 \boldsymbol{\mathcal{U}}^\dagger \not{Z}\boldsymbol{\mathcal{U}}\right\},$$

$$\boldsymbol{\mathcal{U}} \equiv \begin{pmatrix} \overline{u} \\ \overline{\tilde{U}} \\ \overline{U} \end{pmatrix}. \tag{8.23}$$

Notice that the rotation to the mass basis has left the top-left entry of the coupling matrix unchanged. This is very important as it means the mixing with the VLQs does not affect the $Z\bar{u}\bar{u}$ coupling which is tightly constrained experimentally. We see that we have a new coupling between the quark and the VLQ:

$$\mathcal{L}_{ZuU} = -\frac{e}{c_w s_w}\frac{1}{2}s_\theta\left(\overline{u}^\dagger \not{Z}\overline{U}\right) + h.c. \tag{8.24}$$

Now consider the W-boson couplings. The right-handed up quark does not couple to the W in the gauge basis, so the relevant couplings are simply:

$$\mathcal{L}_W = -\frac{g}{\sqrt{2}}\left(\overline{U}_1^\dagger \not{W}^- \overline{D} + \overline{X}^\dagger \not{W}^- \overline{U}_2\right) + h.c. \tag{8.25}$$

$$\subset -\frac{g s_\theta}{2}\left(\overline{u}^\dagger \not{W}^- \overline{D} + \overline{X}^\dagger \not{W}^- \overline{u}\right) + h.c. \tag{8.26}$$

where we moved to the mass basis in the last line.

8.A.2 Decay rates

In this section, we present formulae for the different decay rates used in the text for both the scalar resonance and the U quark.

ϕ decays

We begin by considering the tree-level decays of ϕ. The dominant contribution is

$$\Gamma(\phi \to Zu\bar{u}) = \frac{m_\phi N_c}{4(4\pi)^3}\frac{m_Q^2}{v^2}s_\theta^4\, y_\phi^2\, g_Z(\tau) \tag{8.27}$$

where N_c is the number of colors, $\tau \equiv m_Q/m_\phi$, and

$$g_Z(\tau) \equiv \int_0^1 dx \int_{1-x}^1 d\bar{x}\frac{(1-x)(1-\bar{x})(2-x-\bar{x}-2\tau^2)^2}{(1-x-\tau^2)^2(1-\bar{x}-\tau^2)^2}. \tag{8.28}$$

The other conceivable 3-body decays, $\phi \to hu\bar{u}$, $\phi \to Wd\bar{u}$, and $\phi \to Wu\bar{d}$ vanish identically due to the custodial production.

In addition ϕ has several loop induced decays to vector bosons as well as the Higgs. All the loop induced decays decays violate custodial symmetry. This can easily be seen at the operator level, where the terms

$$\Phi B_{\mu\nu}B^{\mu\nu}, \quad \Phi W^a_{\mu\nu}W_a^{\mu\nu}, \quad \text{and} \quad \Phi G^{\mu\nu}_A G^A_{\mu\nu} \tag{8.29}$$

(where $B_{\mu\nu}, W^a_{\mu\nu}$, and $G^A_{\mu\nu}$ represent the hypercharge, $\mathrm{SU}(2)_L$, and QCD field strength tensors respectively) all violate custodial symmetry and $\mathrm{Tr}\left[\mathcal{H}^\dagger\Phi\mathcal{H}\right]$ vanishes identically. There is a large breaking of this symmetry from gauging hypercharge, which induces decays into $\gamma\gamma$, γZ, and ZZ. Since gauging hypercharge only breaks $SU(2)_R$, the Z interactions are suppressed by powers of the Weinberg angle, resulting in these being generically subdominant to the photon decays. The general computation of these decay rates is made complicated due to the mixing of the VLQs with the up quark, however since these contributions are suppressed by powers of the mixing angle they are generically small. We have checked the size of these corrections by computing the rates numerically using FeynArts3, FormCalc8, and LoopTools2 [36, 37] and we find that the effect is at most 10% in the interesting region of parameter space (though often much smaller), and we neglect these effects for simplicity.

The decay rate of a scalar into two photons mediated by VLQs with mass m_i is [38]

$$\Gamma(\phi \to \gamma\gamma) = \frac{m_\phi^3 N_c^2}{4(4\pi)^5} e^4 \Big(\sum_i \frac{y_\phi^i}{m_i} Q_i^2 A_{1/2}(x_i) \Big)^2 , \tag{8.30}$$

where $x_i \equiv 4m_i^2/m_\phi^2$ and (for $m_i > m_\phi/2$) $A_{1/2}(x) = 2x(1+(1-x)\arcsin(1/\sqrt{x})^2)$. The sum runs over all VLQs and for a bidoublet the sum is

$$\sum_i \frac{y_\phi^i}{m_i} Q_i^2 A_{1/2}(x_i) = \left[\frac{y_\phi}{m_V} \frac{8}{3} \right] A_{1/2}(x_V) \, , \tag{8.31}$$

where the only non-zero contribution arises from the D and X quarks.

The decay to two gluons mediated by VLQs is

$$\Gamma(\phi \to gg) = \frac{m_\phi^3}{2(4\pi)^5} g_s^4 \Big(\sum_i \frac{y_\phi^i}{m_i} A_{1/2}(x_i) \Big)^2 , \tag{8.32}$$

where g_s is the strong coupling constant. For a bidoublet of VLQs with a triplet scalar, the sum is equal to zero showing that gluon fusion is custodially protected as expected.

The decay to ZZ mediated by VLQs is

$$\Gamma(\phi \to ZZ) = \frac{m_\phi^3 N_c^2}{4(4\pi)^5} \frac{e^4}{s_w^4 c_w^4} \Big(\sum_i \frac{y_\phi^i}{m_i} A_{1/2}(x_i)(T_3^i - Q_i s_w^2) \Big)^2 . \tag{8.33}$$

The sum for the bidoublet is:

$$\sum_i \frac{y_\phi^i}{m_i^2} A_{1/2}(x_i)(T_3^i - Q_i s_w^2)^2 = \left[\frac{y_\phi}{m_V} \frac{8}{3} s_w^4 \right] A_{1/2}(x_V). \tag{8.34}$$

The decay to $Z\gamma$ is

$$\begin{aligned} \Gamma(\phi \to Z\gamma) = \frac{8 m_\phi^3 N_c^2}{(4\pi)^5} \frac{e^4}{s_w^2 c_w^2} \Bigg(\sum_i \frac{y_i (T_3^i - Q_i s_w^2) Q_i}{m_i} \\ \times (I_1(x_i, \lambda_i) - I_2(x_i, \lambda_i)) \Bigg)^2 \end{aligned} \tag{8.35}$$

where $\lambda_i \equiv 4m_i^2/m_Z^2$ and

$$I_1(a,b) \equiv \frac{ab}{2(a-b)} + \frac{a^2b^2}{2(a-b)^2}\left[f(a)^2 - f(b)^2\right] + \frac{a^2b}{(a-b)^2}\left[g(a) - g(b)\right], \tag{8.36}$$

$$I_2(a,b) \equiv -\frac{ab}{2(a-b)}\left[f(a)^2 - f(b)^2\right], \tag{8.37}$$

and $f(x) \equiv \sin^{-1}(1/\sqrt{x})$ and $g(x) \equiv \sqrt{x-1}f(x)$. For the bidoublet,

$$\sum_i \frac{y_i}{m_i} Q_i (T_3^i - Q^i s_w^2)(I_1(x_i,\lambda_i) - I_2(x_i,\lambda_i)) = - \left[\frac{y_\phi}{m_i}\frac{8}{3}s_w^2\right](I_1(x_V,\lambda_V) - I_2(x_V,\lambda_V)). \tag{8.38}$$

The $\Phi \to \gamma\gamma,\ Z\gamma,\ ZZ$ decays obey the expected relationship when they all arise from $\Phi B_{\mu\nu}B^{\mu\nu}$:

$$1 \,:\, 2\tan^2\theta_w \,:\, \tan^4\theta_w \tag{8.39}$$

The decay of ϕ to W^+W^- is

$$\Gamma(\phi \to W^+W^-) = \frac{m_\phi^3 N_c^2}{(4\pi)^5}\frac{e^4}{s_w^4}\Big(\sum_i \frac{y_\phi^i}{m_i} A_{1/2}(x_i)\Big)^2. \tag{8.40}$$

For a bidoublet the sum vanishes identically as expected.

Lastly, the ϕhh operator vanishes at tree-level and at one-loop by custodial symmetry but will be generated at two-loops by custodial symmetry breaking.

U^- decays

The vector-like quarks can decay in a couple ways. We will assume $m_Q > m_\phi$ such that the VLQs can decay to the scalar. Furthermore, we will focus on U since that's the only VLQ that will play a role in the phenomenology.

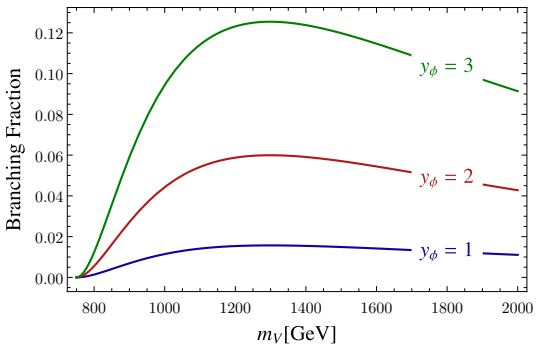

Figure 8.A.1: Branching ratio of the $U \to u\phi$ decay for different value of the couplings. The fraction is independent of the mixing angle.

The decays rates are

$$\Gamma(U \to uZ) \approx \frac{m_V}{64\pi} \frac{e^2 s_\theta^2}{s_w c_w} \frac{m_V^2}{m_Z^2} \tag{8.41}$$

$$\Gamma(U \to u\phi) = \frac{m_V}{32\pi} y_\phi^2 \, s_\theta^2 \left(1 - \frac{M_\phi^2}{m_V^2}\right)^2 \tag{8.42}$$

Notice that the uZ decay is enhanced by m_V^2/m_Z^2 due to the longitudinal polarization of the Z. Thus in order for the ϕ decay to be substantial one needs larger Yukawas. The branching ratio into $\phi\, u$ is shown in figure 8.A.1 for different Yukawas.

8.A.3 Custodial symmetry breaking

In this work we have assumed that the couplings and masses of the VLQs and the triplet Φ preserve the custodial symmetry, which enforces a cancellation in the loop amplitudes corresponding to the gluon fusion production of ϕ as well as the decays to gg, hh, and WW. Assuming no cancellations or large mass hierarchies, a generic scalar ϕ coupling to N_f VLQs with coupling y_ϕ would acquire an effective

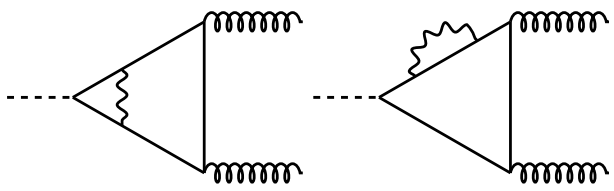

Figure 8.A.2: Prototypical loop contributions to the custodial symmetry breaking amplitudes. Such two-loop contributions can induce gluon fusion production and decays two gluons. Similar diagrams can give rise to decays to W^+W^- and hh.

coupling to gluons of the form

$$\mathcal{L}_{\text{generic}} \supset -\frac{1}{16\pi^2}\frac{N_f g_s^2 y_\phi}{4m_\phi}\,\phi\, G^{\mu\nu,A}G^A_{\mu\nu}\,, \tag{8.43}$$

with similar expressions for the other amplitudes. The explicit breaking of custodial symmetry due to the gauging of hypercharge means that these amplitudes will still be generated, but with an additional suppression of $\mathcal{O}(\alpha/c_w^2)$ compared to the above estimate.

In particular, the VLQ mass renormalization and the renormalization of the $\text{Tr}\left[\overline{V}\Phi V\right]$ couplings due to hypercharge gauge boson loops, illustrated in Figure 8.A.2, will contribute operators of the form $\text{Tr}[T_3^R\Phi]G^{\mu\nu,A}G^A_{\mu\nu}$. Since the mass and vertex renormalizations are logarithmically divergent, they require counterterms which are not calculable in the effective theory. Instead, we calculate the size of the IR contributions and take this as an estimate of the overall size of the irreducible contributions.

The mass renormalization of the VLQs introduces a mass splitting between the different T_3^R states of size

$$\begin{aligned}\frac{\delta m_V}{m_V} &\simeq \frac{3g'^2}{16\pi^2}\log\left(\frac{\Lambda^2}{m_V^2}\right)\Delta\left(Y^2\right) \\ &\simeq \frac{\alpha}{\pi c_w^2}\log\left(\frac{\Lambda^2}{m_V^2}\right).\end{aligned} \tag{8.44}$$

Similarly, the vertex and wavefunction renormalization provide a contribution to the operator $\delta y_\phi \,\mathrm{Tr}\left[\overline{V} T_3^R \Phi V\right]$ of size

$$\frac{\delta y_\phi}{y_\phi} \simeq \frac{6 g'^2}{16\pi^2} \log\left(\frac{\Lambda}{m_V}\right) \Delta\left(Y^2\right) \tag{8.45}$$
$$\simeq \frac{\alpha}{\pi c_w^2} \log\left(\frac{\Lambda^2}{m_V^2}\right).$$

where g' is the $U(1)_Y$ coupling constant. Now, custodial symmetry violating amplitudes of the kind in Figure 8.A.2 can be generated either with an insertion of δm_V instead of m_V, or with the coupling δy_ϕ. Therefore, the amplitude is suppressed by a factor

$$\frac{\delta \mathcal{A}}{\mathcal{A}_0} \simeq \frac{\delta m_V}{m_V} + \frac{\delta y_\phi}{y_\phi} \tag{8.46}$$
$$\simeq \frac{2\alpha}{\pi c_w^2} \log\left(\frac{\Lambda^2}{\mathrm{TeV}^2}\right) \tag{8.47}$$

In the same spirit, one can also generate a mixing between the Higgs and the new scalar ϕ. Such a mixing is induced at two loops from the operator of the form, $y_{\Phi HH} m_\phi \mathrm{Tr}\left[H^\dagger T_3^R \Phi H\right]$. The coefficient of this operator is of order

$$y_{\Phi HH} \simeq y_\phi \frac{\lambda_V^2}{16\pi^2} \frac{2\alpha}{\pi c_w^2} \log\left(\frac{\Lambda^2}{\mathrm{TeV}^2}\right), \tag{8.48}$$

which results in a mixing angle between the Higgs and ϕ of order

$$\simeq \frac{m_V^2 \tan^2\theta}{\sqrt{2} v m_\phi} \frac{y_\phi}{16\pi^2} \frac{2\alpha}{\pi c_w^2} \log\left(\frac{\Lambda^2}{\mathrm{TeV}^2}\right) \sim \mathcal{O}(10^{-4} - 10^{-5}), \tag{8.49}$$

where we have substituted λ_V for the mixing angle. This mixing will induce decays of ϕ to $t\bar{t}$, but due to the smallness of the coupling, we do not expect this decay to be observable in the near future.

8.A.4 Down-type model

We now present the down-type model which can have mixing between the SM down-type quarks and the VLQs. The model is identical to the up-type model but assigning the V bidoublet a $\mathrm{U}(1)_X$ charge of $-1/3$ (as opposed to $+2/3$). This gives the following fields

$$V = \begin{pmatrix} D_2 & U \\ Y & D_1 \end{pmatrix} \quad \overline{V} = \begin{pmatrix} \overline{D}_2 & \overline{Y} \\ \overline{U} & \overline{D}_1 \end{pmatrix} \tag{8.50}$$

where $Q_{D_1} = Q_{D_2} = -1/3$, $Q_U = +2/3$, and $Q_Y = -4/3$. As in the up-mixing case, a mixing is generated between a SM quark and a VLQ through:

$$\mathcal{L}_{VLQ} = m_V \mathrm{Tr}\left[\overline{V}V\right] + \lambda_V \mathrm{Tr}\left[\mathcal{H}^\dagger V\right] \overline{d}^{(0)} + h.c. \tag{8.51}$$

where $\overline{d}^{(0)}$ denotes the down quark in the SM mass basis of the down-type sector. The mixing produces a ZDd coupling resulting in electroweak production of D, which can decay into the diphoton resonance.

8.B Experimental constraints

The LHC has performed searches with significant sensitivity to models with light-quark mixing. The constraints were studied in detail in [14] for both up-quark mixing and charm-quark mixing in the context of a composite model and in [23] for the up-type mixing model. The dominant constraints arise from charged current production of D and X quarks. There are additional constraints from production of the charged $+2/3$ quarks, but since they are always subdominant, we omit these. Instead of recasting the constraints ourselves we make use of the recast performed in Ref. [14]. The authors recast two searches: a 7 TeV search by ATLAS searching

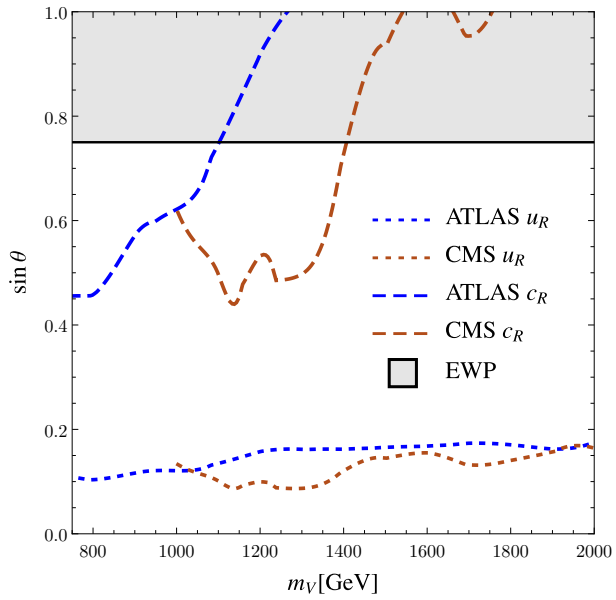

Figure 8.B.1: The constraints on the bidoublet model (reinterpreted from the work of [14]) arising from an ATLAS 7 TeV dedicated search for single production of VLQs [39], a CMS 8 TeV search for W/Z-tagged dijet resonances [40], and electroweak precision (EWP). Areas above the lines are excluded. Here we neglected effects due to additional decay channels of the vector-like-quarks into the scalars in our model.

for the bidoublet model (without the additional scalar triplet) [39] and an 8 TeV search for excited quarks [41] with a similar final state which is not optimized for the single production of vector-like-quarks but shares a similar final state. The two searches have competitive limits. Additionally there are constraints on pair production of VLQs, however these are subdominant in the mass ranges we are interested in. In particular ATLAS has performed a search for VLQs decaying to Wj finding a limit around 700 GeV for a single VLQ [42]. With two copies of such VLQs the limits strengthen but do not extend past 800 GeV. Furthermore, electroweak precision places an additional constraint from additional contributions to the S parameter [17]. One might worry that the additional scalar would complicate the limits, in particular the VLQs can decay to the scalar weakening the constraints. In general these branching ratios are $\lesssim 10\%$ and we ignore such effects

in our discussion.

Our goal is now to convert the single production limits quoted Ref. [14] into our (closely related) framework. In Ref. [14] the authors study a bidoublet model but with an additional VLQ singlet which they denote as $\tilde{U}$. We can decouple the particle to match with our framework. Multiplying their cross sections by the correction factor,

$$s_\theta^2 \left[\cos \frac{v}{f} \sin \left(\tan^{-1} \left(\frac{y_R f}{m_V} \sin \frac{v}{f} \right) \right) \right]^{-2} \tag{8.52}$$

with $f = 600$ GeV, $v \simeq 246$ GeV, and $y_R = 1$ gives the cross sections in our case. Employing this procedure we obtain the limits shown in figure 8.B.1.

BIBLIOGRAPHY

[1] ATLAS collaboration, *Search for resonances decaying to photon pairs in 3.2 fb^{-1} of pp collisions at $\sqrt{s}$ = 13 TeV with the ATLAS detector*, Tech. Rep. ATLAS-CONF-2015-081, CERN, Geneva, Dec, 2015.

[2] CMS collaboration, *Search for new physics in high mass diphoton events in proton-proton collisions at $\sqrt{s} = 13$ TeV*, Tech. Rep. CMS-PAS-EXO-15-004, CERN, Geneva, 2015.

[3] R. Franceschini, G. F. Giudice, J. F. Kamenik, M. McCullough, A. Pomarol, R. Rattazzi et al., *What is the gamma gamma resonance at 750 GeV?*, 1512.04933.

[4] S. Knapen, T. Melia, M. Papucci and K. Zurek, *Rays of light from the LHC*, 1512.04928.

[5] X.-F. Han, L. Wang, L. Wu, J. M. Yang and M. Zhang, *Explaining 750 GeV diphoton excess from top/bottom partner cascade decay in two-Higgs-doublet model extension*, 1601.00534.

[6] F. P. Huang, C. S. Li, Z. L. Liu and Y. Wang, *750 GeV Diphoton Excess from Cascade Decay*, 1512.06732.

[7] J. Liu, X.-P. Wang and W. Xue, *LHC diphoton excess from colorful resonances*, 1512.07885.

[8] A. Berlin, *Diphoton and diboson excesses in a left-right symmetric theory of dark matter*, *Phys. Rev.* **D93** (2016) 055015, [1601.01381].

[9] J. Bernon, A. Goudelis, S. Kraml, K. Mawatari and D. Sengupta, *Characterising the 750 GeV diphoton excess*, 1603.03421.

[10] V. De Romeri, J. S. Kim, V. Martin-Lozano, K. Rolbiecki and R. R. de Austri, *Confronting dark matter with the diphoton excess from a parent resonance decay*, 1603.04479.

[11] P. Agrawal, J. Fan, B. Heidenreich, M. Reece and M. Strassler, *Experimental Considerations Motivated by the Diphoton Excess at the LHC*, 1512.05775.

[12] A. Kobakhidze, F. Wang, L. Wu, J. M. Yang and M. Zhang, *750 GeV diphoton resonance explained as a heavy scalar in top/bottom seesaw model*, 1512.05585.

[13] P. S. B. Dev, R. N. Mohapatra and Y. Zhang, *Quark Seesaw, Vectorlike Fermions and Diphoton Excess*, 1512.08507.

[14] C. Delaunay, T. Flacke, J. Gonzalez-Fraile, S. J. Lee, G. Panico and G. Perez, *Light Non-degenerate Composite Partners at the LHC*, *JHEP* **02** (2014) 055, [1311.2072].

[15] K. Agashe, R. Contino, L. Da Rold and A. Pomarol, *A Custodial symmetry for $Zb\bar{b}$*, *Phys. Lett.* **B641** (2006) 62–66, [hep-ph/0605341].

[16] A. Atre, M. Carena, T. Han and J. Santiago, *Heavy Quarks Above the Top at the Tevatron*, *Phys. Rev.* **D79** (2009) 054018, [0806.3966].

[17] A. Atre, G. Azuelos, M. Carena, T. Han, E. Ozcan, J. Santiago et al., *Model-Independent Searches for New Quarks at the LHC*, *JHEP* **08** (2011) 080, [1102.1987].

[18] M. Redi and A. Weiler, *Flavor and CP Invariant Composite Higgs Models*, *JHEP* **11** (2011) 108, [1106.6357].

[19] T. Flacke, J. H. Kim, S. J. Lee and S. H. Lim, *Constraints on composite quark partners from Higgs searches*, *JHEP* **05** (2014) 123, [1312.5316].

[20] M. Redi, V. Sanz, M. de Vries and A. Weiler, *Strong Signatures of Right-Handed Compositeness*, *JHEP* **08** (2013) 008, [1305.3818].

[21] N. Vignaroli, *Early discovery of top partners and test of the Higgs nature*, *Phys. Rev.* **D86** (2012) 075017, [1207.0830].

[22] N. Vignaroli, *Discovering the composite Higgs through the decay of a heavy fermion*, *JHEP* **07** (2012) 158, [1204.0468].

[23] A. Atre, M. Chala and J. Santiago, *Searches for New Vector Like Quarks: Higgs Channels*, *JHEP* **05** (2013) 099, [1302.0270].

[24] J. F. Kamenik, B. R. Safdi, Y. Soreq and J. Zupan, *'Comments on the diphoton excess: critical reappraisal of effective field theory interpretations*, 1603.06566.

[25] A. Alloul, N. D. Christensen, C. Degrande, C. Duhr and B. Fuks, *FeynRules 2.0 - A complete toolbox for tree-level phenomenology*, *Comput. Phys. Commun.* **185** (2014) 2250–2300, [1310.1921].

[26] J. Alwall, R. Frederix, S. Frixione, V. Hirschi, F. Maltoni, O. Mattelaer et al., *The automated computation of tree-level and next-to-leading order differential cross sections, and their matching to parton shower simulations*, *JHEP* **07** (2014) 079, [1405.0301].

[27] A. Falkowski, O. Slone and T. Volansky, *Phenomenology of a 750 GeV Singlet*, *JHEP* **02** (2016) 152, [1512.05777].

[28] J. Gao, H. Zhang and H. X. Zhu, *Diphoton excess at 750 GeV: gluon-gluon fusion or quark-antiquark annihilation?*, 1512.08478.

[29] C. Cski, J. Hubisz and J. Terning, *Minimal model of a diphoton resonance: Production without gluon couplings*, *Phys. Rev.* **D93** (2016) 035002, [1512.05776].

[30] S. Fichet, G. von Gersdorff and C. Royon, *Scattering Light by Light at 750 GeV at the LHC*, 1512.05751.

[31] C. Csaki, J. Hubisz, S. Lombardo and J. Terning, *Gluon vs. Photon Production of a 750 GeV Diphoton Resonance*, 1601.00638.

[32] ATLAS collaboration, "Diphoton searches in ATLAS." Rencontres de Moriond, 2016.

[33] T. Sjostrand, S. Mrenna and P. Z. Skands, *A Brief Introduction to PYTHIA 8.1*, *Comput. Phys. Commun.* **178** (2008) 852–867, [0710.3820].

[34] DELPHES 3 collaboration, J. de Favereau, C. Delaere, P. Demin, A. Giammanco, V. Lematre, A. Mertens et al., *DELPHES 3, A modular framework for fast simulation of a generic collider experiment*, *JHEP* **02** (2014) 057, [1307.6346].

[35] R. D. Ball et al., *Parton distributions with LHC data*, *Nucl. Phys.* **B867** (2013) 244–289, [1207.1303].

[36] T. Hahn and M. Perez-Victoria, *Automatized one loop calculations in four-dimensions and D-dimensions*, *Comput. Phys. Commun.* **118** (1999) 153–165, [hep-ph/9807565].

[37] T. Hahn, *Generating Feynman diagrams and amplitudes with FeynArts 3*, *Comput. Phys. Commun.* **140** (2001) 418–431, [hep-ph/0012260].

[38] J. F. Gunion, H. E. Haber, G. L. Kane and S. Dawson, *The Higgs Hunter's Guide*, *Front. Phys.* **80** (2000) 1–448.

[39] ATLAS collaboration, *Search for Single Production of Vector-like Quarks Coupling to Light Generations in* 4.64 fb^{-1} *of Data at* $\sqrt{s} = 7$ *TeV*, .

[40] CMS collaboration, *Search for heavy resonances in the W/Z-tagged dijet mass spectrum in pp collisions at 8 TeV*, Tech. Rep. CMS-PAS-EXO-12-024, CERN, Geneva, 2013.

[41] CMS collaboration, CMS, *Search for heavy resonances in the W/Z-tagged dijet mass spectrum in pp collisions at 8 TeV*, .

[42] ATLAS collaboration, G. Aad et al., *Search for pair production of a new heavy quark that decays into a W boson and a light quark in pp collisions at* $\sqrt{s} = 8$ *TeV with the ATLAS detector*, *Phys. Rev.* **D92** (2015) 112007, [1509.04261].

CHAPTER 9

MIXED STOPS AND THE ATLAS ON-Z EXCESS

9.1 Introduction

Supersymmetry (SUSY) is a leading candidate for resolving the large hierarchy problem of the Standard Model. In the Minimal Supersymmetric Standard Model (MSSM) and simple extensions, a necessary feature for a complete resolution of the hierarchy problem is the presence of two light (sub-TeV) colored stops and one light left handed sbottom (to accompany the left handed stop). A common assumption in these models is an exact R-Parity, and the presence of a neutral, stable lightest Supersymmetric particle (LSP). In this case, if the third generation squarks are accompanied by a neutralino LSP, χ^0, then typical decays of these particles include $\tilde{t}_{1,2} \to t^{(*)}\tilde{\chi}^0$ (where the superscript on t indicates the possibility that it is off-shell), $\tilde{t}_2 \to \tilde{t}_1 Z$ and $\tilde{b}_1 \to b\tilde{\chi}^0$. The signatures of this scenario are therefore jets, missing transverse momentum (E_T^{miss}), leptons and b-tagged jets.

Dedicated searches for 3rd generation squarks have found no deviations from SM predictions, placing stringent constraints on its parameter space. On the other hand there remain significant windows allowing the mass of the lightest stop $m_{\tilde{t}_1}$ to be as light as 200 GeV, provided that there is a compressed spectrum which softens the p_T distributions of the final state particles. Intriguingly, a recent ATLAS search found a 3σ excess in final states containing a leptonically decaying Z boson, jets, and large E_T^{miss} [1]. They found 29 events in a combined signal region with expected SM background of 10.6 ± 3.2 events. We wish to explore the possibility that this excess is a first signal for direct production of t_2 followed by the decay $t_2 \to t_1 Z$[1].

[1] See [2] for other recent work on this signature

Various attempts have been made to explain this excess in terms of SUSY models[2] [4–12]. In all of these studies, pair produced colored particles (squarks or gluinos) decay into quarks and an uncolored particle, which then decays into a Z boson and an LSP. The principal challenge faced by these models is in explaining the ATLAS excess while simultaneously evading the many bounds imposed by other searches by ATLAS and CMS for multileptons or jets and $E_T^{\rm miss}$, as well as a similar CMS search for the same final state [13] which saw no excess over Standard Model (SM) backgrounds. This latter search imposed different cuts from the ATLAS search and so does not necessarily rule out new physics explanations for the ATLAS excess, yet it still imposes stringent constraints (see, e.g. [6]).

The phenomenology of the signal proposed in this paper differs from that of the aforementioned possibilities in several key respects. Firstly, the topology differs in that the Z boson is emitted at the first stage in the decay, rather than at the end with the LSP. This opens up the possibility that the CMS search is subject to significant background contamination, as we discuss at the end of section 9.4. More significantly, our scenario requires the presence of three new colored particles in the spectrum which are lighter than in previous explanations, the heaviest of which gives rise to the desired signature. Evading dedicated searches for these particles places very particular constraints on the mass splittings and decays of the squarks. As we shall discuss in section 9.2, this requires a compressed splitting between $\tilde{t}_1$ and $\tilde{\chi}^0$, and possibly also between $\tilde{t}_1$ and $\tilde{t}_2$. This in turn motivates the consideration of flavor violating decays of $\tilde{t}_1$ into $u\tilde{\chi}^0$ or $c\tilde{\chi}^0$, resulting from mixing between the right handed squarks. Such mixings have been discussed in recent years motivated by the question of natural SUSY and light stops [14–16], but without the Z decay necessary to explain this excess.

[2]See [3] for a discussion of this excess in the framework of Composite Higgs models.

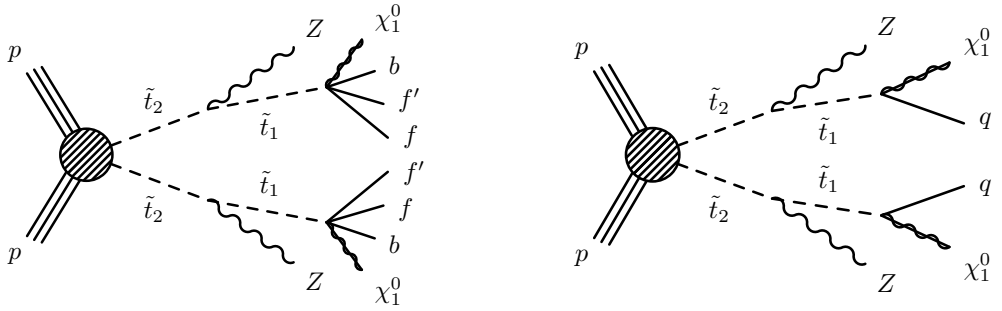

Figure 9.1: Flavor conserving (left) and flavor violating (right) decays contributing to the on-Z excess. In the flavor violating case, q can be either an up or a charm quark.

In section 9.2 we provide a systematic discussion of the possibilities that this minimal stop scenario affords for explaining the excess, identifying three distinct scenarios characterized by the mass splittings involved and the assumed decay mode for the light stop. We proceed in section 9.3 to describe the main experimental searches placing limits on these scenarios, and perform scans of their parameter spaces to find regions in which the excess can be explained while evading those limits in section 9.4. We also note the possibility that the signal topologies that we have identified could cause significant background contamination in the CMS on-Z search.

9.2 Model Overview

In this paper we assume a minimal model including two light stops, $\tilde{t}_1$ and $\tilde{t}_2$, and a left-handed sbottom $\tilde{b}_1$. We also require one neutralino LSP, $\tilde{\chi}^0$. As will be discussed below, the identity of this neutralino is not relevant to collider phenomenology for two of the scenarios that we consider, while for the third case it

will be assumed to be mostly Bino[3]. All other SUSY states are assumed to be heavier than these particles and decoupled. In the MSSM, the stop and sbottom mass matrices in the gauge-eigenbasis are given by [19]:

$$\mathbf{m}^{\mathbf{2}}_{\tilde{\mathbf{t}}} = \begin{pmatrix} m^2_{Q_3} + m^2_t + \Delta_{\tilde{u}_L} & v\left(a^*_t s_\beta - \mu y_t c_\beta\right) \\ v\left(a_t s_\beta - \mu^* y_t c_\beta\right) & m^2_{u_3} + m^2_t + \Delta_{\tilde{u}_R} \end{pmatrix}, \tag{9.1}$$

$$\mathbf{m}^{\mathbf{2}}_{\tilde{\mathbf{b}}} = \begin{pmatrix} m^2_{Q_3} + \Delta_{\tilde{d}_L} & v\left(a^*_b c_\beta - \mu y_b s_\beta\right) \\ v\left(a_b c_\beta - \mu^* y_b s_\beta\right) & m^2_{d_3} + \Delta_{\tilde{d}_R} \end{pmatrix}, \tag{9.2}$$

where m_{Q_3}, m_{u_3}, m_{d_3}, a_t , μ are soft SUSY breaking parameters, c_β and s_β denote the cosine and sine of β, and $\Delta_{\tilde{q}} = (T_{3\tilde{q}} - Q_{\tilde{q}} \sin^2\theta_W) c_{2\beta} m^2_Z$ with $T_{3\tilde{q}}$ and $Q_{\tilde{q}}$ denoting the third component of weak isospin and electric charge respectively. The Higgs vev v is ≈ 174GeV. We assume the right handed sbottom is decoupled, with $m^2_{\tilde{d}_3} \gg m^2_{Q_3}$. We replace the MSSM parameters in these mass matrices with physical parameters: the stop mass eigenstates $m_{\tilde{t}_1}$, $m_{\tilde{t}_2}$, and the mixing angle $0 < \theta_{\tilde{t}} < \pi/2$ which rotates the gauge-eigenstate basis into the mass basis

$$\begin{pmatrix} \tilde{t}_1 \\ \tilde{t}_2 \end{pmatrix} = \begin{pmatrix} c_{\theta_{\tilde{t}}} & -s^*_{\theta_{\tilde{t}}} \\ s_{\theta_{\tilde{t}}} & c_{\theta_{\tilde{t}}} \end{pmatrix} \begin{pmatrix} \tilde{t}_L \\ \tilde{t}_R \end{pmatrix}. \tag{9.3}$$

The sbottom mass is then given by

$$m^2_{\tilde{b}_1} = m^2_{\tilde{t}_1} c^2_{\theta_{\tilde{t}}} + m^2_{\tilde{t}_2} s^2_{\theta_{\tilde{t}}} - m^2_t - \Delta_{\tilde{u}_L} + \Delta_{\tilde{d}_L}. \tag{9.4}$$

We assume the decoupling limit for the Higgs sector, so that the Higgs mixing angle $\alpha = \beta - \pi/2$. The phenomenology of this simplified model varies only slightly with $\tan\beta$ and we therefore choose to fix $\tan\beta = 20$. The remaining free

[3]We do not want to address any cosmological issue in this work but let us notice that a stable Bino is overproduced in the early universe according to the usual thermal freeze-out calculation. On the other hand, a small $\tilde{t}_1$–$\tilde{\chi}^0$ mass splitting of $\mathcal{O}(30$ GeV allows for the possibility that the correct relic density results from stop-neutralino coannihilation [17, 18]. Alternative solutions simple solution are to assume a low reheating temperature or that that the Bino is actually the NLSP (for instance with a gravitino LSP) but still stable on detector lengths.

parameters in the model are $m_{\tilde{t}_1}$, $m_{\tilde{t}_2}$, $m_{\tilde{\chi}^0}$, and $c_{\theta_{\tilde{t}}}$. Even with such a modest amount of new particles, this model admits a rich phenomenology with many possible final states, depending mainly on the assumed mass splittings and mixings involved. We seek scenarios with a large branching ratio (BR) for $\tilde{t}_2 \to \tilde{t}_1 Z$, and which are poorly constrained by dedicated searches for $\tilde{t}_1$ and $\tilde{b}_1$. In the following subsections, we systematically discuss the various possibilities and present a categorization of interesting scenarios based on the assumptions made about the decays of $\tilde{t}_1$ and the mass splitting between $\tilde{t}_1$ and $\tilde{t}_2$.

9.2.1 $\tilde{\mathbf{t}}_1$ decays

The strongest constraints on the $\tilde{t}_1$ apply if it decays directly to a neutralino and on-shell top, leading to final states with large E_T^{miss}, hard b-jets, and leptons. We therefore take the splitting $m_{\tilde{t}_1} - m_{\tilde{\chi}^0} < m_t$, such that the only flavor-conserving decays that are kinematically available to the light stop are into the three- or four-body final states $Wb\tilde{\chi}^0$ or $ff'b\tilde{\chi}^0$ (where ff' are pairs of fermions that may be produced in the decay of an off-shell W). This allows $\tilde{t}_1$ to be as light as 300 GeV for generic values of this splitting, and as low as 200 GeV in some narrow windows of parameter space (see [20] for a detailed discussion).

Due to the substantial kinematic suppression of the partial width into these states, it is possible that flavor violating decays might dominate even with small couplings. This motivates our consideration of flavor violating decays. One well explored possibility arises even with Minimal Flavor Violation (MFV) [21], in which case it is possible that loop-induced decays into charm and neutralino can dominate over four-body decays [22]. In recent years an alternative scenario has been explored, that non-MFV mixings between right handed up-type squarks can

substantially alter stop phenomenology. Briefly, the essential point for our analysis is that the strongest constraints on the size of squark flavor mixings from low energy observables apply to the down sector, and on mixings between up and charm squarks. The constraints on the down sector also impose constraints on the left-handed up type squarks. Crucially, there are no direct constraints on $\tilde{t}_R - \tilde{c}_R$ or $\tilde{t}_R - \tilde{u}_R$ mixings individually, but only on their product (coming from the $D^0 - \bar{D}^0$ system). We refer readers to the papers [14–16] for a more detailed discussion. As a consequence, there may be size-able mixing between $\tilde{t}_R$ and $\tilde{c}_R$ or $\tilde{t}_R$ and $\tilde{u}_R$, but not both.

The degree of flavor mixing can be parameterized by the quantity $\epsilon \equiv (m^2_{\tilde{u}})_{i3}/(m^2_{\tilde{u}})_{ii}$, where $m^2_{\tilde{u}}$ is the up-type squark mass matrix in the Super-CKM basis and i is 1 or 2. We do not require $\mathcal{O}(1)$ mixings in order to change the decay patterns of the lightest stop, so long as it has an $\mathcal{O}(1)$ admixture of $\tilde{t}_R$. In particular, in the four-body region[4], $\epsilon \gtrsim 10^{-3}$ is sufficient for the decay $\tilde{t}_1 \to q\tilde{\chi}^0$ to occur at least 90% of the time, while $\epsilon \gtrsim 10^{-2}$ is sufficient for much of the three-body region. These flavor-mixing angles are sufficiently small not to play a noticeable role in the phenomenology of the $\tilde{t}_2$, and are relevant for $\tilde{t}_1$ only because its flavor-conserving decays are heavily suppressed. It can also be assumed that $(m^2_{\tilde{u}})_{ii} \gg (m^2_{\tilde{u}})_{33}$, such that despite introducing a small admixture of first or second generation squark flavor into the two dominantly stop mass eigenstates, the other mass eigenstates are beyond reach of the first run of the LHC.

We therefore consider separately scenarios where $\tilde{t}_1$ undergoes a flavor-conserving decay (denoted $\mathrm{F_C}$), or a flavor violating one ($\not{\mathrm{F}}$). In either case we will

[4]Even when talking about flavor violating two-body decays, we find it convenient to label the regions of parameter space in the $\tilde{t}_1, \tilde{\chi}^0$ plane by the possible flavor conserving decays. The 'three-body region' is defined by $m_W + m_b < m_{\tilde{t}_1} - m_{\tilde{\chi}^0} < m_t$, while the 'four-body region' is defined by $m_b < m_{\tilde{t}_1} - m_{\tilde{\chi}^0} < m_W + m_b$.

assume a 100% BR for the light stop for simplicity, though as pointed out in [23] the limits on light stops can be substantially reduced for mixed $\not{F}$ and F_C decays. The flavor violating decay may be into $u\tilde{\chi}^0$ or $c\tilde{\chi}^0$, but not both. The only difference this makes regarding collider phenomenology is that the constraints on final states containing charm quarks are often stronger than on up quarks, due to significant progress made on charm flavor tagging by the experimental collaborations. This will be discussed in more detail in section 9.3. It should be noted that the precise measurement of the neutron Electric Dipole Moment (EDM) places constraints on $\tilde{t}_R - \tilde{u}_R$ mixing in the presence of large stop L-R mixing as exists in our model. This comes from loop contributions to the up quark EDM involving gluinos, and depends sensitively on details about the particles which we have assumed to be decoupled in our scenario. Nonetheless, it is demonstrated in [24] that $\epsilon \lesssim 10^{-2}$ can be consistent with the EDM constraints without making unnatural assumptions about the masses of the other particles, or about cancellations between different contributions.

9.2.2 $\tilde{t}_2$ decays

The second important distinction to be made between different classes of scenarios relates to the mass splitting between $\tilde{t}_2$ and $\tilde{t}_1$, and the role that this plays in determining the branching ratios of the three squarks. For sufficiently large mass splittings, the possible two-body decays of the heavy stop are $\tilde{t}_2 \to \tilde{t}_1 Z$, $\tilde{t}_2 \to \tilde{t}_1 h$, $\tilde{t}_2 \to \tilde{b}_1 W^+$ and $\tilde{t}_2 \to t\tilde{\chi}^0$. The BRs into these states are most sensitive to the mixing angle $c_{\theta_{\tilde{t}}}$, and for splitting 150 GeV $\lesssim m_{\tilde{t}_2} - m_{\tilde{t}_1} \lesssim$ 300 GeV the BR into $Z\tilde{t}_1$ is maximized at a value between $0.6 \lesssim \mathrm{BR}(\tilde{t}_2 \to \tilde{t}_1 Z) \lesssim 0.8$ for $0.5 \lesssim c_{\theta_{\tilde{t}}} \lesssim 0.55$, as illustrated in Fig. (9.1). Since we are interested in maximizing the $\tilde{t}_2 \to \tilde{t}_1 Z$

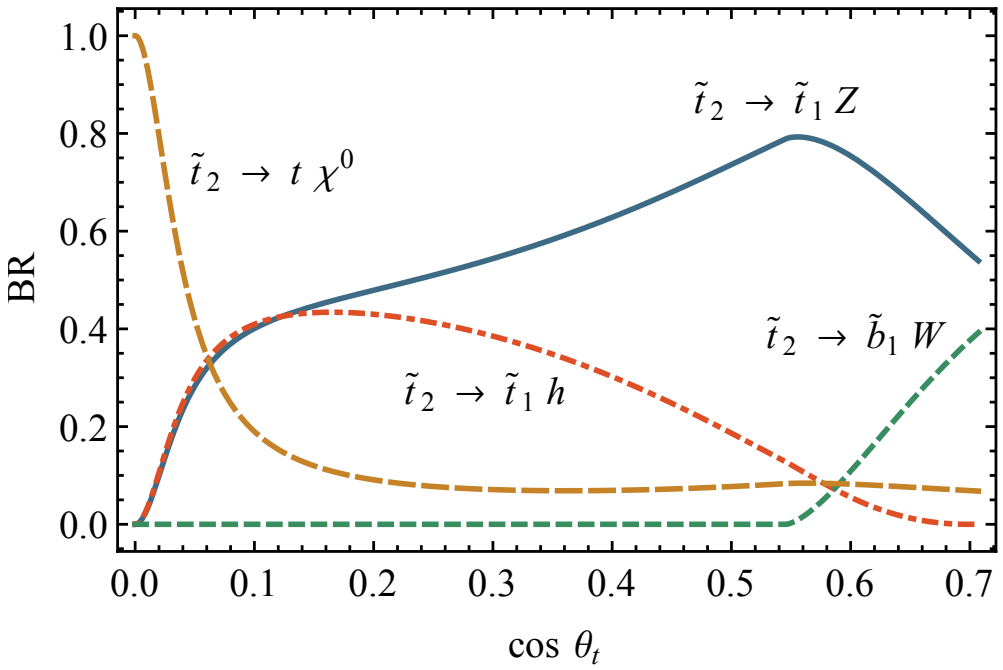

Figure 9.1: Heavy stop branching ratios in the split scenario, for $m_{\tilde{t}_2} = 450$ GeV, $m_{\tilde{t}_1} = 250$ GeV, $m_{\tilde{\chi}^0} = 210$ GeV, $\tan\beta = 20$.

BR we can use this to fix the mixing angle. This class of scenario, which we label 'split', has a three-dimensional parameter space in $m_{\tilde{t}_1}$, $m_{\tilde{t}_2}$ and $m_{\tilde{\chi}^0}$. Note that for small $\cos\theta_t$, $\tilde{t}_1$ and $\tilde{b}_1$ are almost degenerate and hence the decay $\tilde{t}_1 \to \tilde{b}_1 W$ is not kinematically available.

An interesting alternative is that the $\tilde{t}_2 - \tilde{t}_1$ mass splitting is sufficiently small that the only two-body decay kinematically allowed for $\tilde{t}_2$ is $\tilde{t}_2 \to \tilde{t}_1 Z$. For $m_{\tilde{t}_1} - m_{\tilde{t}_2} < m_h$, the decay $\tilde{t}_2 \to \tilde{t}_1 h$ is forbidden. For a wide range of $c_{\theta_{\tilde{t}}}$, the decay $\tilde{t}_2 \to \tilde{b}_1 W^+$ is not kinematically available. Finally, if $m_{\tilde{t}_1} + m_Z < m_{\tilde{t}_2} < m_t + m_{\tilde{\chi}^0}$, the only two-body decay that is kinematically available is the Z decay. Combining the bounds gives the requirement that $m_{\tilde{t}_1} - m_{\tilde{\chi}^0} < m_t - m_Z \approx 85$ GeV. Coincidentally, this turns out to overlap almost exclusively with the four-body region, which is defined by $m_{\tilde{t}_1} - m_{\tilde{\chi}^0} < m_W + m_b \approx 85$ GeV. This condition defines what we call the 'compressed' scenarios, in which the only two-body decay available to the

heavy stop is into $\tilde{t}_1 Z$. The $\tilde{t}_2$ BRs are therefore insensitive to $c_{\theta_{\tilde{t}}}$ in this regime. This parameter does control the mass, and therefore also the decays of $\tilde{b}_1$. A heavy $\tilde{b}_1$ can decay into $\tilde{t}_1 W^-$, but if this is not available it will have $\sim 100\%$ BR into $b\tilde{\chi}^0$. For generic mass splittings this decay is highly constrained by dedicated searches, but having chosen small splittings for $\tilde{t}_1 - \tilde{\chi}^0$ and $\tilde{t}_2 - \tilde{t}_1$, this automatically places also the sbottom decay into the compressed regime in which this channel is particularly challenging for experimental searches. As we shall discuss in more detail in section 9.3, for a broad range of stop mixing angles the sbottom lies in a funnel of parameter space not constrained by these searches.

9.2.3 Three Scenarios

Four combinations of $\mathrm{F_C}$ versus $\not{\mathrm{F}}$ and split versus compressed are possible. Flavor conserving split ($\mathrm{F_C}$ -S) is the most highly constrained by dedicated searches, and we have been unable to find a region of its parameter space which permits an explanation of the Z excess without being excluded by other searches. We therefore do not discuss this possibility in detail in this paper. Three combinations remain, which are summarized in table (9.1). For the compressed scenarios, we choose $m_{\tilde{t}_2} - m_{\tilde{t}_1} = 100$ GeV and explore the $m_{\tilde{t}_1} - m_{\tilde{\chi}^0}$ plane. We set the branching ratios $\mathrm{BR}(\tilde{t}_2 \to \tilde{t}_1 \tilde{\chi}^0) = 1$ and $\mathrm{BR}(\tilde{b}_1 \to b\tilde{\chi}^0) = 1$. In principle, $\tilde{t}_2$ also has competing three-body decays to $\tilde{b}_1$, but these are sensitive to $m_{\tilde{b}_1}$ and would have a BR no more than $\mathcal{O}(5\%)$. We neglect this effect for simplicity. For the split scenario, we explore $\tilde{t}_2 - \tilde{t}_1$ mass splittings between 125 and 300 GeV, choosing $c_{\theta_{\tilde{t}}} = 0.5$ which is close to the optimal value for maximizing $\mathrm{BR}(\tilde{t}_2 \to \tilde{t}_1 Z)$ over most of the parameter space. This angle then also sets the BRs for the $\tilde{b}_1$. We also compute the $\tilde{t}_2 \to t\tilde{\chi}^0$ and $\tilde{b}_1 \to b\tilde{\chi}^0$ BRs assuming a Bino LSP.

Scenario	$\tilde{t}_1$ decay	$m_{\tilde{t}_2} - m_{\tilde{t}_1}$	BR($\tilde{t}_2 \to \tilde{t}_1 Z$)
F_C-C	$ff'b\tilde{\chi}^0$	100 GeV	1
$\not{F}$-C	$c\tilde{\chi}^0$ / $u\tilde{\chi}^0$	100 GeV	1
$\not{F}$-S	$c\tilde{\chi}^0$ / $u\tilde{\chi}^0$	(125 – 300) GeV	0.7 ± 0.1

Table 9.1: The three scenarios considered in this paper, labeled Flavor Conserving Compressed, Flavor Violating Compressed, and Flavor Violating Split. The F_C /$\not{F}$ designation refers to the decays of $\tilde{t}_1$, and the compressed/split designation refers to the splitting between $\tilde{t}_2$ and $\tilde{t}_1$.

9.3 Relevant searches

ATLAS and CMS have a wealth of searches looking for large MET with all types of additional particles in the final state, each potentially providing a limit on stop and sbottom production. Since in general $\tilde{t}_1, \tilde{t}_2$, and $\tilde{b}_1$ will contribute to each bound, the constraints needs to be recast with care. Our goal is to examine all the parameter space with the simplified topology discussed in section 9.2. For the compressed cases this involves a scan in the $m_{\tilde{\chi}^0} - m_{\tilde{t}_1}$ plane while for the split case it involves a scan in both $m_{\tilde{\chi}^0} - m_{\tilde{t}}$ and $m_{\tilde{t}_1} - m_{\tilde{t}_2}$. We will be exploring scenarios with compressed mass splittings, especially between $\tilde{t}_1$ and $\tilde{\chi}^0$. This is a region that is very challenging experimentally. The most robust and model-independent limits in the most compressed regime come from dedicated searches for events with a hard jet coming from Initial State Radiation (ISR), which do not depend sensitively on the details of the $\tilde{t}_1$ decay. Searches for jets and E_T^{miss} are highly constraining for spectra with a large splitting between the LSP and colored particles, but are challenging to interpret in the compressed regime where there are large systematic uncertainties. Searches involving b-tagged jets place important limits on some of our decay channels. Finally, there are dedicated searches for events containing Z bosons which could be sensitive to our model. We discuss the details of these searches in the following subsections, beginning with the ATLAS on-Z search with

a 3σ excess.

9.3.1 ATLAS on-Z

The ATLAS on-Z search looked for final states with two leptons with invariant mass around the Z-pole, $E_T^{\text{miss}} > 225$ GeV, and $H_T \equiv p_T^{\ell_1} + p_T^{\ell_2} + \sum_{i\in\text{jets}} p_T^i >$ 600 GeV. The H_T and E_T^{miss} cuts pick out events with large kinetic energies. ATLAS found 16 events (4.2 ± 1.6 expected) in the electron channel and 13 events (6.4 ± 2.2 expected) in the muon channel for a total of 29 events (10.6 ± 3.2 expected). Running pseudo-experiments they concluded that this corresponds to a 3.0σ deviations from the SM.

To estimate the number of events needed to explain the signal we use a log-likelihood method and profile over the background uncertainties using a Gaussian approximation. Using asyptotic formulae [25] to establish two-sided convidence limits (CL), we find that a minimum of 7.1 (12.4) signal events are required to be consistent with the excess at the 95% (68%) CL.

9.3.2 CMS on-Z

CMS performed a search analogous to that done by ATLAS, looking for events with opposite-sign same-flavor leptons and E_T^{miss} [13] which provides an important constraint on our model. CMS split their on-Z signal regions into six bins, depending on jet multiplicity and E_T^{miss}. Three bins measure events with $n_{\text{jets}} \geq 2$, and three use $n_{\text{jets}} \geq 3$. Our signal model does not produce a significant number of 2-jet events, and we therefore place constraints on our scenarios using the 3-jet

inclusive bins which have higher expected sensitivity. The three bins in this category are split into the following E_T^{miss} windows: 100 GeV $< E_T^{\text{miss}} <$ 200 GeV, 200 GeV $< E_T^{\text{miss}} <$ 300 GeV, $E_T^{\text{miss}} >$ 300 GeV. We use the most constraining of these bins to constrain our scenarios at each point in parameter space, using the 95% CL_s limit to set bounds [26]. In our scans (described in section 9.4) We found that the mid E_T^{miss} bin usually provides the dominant limit, but the high E_T^{miss} bin is sometimes competitive. The low E_T^{miss} bin is never competitive with the other two in our simulations.[5]

9.3.3 $\tilde{t}_2 \to \tilde{t}_1 Z$

Searches for the signal $\tilde{t}_2 \to \tilde{t}_1 Z$ at 8 TeV have been performed both by ATLAS [27] and CMS [28]. The searches have competitive bounds, with ATLAS having a slightly better exclusion. For simplicity we only use the ATLAS search to place bounds on the F_C-C scenario. The main cuts in this search are on the invariant mass of the leptons (which are required to be around the Z pole), the number of jets, number of leptons, and the p_T of the reconstructed Z. We find that the reach of the search is limited in the compressed regime, both due to the small $\tilde{t}_2$–$\tilde{t}_1$ splitting and the small $\tilde{t}_1$–$\tilde{\chi}^0$ splitting. Firstly, the search regions requiring two leptons require a boosted Z candidate which is suppressed in the F_C-C scenario by the small $\tilde{t}_2$–$\tilde{t}_1$ splitting. Secondly, we find that the soft leptons and b-jets coming from the decay of $\tilde{t}_1$ in the 4-body regime reduce the acceptance in the 3-lepton bins and the b-tagging efficiency. Having recasted this search for the F_C-C scenario, we find that it does not place competitive limits and we therefore omit it from our

[5] A possible concern is that the combined limit from different bins could be more severely constraining. We find that usually only one bin is constraining and we do not expect a combination to notably alter the limits.

scans. We note that the CMS search is optimised for mass spitting $m_{\tilde{t}_1} - m_{\tilde{\chi}^0} \simeq m_t$ and has potential sensitivity to our F_C-C scenario only in its 3-lepton bins, and will therefore also have degraded sensitivity in the 4-body region.

9.3.4 Jets+MET+0/1 lepton

The MSSM-inspired jets+MET searches[6] provide an important constraint on our scenarios as $\tilde{t}_1, \tilde{t}_2$, and $\tilde{b}_1$ can all contribute to this signal. ATLAS [29] and CMS [30] have both performed searches for this signature at 8 TeV and interpreted them in terms of a variety of SUSY models, including direct production of squarks decaying via $\tilde{q} \to j\tilde{\chi}^0$ (which is identical to $\tilde{t}_1$ in the $\not{F}$ scenarios). In this work we focus on the 200 GeV $\lesssim m_{\tilde{t}_1} \lesssim$ 350 GeV region but CMS only presents limits for $m_{\tilde{q}} \gtrsim 300$ GeV. Thus to study the bounds from these searches we use the ATLAS analysis. Jets + MET searches in these regions are particularly challenging due to the low p_T of the outgoing particles. As a consequence their search does not constrain single squark production decaying in this channel for $m_{\tilde{\chi}^0} > 160$ GeV. Another key factor which limits the reach of this search in the compressed regime is the systematic uncertainty on the (acceptance $\times$ efficiency) associated with the high sensitivity to ISR. ATLAS provides uncertainties for each signal region in their auxiliary material (available on the ATLAS public results website), and these range from 10% to 50% in constraining bins.

In order to interpret the results of this search in terms of limits on our scenarios, it is necessary to combine the contributions from $\tilde{t}_2$, $\tilde{t}_1$ and $\tilde{b}_1$. Each of these

[6]It was pointed out in [16] that searches using shape-based analyses might have better sensitivity for $\tilde{t}_1 \to j\tilde{\chi}^0$ then jets+MET in the limit of small $m_{\tilde{t}_1} - m_{\tilde{\chi}^0}$. The bounds were computed using 7 TeV data and are not constraining compared to the 8 TeV jets+MET search. It would be interesting to see how these would change with the full 8 TeV data set.

channels will come with its own set of uncertainties which vary from bin-to-bin. Without a dedicated detector simulation it is not possible to robustly account for these effects. Instead, we estimate reasonable sizes for these uncertainties and study the effects of varying these assumptions. The ATLAS collaboration also interpreted their results in terms of some multi-step decay chains, and find uncertainties that range from 10% to 80% in similarly compressed regimes. Using the 'r' method[7] [31], we find good agreement with the ATLAS exclusion on $\tilde{t}_1$ if we assign a uniform systematic uncertainty of 30% on its signal strength across all signal regions We then assign a nominal 30% uncertainty also on the $\tilde{t}_2$ and $\tilde{b}_1$ contributions, consistent with the aforementioned uncertainties quoted by the ATLAS collaboration for other compressed multi-step decay processes. In order to asses the sensitivity of our results to this choice, we also vary the uncertainty on the $\tilde{t}_2$ and $\tilde{b}_1$ channels to 20% and 40%. We used CheckMATE [31] to apply this technique to all our scenarios however we found the bounds of this search to be subdominant in all cases except for the $\not{F}$-S case. This is because this is the only scenario in which we venture close to the existing bounds on $\tilde{q} \to j\tilde{\chi}^0$, where a combination with the other channels might then result in an exclusion.

In addition to jets+MET there are searches which require an additional isolated lepton by both ATLAS [32] and CMS [33], which are potentially sensitive to the F_C-C scenario. However, the limits on the light stop are weaker than the other limits which we consider for this search, and we find that the heavy stop production does not contribute significantly to this signal. We therefore do not include this limit in our scans.

[7] In the r-method, a signal is excluded if $r \equiv (S - 1.96\Delta S)/S_{95}^{\rm obs} > 1$, where ΔS is the systematic uncertainty on the signal strength and $S_{95}^{\rm obs}$ is the limit on the signal strength at the 95% confidence limit.

9.3.5 Sbottom bounds

The sbottom mass is determined by the mixing angle as given in eq. (9.4). The phenomenology of the sbottom differs substantially between the compressed and split scenarios. In the compressed scenario, the only two-body final state available for it to decay into is $b\tilde{\chi}^0$. Furthermore, the mixing angle is a free parameter since the branching ratio of $\tilde{t}_2 \to \tilde{t}_1 Z$ is fixed to 1 by the kinematics. On the other hand, in the split scenario this mixing angle is fixed at $c_{\theta_{\tilde{t}}} = 0.5$ and the sbottom decays almost exclusively into $\tilde{t}_1 W$ in most of the parameter space.

The $\tilde{b}_1 \to b\tilde{\chi}^0$ decay of the compressed scenarios is constrained by dedicated CMS and ATLAS searches [34, 35], and we focus on the ATLAS analysis because it places stronger limits in the compressed regime. This search places strong limits on this channel, but allows for a sbottom with mass $m_{\tilde{b}_1} \simeq 250$ GeV if it has a small mass splitting with the neutralino. We also require that the sbottom is heavy enough to forbid the decay $\tilde{t}_2 \to \tilde{b}_1 W$, i.e., $m_{\tilde{t}_2} < m_{\tilde{b}_1} + m_W$ or in terms of $\tilde{t}_2 - \tilde{t}_1$ mass splitting, $m_{\tilde{b}_1} > m_{\tilde{t}_1} + \Delta m_{\tilde{t}} - m_W$. Combining the bounds gives

$$m_{\tilde{t}_1} < m_{\tilde{b}}^{\lim}(m_{\tilde{\chi}^0}) - \Delta m_{\tilde{t}} + m_W \tag{9.5}$$

where $m_{\tilde{b}}^{\lim}(m_{\tilde{\chi}^0})$ is the maximum allowed value of the sbottom mass for each $m_{\tilde{\chi}^0}$, coming from the ATLAS limit. This provides an additional constraint on the possible values in the $m_{\tilde{\chi}^0}, m_{\tilde{t}_1}$ plane. The additional $\tilde{t}_1$, $\tilde{t}_2$ production channels are not expected to contribute significantly to this search.

In the split scenario, $\not{F}$-S , the sbottom decays predominantly in $\tilde{b}_1 \to \tilde{t}_1 W \to j\tilde{\chi}^0 W$. While there are no direct searches for this signal, there are searches for $\tilde{q} \to \chi^{\pm} W \to j\tilde{\chi}^0 W$. We have checked the constraints due to this signal and found

that we are well within experimental bounds for all regions of parameter space.

9.3.6 Single high p_T jet + $0, 1, 2$ lepton

In this work we are primarily interested in regions of parameter space with small $\tilde{t}_1 - \tilde{\chi}^0$ splitting where many jets may not pass the p_T cuts. In this case we have additional constraints from monojet searches. This search has been done by ATLAS for both $\tilde{t}_1 \to j\tilde{\chi}^0$ and $\tilde{t}_1 \to bffW$ stop decay modes in a search by ATLAS [36]. For the split case $\tilde{t}_1$ is the only production channel which can replicate this signal, but in the compressed cases the $\tilde{b}_1 \to b\tilde{\chi}^0$ could provide additional monojet events. To this end we recast the search including just $\tilde{t}_1$ production and both $\tilde{t}_1$ and $\tilde{b}_1$ but we found comparable exclusions. For this reason we simply include the constraints computed by ATLAS directly in our analysis.

CMS has performed a search for events with a high momentum ISR jet with the additional requirement of one or two soft leptons [37]. The preliminary results of this search provide the strongest existing constraints on the 4-body region of flavor-conserving $\tilde{t}_1$ decays, sensitive to stop masses up to 320 GeV. The strongest bounds are derived from the 2-lepton signal region, and we therefore expect this limit to be highly sensitive to the $\tilde{t}_1$ BR.

9.3.7 Charm-tagging

A final constraint on our signals are charm-tagging searches. ATLAS has two searches that employ charm-tagging looking for both $\tilde{t}_1 \to c\tilde{\chi}^0$ [36] as well as $\tilde{c} \to c\tilde{\chi}^0$ [38]. The $\tilde{t}_1 \to c\tilde{\chi}^0$ search assumes the stop is in the four-body regime

and hence is optimized for our signal. For this reason it has better sensitivity in our region of interest. For this reason we omit it from our plots.

The c-tagging searches put constraints on $\not{F}$ models which involve charm. For the $\not{F}$-S split scenatrio we find that these constraints rule out the region preferred by the ATLAS on-Z excess at the 95% CL. For this reason in this scenario we assume $\tilde{t}_1$ decays to $u\tilde{\chi}^0$. For the $\not{F}$-C scenario the constraints are milder since we are exploring relatively large $m_{\tilde{t}_1}$ values. Recasting the $\tilde{t}_1 \to c\tilde{\chi}^0$ search we find that the limits on this scenario comparable to those directly on $\tilde{t}_1$ alone, and thus we use the limits on this channel that are provided in [36].

9.4 Scan

For the scan we use Madgraph 5 v2.2.3 [39], Pythia 6.4 [40], and PGS [41], including 1-jet matching. For jet clustering we use anti-kT algorithm with $\Delta R = 0.4$. To roughly account for next-to-leading order (NLO) effects we rescale our cross sections to their NLO values calculated by the SUSY Cross Sections group [42]. For jets+MET and double-checking monojet constraints we use CheckMATE [31], which makes use of DELPHES 3 [43], FastJet [44], and the anti-kT clustering algorithm [45]. For the compressed scenarios, F_C-C and $\not{F}$-C , there is one less free parameter (since the range of $m_{\tilde{t}_2}$ has a relatively small range of viable options). We can perform a two dimensional scan over $m_{\tilde{t}_1} - m_{\tilde{\chi}^0}$. $\not{F}$-S requires a 3 dimensional scan but for simplicity we scan over two slices in the parameter space.

The scan showing the signal as well as limits from the different searches is shown in Fig. (9.1), with the regions preferred by the ATLAS on-Z excess indicated by green shading and the contours labelling the 90% and 68% two-sided confidence

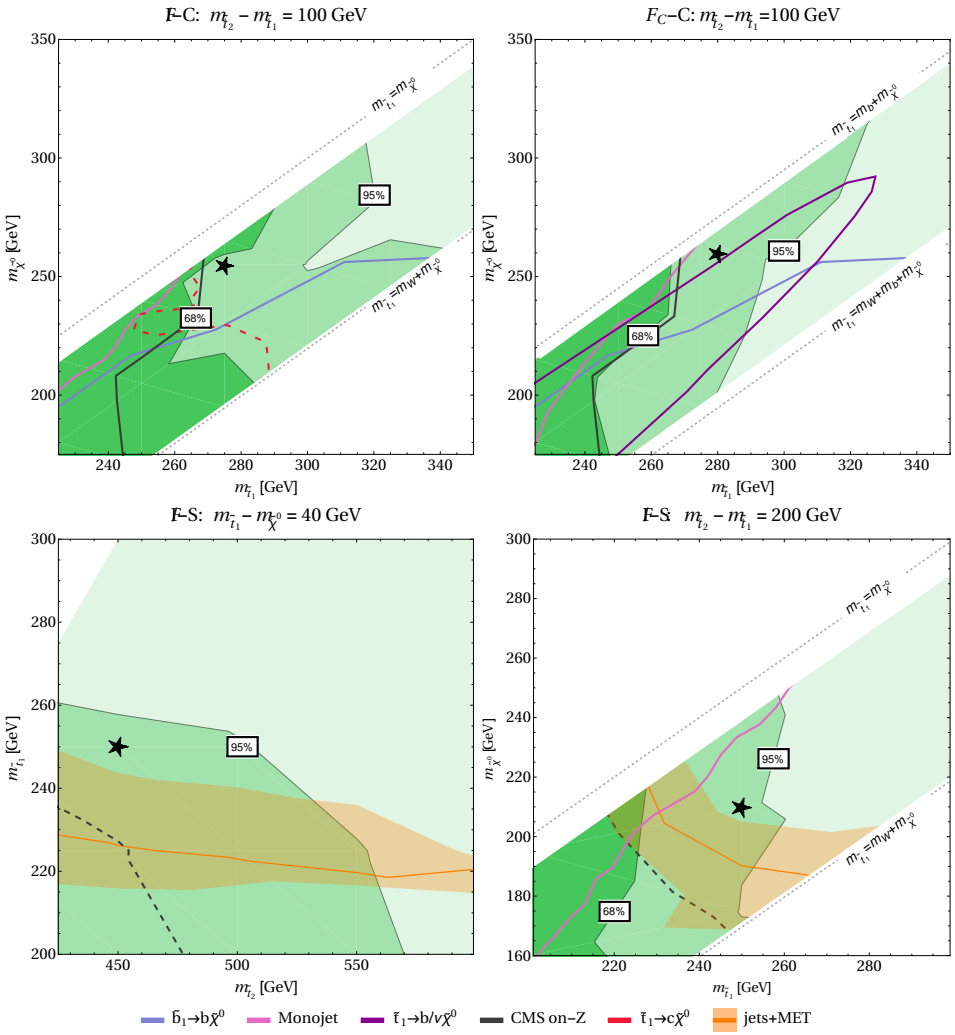

Figure 9.1: Scans of the three scenarios. The regions favoured by the ATLAS on-Z excess are shaded green, with contours indicating 95% and 68% confidence intervals. Additional solid lines indicate the 95% limits described in the text. The dashed lines indicate limits under specific model assumptions that do not necessarily apply, as described in the text. The band on the jets+MET limit illustrates the considerable uncertainty on the strength of this limit. Black stars indicate the benchmark points chosen from each scenario, and they also indicate the region of parameter space that is not excluded by the other searches.

Benchmark	$m_{\tilde{t}_2}$ [GeV]	$m_{\tilde{t}_1}$ [GeV]	$m_{\tilde{\chi}^0}$ [GeV]	p-value
F_C-C	380	280	260	0.095
$\not{F}$-C	370	275	255	0.17
$\not{F}$-S	450	250	210	0.055

Table 9.1: Benchmark points chosen from the three scenarios. All other parameters are as described in section 9.2. The two-tailed p-values are calculated as described in section 9.3.1, and a p-value of 1 would represent perfect agreement with the measured total event rate.

intervals. The constraining 95% confidence intervals discussed in section 9.3 are shown by solid lines. The dashed line in the $\not{F}$-C scan indicates the limit on the decay $\tilde{t}_1 \to c\tilde{\chi}^0$, though the alternate decay $\tilde{t}_1 \to u\tilde{\chi}^0$ is also possible and not constrained by this line. The CMS on-Z limit in the $\not{F}$-S scenarios is dashed as it has been calculated assuming no background contamination. As we shall discuss below, considerable background contamination is expected which severely limits the sensitivity of the CMS search to this scenario. The jets+MET limit in the $\not{F}$-S scenario is plotted with a band indicating the large uncertainties associated with this search in the compressed regime, as discussed in section 9.2. The central line assumes a systematic uncertainty on the signal from all channels and in all bins of 30%. The band is obtained by varying the uncertainty on the $\tilde{t}_1$ and $\tilde{b}_1$ production channels to 20% and 40%.

These plots indicate that all three scenarios can be consistent with the ATLAS on-Z excess at the 90% level and the two compressed scenarios at the 1σ level, allowing for as many as 14 signal events. From each scenario we have chosen a benchmark point indicated by a black star in Fig. (9.1), and detailed in table (9.1).

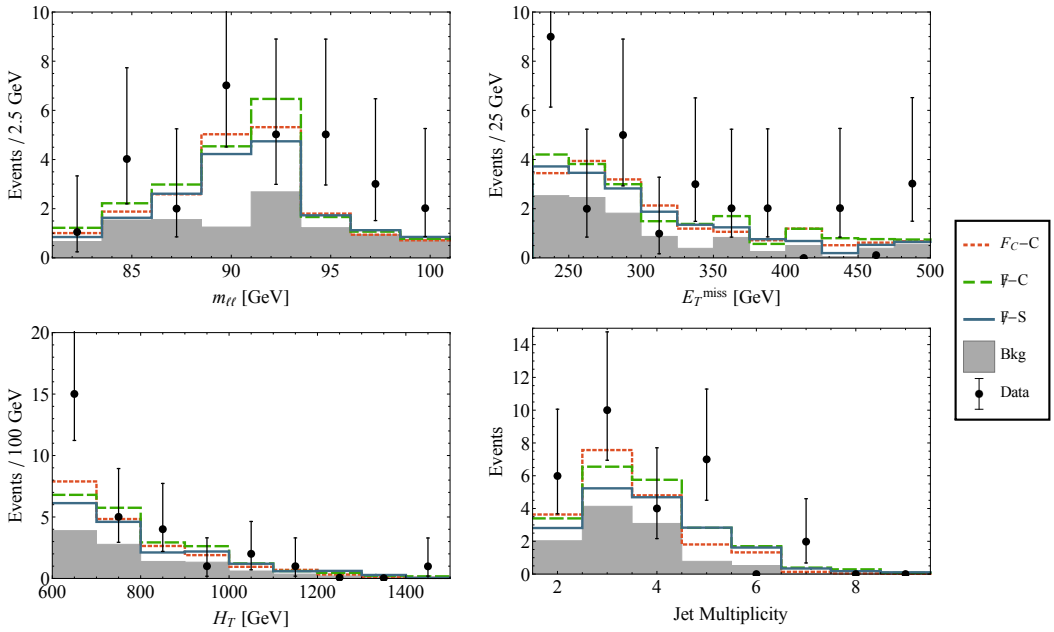

Figure 9.1: The kinematic distributions compared to those of ATLAS in the on-Z search. The simulation predictions are summed with the ATLAS-calculated SM background to produce the model predictions.

9.4.1 Kinematic distributions

To further check the consistency with the data we compare our $m_{\ell\ell}, E_T^{\rm miss}, H_T$, and $n_{\rm jets}$ distributions with those measured by the ATLAS on-Z search (these correspond to Fig.6 and 7 in [1]). To compare the quality of our signal we reproduce these plots in Fig. (9.1) using the results by ATLAS to retrieve the SM background. We see good agreement across all kinematic variables. In particular, unlike for other viable models which tend to peak at high number of jets (large numbers of jets is often accompanied by large H_T), we can roughly reproduce the jet multiplicity plot distributions. If the excess persists this could be a powerful variable to discriminate between candidate interpretations. We also note that this signal peaks at values for H_T and $E_T^{\rm miss}$ far below the the thresholds for the kinematic cuts of the ATLAS search, as opposed to models based on the cascade decays of much heavier particles that have been previously con-

sidered. Nonetheless, we still evade the bounds from the CMS search which has weaker $E_T^{\rm miss}$ cuts, due to the sharp increase in the background. For instance, the CMS background estimates were 478 ± 43, 39.2 ± 6.6, and 5.3 ± 2.3 events in the 100 GeV $< E_T^{\rm miss} <$ 200 GeV, 200 GeV $< E_T^{\rm miss} <$ 300 GeV, and $E_T^{\rm miss} >$ 300 GeV bins with $n_{jets} \geq 3$, while for the $\not{F} - C$ benchmark we predict 35, 11, and 5.4 events respectively. We see that the large event rates in the low $E_T^{\rm miss}$ are well within the background uncertainties.

9.4.2 Background contamination

Another interesting feature of our signal is that it allows for the possibility of significant background contamination in the CMS search for the same final state described in section 9.3.2. One of the most significant backgrounds in this search comes from SM Drell Yan (DY) production of Z bosons. To estimate this background, the CMS collaboration used two independent data-driven methods and took a weighted average. One of these methods is based on the variable 'jet-Z balance' (JZB) [46, 47], which is important particulatly in the high $E_T^{\rm miss}$ search regions which constrain our signal. The JZB of an event is defined by

$$\text{JZB} \equiv \Big| \sum_{i \in \text{jets}} \vec{p}_T^{\,i} \Big| - \big|\vec{p}_T^{\,(Z)}\big| = \big|\vec{E}_T^{\rm miss} + \vec{p}_T^{\,Z}\big| - \big|\vec{p}_T^{\,(Z)}\big|. \tag{9.6}$$

SM processes like DY production typically result in JZB distributions that are symmetric about JZB = 0 GeV (because a non-zero value arises from jet energy resolution effects), while some BSM processes can have JZB distributions that are strongly skewed towards positive values. This is expected when the Z is emitted back-to-back with an invisible particle, e.g. in a decay chain ending in $\tilde{\chi}_2^0 \to \tilde{\chi}_1^0 Z$. For this reason, the JZB method estimates the DY background by assuming all

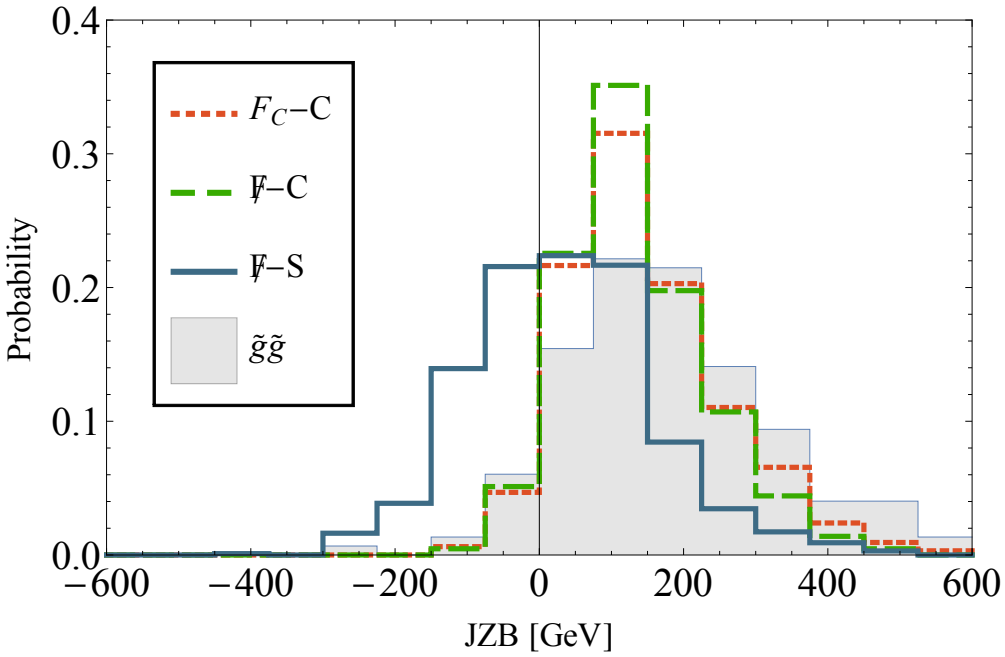

Figure 9.2: JZB probability distributions for the benchmark points when compared with a typical gluino production scenario ($\tilde{g} \to qq\chi_2^0 \to qq\chi_1^0 Z$). The gluino scenario has the most positively skewed JZB distribution, while the $\not{F}$-S has almost symmetrical JZB.

events with JZB < 0 GeV are produced by DY, and extrapolating this to positive JZB values under the assumption that DY production is JZB-symmetric.

It is clear therefore that signals with symmetric JZB distributions would contaminate this background estimate, reducing the sensitivity of the CMS search. In Fig. (9.2) we plot the JZB distributions after applying the cuts for the CMS $n_{\text{jets}} \geq 3$, mid E_T^{miss} bin for our three benchmark points, as well as for a gluino production model with the decay $\tilde{g} \to qq\chi_2^0 \to qq\chi_1^0 Z$ (we have chosen the parameters $m_{\tilde{g}} = 950$ GeV, $m_{\chi^0} = 50$ GeV). We find that the JZB distribution is highly sensitive to the $\tilde{t}_1$–$\tilde{t}_2$ mass splitting in this model. For small splitting, the Z tends to be very soft resulting in positive JZB. For large splitting, the hard Z can result in symmetric or even negatively skewed JZB distributions. The $\not{F}$-S benchmark point has 41% of events with JZB < 0 GeV, comparing with only 8% in the gluino

model. This also highlights the potential for the JZB distribution to be used as a discriminating variable between new physics explanations of this excess should it persist in the next run of the LHC, due to its sensitivity to where the Z is emitted.

9.5 Conclusion

Motivated by the recent 3σ excess reported by the ATLAS collaboration in a Z + jets + E_T^{miss} channel we have studied if it can potentially be explained in the context of a natural supersymmetric spectrum involving light stops. Strong constraints on such scenarios have led us to a compressed spectrum featuring two light and mixed stops and a light LSP. We identified three possible scenarios, characterized by flavor conserving or flavor violating decays of the lightest stop, and the splitting between the two stop masses. We have shown that in all three scenarios it is possible to produce the excess within 2σ, while in $\not{F}$-C and F_{C}-C we can reproduce the excess within 1σ of the ATLAS measurement. While the scenarios should be taken as examples, it is clear that possible interpolations between them are capable of addressing the excess and would retain the same general features. Such features are a light stop with 225 GeV $\lesssim m_{\tilde{t}_1} \lesssim$ 325 GeV, almost degenerate with a Bino-like LSP and mixed with a second light stop with mass 325 GeV $\lesssim m_{\tilde{t}_2} \lesssim$ 550 GeV.

The topology of the process differs from previous attempts to address the excess. The most substantial difference is the production of the Z's in the first step of a decay chain, and not in the last step in association with an invisible particle responsible for the E_T^{miss}. Interestingly, we have shown that it could lead to the contamination of background estimation based on the JZB method. This method

is employed in a CMS search for a similar final state. We have estimated that as much as half of the signal could fall in the background control region, which could lead to over-exclusions. Additionally, we notice that the JZB variable could be used to discriminate between different signal topologies if this excess turns out to be due to new physics.

Should this excess persist in run-II, it will be crucial to distinguish between the signal hypotheses. The signature proposed in this work is distinguished by its light compressed spectrum. This resulted in monojet searches being a highly sensitive probe of our signal. In addition, the search for $\tilde{b}_1 \to b\tilde{\chi}^0$ is highly complementary, and between these searches the region of parameter space which can explain the excess should be fully explored at 13 TeV.

We note in passing that there are additional modest excesses of around two sigma or more in final states containing b-jets, leptons and MET, including a 1.9 sigma 'on-Z' excess in events with low jet multiplicity [48], and various hints of same-sign dileptons with b-jets and MET (see [49] for a summary). Light stops and sbottoms can give rise to all of these signatures, and it is interesting to consider the possibility that if these really are all hints of new physics, they could have a unified explanation in a more complete model. Whether the ATLAS excess is a fluctuation or a first tantalizing hint of new physics will soon be decided.

BIBLIOGRAPHY

[1] **ATLAS** Collaboration, G. Aad et al., *Search for supersymmetry in events containing a same-flavour opposite-sign dilepton pair, jets, and large missing transverse momentum in $\sqrt{s} = 8$ TeV pp collisions with the ATLAS detector*, *Eur. Phys. J.* **C75** (2015), no. 7 318, [arXiv:1503.03290].

[2] D. Ghosh, *Boosted dibosons from mixed heavy top squarks*, *Phys. Rev.* **D88** (2013), no. 11 115013, [arXiv:1308.0320].

[3] N. Vignaroli, *Z-peaked excess from heavy gluon decays to vectorlike quarks*, *Phys. Rev.* **D91** (2015), no. 11 115009, [arXiv:1504.01768].

[4] U. Ellwanger, *Possible explanation of excess events in the search for jets, missing transverse momentum and a Z boson in pp collisions*, arXiv:1504.02244.

[5] J. Cao, L. Shang, J. M. Yang, and Y. Zhang, *Explanation of the ATLAS Z-Peaked Excess in the NMSSM*, *JHEP* **06** (2015) 152, [arXiv:1504.07869].

[6] B. Allanach, A. Raklev, and A. Kvellestad, *Consistency of the recent ATLAS $Z + E\_T^{\rm miss}$ excess in a simplified GGM model*, *Phys. Rev.* **D91** (2015) 095016, [arXiv:1504.02752].

[7] G. Barenboim, J. Bernabeu, V. A. Mitsou, E. Romero, E. Torro, and O. Vives, *METing SUSY on the Z peak*, arXiv:1503.04184.

[8] A. Kobakhidze, A. Saavedra, L. Wu, and J. M. Yang, *ATLAS Z-peaked excess in MSSM with a light sbottom or stop*, arXiv:1504.04390.

[9] M. Cahill-Rowley, J. L. Hewett, A. Ismail, and T. G. Rizzo, *The ATLAS Z + MET Excess in the MSSM*, arXiv:1506.05799.

[10] X. Lu, S. Shirai, and T. Terada, *ATLAS Z Excess in Minimal Supersymmetric Standard Model*, arXiv:1506.07161.

[11] S. P. Liew, A. Mariotti, K. Mawatari, K. Sakurai, and M. Vereecken, *Z-peaked excess in goldstini scenarios*, arXiv:1506.08803.

[12] J. Cao, L. Shang, J. M. Yang, and Y. Zhang, *Explanation of the ATLAS Z-peaked excess by squark pair production in the NMSSM*, arXiv:1507.08471.

[13] **CMS** Collaboration, V. Khachatryan et al., *Search for physics beyond the standard model in events with two leptons, jets, and missing transverse momentum in pp collisions at sqrt(s) = 8 TeV*, *JHEP* **04** (2015) 124, [arXiv:1502.06031].

[14] M. Blanke, G. F. Giudice, P. Paradisi, G. Perez, and J. Zupan, *Flavoured Naturalness*, *JHEP* **1306** (2013) 022, [arXiv:1302.7232].

[15] M. Backovi, A. Mariotti, and M. Spannowsky, *Signs of Tops from Highly Mixed Stops*, *JHEP* **06** (2015) 122, [arXiv:1504.00927].

[16] P. Agrawal and C. Frugiuele, *Mixing stops at the LHC*, *JHEP* **01** (2014) 115, [arXiv:1304.3068].

[17] C. Boehm, A. Djouadi, and M. Drees, *Light scalar top quarks and supersymmetric dark matter*, *Phys. Rev.* **D62** (2000) 035012, [hep-ph/9911496].

[18] C. Balazs, M. Carena, and C. E. M. Wagner, *Dark matter, light stops and electroweak baryogenesis*, *Phys. Rev.* **D70** (2004) 015007, [hep-ph/0403224].

[19] S. P. Martin, *A Supersymmetry primer*, hep-ph/9709356. [Adv. Ser. Direct. High Energy Phys.18,1(1998)].

[20] **ATLAS** Collaboration, G. Aad et al., *ATLAS Run 1 searches for direct pair production of third-generation squarks at the Large Hadron Collider*, arXiv:1506.08616.

[21] G. D'Ambrosio, G. F. Giudice, G. Isidori, and A. Strumia, *Minimal flavor violation: An Effective field theory approach*, *Nucl. Phys.* **B645** (2002) 155–187, [hep-ph/0207036].

[22] M. Muhlleitner and E. Popenda, *Light Stop Decay in the MSSM with Minimal Flavour Violation*, *JHEP* **04** (2011) 095, [arXiv:1102.5712].

[23] R. Grober, M. Muhlleitner, E. Popenda, and A. Wlotzka, *Light Stop Decays: Implications for LHC Searches*, arXiv:1408.4662.

[24] A. Dedes, M. Paraskevas, J. Rosiek, K. Suxho, and K. Tamvakis, *Mass Insertions vs. Mass Eigenstates calculations in Flavour Physics*, *JHEP* **06** (2015) 151, [arXiv:1504.00960].

[25] G. Cowan, K. Cranmer, E. Gross, and O. Vitells, *Asymptotic formulae for likelihood-based tests of new physics*, *Eur. Phys. J.* **C71** (2011) 1554, [arXiv:1007.1727]. [Erratum: Eur. Phys. J.C73,2501(2013)].

[26] A. L. Read, *Presentation of search results: The CL(s) technique*, *J. Phys.* **G28** (2002) 2693–2704. [,11(2002)].

[27] **ATLAS** Collaboration, G. Aad et al., *Search for direct top squark pair production in events with a Z boson, b-jets and missing transverse momentum in sqrt(s)=8 TeV pp collisions with the ATLAS detector*, *Eur. Phys. J.* **C74** (2014), no. 6 2883, [arXiv:1403.5222].

[28] **CMS** Collaboration, V. Khachatryan et al., *Search for top-squark pairs decaying into Higgs or Z bosons in pp collisions at $\sqrt{s}$=8 TeV*, *Phys. Lett.* **B736** (2014) 371–397, [arXiv:1405.3886].

[29] **ATLAS** Collaboration, G. Aad et al., *Search for squarks and gluinos with the ATLAS detector in final states with jets and missing transverse momentum using $\sqrt{s} = 8$ TeV proton–proton collision data*, *JHEP* **09** (2014) 176, [arXiv:1405.7875].

[30] **CMS** Collaboration, S. Chatrchyan et al., *Search for new physics in the multijet and missing transverse momentum final state in proton-proton collisions at $\sqrt{s}$= 8 TeV*, *JHEP* **06** (2014) 055, [arXiv:1402.4770].

[31] M. Drees, H. Dreiner, D. Schmeier, J. Tattersall, and J. S. Kim, *CheckMATE: Confronting your Favourite New Physics Model with LHC Data*, *Comput. Phys. Commun.* **187** (2014) 227–265, [arXiv:1312.2591].

[32] **ATLAS** Collaboration, G. Aad et al., *Search for top squark pair production in final states with one isolated lepton, jets, and missing transverse momentum in $\sqrt{s}$ =8 TeV pp collisions with the ATLAS detector*, *JHEP* **11** (2014) 118, [arXiv:1407.0583].

[33] **CMS** Collaboration, S. Chatrchyan et al., *Search for top-squark pair production in the single-lepton final state in pp collisions at $\sqrt{s}$ = 8 TeV*, *Eur. Phys. J.* **C73** (2013), no. 12 2677, [arXiv:1308.1586].

[34] **CMS** Collaboration, C. Collaboration, *Search for direct production of bottom squark pairs*, .

[35] **ATLAS** Collaboration, G. Aad et al., *Search for direct third-generation*

squark pair production in final states with missing transverse momentum and two b-jets in $\sqrt{s} = 8$ TeV pp collisions with the ATLAS detector, *JHEP* **1310** (2013) 189, [arXiv:1308.2631].

[36] **ATLAS** Collaboration, G. Aad et al., *Search for pair-produced third-generation squarks decaying via charm quarks or in compressed supersymmetric scenarios in pp collisions at $\sqrt{s} = 8$ TeV with the ATLAS detector*, *Phys. Rev.* **D90** (2014), no. 5 052008, [arXiv:1407.0608].

[37] **CMS** Collaboration, C. Collaboration, *Search for supersymmetry in events with soft leptons, low jet multiplicity, and missing transverse momentum in proton-proton collisions at sqrt(s) = 8 TeV*, .

[38] **ATLAS** Collaboration, G. Aad et al., *Search for Scalar Charm Quark Pair Production in pp Collisions at $\sqrt{s} = 8$TeV with the ATLAS Detector*, *Phys. Rev. Lett.* **114** (2015), no. 16 161801, [arXiv:1501.01325].

[39] J. Alwall, M. Herquet, F. Maltoni, O. Mattelaer, and T. Stelzer, *MadGraph 5 : Going Beyond*, *JHEP* **06** (2011) 128, [arXiv:1106.0522].

[40] T. Sjostrand, S. Mrenna, and P. Z. Skands, *PYTHIA 6.4 Physics and Manual*, *JHEP* **05** (2006) 026, [hep-ph/0603175].

[41] J. Conway, *Pretty good simulation*, .

[42] S. Padhi et al., *LHC SUSY cross sections working group*, 2015.

[43] **DELPHES 3** Collaboration, J. de Favereau et al., *DELPHES 3, A modular framework for fast simulation of a generic collider experiment*, *JHEP* **1402** (2014) 057, [arXiv:1307.6346].

[44] M. Cacciari, G. P. Salam, and G. Soyez, *FastJet User Manual*, *Eur. Phys. J.* **C72** (2012) 1896, [arXiv:1111.6097].

[45] M. Cacciari, G. P. Salam, and G. Soyez, *The Anti-k(t) jet clustering algorithm*, *JHEP* **04** (2008) 063, [arXiv:0802.1189].

[46] **CMS** Collaboration, M.-A. Buchmann, *Search for supersymmetry in events with a Z boson, jets and missing energy*, *EPJ Web Conf.* **28** (2012) 12017, [arXiv:1201.3748].

[47] **CMS** Collaboration, C. Collaboration, *Search for Physics Beyond the Standard Model in Z + Jets + MET events at the LHC*, .

[48] **CMS** Collaboration, C. Collaboration, *Search for supersymmetry in pp collisions at* $\sqrt{(s)} = 8$ *TeV in events with three leptons and at least one b-tagged jet*, .

[49] P. Huang, A. Ismail, I. Low, and C. E. M. Wagner, *Same-Sign Dilepton Excesses and Light Top Squarks*, `arXiv:1507.01601`.